UNIVERSITY OF SOUTHAMPTON

FACULTY OF ENGINEERING
AND THE ENVIRONMENT

The Application of the Discrete Element Method to Integral Bridge Backfill

By

YAP, Fook Liong
2 00188107

Thesis for the degree of Doctor of Philosophy
(Civil Engineering)

November 2011

UNIVERSITY OF SOUTHAMPTON

ABSTRACT

FACULTY OF ENGINEERING AND THE ENVIRONMENT

MPhil/ PhD

THE APPLICATION OF THE DISCRETE ELEMENT METHOD TO

INTEGRAL BRIDGE BACKFILL

By Fook Liong, Yap

Expansion joints and bearings of conventional bridges are easily damaged and this commonly incurs high maintenance costs. The concept of the integral bridge was to reduce the maintenance costs by removing those joints. However, the thermally induced expansion-contraction of the bridge superstructure is transferred through the integral bridge's abutments due to lack of expansion joints. Seasonal thermal cyclic displacement of the integral abutment cyclically loads the bridge backfill material. It has been observed that the lateral earth pressure behind an integral abutment increases as a result of the cyclic loading. Previous studies attribute this increase in lateral pressure to the densification of the backfill material. Granular flow was suggested to have occurred displacing the particles to form a denser and therefore stiffer matrix. An alternative suggestion was that the particles reoriented to form a stiffer matrix that wasn't necessarily denser. The objective of this research is to explore the behaviour of integral abutment backfill at a micro-mechanical level by utilising the discrete element method (DEM) and possibly verify these suggested causes of earth pressure build-up behind an integral abutment. DEM models of four granular materials consisting of different particle shapes were tested with 100 cycles of strain. The results indicate that densification occurred for all samples, but the build-up of horizontal pressure did not occur for the more rounded samples. It was further suggested that the particle shape in combination with the change in coordination number closely replicate the behaviour of the sample's horizontal stress. Particle reorientation and displacements were observed to be small for samples of non-circular particles. Particle activity is concentrated in the smallest particles within the material. It is concluded that the build-up of horizontal stress is caused by the increase in particle contacts due to particle reorientation and not densification.

CONTENTS

CONTENTS

<u>CONTENTS</u>

CONTENTS

<u>CONTENTS</u>

APPENDICES

LIST OF FIGURES

LIST OF FIGURES

LIST OF FIGURES

LIST OF TABLES

Notations

2-D – Two dimensional

3-D – Three dimensional

a – particle acceleration

α – Coefficient of thermal expansion

c'_{peak} – Peak effective cohesion

d – Thermal displacement at top of abutment

D_{10} – Particle size of the 10th percentile of material passing through in a sieve test

D_{60} – Particle size of the 60th percentile of material passing through in a sieve test

DEM – Discrete element method

Displacement – Displacement of wall

dt – Time-step

dx – change in horizontal coordinate of a particle

dy – change in vertical coordinate of a particle

dθ – angles turned

|dθ| - absolute angles turned

EBT – Effective Bridge Temperature

$ε_H$ – Horizontal strain (used by Tsang et al., 2002)

$η_0$ – Initial sample porosity

$η_{sample}$ – Sample porosity

$η_{measured}$ – Measured porosity

F – Particle form (used by Clayton and Reddy, 2006)

FRP – Fibre reinforced polymer

$Φ'$ – effective angle of shear

$Φ'_{peak}$ – Peak effective angle of shear

h – Height of sample

h_0 – Initial height of sample

H or $H_{retained}$ – Retained height

K – Coefficient of earth pressure, stress ratio between horizontal and vertical stress

K_0 – Coefficient of earth pressure at rest

K_p – Coefficient of passive earth pressure

K^* – Coefficient of earth pressure accounting the effect of cyclic loading

k – Stiffness value of a particular ball or wall

K – Effective stiffness between two or more entities in contact

L – Width of sample

L_0 – Initial width of sample

m – Particle mass

PSD – Particle size distribution

r – Radii of smaller sphere/ disc in a cluster or clumped particle

R – Radius of largest sphere/ disc in a cluster or clumped particle

R – Particle roundness (used by Clayton and Reddy, 2006)

R_i – Radius of largest inscribed circle in a particle

R_c – Radius of smallest circumscribing circle in a particle

RC – Reinforced concrete

ρ – Particle density

ρ_{design} – Design density

$\rho_{dry\ max}$ – Maximum dry density

$\rho_{95\%}$ - 95% of maximum dry density

Steps – Number of calculation steps

σ_H – Horizontal stress

σ_V – Vertical stress

$\theta_{initial}$ – initial angle of a particle

$\theta_{current}$ – current angle of a particle

θ_{final} – angle of a particle at the end of the cyclic test

U – Uniformity coefficient

$V_{sample\ void}$ – Volume of sample void

V_{solid} – Volume of solid

V_{mc} – Volume of measurement circle

V_{ts} – Total sample volume

v – Particle velocity

v_{wall} – Wall velocity

wexx – Horizontal strain as used in PFC2D

weyy – Vertical strain as used in PFC2D

$(X_{initial}, Y_{initial})$ – Cartesian coordinate of a particle initially

(X_{final}, Yf_{inal}) – Cartesian coordinate of a particle at the end of the cyclic test

Acknowledgements

I express my sincerest thanks to my supervisor Dr. Alan Bloodworth for his advice, and guidance on this research project. I am especially grateful for his patience with me when I always seem to miss my deadlines.

My gratitude also, to Dr. Richard Harkness, Dr. John Harkness and Dr. Lock, who would help fix the connection to the computer running the PFC2D program whenever I couldn't connect. Without his reassuring assistance, it would have been difficult to complete the DEM simulations and gather the data I needed.

I also extend my thanks to Mrs. Jacqui Holmes for sorting out all the administrative things not to mention her constant reminders on deadlines.

A special thanks to my Christian fellowship for their support and prayers throughout this project. I also wish to thank my friends, Lemuel and Geraldine for their help with Microsoft EXCEL when I was processing my data. I especially give thanks also, to my fellow PhD candidate friends Jacq and Mindy, for sharing in the excitement and frustration of academic research. It would have been despairing without a peer experiencing similar hurdles to talk to. Truly, I give thanks to Lord Jesus for this fellowship of support and indeed the challenge that is the research project.

Finally, I express my thanks to my family who've kept encouraging me on this academic pursuit. I am grateful for their patience, empathy, understanding and prayers for my well-being.

DECLARATION OF AUTHORSHIP

I, Fook Liong Yap

declare that the thesis entitled

The application of discrete element method to integral bridge backfill

and the work presented in the thesis are both my own, and have been generated by me as the result of my own original research. I confirm that:

- this work was done wholly or mainly while in candidature for a research degree at this University;

- where any part of this thesis has previously been submitted for a degree or any other qualification at this University or any other institution, this has been clearly stated;

- where I have consulted the published work of others, this is always clearly attributed;

- where I have quoted from the work of others, the source is always given. With the exception of such quotations, this thesis is entirely my own work;

- I have acknowledged all main sources of help;

- where the thesis is based on work done by myself jointly with others, I have made clear exactly what was done by others and what I have contributed myself;

- none of this work has been published before submission, **or** [delete as appropriate] parts of this work have been published as: [please list references]

Signed: …………………………………………………………………..

Date:………………………………………………………………….

Chapter 1: Introduction

1.1 The problem with conventional bridges

Conventional bridges are constructed with expansion joints and bearings at the connection between the bridge superstructure and the abutments. These are to account for the seasonal thermal expansion of the bridge deck. However, joints are prone to damage, incurring repair and maintenance costs post-construction. It is noted that the most serious source of damage to joints is salty water leaking through joints in the deck or service ducts and poor, faulty and badly maintained drainage systems (DMRB BA57/01, 2001).

1.2 The solution: integral bridges

In order to solve the problem with regards to joint damage, the idea emerged to eliminate the joints altogether; hence utilization of monolithic structures known as integral bridges. In an integral bridge, the abutment is connected to the bridge deck without any movement joint for expansion or contraction of the deck (DMRB BA42/96, 2003). In principle, continuous bridge decks should be used wherever possible because they are more durable than simply supported decks.

Figure 1.1 illustrates the difference between integral abutment bridges and conventional bridges. The lack of joints in the integral bridge structure eliminates all associated problems with expansion joints and the costs required to repair or replace them. There are other advantages to integral abutment bridges including an added redundancy which would provide for extreme loading events and a relatively shorter construction time compared to conventional bridges (Mistry, 2005).
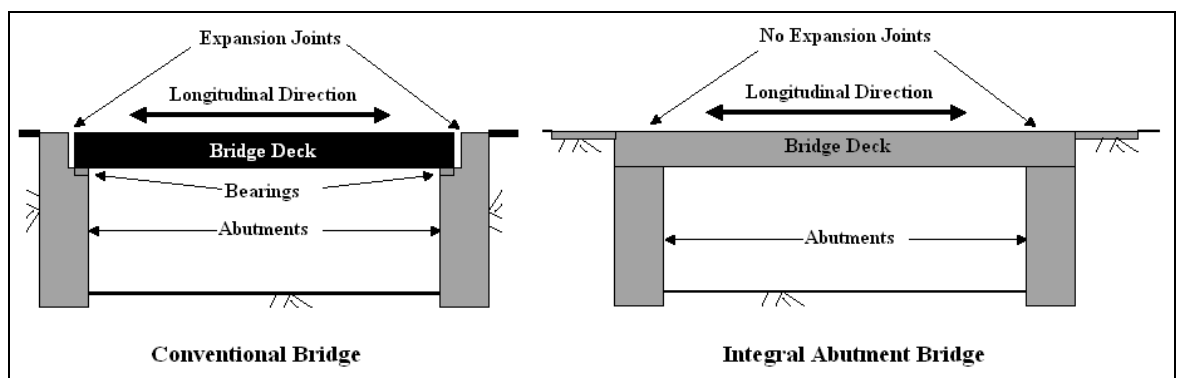
Figure 1.1: Conventional Bridge versus Integral Abutment Bridge (Modified from Horvath, 2005)

1.2.1 Types of integral bridges

There are different types of integral bridges, each associated with the different types of integral abutment constructions. The Design Manual for Roads and Bridges (DMRB BA42/96, 2003) identified four types: frame, embedded, bank pad and end screen; illustrated here in Figure 1.2.
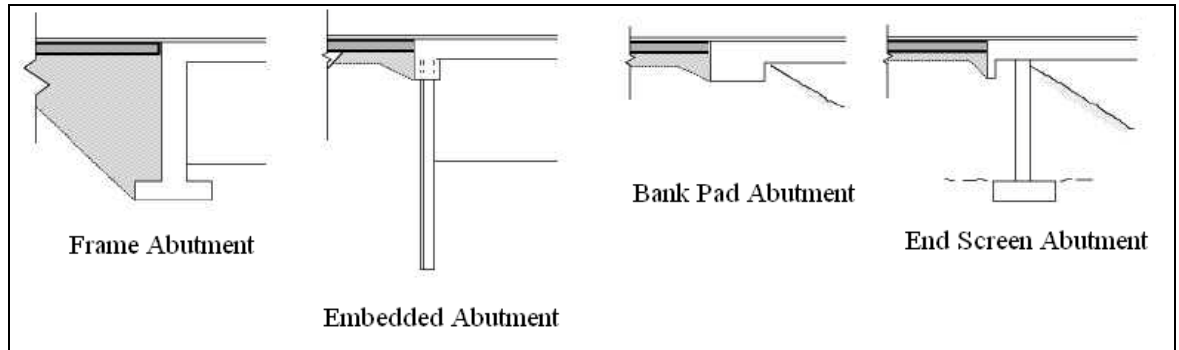
Figure 1.2: Four types of Integral Abutment (DMRB BA42/96, 2003)

The Frame abutment supports the vertical load from the bridge and acts as a retaining wall against the embankment earth pressure. The Embedded abutment extends to a depth below the retained fill like a diaphragm wall (DMRB BA42/96, 2003). These are 'full height abutments' that retain the backfill over the full height of the bridge.

The Bank Pad abutment acts as an end support for the bridge moving horizontally during thermal expansion or contraction of the deck. The End Screen abutment acts as a retaining wall only, transferring the vertical load to separate supports (DMRB BA42/96, 2003). These are 'shallow abutments' since they only retain a shallow layer of soil behind the abutment.

Two types of full height reinforced concrete integral abutment are the embedded abutment and the frame abutment. The embedded abutment is constructed *in-situ* typically in stiff clayey ground while frame abutments are backfilled with granular materials. Both of these full height abutment types are widespread in the UK (Xu, 2005). Shallow abutments such as the bank pad abutments and the end screen abutments are less common in the UK.

Full height abutments are a type of earth retaining wall. Common types of earth retaining structure include L- and T- cantilever walls as well as embedded retaining walls (Powrie, 2004). L- and T- cantilever walls resist lateral pressure by bending while the sliding and overturning of the structure are prevented by the weight of retained soil acting on a platform behind the wall which projects beneath the backfill, or by means of a piled foundation to the base.

Cantilever walls are backfilled walls, where the difference in level is created by building up the retained height of the soil behind. Embedded retaining walls which could be made of steel sheet piles, RC piles or reinforced concrete diaphragm walls are supported by lateral earth pressure of soil in front of the wall. Usually, embedded walls are used in clay soils in built up areas such that the wall could be constructed with minimum disturbance to the surrounding ground, where the difference in level is created by removing soil from in front (Powrie, 2004).

1.2.2 Foundations of integral abutments

Similar to retaining walls, integral abutments will have different foundations for different circumstances. Integral abutments can be founded on spread footings or on piles (DMRB BA42/96, 2003).

The more common foundation type for supporting integral abutments in the United States is the steel H-pile. Depending on the bridge length and site conditions, other foundation systems could be used, such as pre-stressed concrete pile, pipe pile, sheet pile and spread footing (Dunker and Liu, 2007).

A finite element analysis of the interaction between the abutment, the approach fill, the foundation soils and the supporting piles showed that the interaction reduces the stresses in the piles (Duncan and Arsoy, 2003; Arsoy, 2000).

The foundations of integral abutments affect how the abutments respond to thermal movements of the bridge superstructure. This project however will focus solely on the full height spread based frame integral abutment, similar to a T-cantilever retaining wall.

1.3 Problems with integral bridges

Integral bridges do not accommodate for the superstructure's thermal expansion and contraction due to temperature change, which was traditionally dealt with by the expansion joints. With no expansion joints, the thermal expansion and contraction of the bridge is carried over to the integral abutment of the bridge. The integral abutment which retains the backfill soil now loads the retained soil cyclically in accordance with the bridge superstructure's thermal expansion and contraction.

Therefore, the problems that occur due to the temperature variations in integral bridges are geotechnical in nature. Two significant problems for integral bridges have been identified: the seasonal and long term build-up of lateral earth pressure behind the abutments, and the ground surface settlement adjacent to the abutments (Horvath, 2004). Most research into integral bridges associates the build-up of lateral earth pressure, when it occurs, to the densification of the backfill material as it is cyclically loaded by the abutment, leading to an overall stiffer backfill.

While field observations and laboratory tests have investigated these problems, they do not account for the entire service life of the integral bridge. It would be impractical to monitor an integral bridge for its design life of 120 years. Small scale and centrifuge tests in the laboratory have been useful in reducing the difficulties associated with field observations such as the time scale but are still limited by the physical scale and/or experimental design. Field observations, small scale and centrifuge tests enable the observation of the integral abutment and its backfill at system level, involving both the abutment and backfill. They do not provide data directly for understanding the backfill behaviour behind an integral abutment. In other words, further investigations into the behaviour of granular materials subjected to cyclic loading or straining were required.

A cyclic triaxial test was developed by Xu (2005) to study the behaviour of a soil element under cyclic straining. It was inferred from the results that the cause of the increase in earth pressure was due to the reorientation of the non-spherical particles and not necessarily the densification of the granular material.

1.4 Numerical Modelling

The general modelling of soils has been concentrated on monotonic loading, often based on constitutive models with empirical parameters. The backfill behind integral abutments experiences strains and stresses which are cyclical because of the seasonal and daily temperature variations. Existing constitutive soil models does not model the micromechanical aspects of soils, or their behaviour under cyclic loading (without advanced parameters).

Finite element models of the integral bridge problem have been made and were able to reproduce behaviours similar to those observed in a physical centrifuge model test for displacements and earth pressure (Springman et al. 1996). However, neither the numerical model nor the centrifuge tests give any information of the particle behaviour within the backfill material due to the cyclic loading of an integral abutment.

The discrete element method (DEM), which models soil as an assembly of particles, may be a better numerical technique for modelling backfill under cyclic loading conditions. However, in order to properly model the soil-structure interaction problem of integral bridges, large computing power is required. With the advent of increasingly powerful computers, the discrete element method of numerical modelling grows more feasible.

The DEM is utilized in this research project to investigate the micro-mechanical behaviour of integral bridge backfill material. The results provide a better understanding of granular material behaviour when subjected to cyclic strains. They will also verify if the reorientation of non-spherical particles due to cyclic loading increases the overall stiffness of the backfill, as postulated by Xu (2005).

1.5 Objective and research question

The main objective of this research project is to investigate the behaviour of granular material subjected to cyclic straining utilizing the discrete element method (DEM). It will further verify if the reorientation of non-spherical particles is the cause of increasing stiffness in the granular material according to Xu (2005). The aim is to infer from the DEM tests' results the micro-mechanical behaviour of the integral bridge backfill.
The main research questions are:

In light of the DEM simulation data, what is the behaviour of a granular material when subjected to cyclic straining? And what is the cause of lateral earth pressure build-up behind an integral abutment?

1.6 Thesis Outline

Chapter 2 Literature Review – A review of literatures covering integral bridges, lateral earth pressures and the numerical modelling of soils subjected to monotonic and cyclic loading as well as the current UK design standard BA42 and other relevant design manuals for roads and bridges. This chapter provides a brief summary of the relevant findings of previous research on the problems and solutions of integral abutments.

Chapter 3 Preliminaries –This chapter describes important aspects and parameters which are essential to running a DEM model of granular backfill material for this research project. This includes the damping, gravity field, sample size, particle density, stiffness values, particle grading, particle shape, clump logic, the time-step and wall speed concept and the initial sample density. The final section introduces the four particle shapes that were modelled.

Chapter 4 Research Methodology –This chapter details how the four samples of different particle shapes were cyclically strained, how the sample represented an element behind an integral abutment and the parameters monitored. The macro-mechanical parameters are the horizontal and vertical stresses, the horizontal and vertical strains, porosity and coordination number. The micro-mechanical parameters are the position and angles of individual particles within the respective samples which are used in the calculation of particle displacements and angles turned.

Chapter 5 Results and Discussion –This chapter discusses the results of all the DEM simulations in terms of the monitored parameters (stresses, strains, porosity and coordination number, particle displacements and angles turned). The four sample's results were also discussed separately identifying the similarities and differences between them as well as their implications.

Chapter 6 Conclusions and Recommendation –This chapter draws the conclusions based on the results from the previous chapter, attempting to provide an answer to the research question of what causes the horizontal stress build-up. The chapter closes with the noted limitations of the study and gives recommendations for future directions of research with respect to modelling integral abutment backfill with DEM.

Chapter 2: Literature Review

2.1 Popularity of integral bridges

Most existing literatures on the integral bridge have identified its' overall advantage over the conventional bridge. The following is a general summary of the conclusions regarding integral bridges when compared to conventional bridges.

A numerical study concluded that the deck slab stresses (due to live loads) of integral bridges are lower than that of an equivalent simply supported bridge. Results indicated that integral bridges distribute loads more uniformly than their jointed counterpart (Mourad, 1999). This is because the integral joints provide partial fixity at the joint, reducing the maximum bending moment experienced by the bridge superstructure. This is further confirmed in a numerical study involving 3-D models of a simply supported bridge and an integral bridge where it was observed that the deflection and bending moments were greatly reduced in the integral bridge (Mayur Babu and Bhandari, 2006).

Although bridges with deck-end joints still predominate, there is an increasing trend towards the use of integral abutment bridges (Mistry, 2005). A survey conducted in the United States in 2004 indicated integral bridges usage increased by over 200% within 10 years (Maruri et al, 2005).

There is a subsequent deterioration of bridge performance when joints do not perform satisfactorily. The cost associated with proper maintenance of the joints and the FHWA's (Federal Highways Agency, USA) goal to build bridges with 75-100 years' service life with minimal maintenance are some reasons that integral bridges are the construction of choice where feasible (Maruri et al, 2005). Departments of Transport of most states (in the United States) have a pro-integral bridge policy due to their experience of excellent service performance with these structures (Yannotti et al, 2005; Conboy et al, 2005).

Integral bridges are also increasingly popular in the UK and widely encouraged. In principle, bridges with lengths not exceeding 60 m and skews not exceeding 30° shall be designed as integral bridges, with the abutments connected directly to the bridge deck without movement joints for expansion or contraction of the deck (DMRB 1.3.7, BA57/01: 2.3, 2001). However, there have been constructions of integral bridges of over 300 m in length in the United States, for example the Tennessee State route 50 over Happy Hollow Creek with an overall span of 358 m (Hassiotis and Roman, 2005).

Increasing popularity of the integral bridge will require more economic design in the near future. It is therefore important to understand any problems associated with integral bridge structures, especially the build-up of lateral earth pressure behind the abutment.

2.2 Integral abutment movements

2.2.1 Thermal expansion and contraction

Bridges expand and contract due to temperature changes and these movements are estimated for design (Roeder, 2003). An analysis of data from a full scale testing of an integral abutment bridge showed that the bridge displacement is a linear function of the temperature (Hassiotis et al., 2005).

Daily and seasonal fluctuations in shade air temperature and solar radiation cause changes in the effective temperature of a bridge which in turn govern its movement (DMRB BD37/01, 2001). The Effective Bridge Temperature (EBT) is defined as an average temperature within the superstructure which governs the longitudinal movement of the deck (Emerson, 1976; cited by Xu, 2005). Minimum and maximum EBT for design purposes are derived from minimum and maximum isotherms of shade air temperature for different type of construction (e.g. concrete, steel, composite). However, these data are applicable to UK locations only (DMRB BD37/01, 2001; cited by Xu, 2005).

According to the design manual DMRB BA42/96 (Highways Agency, 2003), the longitudinal movement of integral abutments should be limited to ±20mm (nominal, 120-year return period) from the position at time of restraint during construction. This is an arbitrary design limit to ensure that the integral abutments does not displace excessively.

Thermal movement of the bridge deck is determined by first obtaining the EBT range from the maximum and minimum isotherm (based on meteorological office data) of a particular area; then multiplying it with the coefficient of thermal expansion, α, which is taken as $12\times10^{-6}/°C$ for concrete (Highways Agency, DMRB BD37/01, 2001).

For a 60 m concrete integral bridge in London, the EBT range would be approximately 43°C. Multiplied by the deck length and the coefficient of thermal expansion, the total thermal movement of the bridge deck is 0.03096 m, or approximately 31 mm. Assuming that the thermal movement is equal at both ends of the bridge, then the total abutment top horizontal movement is approximately 16 mm. Xu (2005) estimated annual deck length change and abutment top horizontal displacement for different deck lengths, assuming $\alpha = 12\times10^{-6}/°C$, the coefficient of thermal expansion for concrete. These estimates are shown in the following table 2.1.

Table 2.1: Annual concrete deck length change and abutment top horizontal displacement (Xu, 2005)

Concrete Deck Length (m)	Annual total deck length change (mm)	Annual total abutment top horizontal displacement d(mm)	$\pm d/2$ (mm)
90	48	24	±12
60	32	16	±8
30	16	8	±4

It is noted that the nature and magnitude of the cyclic displacements imposed on the abutments and backfill soil are dependent not only on the environmental temperature but also on the type of bridge deck construction. This is largely due to the different thermal properties of the material used whether it's steel, concrete or composite steel-concrete (England et al., 2000).

2.2.2 Starting seasons

The thermal movement of the bridge superstructure causes movement in the integral abutments attached to it since there are no expansion joints. As the integral bridge enters service, it is already affected by the seasonal thermal movement, inducing cyclic loading on the backfill. Therefore the initial direction of the integral abutment's cyclic movement will depend on the completion date of the integral bridge.

England et al. (2000) showed that the starting season only affects the early stresses in the first thirty large cycles (representing thirty years). During these early cycles, a winter-start results in the largest horizontal stress on the abutment and summer-start results in the lowest with spring-start in between them. These differences cease to be significant in the long term as the stresses converged. It was therefore concluded that the starting season affects the stresses in the early cycles but has no significant influence in the long term (England et al., 2000).

2.2.3 Seasonal and daily thermal movement

Seasonal and diurnal (daily) cyclic action of the abutment may lead to densification of the backfill and an increase in the peak lateral stresses acting on the abutments in the summer months (Barker and Carder, 2001).

The diurnal components of temperature change consist of daily shade temperature changes and a solar effect (Oesterle and Volz, 2005). The effects of environmental loading due to solar radiation and changing ambient temperature were found to be as large as or larger than the effects of live loads for an integral bridge in Rochester, Minnesota, USA. (Lawver et al., 2000; Huang et al., 2004)

Experimental results showed the importance of the inclusion of daily thermal displacement cycles with the seasonal. An analysis that considers the seasonal loads only ignores the detrimental contribution of the daily loads (Arsoy et al., 2005). A scaled model experiment also showed that the daily wall movements induce more soil densification and deformation. The inclusion of daily wall movements with the seasonal movements may increase the settlement adjacent to the wall (England et al., 2000).

The daily thermal movements can be described as small cyclic movements that are more frequent than the larger and slower seasonal thermal movements. Daily thermal loading only exacerbates the effects of cyclic loading or straining of the granular material, i.e. larger horizontal stress, greater densification and increased settlement. It does not affect the overall trend of the pressure build-up and settlements, but contributes to it. As such, the daily thermal movement will not be included in this research project but only the seasonal thermal movement is considered.

2.2.4 Types of integral abutment movement

Centrifuge model tests of a spread based integral bridge abutment identified two forms of abutment movement (Springman et al., 1996), as shown in Figure 2.1:

1. Rigid body motions which consists of translational and rotational motion; and
2. Bending deflections
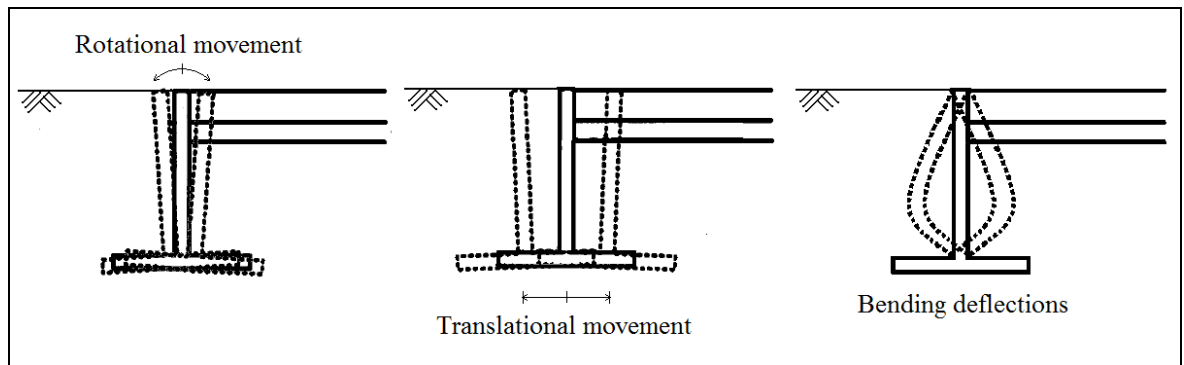
Figure 2.1: Rigid body movements and bending deflections (Modified from Springman et al., 1996)

Rigid body motions of the integral abutments are more common than bending deflections as reported in the literature on field observations of integral bridges. This project will only consider the rigid body motions.

Rotational movement

The integral bridge at Scotch Road, Trenton, New Jersey, USA, was observed to have abutment rotation in the summer months (up to 0.1°) that were twice as large as those observed in winter months (up to -0.06°) (Hassiotis et al., 2005). Rotational movement is

mainly due to the temperature variation along the depth of the girder which is negligible during the winter.

2-D and 3-D finite element models of an integral bridge verified by field data indicate that its primary accommodation of superstructure expansion and contraction is through rotation of the abutment about its base rather than longitudinal translation (Fenema et al., 2005). The field data was obtained from a Pennsylvania bridge site. The integral bridge is similar to an embedded abutment supported by a single row of H-piles.

Translational movement

However, field measurements of another integral bridge similar to an embedded abutment supported by H-piles for the Department of Transport of Indiana, USA, showed that the abutment primarily translates or 'slides' longitudinally in response to thermal expansion and contraction of the bridge. Minor rotations of the abutment did occur, but are insignificant for this case (Frosch et al., 2005). The abutment of an integral bridge in Rochester, Minnesota, USA, was observed to accommodate superstructure expansion and contraction through horizontal translation as well (Lawver et al., 2000; Huang et al., 2004). The integral abutment concerned was supported on H-piles.

Rotational + Translational movement

An evaluation of collected data from the Orange-Wendell Bridge in Massachusetts concluded that the abutments undergo rigid body displacements which comprise translational and rotational components. The complex relationship between translation and rotation exhibited yearly variations but fully characterises the abutment deformation response (Brena et al., 2007).

Contradicting observations in both field measurements and finite element models show that the integral abutment accommodates thermal movements by horizontal translation and/or rotation. Generally, the integral abutment displacement is a combination of both translational movement and rotational movement (about its base) in which one may dominate over the other.

At mid-depth behind the integral abutment, an element of the backfill experiences similar cyclic loading from the abutments' movement regardless of whether it was a translational, rotational or a combination of both types. This research project is focused on the backfill behaviour rather than the abutment itself. For the simulation models, a rigid translational movement of the abutment was assumed.

2.3 Effects of integral abutment movements

Literature suggests that the main effects of the cyclic movements of the integral abutments due to seasonal and diurnal temperature changes are:

1. Increasing lateral earth pressure
2. Soil settlement behind the integral abutment

A secondary issue to consider is whether the lateral earth pressure would perpetually continue to increase with cycles or come to a steady stress value after a certain number of cycles. Similarly, for the soil settlement there is a question of whether or not the soil would continue settling downwards with cycles or reach a steady level after some cycles.

2.3.1 Increasing lateral earth pressure

An integral abutment bridge in Scotch Road, Trenton, New Jersey (USA) was monitored as part of a program by the New Jersey Department of Transportation to revise design specifications on integral bridges (Hassiotis, Lopez et al., 2005). The bridge is a two-span continuous steel-girder structure supported on a conventional pier with fixed bearings and integral abutments at both ends. It is 90.9 m long with a skew of 15°. The abutments are 900 mm thick and averages 3.34 m in height, each supported on single row piles. Thermocouples, strain gauges and pressure gauges were placed on and around the bridge to monitor the bridge temperature, bending moments in piles, axial stresses in the girders and also the soil pressure variation behind the abutment wall. The bridge was instrumented during construction and continually monitored for two years. Excellent correlation between temperature and abutment displacement was observed. It was further observed that a steady build-up of soil pressure was measured behind the abutment. This significant pressure build-up was attributed to sand particle flow and densification due to cyclic loading as well as the shearing of dense sand during bridge expansion (Khodair, 2006).

An integral abutment bridge spanning the Millers River on Wendell Depot Road between the towns of Orange and Wendell was instrumented and monitored for a period of three years from 2002 to 2004. The bridge consists of three continuous spans with a total length of 82.3 m supported at 0° skew on integral abutments at each end and two reinforced concrete beams. Peak earth pressure at 2.5 m depth from the top of the abutment was observed to increase yearly from 245 kPa (2002) to 280 kPa (2003) and 315 kPa (2004). Similar increases in earth pressure were also observed from pressure cells located at other depths behind the abutment. (Brena et al., 2007).

The Manchester Road Overbridge consists of two 40 m span integral bridges side by side carrying the A62 over the M66 Manchester Outer Ring Road (Denton to Middleton). The field performance of the two integral bridges was monitored during construction and over the first two years of service. The first bridge (phase 1) was a conventional portal frame structure retaining granular backfill. The second bridge (phase 2) was constructed with contiguous bored pile abutments founded on glacial till. Particularly for phase 1, as the bridge deck expanded, lateral stress increased implying a strong correlation between lateral stresses and bridge temperature. The lateral stresses after backfilling were consistent with values predicted using the earth pressure coefficient at rest (K_0), calculated from experimentally obtained value of effective angle of shear Φ'. Backfilling took place in the summer months and the measured lateral stress started to reduce as the bridge deck contracted with the approach of winter. In the following summers, lateral stresses were slightly more than those calculated from the earth pressure coefficient at rest. As backfilling and earth reinforcement took place during summer, the first indication of significant lateral stress escalation behind the abutment was expected to develop after many more seasonal cycles of movement (Barker and Carder, 2000).

Field performance of a two-span integral bridge of 50 m total length over the M1-A1 Link Road at Bramham Crossroads, North Yorkshire was monitored. The bridge deck consists of pre-stressed concrete beams with in-situ deck which are structurally connected to full height integral abutments founded in magnesium limestone. Field measurement was obtained during construction and over the first three years of service. Measured lateral earth pressures after backfilling was consistent with values predicted from coefficient of earth pressure at rest (K_0) calculated based on estimated value of effective angle of shear Φ'. Data indicates that the lateral earth pressure were slightly higher than the K_0 values each following summer (Barker and Carder, 2001).

The Manchester Road Overbridge, A62 and the integral bridge over the M1-A1 Link Road at Bramham Crossroad were revisited three years later in 2004 to monitor the change in lateral earth pressures with deck temperatures over the next year (until 2005). For the Manchester Road Overbridge A62, no indication of any lateral earth pressure escalation was observed from the pressure cells since 2001. However, it was reported that the construction detail of the abutment, consisting of a 25 mm thick compressible packing layer separating the 2.4 m deep reinforced earth backfill from the top of the abutment wall may have eliminated the possibility of stress escalation in the structure's early life. For the integral bridge over the M1-A1 Link Road at Bramham Crossroads, some escalation of lateral earth pressure was observed especially in the shallower pressure cells although these pressure changes were quite small. Data indicates that the effects of creep and shrinkage of

the prestressed deck beams are complete. Further monitoring of the integral bridge was recommended to establish if the observed small stress changes would continue to escalate annually or if the stress levels have stabilised. (Barker and Carder, 2006)

The increase of lateral earth pressure in integral bridge backfill is further confirmed in a cyclic triaxial test on Leighton Buzzard Sand (Xu, 2005). Figure 2.2 illustrates the curves of deviator stress and earth pressure coefficient K of samples under cyclic straining. Samples of different densities were subjected to cyclic radial strain ranges that were expected in a soil element at mid-height behind a typical frame integral abutment. The results show that maximum horizontal stress continued to build up towards the passive state. The horizontal stress is expressed in terms of deviatoric stress for a constant vertical stress.
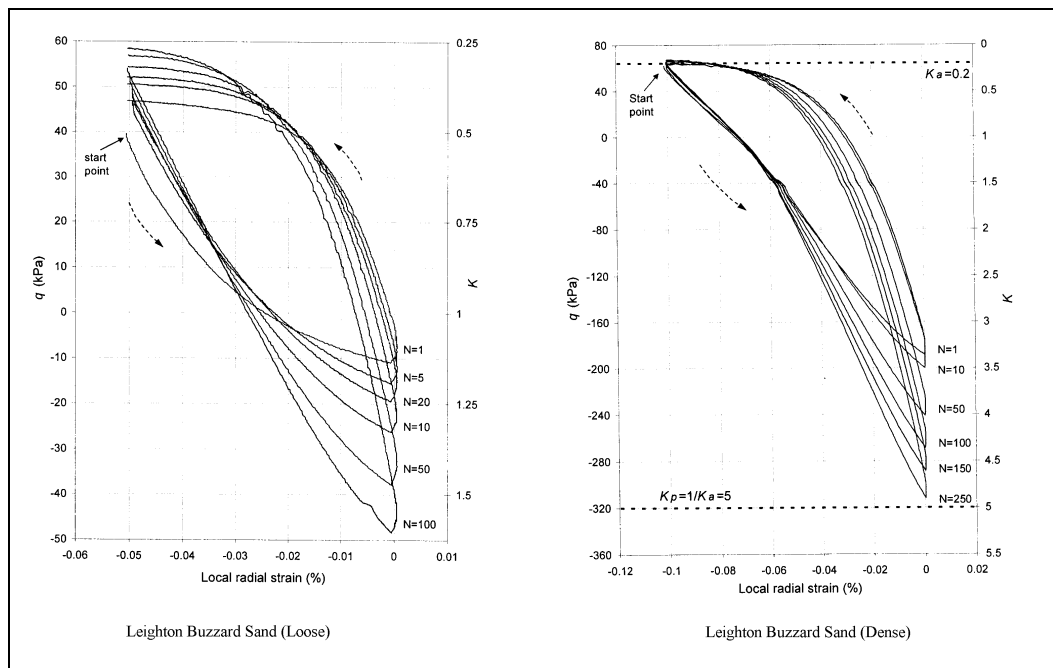
Figure 2.2: Curves of deviator stress and earth pressure coefficient K against local radial strain for loose and dense sand specimen (Xu, 2005)

Ng C.W.W et al. (1998) carried out centrifuge model tests on a spread based integral abutment subjected to cyclic deformations, which simulated expansion and contraction of bridge deck due to effective temperature change. The model wall was designed to represent a typical 1m thick spread-based reinforce concrete abutment wall with 1.5% of steel reinforcement, retaining approximately 6 m of dry granular fill. A 9.9 mm thick mild steel deck section was used for the test, corresponding to the integral abutment by a specified scale in terms of flexural stiffness. Leighton Buzzard silica sand was used to model the backfill soil due to its small grain size, granting a high model to particle size ratio in the order of 1000. The tests were carried out with 100 controlled displacement cycles. A range of controlled displacements were derived based on diurnal and seasonal temperature changes. One of the main findings from these tests is that the measured lateral earth

pressure increased with the amplitude of the passive displacements and number of cycles, but at a decreasing rate.

A model retaining wall apparatus was constructed by England at al. (2000) to study the integral bridge problem, simulating temperature variation by imposing rotations on the pin-based retaining wall which would represent the integral abutment. The 300 mm wide stiff model retaining wall was hinged at the bottom, and the cyclic loading was carried out by rotating the wall back and forth about its bottom hinge. It was constrained to move about that axis in between two parallel glass side panels which maintain a plain strain condition. The model retaining wall apparatus could tests up to 570 mm of retained soil depth. Cyclic rotations of the model wall of different amplitudes and conditions were carried out resulting in the escalation of lateral earth pressure. The escalation of soil-abutment stresses led to the escalation of the earth pressure coefficient K, at a progressively decreasing rate.

A parametric study from the model retaining wall tests and companion numerical model suggested that lateral stresses behind an integral abutment change quickly to the isotropic stress state (where $K = 1.0$) from the early cycles and settles to a peak stress ratio of $K \approx 1.2$ for a 60m bridge over a service life of 120 years (England, et al., 2000).

For the design of integral bridges in the UK, the design manual DMRB BA42/96 (Highways Agency, 2003) addressed the matter of the lateral earth pressure build-up with specific recommendations. A special coefficient of earth pressure to account for the effect of cyclic loading, labelled as K^* was specified based on experimental and analytical data. Different formulae for K^* were specified for different integral abutment types. K^* is calculated based on retained height $H_{retained}$, thermal displacement at top of abutment, d, earth pressure coefficient at-rest, K_0 and passive earth pressure coefficient K_p. For a full-height frame abutment hinged at the base:

$$K^* = K_0 + (d / 0.05 H_{retained})^{0.6} K_p$$

Various numerical models including finite element and static pushover analysis have shown that the backfill pressure or lateral earth pressure (related to the soil stiffness) is dominated by the compaction of the granular backfill. The compaction of the backfill in turn is affected by factors such as the wall stiffness, the abutment height and the magnitude of cyclic seasonal movement induced by temperature change (Dicleli, 2005; Faraji et al., 2001; Xu et al., 2003; Kumar et al. 2006).

Literatures on the subject have established that the lateral earth pressures on the integral abutments escalate to values in excess of those at the time the structure entered service. The upper limits of the stress escalation, however, are not well known (England et al., 2000).

2.3.2 Soil settlement

Soil settlement was shown to occur in sands when subjected to cyclic loadings similar to those experienced by real integral bridge backfills. It was observed from a centrifuge model (Ng et al., 1998) and a scaled model retaining wall (England et al., 2000) as described in the previous section. The following Figure 2.3 shows observable soil settlement from a sketch of the centrifuge model after 100 cycles of ±60 mm perturbations and pictures from the scaled model retaining wall after 65 seasonal cycles of about ±65 mm ($d/2H = \pm0.125\%$ and retained height H = 520 mm). These show that significant soil settlement can occur.
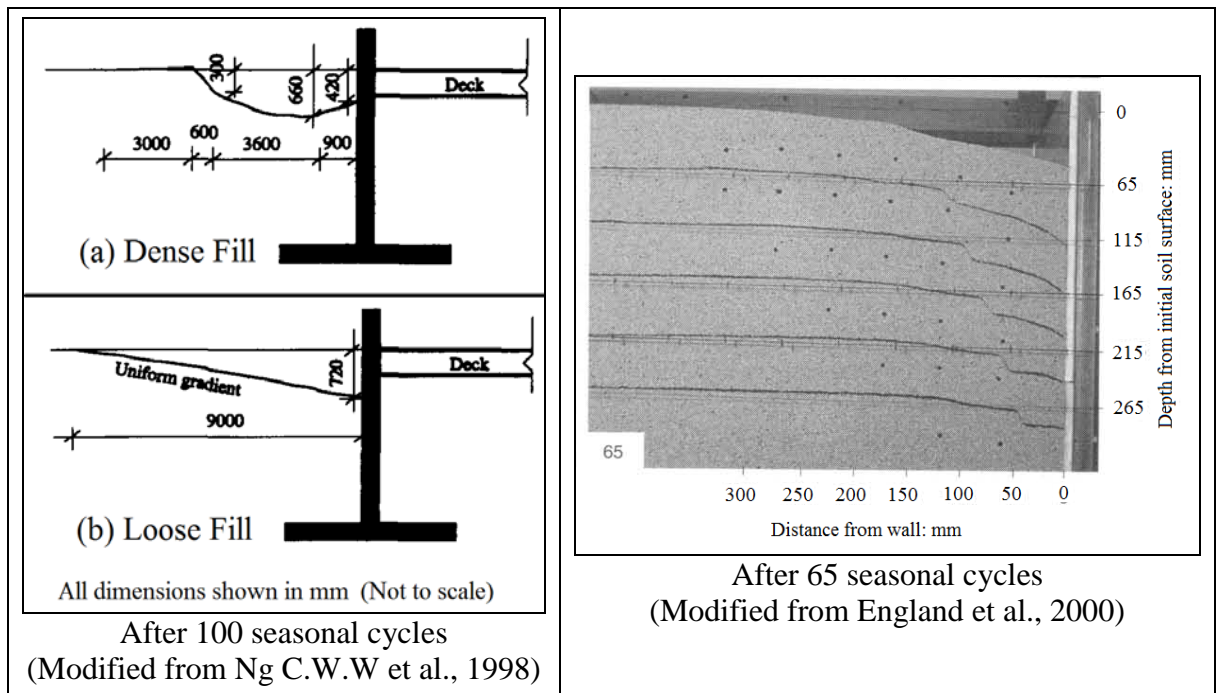
Figure 2.3: Soil settlement as observed in the centrifuge model (Ng C.W.W. et al., 1998) and scaled model (England et al., 2000)

Centrifuge modelling of a spread-base abutment by Ng et al. (1998) as described in the previous section, showed significant settlement behind the abutment which is thought to be the result of soil densification, strain ratcheting, horizontal sliding and the rocking motion of the abutment.

Scaled model tests of the integral bridge problem utilizing a model retaining wall conducted by England et al. (2000) as described in the previous section, also showed soil settlement adjacent to the abutment. It was suggested that the extent of soil settlement was determined primarily by the magnitude of the EBT fluctuations and the bridge dimensions; essentially the magnitude of the integral abutment movement (England et al., 2000).

In a laboratory scaled model test of an abutment and loose backfill, cyclic rotations of an abutment resulted in significant volumetric contraction of the sand mass in the vicinity of the abutment. The applied displacements at the top of the abutments were sufficient to allow the backfill to reach active conditions from the first cycle and it is within the associated active wedge that significant sand contraction occurred and where surface settlement predominated (Cosgrove and Lehane, 2003).

Lock (2002) noted that settlement due to thermal movement of the integral bridge deck is often addressed by incorporating an approach slab to the integral bridge. However, it was suggested that an approach slab was unnecessary with the proper amount of compaction. Springman et al. (1996) warned that loose backfill should not be used behind an integral abutment to prevent excessive soil settlements. The design manual for integral bridges DMRB BA42/96 (Highways Agency, 2003) does not mention the use of approach slabs, but compaction of the backfill material is recommended to limit the soil settlement due to thermal movements of the structure.

Considerable soil settlement due to cyclic loading (or straining) were observed in scaled models (England, 2000) and laboratory tests (Springman et al., 1996) which leads to the anticipation that it would be an issue behind integral abutments. Circumstantial evidence collected from correspondence with practising engineers by Lock (2002) suggested that settlements of this magnitude were not occurring in the field. A survey of the Highway Agency maintenance records of existing integral bridges in the UK revealed that aside from isolated cases, most bridges showed no settlement problems. Other field studies were similar in which very few reported on soil settlement issues. Generally, settlement behind an integral abutment is not an issue in the UK due to compaction specifications.

2.4 Integral Bridge Backfill

In the UK, the backfill material should be free draining selected granular fill with properties and grading based on classes 6N or 6P of Table 6/1 of the Specification of Highway Works cited in DMRB BA42/96 (Highways Agency, 2003).

Classes 6N or 6P from Table 6/1 of the Specification of Highway Works specify the materials as *well-graded granular material* (Class 6N), or simply *granular material* (Class 6P) which could include constituents such as natural gravel, natural sand, crushed gravel, crushed rock, crushed concrete, slag or chalk. Table 6/2 specifies that 100% of the backfill must be no larger than 75 mm in size for both 6N and 6P class. The backfill would have a well-graded spread of particle size up to the size of 75 mm according to the specification MCHW 1.600 (Highways Agency, 2005).

DMRB BA42/96 (Highways Agency, 2003) further specifies that the representative value of c'_{peak} and Φ'_{peak} for the fill material (for design calculation) is to be based on the compaction to 95% of maximum dry density in accordance to BS1377: part 4 using the vibrating hammer method. The zone of granular backfill should extend from the bottom of the abutment wall to at least a plane inclined at 45° to the wall.

2.5 Soil behaviour under cyclic loading

Most researchers attribute the build-up of lateral earth pressure behind an integral abutment to the increasing stiffness of the backfill material. The increasing stiffness is in turn attributed to the overall densification of the backfill material through granular flow as a result of cyclic loading or straining from the integral abutment. Hence, lateral pressure build-up was explained by the flow of granular materials during cyclic loading known in most literatures as *strain ratcheting* (Hassiotis, Lopez et al., 2005).

Ratcheting is also observed in a grain scale DEM investigation of the cyclic loading response of polygonal particles (Marroquin and Hermann, 2004). A 2-D polygonal packing was generated and loaded cyclically. The results showed a constant accumulation of plastic deformation in the material per cycle due to the particles sliding over each other. The particles were permanently displaced into a new position and thus produce the effect observed as strain ratcheting.

The model retaining wall experimental investigation into the behaviour of a full-height integral abutment conducted by England et al. (2000), tested out cyclic loading against Leighton Buzzard sand as described in section 2.3.1. Tsang et al., (2002) further expounded on that experiment, reporting that the results showed that the build-up lateral earth pressure profile after many cycles is not linear but D-shaped as shown in Figure 2.4. The horizontal earth pressure increases linearly with depth from the soil surface to approximately half-depth and then decreases to insignificant values close to the hinge. All tests showed a similar stress ratio and horizontal stress profile with larger values corresponding to larger wall rotations.
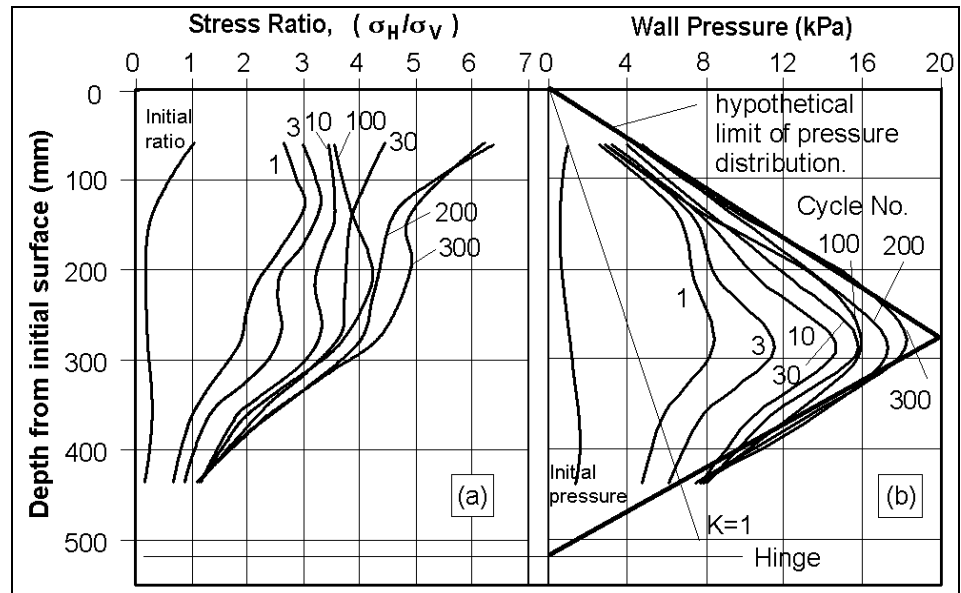
Figure 2.4: Stress ratio profile and lateral wall pressure profile with depth (Tsang et al., 2002)

Two distinct mechanisms were attributed to be responsible for the earth pressure escalation: granular arch for small amplitudes and granular flow for large amplitudes.

2.5.1 Granular Arch

In the granular arch hypothesis, small amplitude wall rotations causes a densification of sand away from the wall which would form a *hard* bounding plane inclined at an angle of 45° or less towards the hinge. The hinge is the assumed point at the base of the abutment about which the wall rotates about cyclically. *Small amplitudes rotations* are movements which do not cause an active failure plane to occur. A steady state of soil behaviour can be reached after many cycles confining soil displacements to a wedged-shaped soil mass adjacent to the retaining wall. *Granular arching* is thought to occur within this wedge soil mass, between the retaining wall and the *hard* bounding plane of the densified soil. Generally, the arch mechanism reduces the vertical stresses acting on the soil behind the lower half of the wall resulting in lower horizontal earth pressures there (Tsang et al., 2002).

2.5.2 Granular Flow Mechanism

In the granular flow hypothesis, large amplitude wall rotations cause progressive ratcheting soil movements at repeating soil stresses. Figure 2.5 shows a three element model describing this process. Element 'a' next to the wall is subjected to cyclic stressing conditions with 90° changes in principal stress directions (stress ratio crosses 1.0) resulting in ratcheting shear with extensional horizontal strains. Element 'b', away from the wall is subjected to cyclic stress fluctuations without change in principal stress directions (stress ratio > 1.0) resulting in ratcheting shear opposite from element 'a'. Element 'b' thus undergoes compressive horizontal strains and extensional vertical strains. Basically, element 'a' expands horizontally while element 'b' is compressed horizontally and element 'c' remains unchanged (Tsang et al., 2002).

In Figure 2.5, K refers to the stress ratio and ε_H refers to the horizontal strain whether compressive (as in element 'b') or extensional (as in element 'a').

Three element model (a, b & c) to illustrate the granular flow mechanism
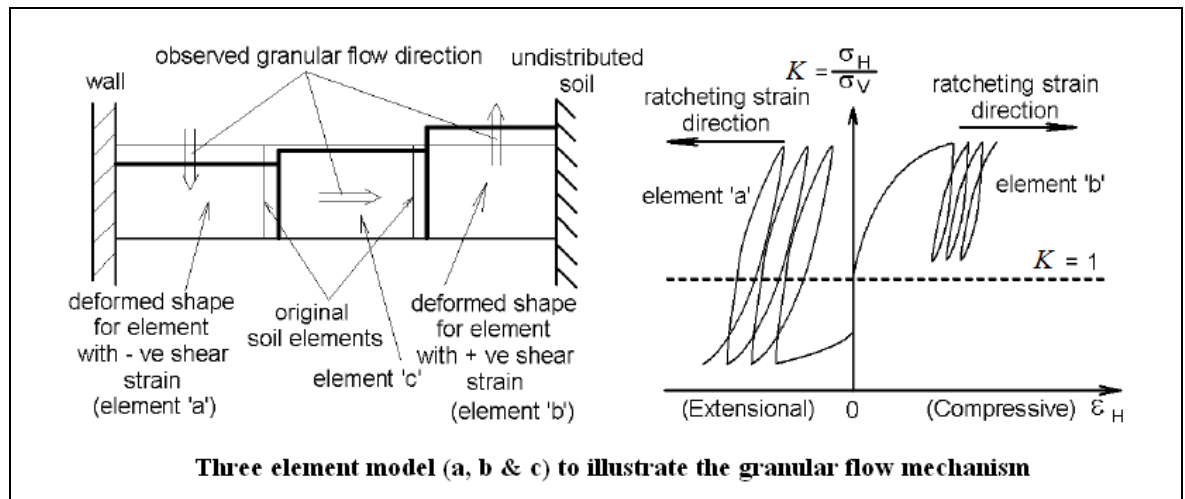
Figure 2.5: Granular flow mechanism, described by a 3 element model (Modified from Tsang et al., 2002)

Separate biaxial tests on independent elements showed that granular soil is capable of deforming continuously under repeated cyclic testing. These deformations cause *flow* in the soil at some distant from the wall. The compressive strains lead to densification and the deformations eventually cease for small wall rotations as the *granular arch* sets in, but will continue for large wall rotations. Generally, the flow mechanism allows a continuous deformation of the soil mass in one direction (Tsang et al., 2002).

Thermal length change of the bridge deck dictates which mechanism dominates this stress behaviour. A dominant arch mechanism relates to small wall rotations while a dominant flow mechanism relates to large wall rotations (Tsang et al., 2002).

2.5.3 Particle reorientation

An alternative explanation to the granular flow theory was postulated by Xu (2005) in which the increase in lateral earth pressure of the backfill material was due to particle reorientation that readjusted the soil fabric instead of densification.

A laboratory experiment was conducted by Xu (2005) to investigate specimens of Atherfield I clay (platy particles), Leighton buzzard sand (granular materials) and glass ballotini (spherical particles), under cyclic loading through an automated triaxial test. The results showed that the Atherfield I clay and the glass ballotini specimens did not exhibit any obvious build-up of horizontal stress with successive cycles as shown in Figure 2.6.

Further experiments on stiff over-consolidated Atherfield clay, reported that no build up in lateral earth pressure was observed with successive cycles and the stress-strain behaviour and stiffness behaviour were not affected by continued cycling (Xu et al., 2007). Horizontal stress build-up was only observable in Leighton buzzard sand as shown in Figure 2.2. Usually, increase in lateral earth pressure due to cyclic loading is associated with granular backfill materials.
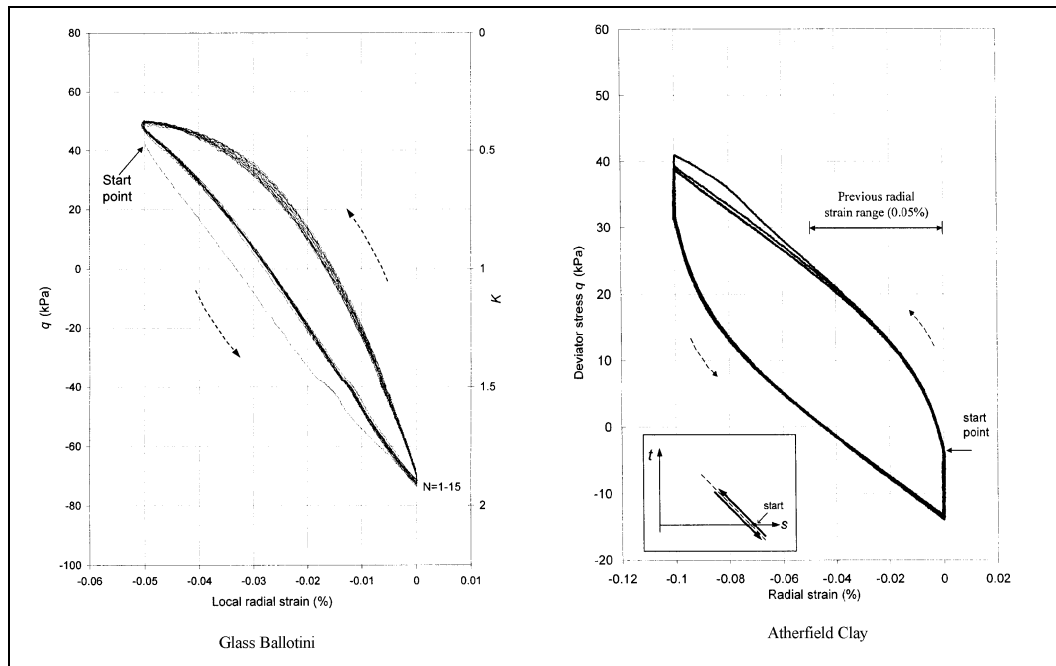
Figure 2.6: Curves of deviator stress and earth pressure coefficient *K* against local radial strain for Glass ballotini (0.05%) and Atherfield clay (0.1%) (Xu, 2005)

The differences in particle shapes (platy, sub-round and spherical) were thought to be responsible for the differences in stiffness and stress-strain behaviour of the stiff clay (Atherfield clay), coarse sand (Leighton buzzard sand) and glass ballotini under cyclic loading. For the clay, the platy particles cannot reorient themselves easily so the fabric of the material remains essentially unchanged. Furthermore, the platy particles of the stiff clay could deform under loading, showing signs of elasticity, resulting in relatively low stiffness and no pressure build-up of lateral stresses.

For the Leighton Buzzard sand, the non-spherical particles change their orientation under loading by rolling and sliding during the active state, generating a greater degree of interlocking progressively in the loading process and thus resulting in an increase in soil stiffness and therefore the horizontal stress. This is how particle reorientation causes the build-up of lateral earth pressure (Xu, 2005).

The perfectly spherical particles of the glass ballotini specimen would also roll and slide relative to each other under loading, but their spherical shape prevents them from interlocking, hence resulting in no horizontal stress build up (Xu, 2005). Figure 2.7 shows an idealised illustration to explain the influence of particle shapes and particle reorientation.

These results suggest that the build-up of maximum horizontal stress with strain cycling is associated with the readjustment of irregular but relatively rotund shaped particles close to or at the active state (Clayton et al. 2006).
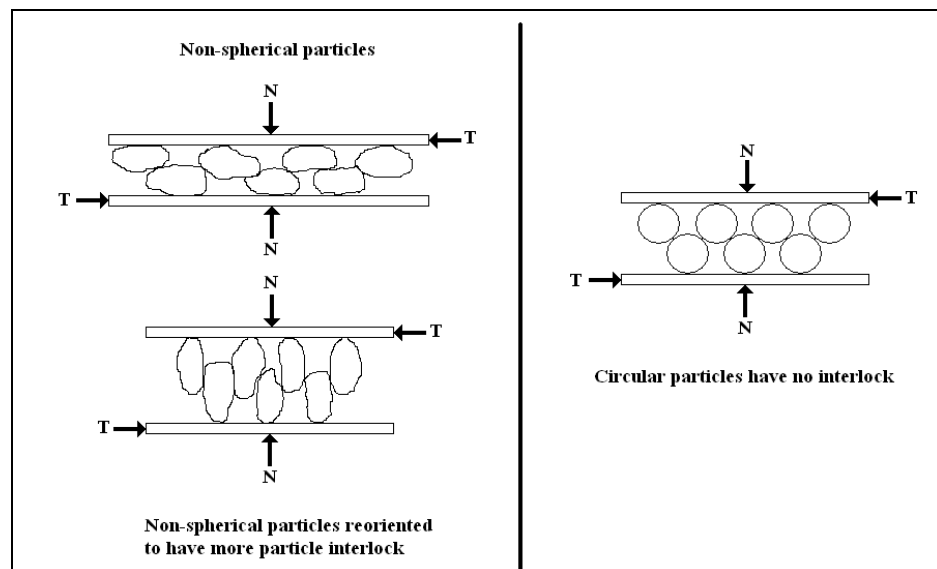
Figure 2.7: Non-spherical particles' reorientation generates particle interlock while circular particles don't interlock. (Modified from Xu, 2005)

The significance of these findings is that the build-up of lateral earth pressure in granular material may not solely be due to densification. Rather it could be caused by the readjustment of the soil fabric due to particles reorienting under cyclic loading or straining. It is noted that the particles must be non-spherical in order for there to be a readjustment in soil fabric. Therefore, the particles' shape is an important factor to consider.

2.5.4 Role of particle shapes

Particle shapes emerged as a parameter that has a significant effect on soil behaviour (Santamarina and Cho, 2004). There are three principal scales in characterizing particle shape; sphericity (or *Form*), roundness (or *Angularity*) and *surface roughness* that affect the overall soil behaviour. The characteristics of sphericity and roundness are shown in Figure 2.8. Sphericity is quantified as the diameter ratio between largest inscribed and the smallest circumscribing sphere. Roundness is quantified as the average radius of curvature of surface features relative to the radius of the maximum sphere that can be inscribed in the particle (largest inscribed sphere). The inverse of roundness is angularity.

Particle roughness deals with the surface features of a particle, whether it's smooth or rough. In that sense, this factor is best characterized by inter-particle friction. This can be adjusted in the PFC2D program by setting the friction coefficient for all the particles generated. Particle roughness is distinguished from the angularity of the particle in the sense that angularity is dealing with 'observable' edges on a particle.
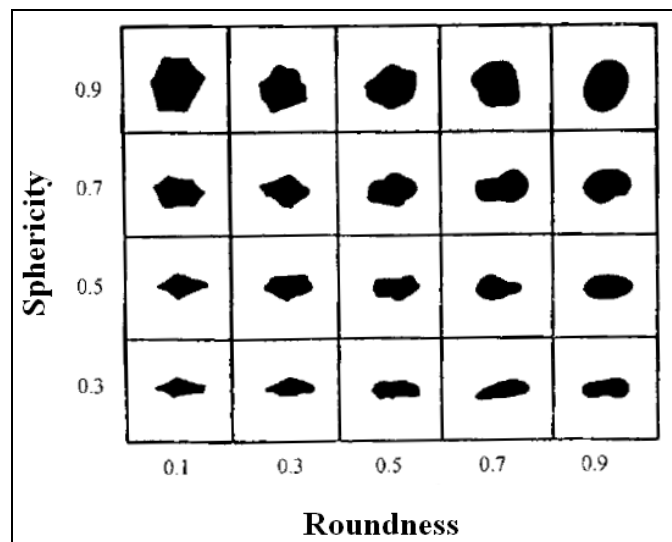
Figure 2.8: Particle Shape description (Santamarina and Cho, 2004)

Figure 2.9 illustrates the particle form and roundness of a non-circular particle. Particle form, *F* measures the overall shape of the particle, ranging from the spherical to platy. Numerically, it is the ratio of the largest inscribed circle diameter to the smallest circumscribing circle diameter. A perfectly spherical particle will have a particle form of 1.0 while more platy particles will have a form that approaches 0.0.

Particle roundness, *R*, or interchangeably particle angularity, is a measure of the roundness of the particle as opposed to being angular. Numerically, it is the ratio of the average radii of 'corners' of the particle over the largest inscribed circle. A perfectly spherical particle or a particle whose average radii of its corners are the equivalent to its

largest inscribed circle has an angularity of 1.0. The more edges a non-circular particle has, the lower its value of angularity (Clayton and Reddy, 2006).
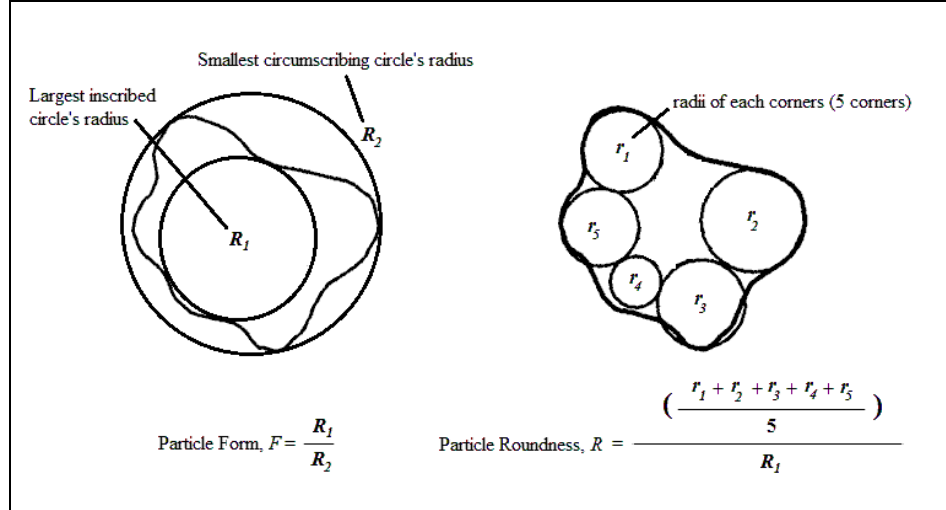
Figure 2.9: Particle form and roundness definition (modified from Sallam, 2004)

A 3-D discrete element method model of non-spherical particles in a shearbox and biaxial test showed that particle shapes have a significant effect on the stress-strain behaviour of a sample. Generally, the non-spherical particles are not as free to rotate as spherical particles, due to interlocking. This contributes to an increase in the bulk friction angle of the sample where non-spherical particles are involved (Ni, 2003).

Literature on particle form

Results from a two-dimensional DEM numerical study on the influence of particle form on initial packing indicate that post-depositional void ratio and anisotropy of initial particle orientation and subsequent volumetric straining during shear are highly dependent on particle form and less dependent on roundness. (Clayton and Reddy, 2006)

The DEM simulation of a biaxial drained shear test concluded that dilation decreases with decreasing particle form, that is, as the particles become less circular. The particle roundness (or angularity) has little or no influence on the compression and dilation of these assemblies of particles. During drained shear, for the porosities and confining stress used, only particles with form greater than 0.5 (more circular) were found to dilate, regardless of shape. For platy particles (F<0.5), volumetric compression increased with decreasing particle form (Clayton and Reddy, 2006).

Literature on particle angularity

Nouguier-Lehon et al. (2003) conducted a two-dimensional discrete element method (DEM) study on the influence of particle angularity on the behaviour of granular materials. Results show that the angle of internal friction was lower for round grains than for angular ones. It was concluded that angularity in the particles tend to strengthen the granular material globally.

The mean particle rotation value remains close to zero for isotropic grains sample; an increase is observed in the case of the elongated polygonal grain sample loaded in the direction perpendicular to the initial deposit. For isotropic grains, angularity tends to strengthen (increase shear angle) the sample and slow down either local or global phenomena. Grain angularity generally increases both initial anisotropy due to deposit under gravity and the level of 'critical anisotropy'. (Nouguier-Lehon et al., 2003).

Results from a DEM investigation on the effect of particle shape on the interface shear behaviour of granular materials showed that the void ratio increased as the angularity or roughness of the particles increased (Jensen et al., 2001).

Mirghasemi et al. (2002) conducted 2-D discrete element model tests on particle angularity (or roundness) was also found to influence the behaviour of the simulated granular material. Peak shear strength of angular material was observed to occur at higher axial strains than rounded material with less significant reduction in post peak strength. Rounded material was also observed to reach a steady state at a lower axial strain. In general, the shear strength of the material was observed to increase with angularity.

Literature on inter-particle friction

In granular materials, forces are transmitted through inter-particle contacts. Particles will fail to withstand applied shear force in the absence of inter-particle friction at contacts resulting in an overall lower effective shear angle for the material. As such, the inter-particle friction is an important parameter to consider when modelling granular materials. A 2-D DEM simulation of a biaxial cyclic shear test on oval particles with different inter-particle friction angles showed that the width of the stress-strain cyclic loop decreases as the inter-particle friction increases (Sazzad and Suzuki, 2011).

An attempt was made to use an equivalent inter-particle friction to model different particle shapes. This would eliminate the need to have non-circular particles if the effect of particle shape can be emulated with large friction coefficient value on circular particles. However, it was concluded that there is no one-to-one equivalency between inter-particle friction and particle shape or angularity (Sallam, 2004).

2.5.5 Long observation period

The integral abutment movement due to seasonal thermal changes basically causes earth pressure build-up and soil settlement over many seasonal cycles. Field observations and laboratory experiments are important for investigating the backfill behaviour in such cases. Often these are accompanied by numerical simulation models which should corroborate with observations from the field and/or the laboratory.

In the case of the increasing lateral earth pressure behind an integral abutment, the earth pressure can be monitored through pressure cells installed on the back of the integral abutment. However, the long term effect of the abutment's movement cannot be known unless the bridge is monitored for its entire service-life span (usually 120 years). In section 2.3.1, two full-height integral bridges in the UK were observed for up to six years (approximately from 1998 to 2005) by Barker and Carder (2000; 2001; 2006). The results obtained were invaluable and further monitoring of the bridges was strongly recommended, mainly because significant earth pressure escalation was expected after more seasonal cycles but partly also because of the major investment in the instruments on the site. (Barker and Carder, 2000; 2001)

The long observation period is also a problem for laboratory experiments as the earth pressure escalation behind an integral abutment is expected to occur after many cycles of loading (or straining). Furthermore, the question of whether the earth pressure would continue to increase or level off to a steady value towards the end of the integral bridge's service-life implies a hypothetical 120 year observation period.

A numerical simulation model overcomes this problem of long observation period. Numerical models are essential to the investigation of backfill behaviour as they will provide results which can be compared to those from field observations and laboratory tests. They can help verify or dispel theories on what causes the lateral earth pressure escalation and the soil settlement behind an integral abutment. Soil is conventionally modelled as a continuum, but the objectives of this project would require the discrete element method of modelling soils as described in the next section.

2.6 DEM versus conventional continuum model

Soil is essentially a body of solid particles, with voids in between them. The voids can be partially or completely occupied by water. The assemblage of particles in contact is usually referred to as the soil matrix (Powrie, 2004).

For analysis, an equivalent continuum model is created in order to describe materials that are composed of individual particles but also exist in a form where the particles interact beneficially (as a matrix or fabric) so that they can be relied upon for engineering applications that are much larger than the individual particles themselves. These continuum models are a simplification of the soil's behaviour, inspired by experimental observations. An increase in complexity of the model means an increase in the number of material properties that must be defined from laboratory or *in- situ* tests (Wood, 2004).

The drawback of these methods is that the required constitutive relationship (stress-strain law) for the soil may not exist, or is excessively complicated with obscure parameters. In discrete element modelling (DEM), assemblies of discrete particles could capture the complicated behaviour of actual soil materials. Figure 2.10 shows the difference between the finite element method as an example of a continuum model and the discrete element method.
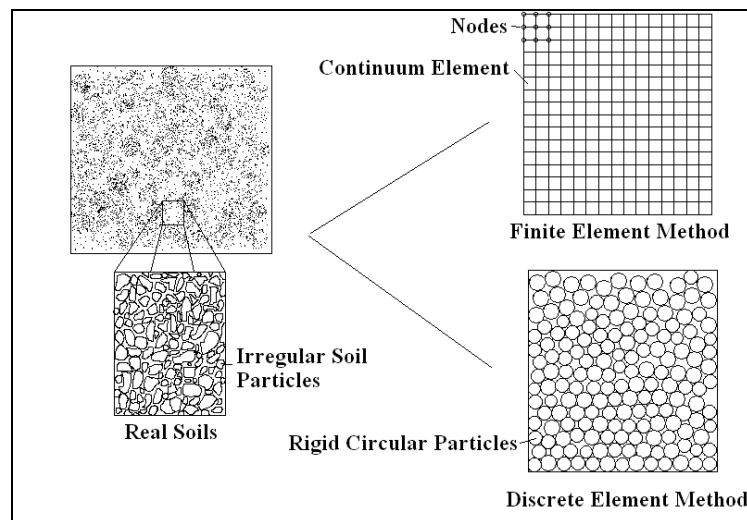
Figure 2.10: Difference between the Finite Element Method and the Discrete Element Method

A comparison of the difference between discrete element modelling and continuum modelling confirmed that the discrete element model could produce the same result as a Mohr-Coulomb model for a monotonic biaxial test (Van Baars, 2005). This illustrates that discrete element modelling can accurately model the same material as a Mohr-Coulomb model which is widely used in modelling soils.

The complex overall behaviour of the granular material would arise as an emergent property of the discrete element assembly. The simulation of thousands of particles for a certain system may be complicated but the overall methodology is conceptually simple. However, time must be spent calibrating the synthetic material and learning how various microstructures affect the overall behaviour in order to properly model the system of particulate media (Cundall, 2001).

Another reason for modelling soils with the discrete element method is because two factors that have a significant influence on the behaviour of an assemblage of particles are the grain size distribution and grain shape (Rouse, et al. 2008 and Santamarina & Cho, 2004), neither of which can be represented in a continuum model.

Furthermore, the DEM would enable the observation of the particles' displacement and rotation. For example, in a numerical examination of the direct shear test by DEM (Zhang and Thornton, 2007), it was observed that the shear strain concentrates at the mid-height of the specimens to form a shear zone. Correspondingly, significant particle rotations localise within the shear zone, with the average particle rotation increasing linearly with shear deformation. This demonstrates the level of micro-mechanical detail that can be provided from a DEM simulation.

The main concern of this research project is the increase in lateral earth pressure behind an integral abutment, which literature attributes to behaviour within the backfill at the micro-mechanical level (see section 2.5.1 to section 2.5.3). Whilst conventional continuum models are well established, the discrete element method models the backfill material at the micromechanical level which is more suited to the objectives of this project.

2.7 Modelling soil in DEM

In the discrete element method (DEM), the interaction of particles is treated as a dynamic process, applying the *law of motion* and the *force-displacement law* to individual particles. Figure 2.11 shows a DEM calculation example in which a circular particle (disc) of a certain radius is generated in a DEM model, having a *position* as well as a specified *particle density*. Let's say a *force* acts on the particle from a certain direction and the simulation is run to simulate what happens after one second. So the force acting on the particle with its *mass* (particle density x particle volume) causes an acceleration of the disc. From an at rest position, the disc gains a velocity in the direction of the force and displaces. After one second, the disc is now in a new position with acceleration and a velocity in one direction. This entire process is one *calculation cycle*. The process is repeated in the next calculation cycle from the particle's new position.
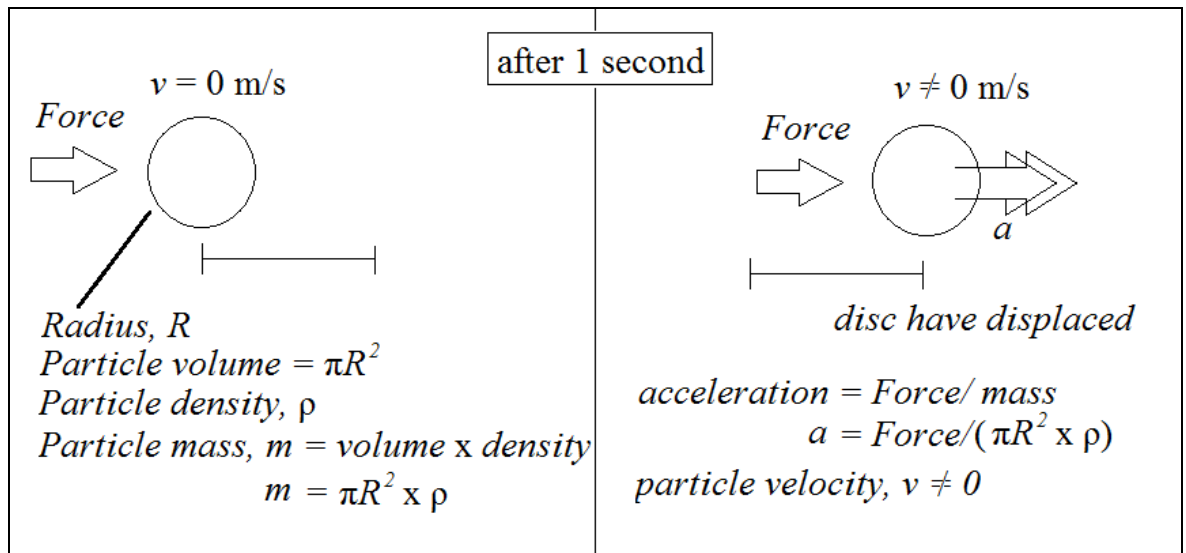
Figure 2.11: A calculation cycle for a disc when a force is applied

The rotation of the particles is also similarly calculated, applying a resultant moment on the particle and gaining rotational velocities. The following Figure 2.12 shows the process of one calculation cycle in PFC2D.
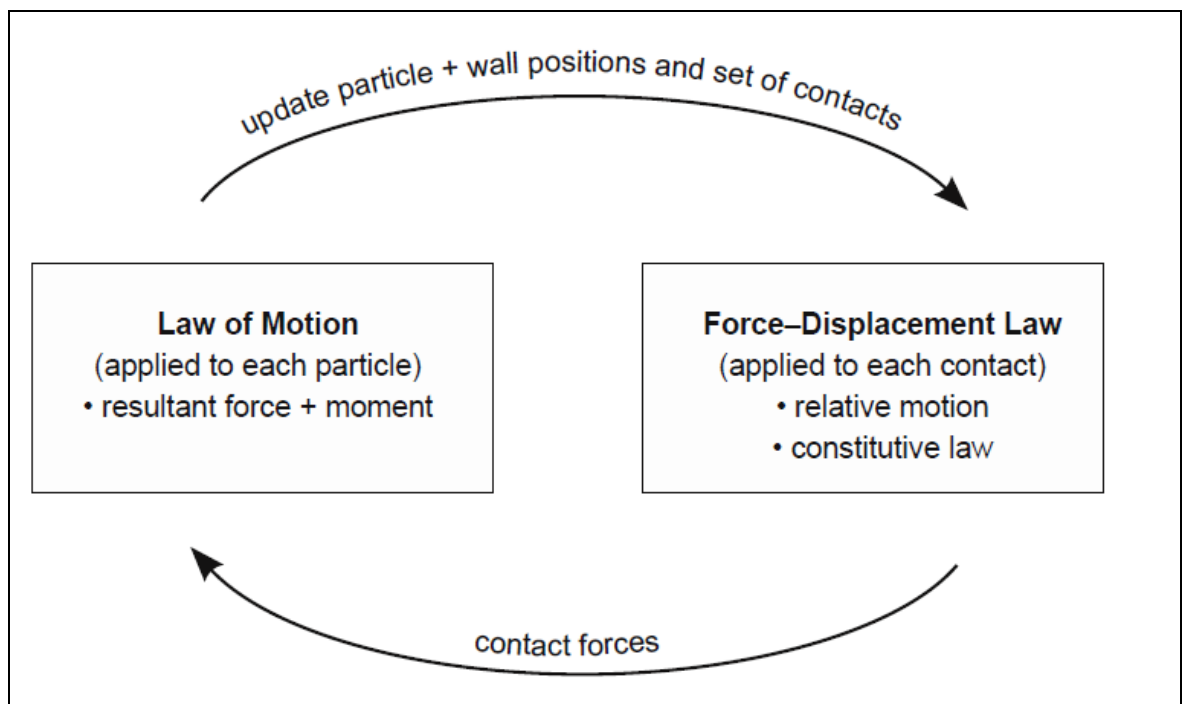
Figure 2.12: The calculation cycle in PFC2D (Itasca Consulting Group, 2002)

There are two entities in a DEM model: particles and walls. Unlike particles, the walls in PFC2D are not subjected to the *laws of motion* and the *force-displacement law*. Walls interact with the particles by generating contact force when particles are in contact with them. For the purpose of simulation, walls are usually used to contain the particles.

A resultant force on any particle is often due to the particles interaction with either the walls or other particles. The force generated is based on the specified normal and shear stiffness of the particles and the walls (see section 3.5).

DEM has been verified to successfully represent real granular materials such as soils through comparisons with laboratory tests and continuum models.

A numerical modelling of plane strain tests by DEM with non-spherical particles consisting of two bonded spheres; concluded that particle rotations showed the extent of structural disturbance in the soil and proved a useful indicator of deformation mechanisms. In general, it was shown that simulations with the DEM could reproduce the behaviour of soil elements as observed in laboratory tests (Powrie et al. 2005).

A comparison between DEM models and laboratory tests verified that the discrete element method could approximately model the real soils behaviour in biaxial tests, yielding similar peak shear angle Φ'_{peak}. Factors such as particle shape, surface friction, size distribution and packing configurations have to be accurately represented in simulation in order to capture observed laboratory response well (O'Sullivan et al., 2002; 2004).

2.7.1 Disc clusters representing particle shapes

As discussed in section 2.5.4, the non-circular particles shapes have a significant effect on the soil's behaviour. While the Particle Flow Code in 2-D (PFC2D) generates only circular disc particles, different particle shapes could be approximated by combining several circular ones together. Figure 2.13 shows three circular particles being clustered together to form a non-circular particle.

The use of two-dimensional circular elements is an unrealistic simplification of the particle shapes of granular materials, as they will roll excessively resulting in lower effective angle of shear compared to real granular materials in biaxial and direct shear tests (Thomas and Bray, 1999).

Commercial software such as the Particle Flow Code (PFC) by Itasca Consulting Group utilizes a *cluster* feature for joining circular particles together to form particles of different shapes. A disc cluster is a particle type where a group of circular discs are permanently connected to form an irregularly shaped particle that could better represent the particle shapes of granular materials (Thomas and Bray, 1999).
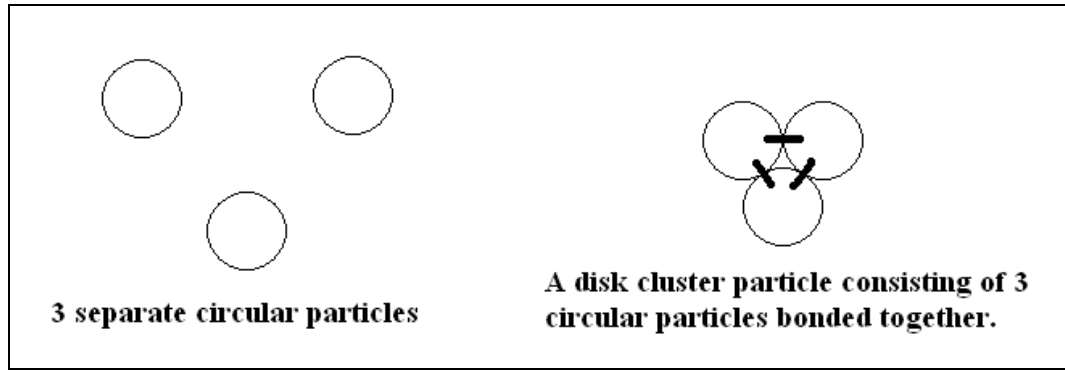
Figure 2.13: Three Separate circular particles joined together to form a cluster approximating a triangle

Irregularly shaped particles could more accurately model the geometry-dependent behaviour of the particles, such as interlocking and resistance to rolling. Shear test simulations, performed with both clustered and non-clustered particles indicates that the clustered particles undergo less rolling and provide for increased shear resistance of the medium. Another feature of clustering is the opportunity to incorporate particle damage such as grain crushing for possibly more realistic simulation of a particle medium (Jensen et al., 1999).

2.7.2 Effect of particle size

While particle shape is very important to an assembly, simulations of an assembly based on individual particles require also the understanding of the effect of the particle size(s) that make up the assembly. It was concluded by Ni (2003) that as particle size decreases (number of particles increase from 5000 to 50000 to fill the same volume) there is a significant reduction of the bulk friction angle and the volumetric dilation of the sample.

Simulation on parallel graded assemblies (same grading but at a different size range) of sizes 30-70 mm, 70-110 mm, 90-130 mm and 110-150 mm indicate that an increase in particle size causes a marginal increase (or no increase) in the angle of internal friction during biaxial loading conditions (Sitharam and Nimbkar, 2000). Therefore, no significant change in the shear strength is observed with larger particle sizes. It can be argued, however, that these samples have perfectly parallel gradations and therefore have similar fabric. A similar fabric implies similar behaviour under similar loading conditions despite having overall different particle sizes. This is because the volume of each assembly was scaled such that it accommodated 1000 particles in order to eliminate the effect of sample size on the assembly behaviour.

Hence it is noted that for a sample to occupy a particular space, the increase in particle size (and therefore the decrease in particle count) would increase the bulk friction angle marginally as noted by Ni (2003) and Sitharam and Nimbkar (2000). However, as long as there is a large enough particle count (about 10000 particles), the sample will still exhibit granular material behaviour.

2.7.3 Effect of particle grading

The results of DEM tests on granular material with from 30-70 mm gradation to 30-110 mm (wider) gradation showed that there is a decrease in the angle of internal friction and an increase in volumetric strain to a considerable extent (Sitharam and Nimbkar, 2000). Ni (2003) also suggested that the distribution of particle size is an important factor when a sample comprising a variety of particle sizes produced a higher shearing resistance than a sample comprising of uniform sized spheres.

DEM simulated cyclic biaxial tests were conducted on assemblages of loose and dense system with monodisperse (uniform) and polydisperse (well-graded) samples. Results indicate that polydisperse (well-graded) systems have stronger shear strength (larger angle of shear Φ') than monodisperse (uniform) sample when subjected to cyclic loading (Sitharam, 2003).

This research project involves the DEM simulation of granular material meant to represent the 6N/6P backfill material described in the specification (MCHW 1.600, 2005) as described in section 2.4.1. Therefore, the material to be considered in this thesis is well-graded only.

2.8 Other integral bridge issues

There are various issues concerning the integral bridge, all of which relates to the movement of integral abutments. Essentially, all full-height integral abutments will cause pressure build up in its' backfill. Depending on the integral bridge's design and construction, the seasonal changes in temperature will cause superstructure issues and earth pressure build up in the backfill that are larger than the conventional estimate outlined in the design specification (DMRB BA42/96, 2003).

2.8.1 Integral bridge superstructure issues

Observations on individual bridges highlighted the following issues associated with integral bridge superstructures. From various field observations, it was identified that the integral bridge superstructures had problems of becoming progressively shorter (Huang et al., 2004) and extensive cracking on the deck before the bridge was in service (McGowan, 2005).

The extensive cracking was primarily due to temperature changes and dry shrinkage which increased stress levels, particularly because the bridge under study (in Evansville, West Virginia), had constraints placed on the deck by shear studs and integral abutments. (McGowan, 2005)

Differing thermal properties of different sections of the deck, which result in variations in material response to temperature changes, would have also contributed to the cracking (McGowan, 2005). Data from another field observation of an integral bridge with a composite superstructure (concrete deck and steel girders) indicated that the differential expansion of the bridge superstructure during summer led to excessive axial stresses in the steel girders (William et al., 2005). Figure 2.14 shows the effect of differential expansion.
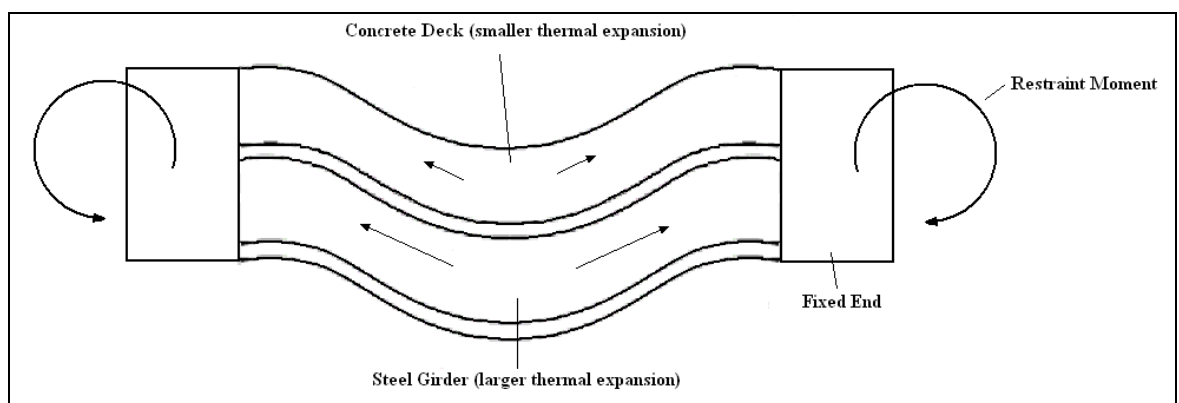
Figure 2.14: Differential thermal expansion in the bridge superstructure causes axial stress in the steel girder. (Modified from Ariockiasamy and Sivakumar, 2005)

Figure 2.15 shows the effect of concrete creep and shrinkage. The girder axial stresses of a composite superstructure were suspected of being influenced by creep and shrinkage as well as the backfill stiffness during bridge expansion (Fenema et al., 2005). The effect of creep and shrinkage of the concrete in a composite superstructure also causes similar axial stresses in the steel girder, all due to the differential change in length in the constituents of the composite superstructure. As a result, restraint moments developed in the superstructure due to the continuity and time-dependent creep, shrinkage and thermal effects (Ariockiasamy and Sivakumar, 2005).
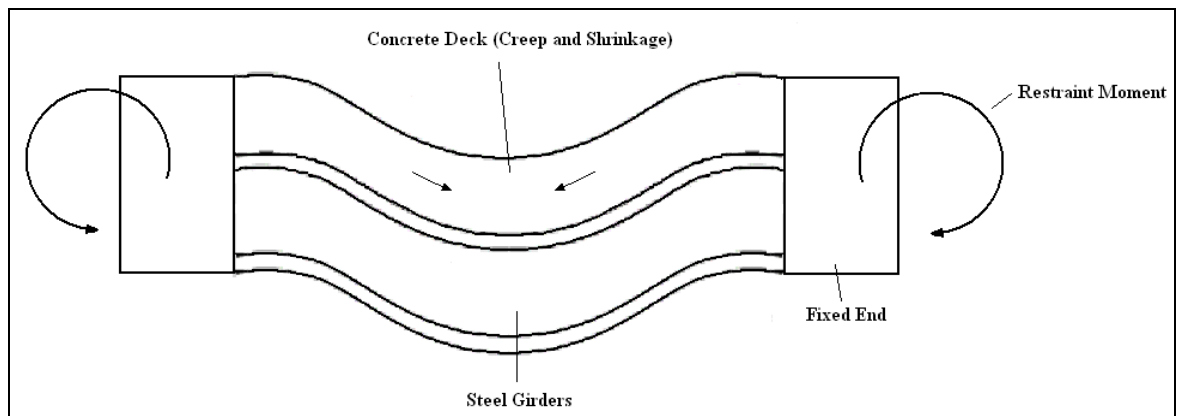
Figure 2.15: Concrete creep and shrinkage in the bridge superstructure causes axial stress in the steel girder. (Modified from Ariockiasamy and Sivakumar, 2005)

It was also pointed out that creep and shrinkage may have some benefits to the integral bridge as it indirectly decreases the lateral earth pressure on the abutments, in which case, integral bridges have been observed to perform without much problems.

Barker and Carder measured the performance of an integral bridge over the M1-A1 Link Road at Bramham Crossroads. In the first three years of service, the shortening of the deck indicated that creep and shrinkage deformation had occurred and produced small lateral movements of the bridge abutments away from the retained ground, relieving any high lateral stresses in the backfill (Barker and Carder, 2001). It was then suggested that integral bridge length could be longer than the 60 m specified in DMRB BA42/96 (Lock, 2002).

The conclusions drawn are based on particular bridges being observed and as conditions differ for each bridge; so too does their individual behaviour. Also note that the integral bridges under study which were observed to have these problems have a composite superstructure with a concrete deck fixed and supported on steel girders.

However, creep and shrinkage is not the dominant effect on the integral bridge. In the long term, creep and shrinkage effects became negligible and the integral bridge movement would be dominated by thermal expansion and contraction of the deck (Barker and Carder, 2001).

2.8.2 Differential movement of integral abutment

Most analysis of integral bridges assumed that the expansion of the bridge deck would affect both the abutments at each end similarly, in a symmetric fashion. Field observations have also indicated the occurrence of differential movement between the abutments at opposite ends of an integral bridge.

During remedial work, the South and North abutments of a portal frame integral bridge at the A62 Manchester Road did not move identically and some lateral movement (4mm) of the bridge towards the North occurred (Barker and Carder, 2000).

In the evaluation of data from the Orange-Wendell Bridge in Massachusetts, differences in performance between the North and South abutments were observed even though the bridge was constructed without any skew. This was attributed to differences in construction conditions (Brena et al., 2007; Bonczar et al., 2005).

In the case of an integral bridge with unsymmetrical abutments, as shown in Figure 2.16, the finite element analysis results showed that the taller abutment will exhibit most of the thermal induced movement as the smaller abutment will be stiffer (Knickerbocker et al., 2005).
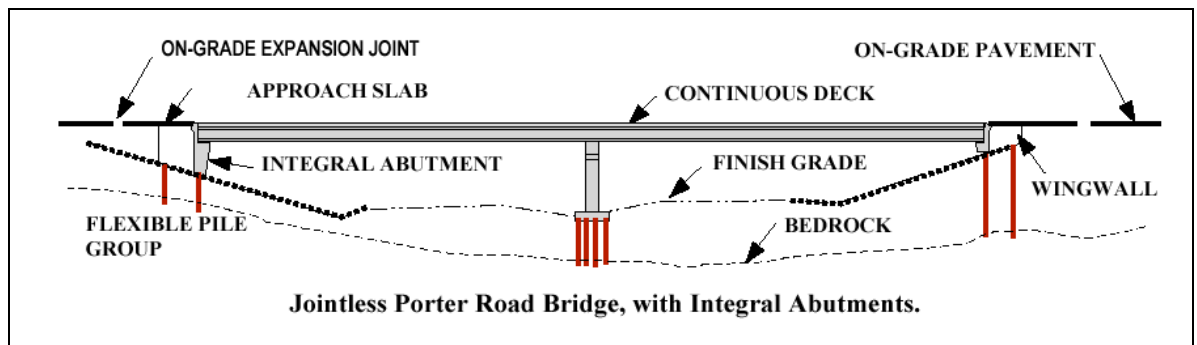
Figure 2.16: Schematic of an integral bridge with unsymmetrical abutments. (Modified from Knickerbocker et al., 2005)

2.8.3 Skewed integral bridges

Skewed integral bridge respond to temperature change with both transverse and longitudinal movement. The magnitude of the transverse movement component is related to the skew angle of the bridge which was observed from field measurements and laboratory experiments. It was recommended that a skew angle of 20° would be the upper limit, below which considerations for transverse movements are not needed (Oesterle and Lofti, 2005).

It is noted that the design guide BA42 specified a skew for integral bridge that does not exceed 30° (DMRB BA42/96, 2003). This refers to the skew angle as shown in Figure 2.17.
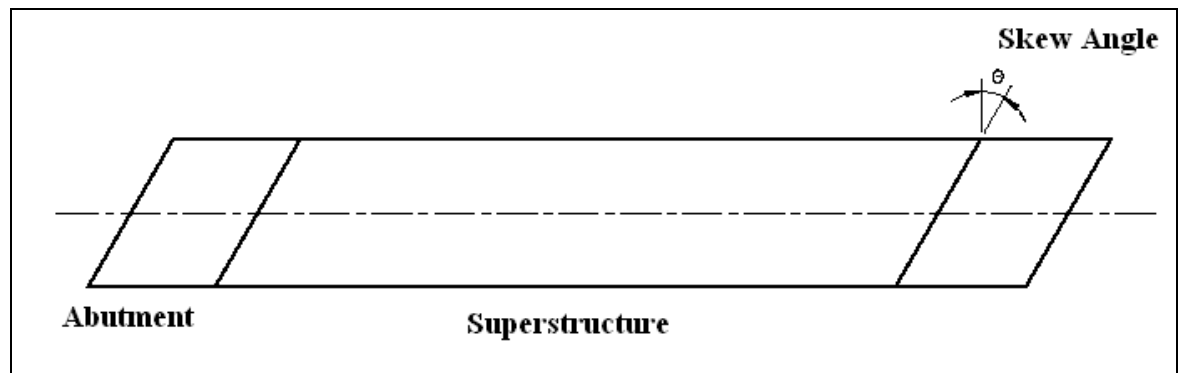
Figure 2.17: A plan view of a skewed integral abutment bridge. (Modified from Oesterle and Lofti, 2005)

These issues may be very important when considering integral bridge construction under very peculiar geographic conditions. However, the scope of the research will not look into these since these cases are far more complex problems. Nonetheless, they also require a better understanding of how backfill soil behaves under cyclic loading. Hence, the study of a symmetrical integral bridge with assumed symmetrical thermal movement will suffice.

2.9 Solutions to the integral bridge problem

There are currently a few solutions to the integral bridge problem. The geotechnical problems of integral abutment bridges consists of both seasonal and long term build-up of lateral earth pressures on abutments and ground-surface settlement adjacent to the abutments. A successful solution must address both those issues (Horvath, 2004).

2.9.1 Geosynthetics

Research indicates that the relatively simple and cost effective design solutions of geosynthetics and ground improvement technologies could solve both issues (Horvath, 2005). The field study of an integral back wall with elastic inclusion (a block of elastic material between the abutment and the retained soil) resulted in observations of significantly attenuated lateral earth pressures and tolerable settlements of the approach fill (Hoppe, 2005). Figure 2.18 shows how geosynthetics or a compressible EPS Geofoam could be utilized in an integral bridge construction.
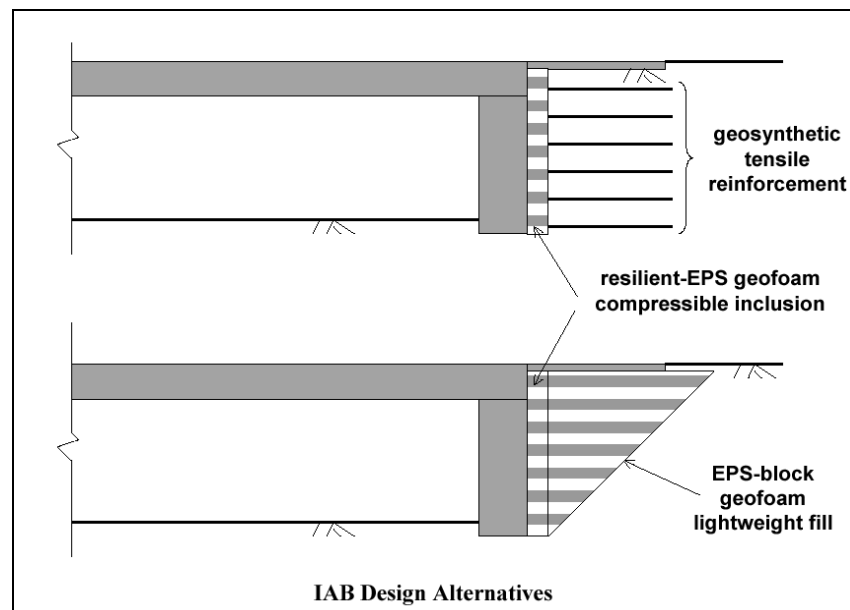
Figure 2.18: Geosynthetic and Elastic backwall inclusion as possible solution to the integral bridge problem. (Modified from Horvath, 2005)

2.9.2 Fibre reinforced polymer (FRP) superstructure

A case study of two integral abutment bridges with FRP (Fibre Reinforced Polymer) deck indicated that there was no sign of cracking on the abutment. They were compared to jointless bridges with concrete decks which were observed to have extensive cracking. Furthermore, the erection time of an FRP composite deck is about 1/8 to 1/10 of a conventional concrete deck (Shekar et al. 2005).

2.9.3 Semi-integral bridges

Experimental and analytical investigations concluded that semi-integral abutments offer benefits over fully integral abutments by reducing pile stresses (Arsoy, 2000; Duncan and Arsoy, 2003; Arsoy et al., 2004). Semi-integral bridges are defined as single or multiple-span continuous bridges with rigid, non-integral foundations and movement systems primarily composed of integral end diaphragms, compressible backfill and movable bearings in a horizontal joint at the super-structure abutment interface (Mistry, 2005).

Essentially, semi-integral bridges retain a bearing support, which still requires some maintenance while fully integral bridge does not have any joint related problems. Figure 2.19 shows a simplified illustration of the difference between a fully integral and a semi-integral abutment.
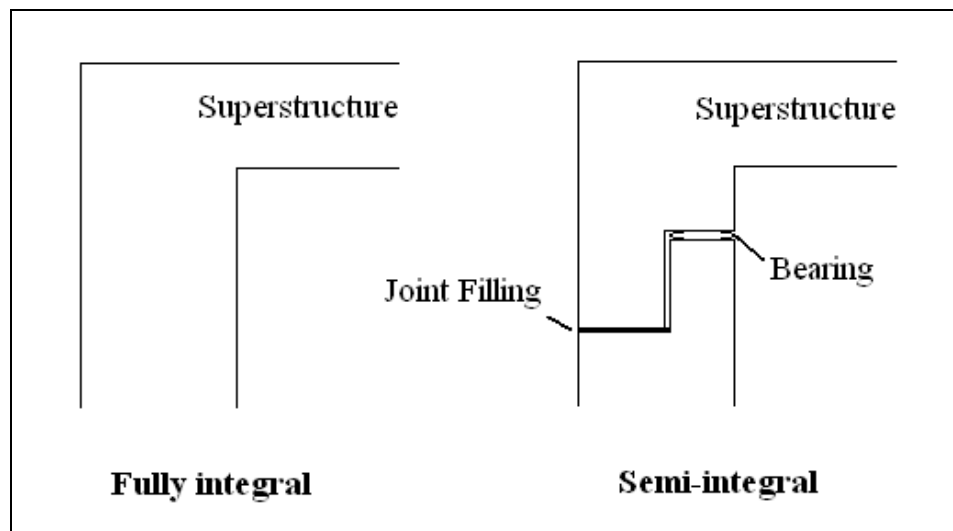
Figure 2.19: A fully integral and a semi-integral abutment

While these solutions are potentially better than the conventional integral bridge design, it doesn't escape the fact that the behaviour of soils under cyclic loading is not fully understood. What these solutions do is reduce the pressure build up and the ground subsidence adjacent to the abutment due to cyclic loading. It is still necessary to have a thorough understanding of the soil's behaviour under cyclic loading.

2.10 Summary of literature review

1. Integral bridges are increasingly popular in the UK and widely encouraged for bridges no longer than 60 m and less than 30° skew. The popularity is mainly due to cost savings from the lack of need for joint maintenance.

2. Cyclic integral abutment movements are caused by seasonal thermal expansion and contraction of the superstructure. The integral abutment movement can be estimated from the range of Effective Bridge Temperature (EBT) which is calculated based on meteorological data for the location of the bridge.

3. Integral abutment movement is a combination of rotational and translational movement in which one dominates the other. An element at mid-depth behind an integral abutment would experience similar cyclic strains whether the abutment undergoes translational or rotational movement. A rigid translational cyclic abutment movement was assumed for this project.

4. Cyclic integral abutment movement causes soil settlement behind the abutment and lateral earth pressure build-up.

5. Soil settlement behind the integral abutment can be solved with the proper amount of compaction in the backfill material but is not an issue in the UK as a result of compaction specifications.

6. The build-up of earth pressure behind integral abutments was attributed to the densification of the backfill material caused by cyclic loading. Investigations have led to proposals of how the material undergoes densification involving granular flow or reorientation of non-circular particles leading to the earth pressure build-up.

7. Particle shapes are very influential on the overall soil behaviour. It is characterized by three principal scales; form, angularity and surface roughness.

8. The field observation of real integral bridges yields invaluable information but it requires a long observation period. Long observation period is similarly a problem for laboratory experiments. Numerical simulation models however do not have this problem. Therefore a numerical model is useful for investigating integral bridge backfill behaviour over long periods and often accompanies both field observations and laboratory experiments.

9. Soils are conventionally modelled as a continuum. The discrete element method (DEM) models soil as an assembly of discrete particles and may be better suited for the objective of this project which concerns the micro-mechanical behaviour of the particles of an integral bridge backfill material.

10. Different shapes of particles could be approximated in the DEM model by combining several circular particles (discs) together.

11. Larger particle sizes within a sample had marginal effects on the sample's bulk friction angle and by extension, the sample's strength and overall stresses. It was noted that a sample with a large enough particle count (about 10000 particles), it should still behave as a granular material.

12. Particle grading is an important aspect of a granular sample and investigations have shown that well-graded material have a larger angle of shear compared to uniform materials. The backfill material for this project will be well-graded as specified in the design manual.

Chapter 3: DEM preliminaries

The basic objective of this research project is to investigate the behaviour of a granular sample under cyclic loading via the discrete element method (DEM) simulation. Simulations will be performed in Itasca's Particle Flow Code in 2-Dimensions (PFC2D version 3.0). The first part of this chapter will briefly explain the reason for a two dimensional biaxial test instead of a three dimensional DEM model.

The rest of this chapter identifies and generally expound on the values of various parameters that are required to generate a DEM model that sufficiently represents the backfill material. The parameters are: the damping and gravity field, the sample size, the particle density, the particles' and walls' stiffnesses, the particle grading including the particle size distribution (PSD), the particle shape, clump logic, time-step and wall speed and finally, the initial sample density. The main consideration when choosing the value of these parameters is to balance between adequately representing the backfill material and the simulation run times.

3.1 Two dimensional (2-D) biaxial analyses

A two dimensional (2-D) model requires less computational resources than a three dimensional (3-D) model, because it has only three spatial parameters to consider; x-coordinate, y-coordinate and angle about z-axis, whereas a 3-D model has 6 spatial parameters; the x- y- z- coordinates and angles about the x- y- z- axes respectively. Consequently, a 3-D model will have alot more particles and have more inter-particle contacts, requiring more computation. Consuming less computational resources implies a faster simulation run time.

Furthermore, the objective of this project requires the simulation of a large number of particles over many cycles. Hence, the computational resource required by the simulation of a 3-D model is impractical.

Regardless of whether its' 2-D or 3-D, the simulation run times of a DEM model are affected by many other factors. In view of the scope of this research project, 2-D DEM biaxial test is used as a precursor to a 3-D DEM simulation of granular materials subjected to cyclic loading.

Even with a 2-D DEM model, to model the full retained height would require too many particles. It would be more practical to model a representative backfill element at mid-depth behind an integral abutment. Therefore a 2-D biaxial test was considered most suitable for modelling that representative element of backfill material.

3.2 Damping and gravity field

Energy supplied to the system of particles when it is disturbed is usually dissipated through frictional sliding. Frictional sliding may not always be active in a model. Sometimes, even if frictional sliding was active, a steady state may not be reached within a reasonable time. Damping is introduced in the models to dissipate kinetic energy. The local damping coefficient has a default value of 0.7 in PFC2D (Itasca Consulting Group, PFC2D manual, 2002). This default value is used in all the DEM models for this research project.

A gravity field is set at -9.81 m/s^2 vertically to include the effects of gravity for all models. This will ensure that the particles will always 'fall' and hasten a steady state when preparing the DEM samples for cyclic testing.

3.3 Sample size and boundary conditions

The sample size for this project is determined by a combination of the expected strain size and the expected displacement of the abutment wall as it pushes or pulls away from the backfill material.

For an expected strain size, Xu (2005) estimated that a soil element at mid-height behind an integral abutment of 8 m undergoes a strain of about 0.1%. This value was obtained from finite element analyses of soil behind an integral abutment. A cyclic displacement of 16 mm was applied at the top of the abutment to simulate the annual expansion contraction of a 60 m long concrete bridge deck. This resulted in a total annual cyclic strain range of 0.093% to 0.099% in the representative soil element which is at mid-height behind the abutment.

Wood and Nash (2000) made finite difference models of an 8.8 m retained backfill material of various stiffness values behind an integral abutment. Their results indicated that the abutment's horizontal displacement at the mid-height of the abutment was about 4 mm due to a thermal expansion of 11 mm which was imposed at the top of the abutment.

Primarily based on Wood and Nash's (2000) as well as Xu's (2005) estimates, it was decided that the sample should be at least 4 m in width so as to accommodate a horizontal displacement of 0.004 m which coincides with a 0.1% lateral strain.

Triaxial tests apparatus typically consist of cylindrical samples with a height: diameter ratio of 2:1 (Powrie, 2002). So a 2 m tall cylindrical sample would have a diameter of 1m. This ratio was also adopted for the biaxial tests in this project.

The samples are usually loaded vertically in a triaxial test. Since the DEM biaxial sample will be strained laterally, a 2 m height and a 4 m width was believed to be suitable. This sample will represent a 2 m by 4 m element at mid-depth behind an abutment with 8 m retained height as shown in Figure 3.1. The sample will be consists of four walls containing the granular material. The overburden on the sample could be estimated. Assuming a unit weight of 20kN/m^3, the element would be subjected to a constant average vertical pressure of 80 kN/m^2 (or 80kPa) due to weight of overburden, as calculated by Xu (2005).

$$4m \times 20\,kN/m^3 = 80\,kN/m^2 \equiv \underline{\underline{80kPa}}$$

Figure 3.1: The sample as a 2m by 4m element at mid-height behind an integral abutment.

The following Figure 3.2 shows the biaxial test as generated in PFC2D for the main model. The main model for the biaxial test will be 4 m in width and approximately 2 m in height as discussed. The left wall and bottom wall will be permanent non-moving walls. The top wall will be programmed to maintain an average 80 kPa vertical stress on the sample to represent the overburden. The right wall will be the moving wall which will strain the sample cyclically. All four walls will have coefficient of friction of 0.0.

Figure 3.2: Biaxial test generated in PFC2D

3.4 Particle density

The density of the individual particles is required and must be specified in the PFC2D program before any DEM simulation can be started. A particle with no density will not be affected by any external forces acting on it. As this ultimately reflects on the unit weight of the backfill material, a particle density value was calculated based on an assumed bulk unit weight of 20 kN/m^3 (Xu, 2005), by the following method.
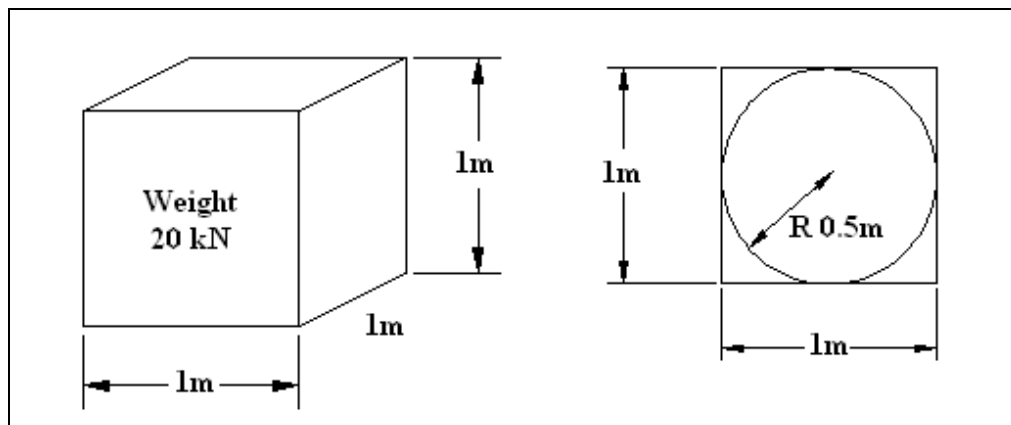
Figure 3.3: A 1m by 1m unit thick block and the circular particle of 0.5m radius

In Figure 3.3, assuming that a 1m by 1m unit thick block of material would weigh 20kN, its mass would be 2038.7 kg. Assuming that the 1 m^2 space contains only one unit thick disc of radius, R = 0.5 m that fits snugly in the space; the density of the disc can be calculated. The volume of the unit thick disc is;

$$\pi(0.5)^2 \times 1 \approx 0.7854 m^3$$

The particle density will be calculated with the mass of the material (one unit thick disc) in the space divided by the volume;

$$\frac{2038.7kg}{0.7854m^3} \approx 2595.7\,kg\big/m^3 \approx 2600\,kg\big/m^3$$

Therefore, a particle density of 2600 kg/m^3 will be used. The particle density for particles of different shapes will be adjusted to have the same resultant bulk unit weight (See Section 3.11).

3.5 Particle stiffness and wall stiffness

For the purpose of explaining the interaction between particles and walls within the PFC2D program, the particles will now be referred to as 'balls' within this section. This is how the PFC2D manual describes them in their explanation (Itasca Consulting Group, PFC2D Manual, 2002).

In Itasca's PFC2D program, the balls and walls entities have a stiffness model which provides an elastic relation between the contact force and relative displacement. The ball-ball contacts displace each other. Ball-wall contacts would displace only the ball while the wall experiences the contact force (Itasca Consulting Group, PFC2D manual, 2002). Figure 3.4 shows how the contact force is calculated in ball-ball and ball-wall normal contacts.
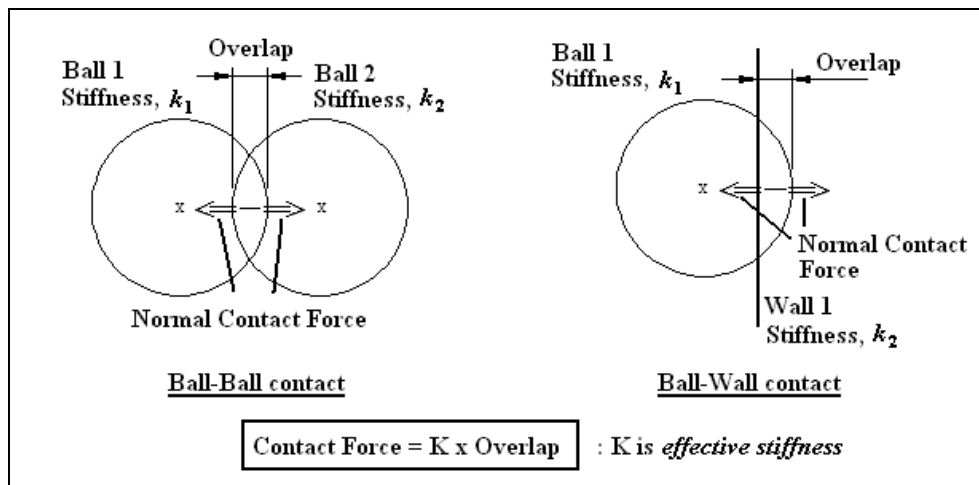
Figure 3.4: Ball-ball and Ball-wall normal contact

The stiffness value is the relationship between the contact force generated and the overlap of ball-ball and ball-wall contacts. When two entities (ball-ball or ball-wall) are in contact, the effective stiffness is assumed to be the entities' respective stiffness acting as springs in series. This is the linear contact model utilised. The effective stiffness, K is calculated by;

$K = \dfrac{k_1 k_2}{k_1 + k_2}$: Where k_1 and k_2 are the stiffness value of two respective entities as shown in Figure 3.4.

This is true for both normal and shear stiffness. Both normal and shear stiffness must be specified for every particle and walls in PFC2D. For this research project, the normal and shear stiffnesses will have the same value so that the particle is equally stiff in both normal and shear directions during contact with another particle or wall.

If the ball stiffness and wall stiffness are different, the *harder* (higher stiffness value) material would *sink* into the *softer* (lower stiffness value) material when they are pushed against each other. An equal stiffness between the ball and wall ensures no *sinking* when ball meets wall. Therefore, the ball-wall contacts needs to be similar to ball-ball contacts. Therefore, the wall stiffness and ball stiffness will have the same value.

A high stiffness value will cause *oversensitivity* in the objects, resulting in large changes in the contact forces due to insignificant movement. A low stiffness value however, would dull the object's *sensitivity* resulting in the need for large movements before any significant changes in the contact forces can be observed.

A typical value of stiffness in the examples shown in the PFC2D manual was 1.0E8 N/m. A suitable stiffness value would likely be within the vicinity of that order. Several values of ball and wall stiffness were tested to determine a suitable stiffness value. High stiffness samples gave results with a lot of *noise* as the slightest movement causes large changes in the contact forces as explained previously. If the stiffness was too low, the samples were not sensitive to changes, and had results that did not make sense. The details of the testing process will not be described in this thesis. In short, a stiffness value of 5.0E8 N/m was deemed to be suitable and therefore utilized for this research project. All particles will have the same stiffness values, regardless of its sizes. Both the particles for the samples and the DEM walls will have a stiffness value of 5.0E8 N/m for both normal and shear stiffness.

3.6 Choice of particle size and grading

Real backfill materials consist of particles of different sizes. The small particles fill the voids of the large particles and contribute to the overall stiffness of the granular assembly. In soil mechanics, this is characterized by soil grading, which maps out the distribution of particle sizes in a sample in terms of mass.

Ideally, the particle size would be the same as that specified in DMRB BA42 for bridge backfill; no greater than 75 mm. In the context of a simulation however, it is prudent to ensure a minimal run time. In the discrete element method, larger particle sizes imply a smaller number of particles to fill the same volume of space. The aim is that, despite having larger particles the sample still behaves as a granular material and reflects

the micromechanical behaviour of the sample with the smaller original particle size as specified in DMRB BA42 (2003).

For the purpose of this project, it was decided that the particle size distribution (PSD) curve for the samples will be approximated by 10 discrete particle sizes. The reason for this is that with 10 particle sizes, it would be convenient to split each particle size into 10% of the overall sample space respectively. The sample will be considered to be well-graded by fulfilling the criteria of the Uniformity Coefficient, U.

The criterion for a well-graded material is that the uniformity coefficient, U must be greater than 10. The uniformity coefficient is defined as the ratio of the 60th percentile to the 10th percentile particle size passing through in a sieve test (denoted by D_{60} and D_{10} respectively).

Generally, literatures suggest that well-graded materials have stronger shear strength and therefore greater resistance to shear and cyclic loading than uniform or monodisperse materials (Sitharam, 2003; Ni, 2003). It is therefore necessary to have a sample that is well-graded rather than uniformly graded. Although the main reason a well-graded material is necessary in this project is because it was specified in DMRB BA42 (2003).

3.6.1 Larger particle size for simulation

DEM by Ni (2003) showed that samples with larger particle sizes have larger bulk friction angle, which should translate to higher critical deviatoric stress. However, in Ni's (2003) DEM model, the comparison was between 5000 large particles and 50000 small particles filling the same volume. The large particles were about 10x the size of the small particles. It may be that the effect of particle size is only significant when the differences in sizes are large (in this case 10x). Sitharam and Nimbkar's (2000) DEM test on granular material with different size ranges compared the effects of particle sizes on a more moderate scale. Four samples consisting of parallel gradation with the sizes 30-70 mm, 70-110 mm, 90-130 mm and 110 to 150 mm respectively, were subjected to biaxial tests. They concluded that an increase in particle size only marginally increases the friction angle and therefore had no significant effect. It is safe to assume that a scale of 3x the original particle size has only marginal effect on the sample's stiffness.

3.6.2 The particle size distribution approximation

Considering the above, it was decided that particle sizes 3x the original BA42 specification were to be used in all subsequent simulation testing. The largest particle size must not have an overall size or diameter greater than 75 mm x 3 = 225 mm. The sample's particle size distribution (PSD) will range from 0.01 m-0.225 m diameter.

From Table 3.1, the 10th percentile is the particle size of 0.005m and the 60th percentile is the particle size of 0.1250 m. Hence the uniformity coefficient of this sample would be:

$$U = D_{60} / D_{10} = 0.1250m / 0.01m = 12.5 > 10$$

So, the main model's (see Figure 3.2) material is assuredly well-graded.

Table 3.1: Particle size and its distribution in percentile passing for 10 particle sizes

Particle Size (m)	0.0100	0.0250	0.0500	0.0750	0.1000	0.1250	0.1500	0.1750	0.2000	0.2250
% passing	10%	20%	30%	40%	50%	60%	70%	80%	90%	100%

Figure 3.5 shows the Particle size distribution (PSD) plot for the DEM main model material, as compared to the smooth curves of the well-graded material for both the original size and the enlarged 3× original size. Particle size in the x-axis is in terms of the particle diameter.
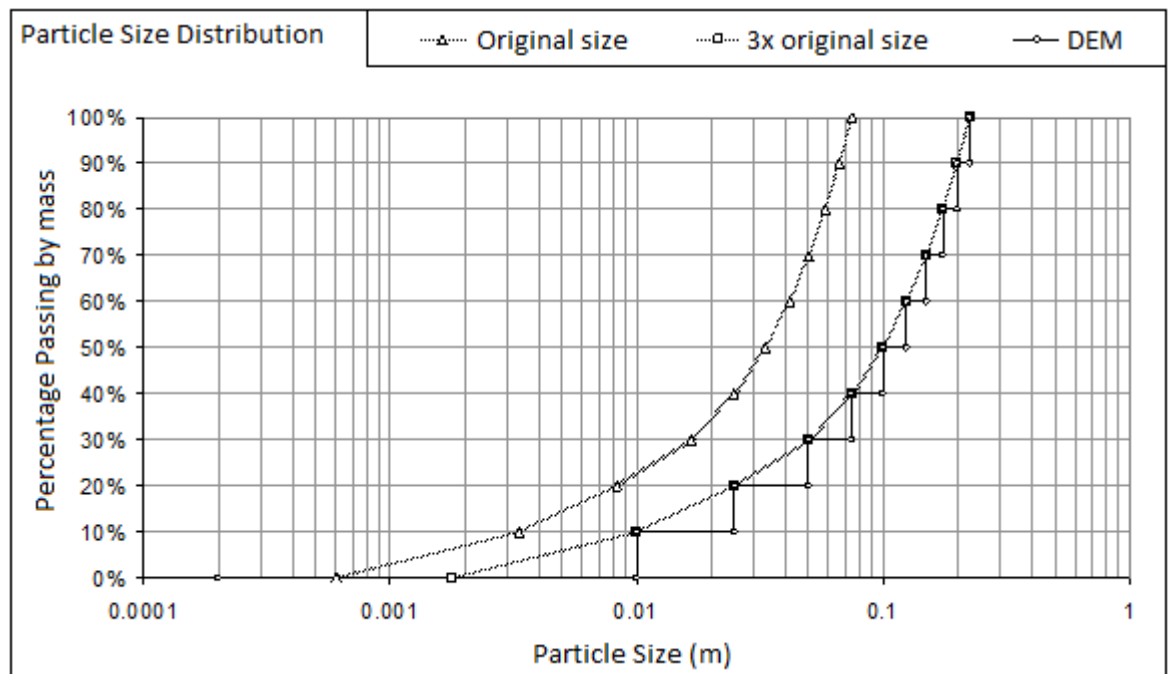
Figure 3.5: PSD curve for Original Size, 3× Original Size and the gap-graded DEM model

3.7 Representation of particle shape

Real backfill material consists of particles with non-circular shapes. The particle shape is characterised by three principal scales; the form, angularity and roughness (Santamarina and Cho, 2004) as described in section 2.4.4.

Ni (2003) generated 3-D particles that consisted of two bonded spheres. The contact bond stiffness value was high enough such that each pair of spheres behaves as a single rigid particle and no breakage occurs. It was characterized by a shape factor defined as $(R+r)/R$, where R and r are the radii of the larger and smaller spheres respectively as shown in Figure 3.6. A single spherical particle would have a shape factor of 1.0. A shape factor of 1.5 was confirmed by Ni (2003) to be able to provide a reasonable representation of the behaviour of real sand. This was based on the DEM investigations of Rothenburg and Bathurst (1992) in which a peak friction angle of 42°, comparable to real sand, was obtained when their elliptic particle aspect ratio (length over width) was 1.5. The volumetric dilation of the assembly was close to that of real sand as well.
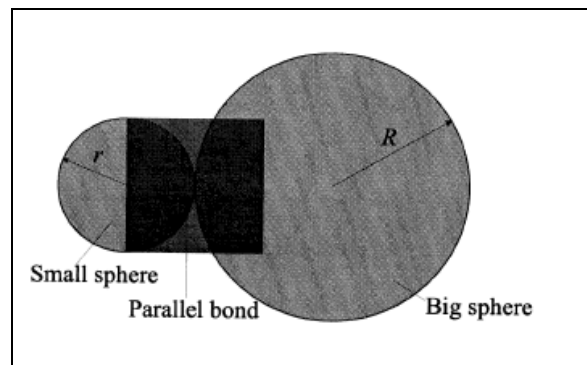
Figure 3.6: Schematic illustration of a bonded particle and the radii that relate to the shape factor (Ni, 2003)

Ni (2003) further cited Ting (1993) for reporting that an increase of 20° (from 25° to 45°) in the peak friction angle was observed when the particle aspect ratio was increased from 1.0 (circular particles) to 2.0 (ellipsoid particles). Lin and Ng (1997) also observed similar behaviour in three dimensional DEM tests of elliptic particles.

According to Ni's (2003) definition of the particle shape factor, it works out to be the inverse of particle form. A shape factor of 1.5 is equivalent to a particle form of 1/1.5 or 2/3. Hence, the particle form of 2/3 or 0.6666 was adopted for the main model sample. Similarly, a shape factor of 1.5 with this configuration of particles gives an angularity of 0.5; that is $R=2r$ as shown below;

$$\frac{(R+r)}{R} = 1.5 = \frac{3}{2}$$
$$2(R+r) = 3R$$
$$2R + 2r = 3R$$
$$\underline{\underline{2r = R}}$$

Cho et al. (2006) reported that manufactured crushed sands have a form range of 0.7 to 0.8 and angularity range of 0.2 to 0.3. Natural sands however have a wider range with a form range of 0.5 to 0.9 and angularity range of 0.3 to 0.9. The proposed particle shape with form 0.6666 and angularity 0.5 seems to fall into the shapes of natural sands. The backfill material for integral bridge was specified in the design manual (DMRB BA42/96, 2003) to be selected granular material complying with class 6N or 6P in Table 6/1 of the Specification for Highway Works. That material consists of both natural and crushed, gravel and sand among other permitted constituents (MCHW 1.600, 2005) as described in section 2.4.1. The chosen particle form and angularity is within the range of what is expected in the particle shapes of the backfill material.

3.7.1 Representation of surface roughness

For a DEM biaxial test, Ni (2003) utilized a typical inter-particle friction angle of 26° based on medium quartz sand, citing Rowe (1962); Rowe and Barden (1964); Procter and Barton (1974) for this value. This is equivalent to a friction coefficient of:

$$Tan\ 26° = 0.4877 \approx \underline{\underline{0.5}}$$

A coefficient of friction of 0.5 was therefore adopted for all particles in the DEM tests of this project. In summary, the particle shape for this project will have a form of 2/3 and angularity of 0.5, which is equivalent to a shape factor of 1.5 as described by Ni (2003). The surface roughness, represented by the inter-particle friction coefficient, will be 0.5.

3.8 Clump Logic

A parallel bond was utilised in Ni's (2003) particle with shape factor 1.5. The contact bond value was set very high such that no breakage occurs and the particles could be considered rigid. The reason for this is because the research project was not interested in particle breakage. Similarly, this research project is not interested in particle breakage due to crushing. Particle crushing cause changes in the soil grading influencing the basic constitutive properties of the soil (Wood and Maeda, 2008). However the issue with particle crushing is beyond the scope of this project.

Instead of utilising a very strong parallel bond between the discs, the clump logic in PFC2D is used. The clump logic provides a means to create and modify a group of slave particles, or *clumps*. The clumps behave as rigid bodies. Contacts internal to the clump are skipped during calculation cycles resulting in a saving in simulation time. Contacts external to the clump are not affected and the DEM contact models apply. Furthermore, the discs within a clump may overlap as contact forces are not generated between them (Itasca Consulting Group, PFC2D manual, 2002).

The particles in this project will consist of several discs clumped together to create different shapes. The rigid particles that result, where no breakage will occur, are suitable for the scope of this project.

3.9 Time-step and wall speed

The time-step value (symbolised by dt) is a time scale that represents one calculation step in the DEM simulation. A calculation step is the step in which the discrete element calculations of the forces acting, the displacement caused and the new coordinates of each particle are done. The dt can be described as a proportion of a unit time used in the model. For example, if the unit time is in seconds;

1 unit time = 1 s

dt = time-step (unit time in seconds within 1 calculation step)

If dt = 1.0E-5 s/step; then 1 calculation step = 1.0E-5 seconds or 0.00001 s.

In other words, it would take 1.0E+5 or 100000 calculation steps in order to describe the new particle positions and the forces acting on it in 1 second. The time-step is an important scale as it involves the detailed movement of particles (and walls) in the model within the chosen unit time. If for example, dt =1.0 s/step; then 1 calculation step = 1.0 s. While this would be efficient, small displacements and new particle contacts that form or break within that 1 second is missed. Time-step would also relate to the consideration of wall speed as the intention of this project is to strain the granular sample by moving the right wall cyclically against the material.

The following Figure 3.7 illustrates the effect of different time-steps for a particle travelling at 1 m/s over a length of 1 m.
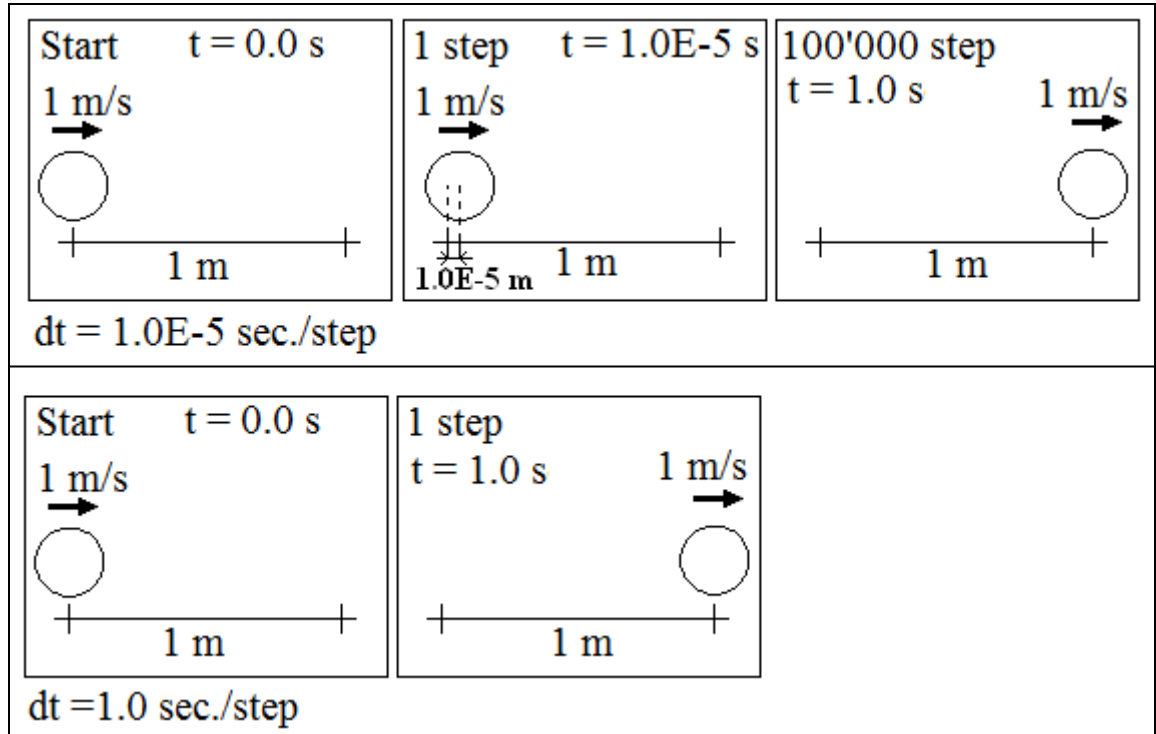
Figure 3.7: Effect of different time-step value *dt* for a particle of speed 1m/s to travel 1m

The walls' movement are subjected to the time-step in a similar fashion. In moving the walls, a velocity is specified for the moving wall. The relationship between wall speed and time-step can be described as follows:

v_{wall} = wall velocity in m/s

dt = time-step (unit time in seconds within 1 calculation step)

Steps = number of calculation steps

Displacement = the total distance moved by the wall

$$v_{wall} \cdot dt = \frac{Displacement}{Steps}$$

By default, a stable time-step *dt* is calculated automatically in PFC2D (Itasca Consulting Group, PFC2D manual, 2002). In the process of preparing the sample, the automatic time-step in the simulation was varying at about 6.0E-5 s/step as it was adjusted by PFC2D. However, a constant time-step enables the precise calculation of the number of steps when moving the walls at a certain speed to reach a precise displacement. Hence, a time-step *dt* value of 1.0E-5 s/step was chosen for all samples.

In choosing the wall speed for the moving wall, it was noted that as the wall moves, it must not *pass through* any particles in one calculation step for the same reason as described earlier and in Figure 3.7. Otherwise, the particles would *escape* from the confinement of the four walls. The smallest Ni particle has a size (diameter) of 0.01m (section 3.6.2- Table 3.1). Therefore, it was noted that the wall must not travel greater than 0.005 m in a calculation cycle. This is not an issue as long as the time step *dt* is small enough. With the time-step *dt* set at 1.0E-5, the moving wall was unlikely to pass through even the smallest particles.

However, the slower the wall speed, the better it will represent the annual cyclic load of an integral abutment. If the wall speed was too slow, it would prolong the simulation run times. An optimum wall speed would be fast enough such that the simulation run times were acceptable, but slow enough that it does not compromise the overall stability of the particles (i.e. particles escape or move in high velocities within the sample.)

Following that, the wall speed was chosen by trial and error with the testing of a range of wall speed applied on a sample of particles under the same conditions. The details of those tests will not be explained in this thesis. In the end the wall speed of 0.005 m/s was deemed suitable for this project. It was large enough that there was an acceptable simulation run times, but slow enough that the particles should remain stable. With *dt* = 1.0E-5 s/step, it would take 100'000 calculation step for the wall to move by 0.005 m. Effectively, the wall movement is 5.0E-8 m per calculation step.

Ni (2003) conducted 3D DEM numerical biaxial tests by driving the rigid loading platen at the top and bottom of the sample against each other at a relative speed of 3.0E-8 m per calculation step. The numerical shearbox test of spherical particles was sheared by moving the bottom half of the sample at 2.5E-8 m per calculation step. The platen speed that was chosen in Ni's (2003) tests was such that numerical stability was maintained in the DEM sample.

The wall movement of 5.0E-8 m per calculation step chosen for this project is slightly higher than Ni's (2003) loading platen speed but the values are of the same order. Compared to the monotonic tests that Ni (2003) conducted, a higher wall speed is necessary for acceptable computation times. Nonetheless, it is believed that numerical stability of the sample was maintained under this wall speed.

3.10 Initial sample density

Literature suggests that the backfill undergoes densification due to cyclic loading. The initial density of the sample affects how much the sample can increase in density. It is therefore important in this study to also monitor the sample's density, so as to confirm or eliminate it as a factor in the build-up of lateral earth pressure in the backfill.

The design manual specified that the backfill material is to be compacted to 95% of maximum dry density as described in section 2.4.1. Banks (2009) showed that for Leighton Buzzard Sand, the 95% of maximum dry density is approximately equivalent to 70% relative density, based on values used in Xu's (2005) thesis. Xu (2005) conducted cyclic triaxial tests on three initial relative densities of Leighton Buzzard Sand; 18%, 70% and 92%. It was shown that regardless of initial relative density, the lateral earth pressure continued to increase with cycles without stabilising (Xu, 2005). Nonetheless, an initial sample density is required for the setting up of the DEM model.

A sample at 95% of the maximum dry density was utilised for this project. The maximum dry density was first obtained by generating a sample of particles with shape factor 1.5 as prescribed by Ni (2003) to fill a 1 m wide 'box' shown in Figure 3.8. A well-graded material with 10 particle sizes was generated with a total particle volume (volume of solids) of 1 m^3. The total mass of this sample was calculated to be about 3034.65 kg. Details of calculating the design density are shown in Appendix 1.
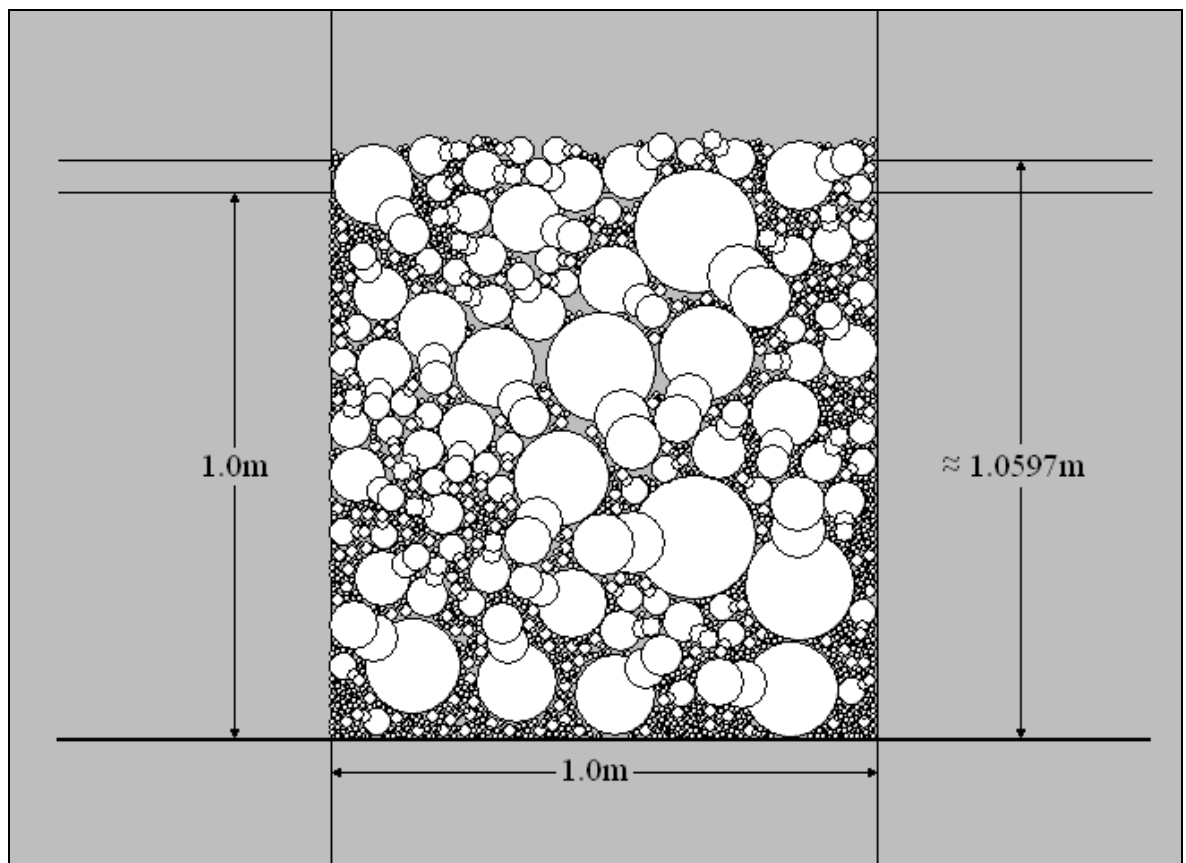

Figure 3.8: 1m wide 'box' for calculating maximum dry density

The sample was then compacted into the 'box' as much as possible with inter-particle friction set at 0.0. Then the sample was left to settle by itself under standard gravity (9.81 m/s^2) over a few million calculation cycles without any vertical pressure from the top. The overall height of the sample within the 'box' was estimated to be about 1.0597 m. An approximate overall volume of the sample is estimated to be 1.0597 m^3 (1.0597m× 1.0m× 1.0m).

The maximum dry density is obtained by dividing the total mass by the estimated total volume. The total mass of the particles is then calculated for an 8 m^3 (2m × 4m× 1m) sample space based on 95% of this maximum dry density. The total mass of the particles are calculated as follows:

$$\rho_{dry\ max} = \frac{Total\ mass}{Total\ volume} = \frac{3034.65kg}{1.0597m^3}$$

$$\rho_{dry\ max} = 2863.6862kg/m^3 \approx 2863.69kg/m^3$$

$$\therefore \rho_{95\%} = \rho_{design} = 0.95 \times 2863.69 = \underline{\underline{2720.3055kg/m^3}} \approx 2720.5kg/m^3$$

$$For\ an\ 8m^3\ space;$$

$$Total\ mass = 2720.5 \times 8 = \underline{\underline{21764kg}}$$

The number of particles based on this design density (ρ_{design}) was also calculated as shown in Appendix 2. The total number of separate particles in the sample is 8853, maintaining an approximate 95% maximum dry density value of 2720.5 kg/m^3 in an 8 m^3 sample space. This will be the sample's initial density.

3.11 Comparing different particle shapes

The effect of particle shape on the overall soil behaviour is well established in section 2.5.4. In DEM, the different particle shapes can be represented by clumping several discs together as discussed in section 3.7 and 3.8. While there the main model contains particles with the shape inspired by Ni's (2003) 3-D particle of shape factor 1.5 described in section 3.7, it was important to have other shapes for which the main model's *Ni particle* can be compared to.

Overall, there are four different particle shapes tested in this project. They are labelled; the *Ni particle*, the *Disc*, the *Elliptic* and the *Triangular* as shown in Figure 3.9. The different shapes enable the comparison of different forms and angularity. The Ni particle and the Elliptic have the same form of 2/3, but different angularity. The Elliptic and the Disc however have the same angularity of 1.0 (rounded) but different form. The Triangular shares the same form and angularity with the Ni particle illustrating the limitations of the description of particle shape by those factors.

The Triangular is ultimately different from the Ni particle and was expected to behave differently. The mass and volume for each particle shape is adjusted to be equivalent to one another. This was achieved through an iterative process in PFC2D.
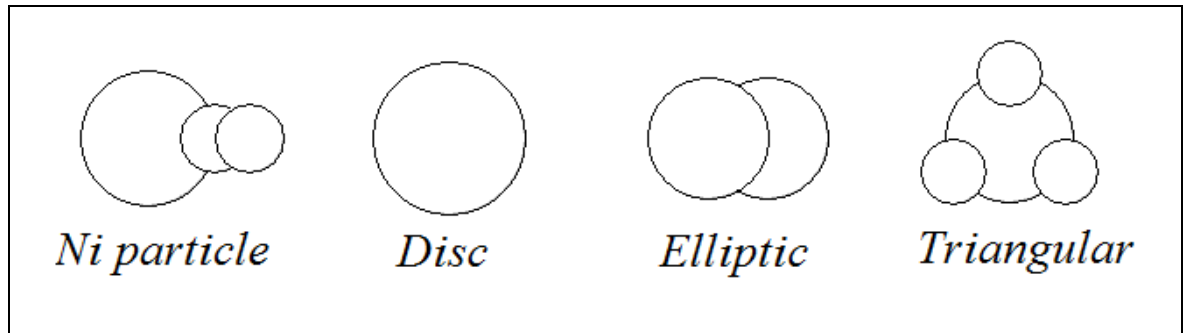

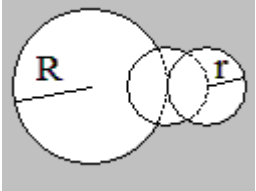**Figure 3.9: The four different particle shapes**
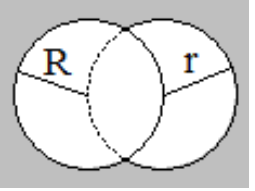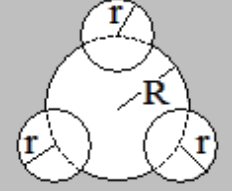
The *Ni particle* was inspired by the particle with shape factor 1.5 used by Ni (2003). It consists of three discs clumped together; one large disc and two small ones. The smaller discs are half the size of the large disc, giving a particle angularity of 0.5. The Ni particle was used as the main particle shape type on which its mass and volume of one particle were replicated for the other three particle shapes. This enables all four samples with their respective particle shapes to have the same total mass, particle count and grading as well as an approximately similar total volume of 8 m^3.

The *Disc* is as the label implies and represents a sample consisting of circular particles. The *Elliptic* consists of two discs of the same size clumped together, forming an approximate elliptic shape. The *Triangular* consists of four discs clumped together; one large disc at the centre and three smaller ones at three different positions approximating a triangular shape. The smaller discs are half the size of the one large disc, thus giving a particle angularity of 0.5 similar to the Ni particle.

For the largest Ni particle, the larger disc, which defines the overall size of the particle, has a radius of 0.1125m (section 3.6.2). A ball density of 2600 kg/m^3 was set for the Ni particle only. This is the density of each constituent discs that make up the clump. The radii for the Disc, Elliptic and Triangular particles were adjusted until they all have an equivalent porosity value inside their respective measurement circle. The ball density for each of the shapes was also adjusted until they had the same mass (for 1 particle). This process was repeated for all ten particle sizes as defined in section 3.6.2.

The following table 3.2 shows the four particle shapes and their particle density value that gives them equivalent mass and volume based on the values of their largest particles' radii.

Table 3.2: Four different particle shapes

	Ni Particle	Disc	Elliptic	Triangular
Radius value for a single largest particle				
R (m)	0.1125	0.1278	0.10075	0.10743
r (m)	[=R/2] 0.05625	-----	[=R] 0.10075	[=R/2] 0.053715
Volume (1 particle)	0.05131 m^3	0.05131 m^3	0.05131 m^3	0.05131 m^3
Ball density	2600 kg/m^3	3021 kg/m^3	2431 kg/m^3	2444 kg/m^3
Mass (1 particle)	155 kg	155 kg	155 kg	155 kg
Radius of largest inscribed circle (m)	$R_i = 0.1125$	$R_i = 0.1278$	$R_i = 0.10075$	$R_i = 0.10743$
Radius of smallest circum-scribing circle (m)	$R_c =$ $R+r = 1.5R$ $= 0.16875$	$R_c =$ 0.1278	$R_c =$ $(2R+r)/2 = 3R/2$ $= 1.5R$ $= 0.151125$	$R_c =$ $R+r = 1.5R$ $= 0.161145$
Form [R_i/ R_c]	0.6666	1.0	0.6666	0.6666
Angularity [r/R_i]	0.5	1.0	1.0	0.5

3.11.1 Generating the four samples

Four samples, each consisting of particles of the specific shapes, were generated. As the different particle shapes are equivalent in volume and mass, the same number (8853) of separate particles were generated for each sample with the exact particle grading and 10 separate particle sizes. This was based on the design density (initial density) as calculated

in the previous section 3.10. The process of generating the particles and clumping them together was automated by programming PFC2D as detailed in Appendix 3.

All the particles for each sample were generated in an orderly fashion consisting of rows and columns, specified to give exactly 8853 separate particles according to their respective sizes. The friction coefficient, normal and shear stiffness values for all the particles were entered. The density value for each particle shape was also entered for their respective sample. Figure 3.10 shows the Ni particles generated in an orderly manner.

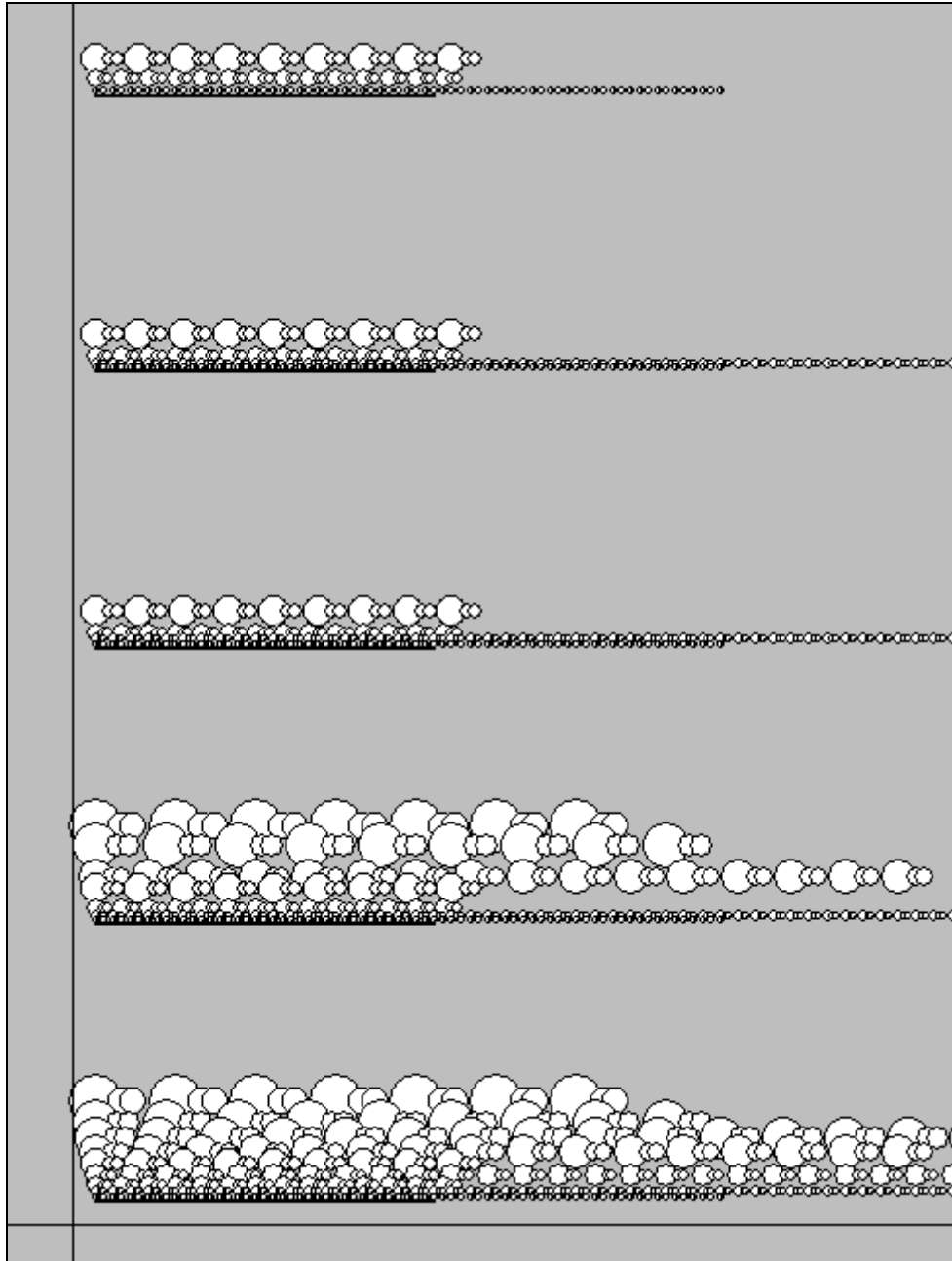**Figure 3.10: Generating Ni particles in an orderly manner**

The particles were generated within a wide space in PFC2D, about 100 m in height and 4 m in width, and then compressed to a smaller confined space (about 6 m in height) for *mixing*. They were mixed within the confined space by switching the scale and direction of the gravity field in the program. The gravitational field is controlled by setting

the gravitational acceleration on the vertical and horizontal direction. Figure 3.11 shows part of the mixing process for the Ni particle in which the direction of gravity was changed from downwards and to the left.
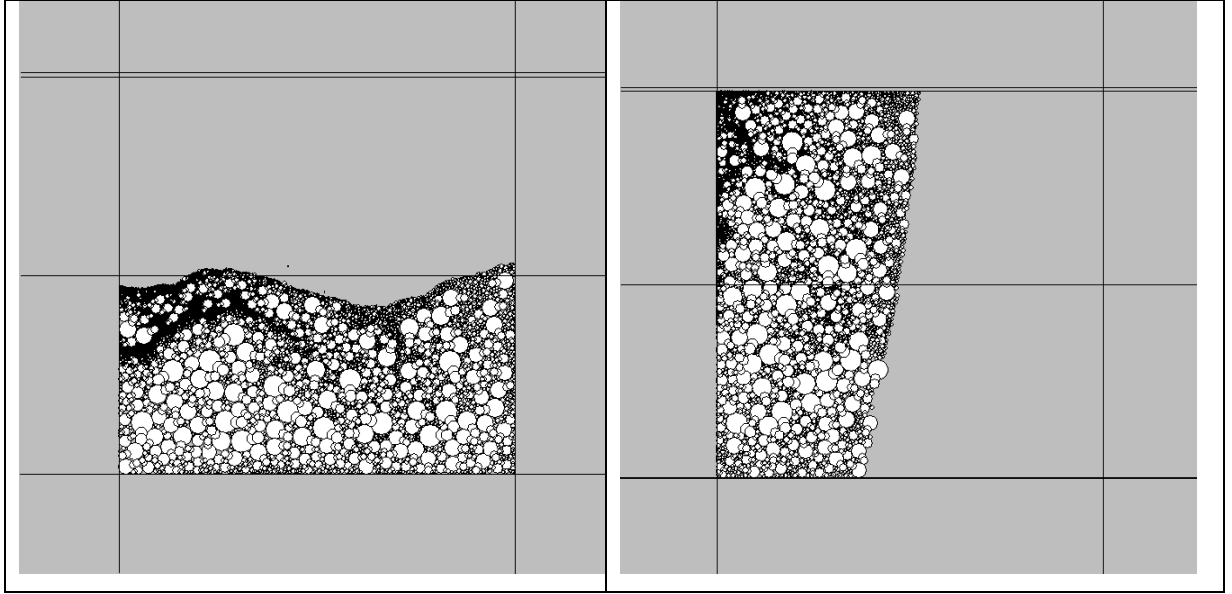

Figure 3.11: The mixing process for the Ni particle by changing the direction of gravity

Specifying a positive gravity field on the vertical axis causes the particles to accelerate upwards while a negative gravity field means a downward acceleration. Similarly, a positive gravity field on the horizontal axis causes the particles to accelerate to the right while a negative gravity field means the particles will accelerate to the left. For example, the gravitational acceleration can be set at -500 m/s^2 in the vertical direction and +250 m/s^2 in the horizontal direction. By changing the scale and vertical-horizontal combination of the gravitational acceleration, the particles can be sent *falling* in various directions over a few ten thousands of calculation cycles until it is well mixed. This is indicated from observing that the particles of different sizes are not grouped together within the sample and distributed randomly over the sample space. This is a subjective process.

Finally, the gravity field was set to 9.81 m/s^2 in the vertically downward direction only. The particles were compressed downward to an approximate sample size of 2m by 4m. This was done by having the top wall move downward making contact with the top layer of particles. The average vertical pressure on the sample was set at 80000 N/m^2 for which the top wall was instructed in the PFC2D code to move up or down in an iterative manner until that value is achieved, with a tolerance of 0.001. That means that the average vertical pressure must be within the range of 79999.999 N/m^2 and 80000.001 N/m^2.

The long iterative process also enables the particles to settle down in the sample space, indicated by a low maximum particle velocity (i.e. sample at rest). The sample is considered ready for testing when these conditions were achieved. The following Figure 3.12 shows the four samples of different particle shapes ready for testing.
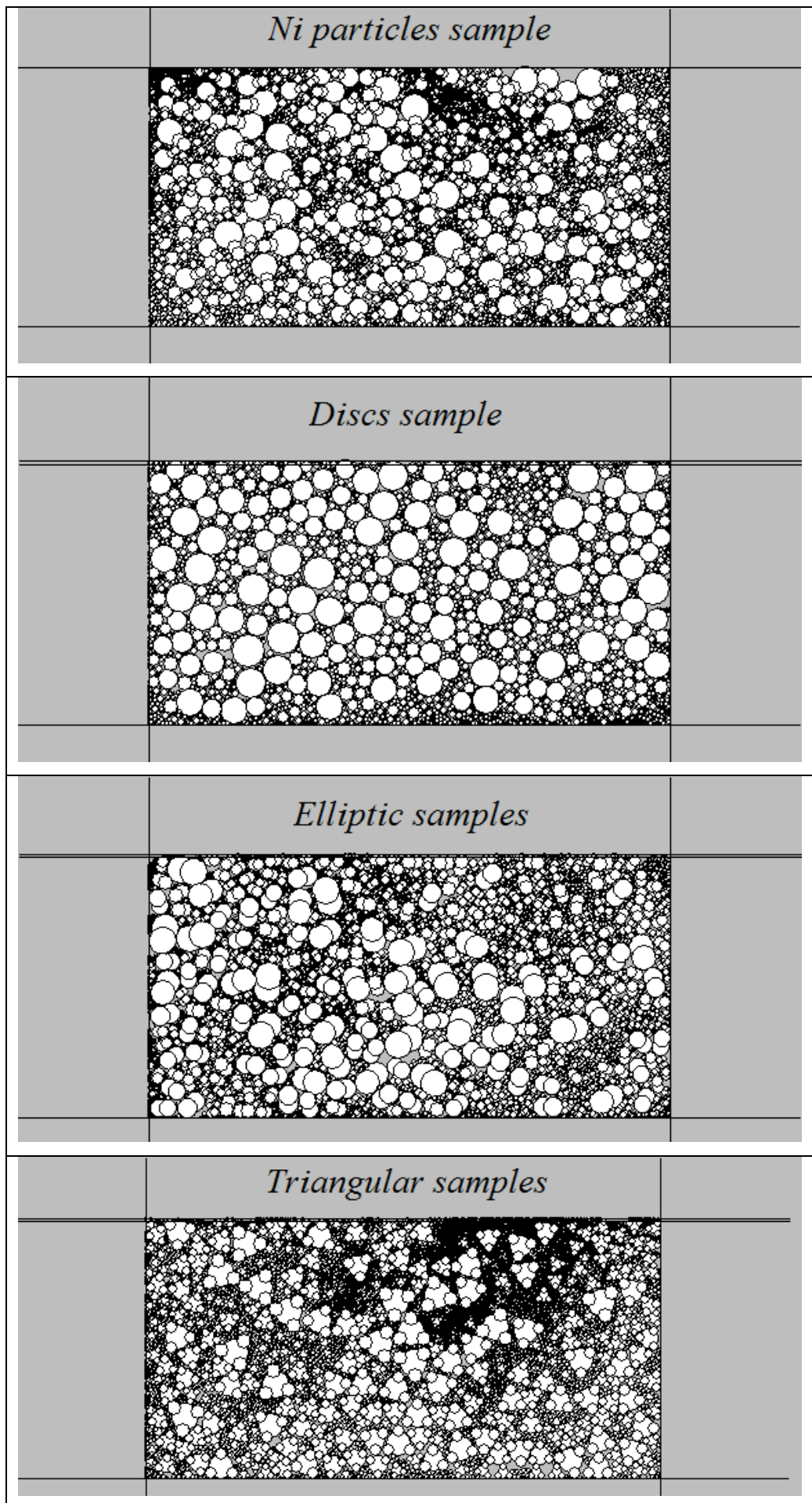
Figure 3.12: The four samples of different particle shapes ready for cyclic straining

3.12 Summary of DEM preliminaries

1. The backfill behaviour behind an integral abutment was modelled by a 2-D DEM biaxial test on a granular sample. The 2-D model is simpler than a 3-D model and requires less computing power resulting in faster simulation run times.

2. The damping coefficient is set at the default value of 0.7. The gravity field is set at 9.81m/s^2 vertically downward for the cyclic test.

3. The sample will be 2 m in height and 4 m in width, representing a 2 m by 4 m backfill element at mid-depth behind an integral abutment. The sample will be subjected to a lateral strain of 0.1%. An overburden stress of 80 kPa will be applied on the top of the sample.

4. Particle density is set at 2600 kg/m^3 for the main sample (Ni particles). The value of particle density for different shaped particles will be adjusted such that they will have an equivalent resultant weight to that of the main sample's particles.

5. The particle stiffness and wall stiffness were set at 5.0E8 N/m for both normal stiffness and shear stiffness.

6. The backfill material is well-graded with 10 particles sizes, one for every 10th percentile; enabling the convenient calculation of the uniformity coefficient, $U = D_{60}/D_{10} = 60^{th}$ percentile/ 10th percentile. The sample used will have a uniformity coefficient $U = 12.5$ where $U > 10$ is considered well-graded.

7. The particles will be 3x the original size. This was done for practicality since generating enough particles at the original size to fill a 2m by 4m space was unfeasible due to slow downs and the sheer demand on computing resource. Literatures have shown that an increase in particle sizes (up to 10x) only caused a marginal increase in the bulk friction angle.

8. The particles shape factor of 1.5 causes the material's behaviour to be comparable to real sand. The particle used by Ni (2003) based on this shape factor has a form of 2/3 (or 0.6666) and angularity of 0.5. This form and angularity of the particle are within the range of natural sands. The surface roughness can be accounted for by setting the friction coefficient of the particles to 0.5.

9. The different particle shape can be generated by utilizing the *clump* feature in the PFC2D software. The circular discs *clumped* together become a new rigid particle.

10. The time-step, *dt* is set at 1.0E-5 and the speed of the straining wall is set at 0.005 m/s. Therefore, in 1 calculation step the wall will move 5.0E-8 m.

11. Initial sample density is to be 95% of maximum dry density as specified in the design manual (DMRB BA42/96, 2003).

12. The main sample will consist of particles with the shape inspired by Ni (2003), labelled as the Ni particle. Other particle shapes sample was made to compare with the main sample. Overall four different particle shapes were made, respectively labelled as the Ni particle (for the main sample), Disc, Elliptic and Triangular particles.

13. The samples were generated in an orderly manner and were mixed by changing the scale and direction of the gravity field. This was done over several millions of calculation steps before finally setting the gravity field to 9.81 m/s^2 vertically downwards and compressing the sample into the 2 m by 4 m space and applying an 80 kPa vertical stress from the top. The samples were then finally ready for the cyclic straining tests.

Chapter 4: Research methodology

This chapter describes the research methodology of this project. The first section outlines the overall cyclic straining programme detailing how the DEM sample will be tested in PFC2D. This is followed by specifications of the macro-mechanical and micro-mechanical parameters that were monitored and recorded for analysis from the PFC2D generated DEM biaxial cyclic test.

4.1 Overall cyclic straining programme

The sample were subjected to 100 cyclic strains of 0.1% by displacing the right wall horizontally at a speed of 0.005 m/s and time-step dt of 1E-5 s/step. The reasons behind the choices of time-step and wall speed were described in section 3.9 and the reason for having a strain size of 0.1% was described in section 3.3.

The design manual (DMRB BA42/96, 2003) defined a soil stress profile for integral abutment which was predicted for maximum bridge deck expansion at the end of a 120 year design life. It was decided that 100 years of a 120 year design life was sufficient for the purpose of this research project which is to monitor the particles behaviour when the backfill material is subjected to cyclic movement of the abutment. Any drastic change within the backfill material subjected to cyclic straining is likely to occur within those 100 years. In any case the 100 annual thermal cyclic movement of an integral bridge's design life is represented by 100 cyclic strains against the DEM sample. Simulating 100 cyclic strains instead of 120 also shortens the simulation run times.

One straining cycle is defined as when the sample has completed an expansion phase followed by a compression phase. The expansion phase is completed when the right wall has moved horizontally outward to 0.1% strain. The compression phase is completed when the right wall has moved back to 0.0% strain (its' starting position) from the previous 0.1% strain, thus completing one strain cycle.

The cyclic straining will begin with the right wall moving away from the sample first. This invokes a 'summer-start' condition in terms of the starting seasons and the sample goes into an active stress state at the start. Although the starting season was noted to not have a significant effect in the long term (see section 2.2.3), Xu (2005) inferred that the build-up of horizontal stress was associated with the rolling of non-circular particles close to or at the active stress state. It was prudent to give the sample the best condition in which particle reorientation could occur for the purpose of this research project.

Figure 4.1 shows details of the sample space as generated in PFC2D with the four walls and the measurement circle encircling the sample measuring porosity and coordination number. Preparing the 2m and 4m sample space in PFC2D was done by first using a modified code for a biaxial test found in the PFC2D manual (Itasca Consulting Group, PFC2D manual, 2002) to generate the four walls forming the sample space with the upper wall programmed to maintain an average vertical stress of 80 kPa. The left wall and the bottom wall are fixed in position. The horizontal and vertical stresses and strains as well as the porosity and coordination number were programmed to be monitored during the cyclic strains. The sample was then strained by moving the right wall. Appendix 4 shows the code used in PFC2D for carrying out this process.
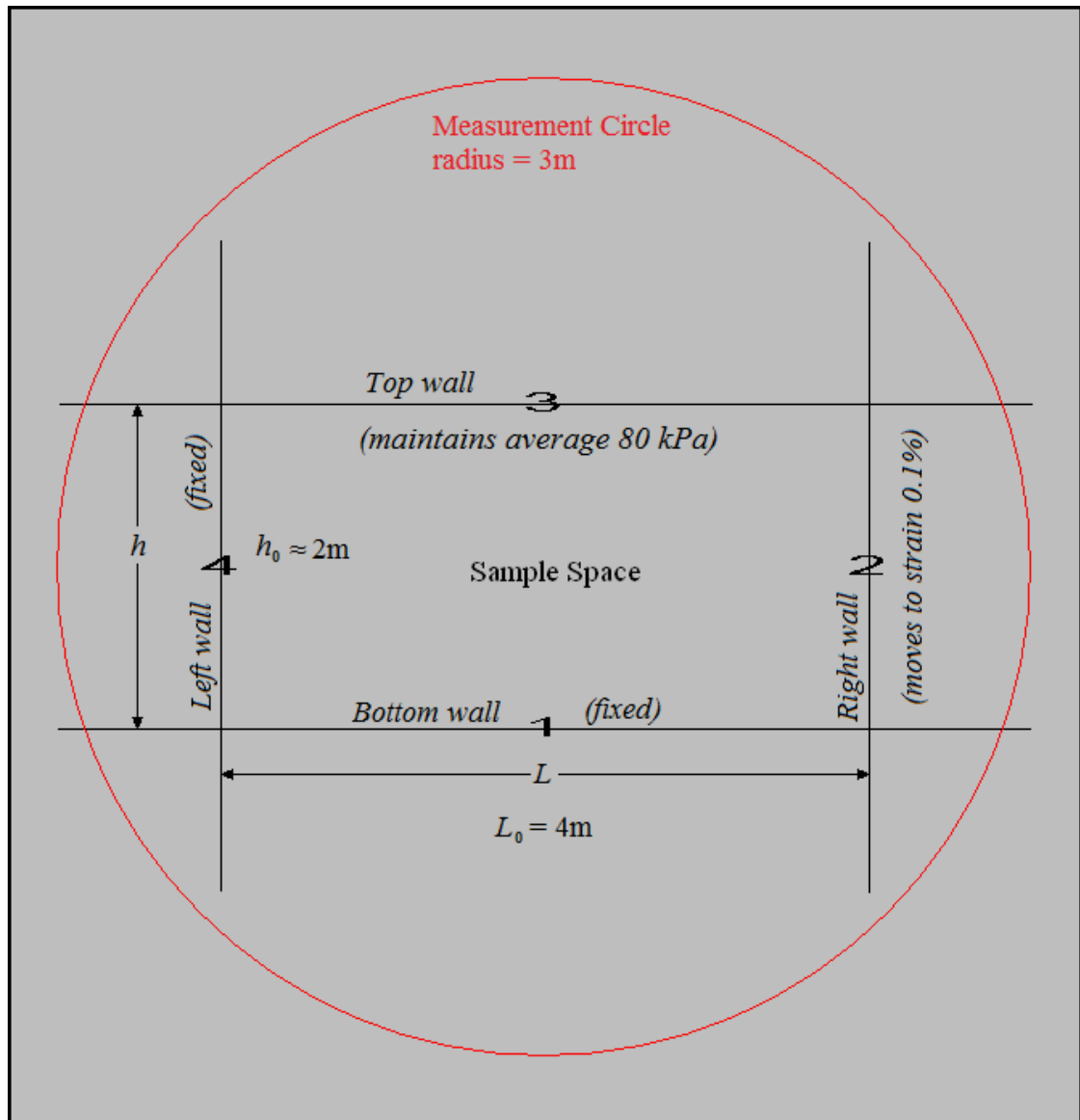

Figure 4.1: The sample space and the measurement circle

There are 6 parameters that are monitored continuously during the cyclic straining process of the samples. They are the horizontal strain, horizontal stress, vertical strain, vertical stress, porosity and the coordination number.

4.2 Measurement of stresses and strains

The horizontal strain (labelled as *wexx*) is measured as the displacement of the right wall divided by the initial sample width L_0 of 4m. The right wall was programmed to displace by 0.004m to correspond to a 0.1% strain. It was monitored to ensure that this is the case. The horizontal stress (labelled as *wsxx*) is measured as the average of the total forces on the left and right walls divided by the current height of the sample (i.e. the position of the top wall from the bottom wall) *h*.

The vertical strain (labelled as *weyy*) is measured as the displacement of the top wall divided by the initial sample height h_0 of about 2m. The top wall was programmed to maintain an average vertical stress (labelled as *wsyy*) of 80 kPa. This is achieved by displacing the top wall vertically; upwards to decrease and downwards to increase the vertical stress. The vertical stress is measured as the average total force between the top and bottom wall, divided by the current width of the sample which starts at 4m and expands to 4.004m.

Due to the dynamic nature of the cyclic biaxial test, the *total sample volume* will vary with each cycle. The *total sample volume*, notated as V_{ts} can be calculated based on the horizontal and vertical strains. Let:

- L_0 = initial width of sample, precisely 4m for each sample
- h_0 = initial height of sample, approximately 2m but differs for each sample.
- *wexx* and *weyy* = horizontal and vertical strains respectively
- d*L* and d*h* = change in width and change in height respectively
- *L* and *h* = the width and height of the sample respectively, at any given time

$$
\begin{array}{|l|}
\hline
weyy = \dfrac{dh}{h_0} \\
h = h_0 + dh \\
h = h_0 + h_0 weyy \\
h = h_0(1 + weyy) \\
\hline
\end{array}
\qquad
\begin{array}{|l|}
\hline
wexx = \dfrac{dL}{L_0} \\
L = L_0 + dL \\
L = L_0 + L_0 wexx \\
L = L_0(1 + wexx) \\
\hline
\end{array}
$$

The total sample volume, V_{ts} equals to *h* x *L* x 1m (unit thick) at all times. Therefore;

$$Total\ sample\ volume, V_{ts} = h \times L \times 1 = \underline{\underline{h_0 L_0 (1 + weyy)(1 + wexx)}}\ m^3$$

Initially the total sample volume is approximately 2m x 4m x 1m = 8m^3.

4.3 Sample porosity and coordination number

A *measurement circle* of 3m radius was placed over the DEM sample to measure the porosity and the coordination number as shown in Figure 4.1 in the previous section. Porosity is defined as the ratio of void volume to the total volume.

In PFC2D the total volume for the *measured porosity* is the volume of the measurement circle (unit thickness), notated as V_{mc}, and is equal to π x (3^2) x 1 = 9π m^3. The volume of void for the measured porosity includes the empty space outside the sample space but within the measurement circle. The following Figure 4.2 shows the difference between the *measured porosity* and *sample porosity*. Volume used is highlighted in grey.
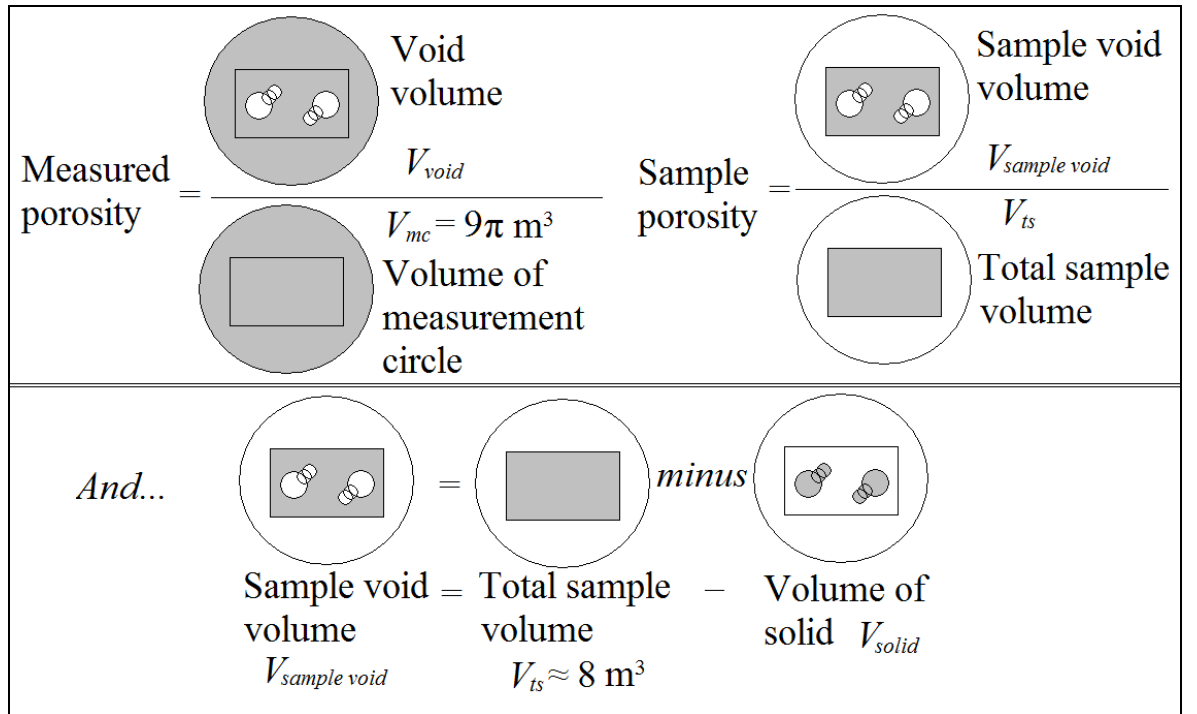

Figure 3.2: Measured porosity, sample porosity and sample void volume

The *sample porosity*, η_{sample} is different from the *measured porosity* $\eta_{measured}$ as *total sample volume* V_{ts} excludes the empty space outside of the 2m by 4m sample space. *Sample porosity* η_{sample} is the ratio of the *volume of sample void* $V_{sample\ void}$ (i.e. void within the sample space) to the *total sample volume* V_{ts}. In order to calculate the *sample porosity* η_{sample}, the *volume of solid* V_{solid} must first be obtained from the *measured porosity* $\eta_{measured}$:

measured porosity, $\eta_{measured} = \dfrac{V_{void}}{V_{mc}}$, $V_{mc} = 9\pi$

$(\eta_{measured}) \times V_{mc} = V_{void}$

$V_{void} = 9\pi \cdot (\eta_{measured})$

But, $V_{solid} = V_{total} - V_{void}$

$\therefore V_{solid} = 9\pi - 9\pi \cdot (\eta_{measured}) = \underline{\underline{9\pi(1 - \eta_{measured})}}$

The *volume of sample void,* $V_{sample\ void}$ is equivalent to the *total sample volume* V_{ts} minus the *volume of solid* V_{solid}.

$V_{sample\ void} = V_{ts} - V_{solid}$

$V_{sample\ void} = V_{ts} - 9\pi(1 - \eta_{measured})$

$\therefore$ *sample porosity*, $\eta_{sample} = \dfrac{V_{sample\ void}}{V_{ts}} = \dfrac{V_{ts} - 9\pi(1 - \eta_{measured})}{V_{ts}}$

$\eta_{sample} = \underline{\underline{1 - \dfrac{9\pi(1 - \eta_{measured})}{V_{ts}}}}$

Figure 4.3 illustrates four different simple cases of balls and walls interaction and how the coordination number is calculated for each. The coordination number is the average number of contacts between all particles. It is defined as the total number of contacts (ball-ball and ball-wall) divided by the number of particles. In PFC2D, the number of particles always refers to the number of discs regardless of whether they are clumped or not. As the number of discs per clumped particles for each sample is always constant, multiplying the coordination number by the number of discs per clump will give the desired coordination number based on the number of separate particles. There are no contacts between discs that are clumped together.

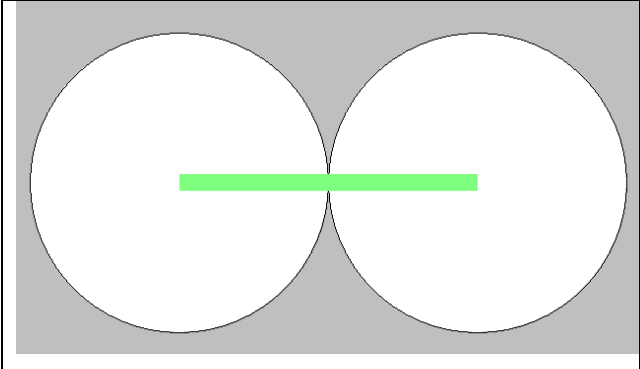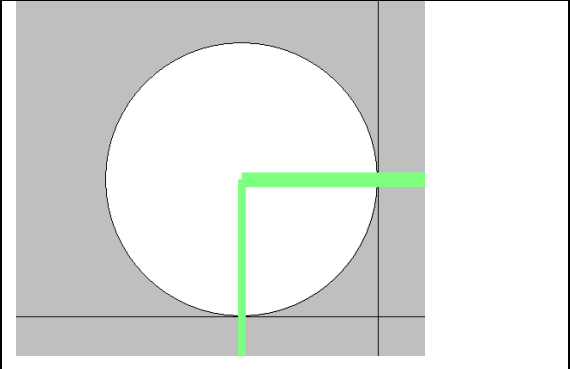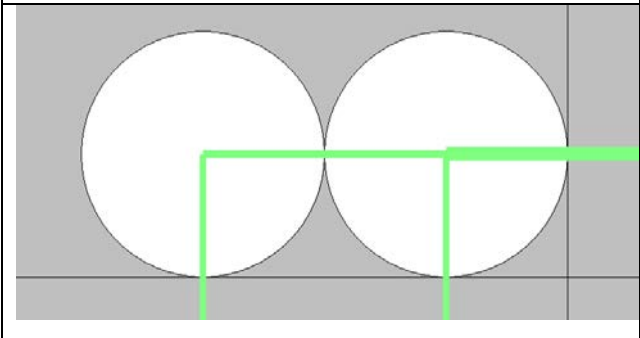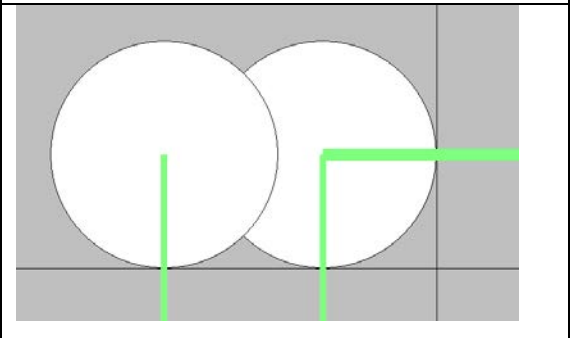|	
Ball-ball contact: $coord.no. = \dfrac{1\ contact(ball\ 1) + 1\ contact(ball\ 2)}{2\ balls}$ $coord.no. = \underline{\underline{1.0}}$	Ball-walls contact $coord.no. = \dfrac{2\ contacts(ball\ 1)}{1\ balls}$ $coord.no. = \underline{\underline{2.0}}$
Balls-walls contact $coord.no. = \dfrac{2\ contact(ball\ 1) + 3\ contact(ball\ 2)}{2\ balls}$ $coord.no. = \underline{\underline{2.5}}$	Clumped balls-walls contact $coord.no. = \dfrac{1\ contact(ball\ 1) + 2\ contact(ball\ 2)}{(2\ balls)}$ $coord.no. = 1.5 \times 2\ balls = \underline{\underline{3.0}}$

Figure 4.3: Calculating the coordination number for different situations.

4.4 Micro-mechanical parameter: particle positions

The micro-mechanical parameters are different from the macro-parameters which concern the global granular assembly; overall stresses and strains etc. The micro-mechanical parameters as described in this section concern the behaviour of the individual particles. Each of the 8853 individual particles' positions and angles were recorded for every 10th cyclic strain up to the 100th. Specifically, the particles' position and angle were recorded at the end of the compression phase of the cyclic straining process. This is because the horizontal stress is higher during the compressive phase and it is this value of the horizontal stress that was expected to build-up. Hence, the recorded change in the particles' positions and angles, if any, could correspond with any build up of the sample's horizontal stress.

Figure 4.4 highlights the *main disc* for each particle shape clump and the coordinate of its centre point which is recorded as the position of the particle. The *main disc* is the larger disc within the clump for the Ni particle and the Triangular. For the Elliptic particle, since both discs that make up the particle are the same size, one was chosen. The Disc particle's position coordinate is the centre point of the single disc.
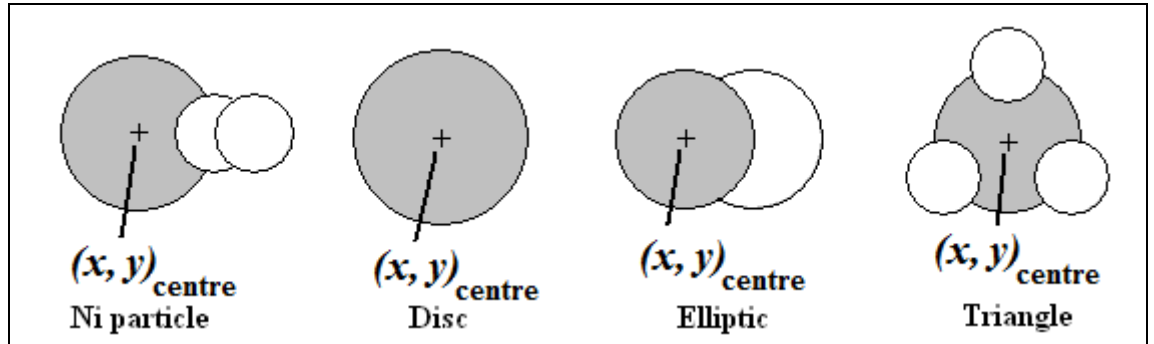
Figure 4.4: Centre point of main disc in clump as coordinate of particles

Figure 4.5 shows a change in position and angles turned by a Ni particle, as an example. The position of the particles were recorded every 10th cyclic strain in terms of their Cartesian x-y coordinates. The origin (coordinates x = 0, y = 0) is at the bottom left of the sample space.

The displacement of each particle is calculated in each coordinate direction, vertical ($dy = y_{final} - y_{initial}$) and horizontal ($dx = x_{final} - x_{initial}$). An overall displacement for the particle is as a resultant of the dy and dx:

$$particle\ displacement = \sqrt{(dx^2 + dy^2)}$$

4.5 Micro-mechanical parameter: particle angles

The angles of the particles are similarly measured based on the main disc of the clump for the non-circular particles. All the particles were generated facing the right in PFC2D. With this direction defined as 0°. The angles can change up to 360° as the particles are mixed and compressed into the 2m by 4m sample space. At every stage of the test, each particle will have an *orientation* defined by its angle θ. The angle can be greater than 360° if the particle complete more than one revolution.
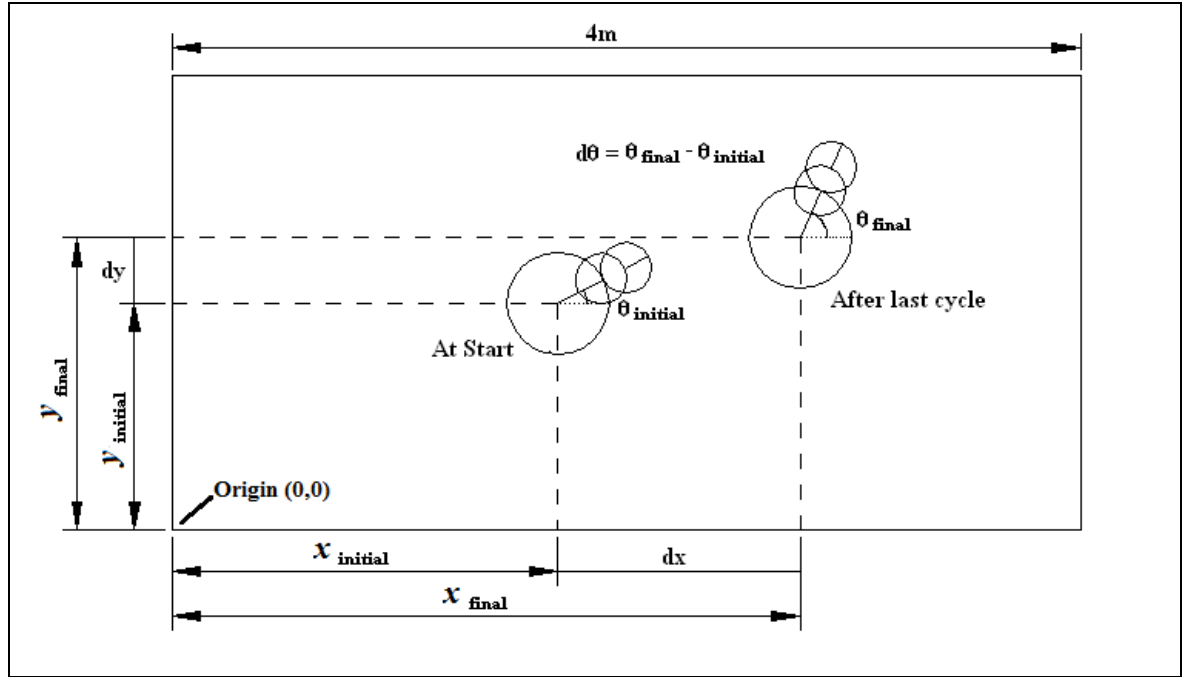
Figure 4.5: Position and angles turned for a Ni particle.

The particle orientation is not necessarily the same as its angle though most literatures (Oda, 1972; Clayton and Reddy, 2006) loosely defined it as such. Particle orientation is related to the particle shape as well as its angle. Figure 4.6 shows the difference between particle orientation and angles for the four particle shapes. Particles in real soils have random shapes that are not symmetric about any axis. Therefore their orientation can be defined by an angle within 360° from an axis of reference which justifies their use in other literatures.

For the idealised 2-D particle shapes used in this project however, the symmetry of the particle shapes meant that after a certain amount of rotation, the particles will be back to its original orientation. The *orientation range* of a particle is an angle in which if the particle rotate that much, it ends up in the same orientation as before it started rotating. For example, if the Triangular particle rotated 120° from 0°, it still has the same orientation. Therefore, the Triangular particle has an orientation range of 120°. The Elliptic particle has an orientation range of 180°.

To illustrate the difference between orientation and angle, the most obvious case is the circular Disc particle where its angles of rotation can be measured but its orientation will remain constant since its orientation range is 0°.

Of the four particle shapes, the Ni particle is the only one with a 360° orientation range. So the Ni particle can be considered the best in describing real particles as far as the orientation is concerned. Nonetheless, the orientations of all the particles are still defined by their angles. This is important when dealing with the *change in orientation* which can only be described by *angles turned*.
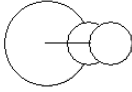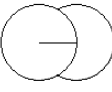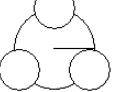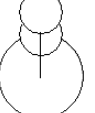
Ni particle	Disc	Elliptic	Triangular
Orientation = right Angle = 0°	Orientation = circle Angle = 0°	Orientation = horizontal Angle = 0°	Orientation = point up Angle = 0°
Orientation = up Angle = 90°	Orientation = circle Angle = 90°	Orientation = vertical Angle = 90°	Orientation = point down Angle = 60°
Orientation = left Angle = 180°	Orientation = circle Angle = 180°	Orientation = horizontal Angle = 180°	Orientaion = point up Angle = 120°

Figure 4.6: Difference between particle orientation and angles turned

The angles turned $d\theta$, by a particle for each cyclic strain is used to describe the change in orientation which is the difference between the current angle $\theta_{current}$ and the initial particle orientation, angle $\theta_{initial}$. For the total change in orientation after 100 cyclic strains, it would be the final particle orientation, defined by θ_{final}, minus the initial one.

The angles turned by each particle were recorded in terms of positive (anti-clockwise) and negative (clockwise) angles in radians. In principle, taking the average will result in some angles turned cancelling each other out as there will be positive and negative angles turned.

Figure 4.7 shows the absolute angles turned $|d\theta|$ compared to the angles turned $d\theta$. In order to measure the magnitude of the activities within the samples in terms of angles turned regardless of direction, it was necessary to disregard the direction of the particles' rotation or rolling (the positive and negative signs of angles turned). Hence an *absolute* value of the angles turned was utilized to find an average and standard deviation.

θ_{final}

$\theta_{initial}$

$-\theta_{final}$

$d\theta = \theta_{final} - \theta_{initial} = +d\theta$

angles turned

$d\theta = -\theta_{final} - \theta_{initial} = -d\theta$

$|d\theta| = \theta_{final} - \theta_{initial} = +d\theta$

absolute angles turned

$|d\theta| = -\theta_{final} - \theta_{initial} = +d\theta$
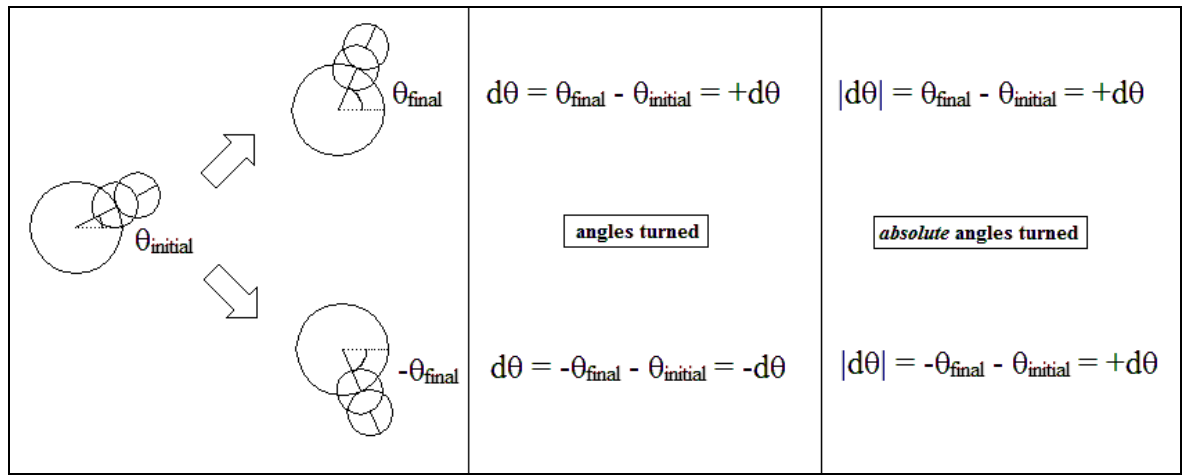
Figure 4.7: Absolute angles turned compared to angles turned.

4.6 Initial conditions

The following table 4.1 shows the initial condition for all four samples. The initial earth pressure coefficient, K_0 is the ratio of horizontal stress over vertical stress.

Table 4.1: Initial conditions of the four samples

Samples	Ni particle	Disc	Elliptic	Triangular
Vertical Stress (Pa)	80000	80000	80000	80000
Horizontal Stress (Pa)	51792	94847	61162	82644
K_0	0.6474	1.1855875	0.764525	1.03305
Sample Volume (m^3)	7.9568	8.1351	8.0779	8.0871
Porosity, η_0	0.09486	0.11477	0.10832	0.10968
Coordination Number	4.1340	3.4030	3.7760	5.3560

The initial vertical stresses for all samples were about 80 kPa. Their initial horizontal stresses were different from one another. As a result, the Disc and Triangular particles have at-rest earth pressure coefficient K_0 above 1.0. The Ni particle and Elliptic particles have an at-rest earth pressure coefficient between 0.5 and 1.0. All K_0 values corresponds to earth pressure coefficient of overconsolidated soils obtained from results of model retaining wall experiments on well-graded dry silica sand and theoretical calculations by Hanna and Al-Rohmein (2008). The compacted nature of the backfill material as a result of how the samples were set up in this project's DEM model suggests that the sample might be overconsolidated.

However, literatures report K_0 values of 0.33 from field observations of integral bridge backfill (Barker and Carder, 2000; 2001) whilst in laboratory experiment, K_0 values of 0.5 (Xu, 2005) and 0.4 (England, et al., 2000) were estimated and used. These K_0 values from the literature are less than the K_0 obtained for the four samples of different particle shapes. The K_0 values used in literature were predicted by utilizing the equation in accordance to the design manual (DMRB BA42/96, 2003):

$K_0 = 1 - \mathrm{Sin}\ \Phi'$; in which Φ' is the effective angle of shearing resistance obtained from shear tests on the materials used.

It was further noted from a model retaining wall test on Ottawa sand that extra horizontal stress was induced in compacted sand when compared with loose sand. The compaction had insignificant influence on the vertical stress of the sand. Furthermore, it was noted that compaction only influenced the sands down to a certain depth, below which the horizontal stress can be predicted based on the calculation of K_0 (Chen and Fang, 2008). Xu (2005) cited Clayton and Symons (1992) in demonstrating that the depth to which compaction pressures are significant will not exceed 3m to 4m, below which the horizontal earth pressure coefficient can be assume to follow the calculated K_0 profile.

The backfill material at a depth of 4m may be in transition between overconsolidated and normally consolidated. As such, an overconsolidated sample may represent the real conditions of the backfill material. Generally, the K_0 values obtained for the four samples are in a practical range and well within the order of magnitude seen in realistic values.

Sample volumes and porosities between the samples were similar to one another. Sample volume was about 8 m^3 as defined by the 2m by 4m sample space. Initial sample porosity was about 0.1 for all samples. The coordination number was different between the samples. The Triangular particle had the highest coordination number at about 5.3 followed closely by the Ni particle at 4.1 while the Elliptic particle's was at about 3.8. The Disc particle's coordination number was the lowest at about 3.4. This generally suggests that rounded particles (Disc and Elliptic) have fewer contacts per particle than angular particles (Ni particle and Triangular).

4.7 Summary of research methodology

1. The overall cyclic straining programme is to subject a 2 m by 4 m sample to 100 cyclic strains of 0.1% by moving the right wall at 0.005 m/s away from the sample first and then back to its original position with a time-step of 1.0E-5 s/step.

2. The macro-mechanical parameters that were monitored throughout the cyclic straining process are the horizontal stress and strain, the vertical stress and strain, porosity and coordination number. The micro-mechanical parameters of the 8853 individual particles' position and angles for each sample were recorded for ever 10th strain cycle.

3. The sample volume was calculated based on the horizontal and vertical strain. The sample porosity as it relates to the sample size was also recalculated based on the fluctuating behaviour of the sample volume.

4. Particle displacement and angles turned were to be calculated for every 10th strain cycles based on the difference of each particles' position and angle from its initial values. This will show the overall activity of the particles within the sample as it is cyclically strained.

5. The initial conditions of all four samples indicated that they were overconsolidated. While the at-rest conditions of backfill materials in literatures are generally normally consolidated with at-rest earth pressure coefficient K_0 values between 0.3 and 0.5, it was argued that the material at 4 m depth behind an abutment was in transition between overconsolidated and normally consolidated conditions. In any case, the range of at-rest earth pressure coefficient K_0 obtained from the samples were in a practical range and within the order of magnitude seen in realistic values.

Chapter 5: Results and discussion

This chapter reports and discusses the results from the tests described in the previous chapter. The first section describes the controlled parameters of vertical stress and horizontal strain. This is followed by general observations of the sample volume, porosity, coordination number, particles displacement and angles turned. Then the results from the cyclic biaxial test of all four particle shapes were presented. Finally, the behaviour of the particles of different sizes within each sample was discussed.

5.1 General observations

5.1.1 Vertical stress and horizontal strain

Vertical stress and horizontal strain are two of the controlled parameters for the cyclic strain tests. The average vertical stress was fairly maintained at about 80 kPa as programmed. Given the cyclic nature of the tests however, the vertical stress was observed to oscillate about the 80 kPa value. The following Figure 5.1a and Figure 5.1b shows the typical vertical stress for the Ni particle sample and the wider range vertical stress for the Elliptic sample respectively which had the uncommon larger range between 70 kPa to 90 kPa. This difference in vertical stress range could be due to the overall larger particle movements in the Elliptic sample which will be discussed in section 5.2.3.
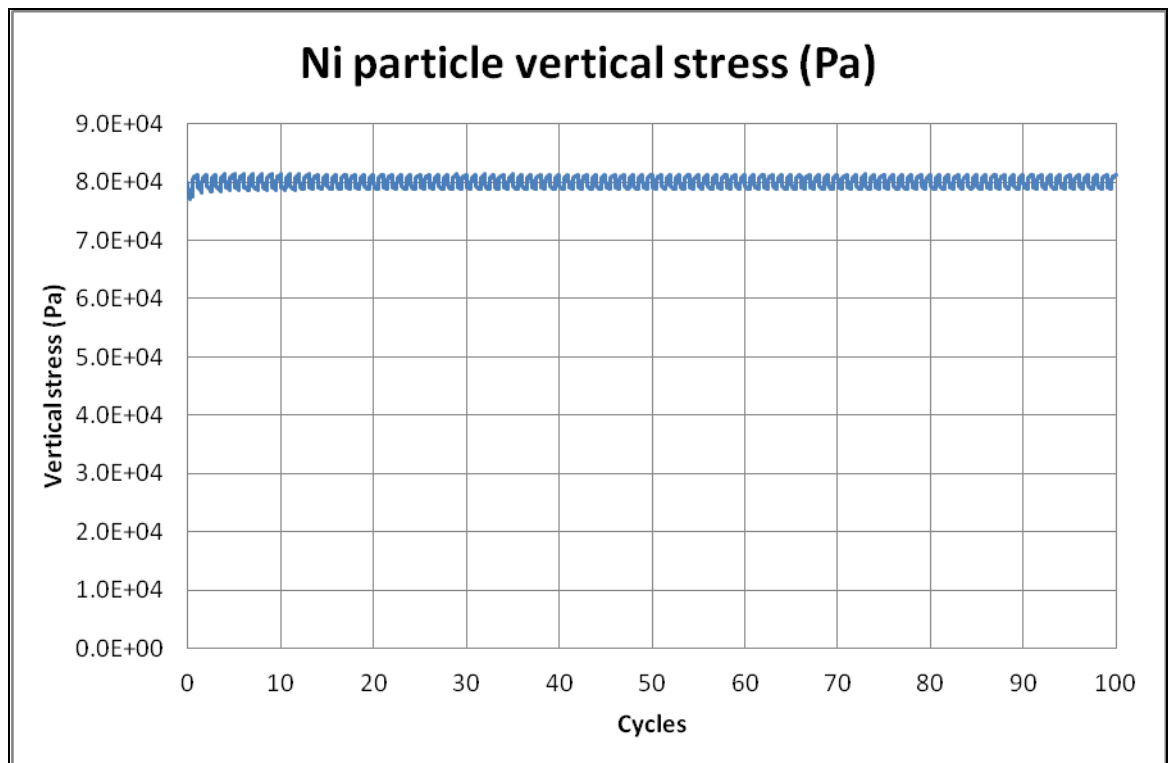
Figure 5.1a: Typical vertical stress on the Ni particle sample
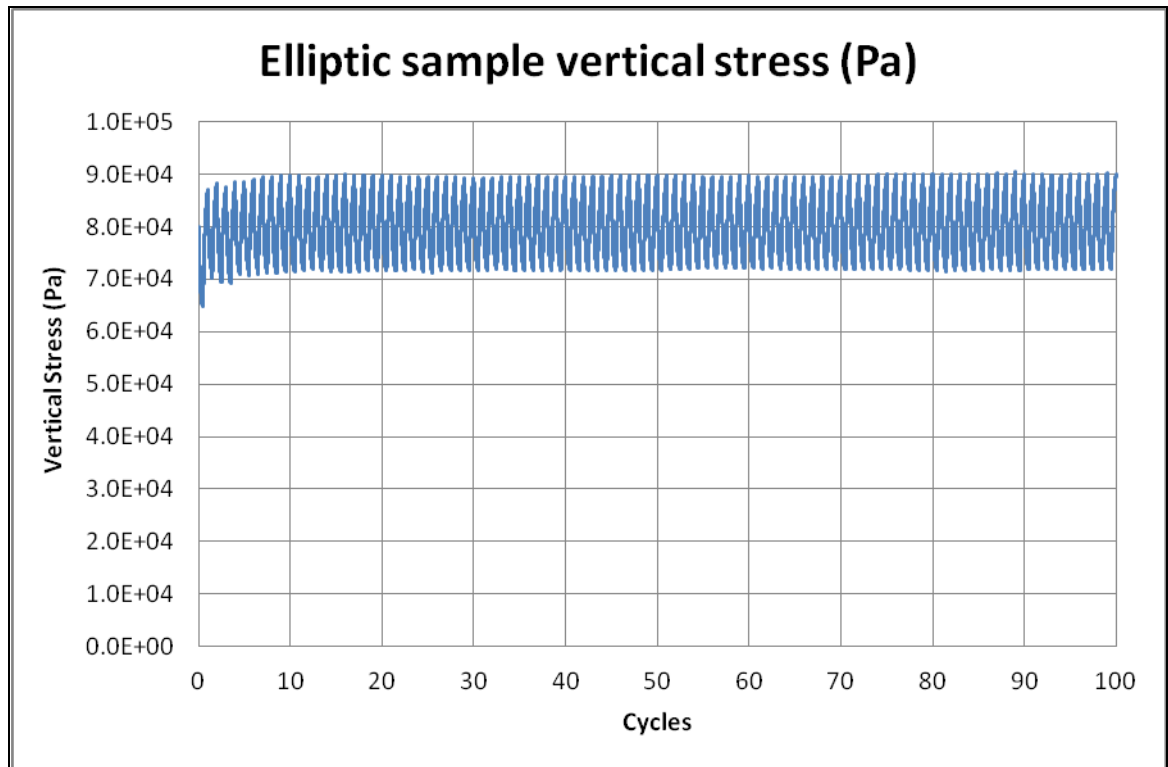
Figure 5.1b: Wider range of vertical stress on Elliptic sample

The horizontal strains had a range between 0.1% and 0.0% as programmed. As this was based on the displacement of the right wall, there were no significant errors as to the precision of the horizontal strain value, for all the tests.

5.1.2 Increase in horizontal stress

The horizontal stresses for all samples were observed to have increased in the course of 100 cyclic strains. The Ni particle's horizontal stress increased steadily with cycle and mimics the trend expected of real backfill materials. A slight build-up of horizontal stress can be observed in the Elliptic sample, but not as prominent as the Ni particle sample's. Both the Disc and Triangular samples' horizontal stress increased to a steady value after the first 10 cycles. The build-up of horizontal stress for each sample will be further discussed in section 5.2.

5.1.3 Decrease in sample volume

The vertical strains were observed to increase as a negative value for all samples. The following Figure 5.2 shows the vertical strain of the Ni particle sample which shows the general trend of vertical strains becoming more negative with cycles for all samples. The vertical strain for the Ni particle sample is quite small, at about 0.001%. The Triangular sample had a similar range. Larger strains at up to 0.2% were observed in the Disc and Elliptic samples.
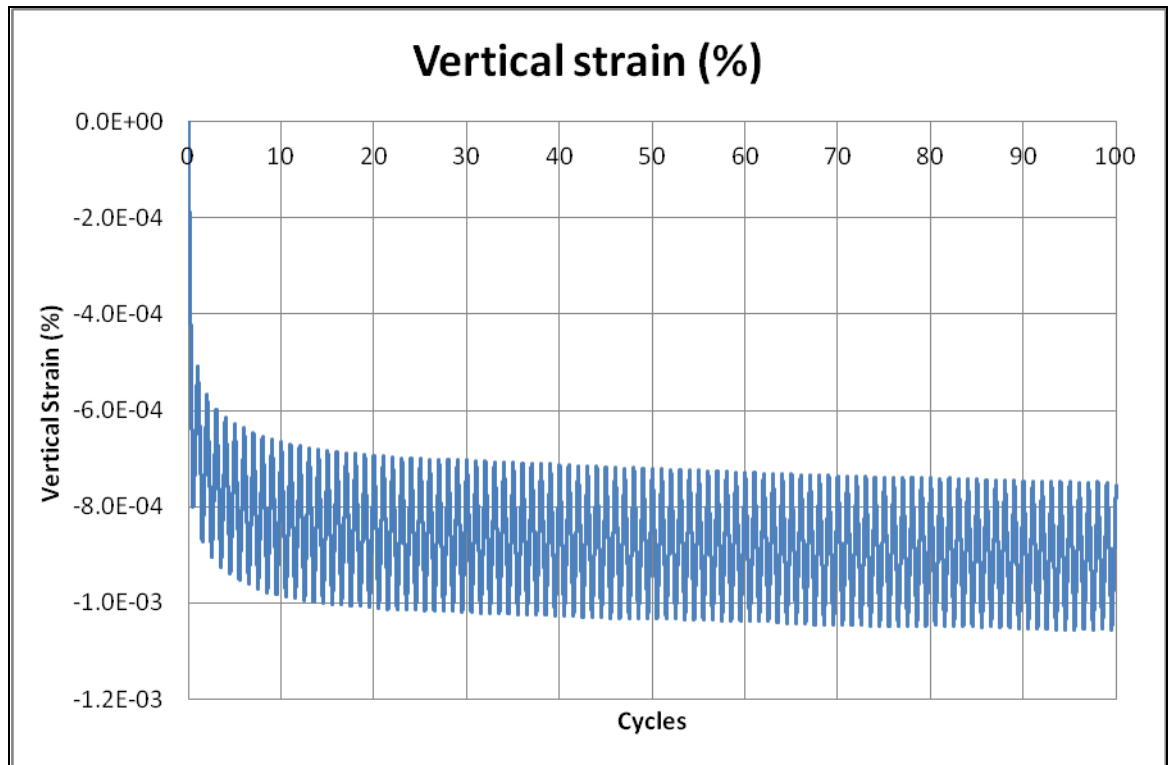
Figure 5.2: Vertical strain against cycles for the Ni particle sample

Figure 5.3 shows the decreasing volume of the Ni particle sample. Combining the horizontal (*wexx*) and vertical (*weyy*) strains enable the calculation of the total sample volume, V_{ts} as noted in the previous chapter. Generally the behaviour of the vertical strain is an indicator of the sample volume's behaviour. Since the vertical strain for the Ni particle was small, the change in sample volume was similarly small, in the order of 0.001 m^3. All samples had similar small decreases in volume and by extension settlement behind an integral abutment would be relatively small due to a well-compacted backfill material as concluded in section 2.3.2.

It is understood that the scale of the vertical strain relative to the sample size is small and therefore, its effects on the sample volume was marginal. A decrease in total sample volume, however small, implies an increase in the density of the sample.
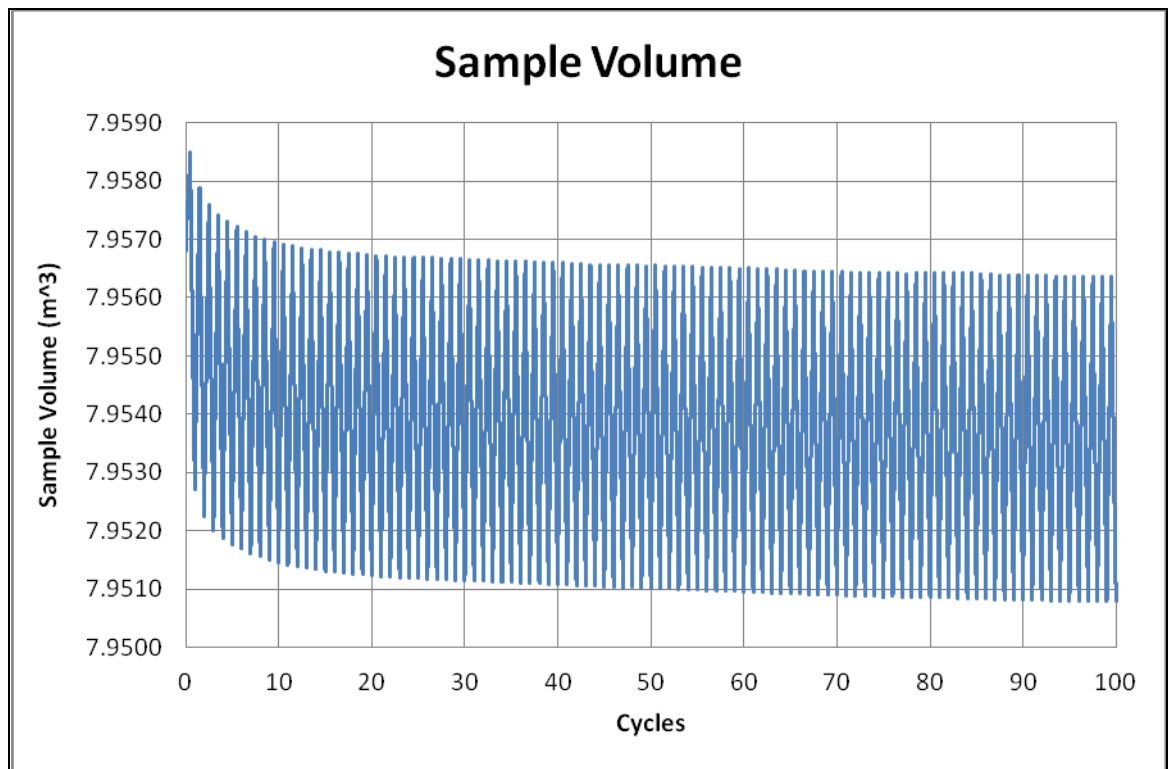
Figure 5.3: Ni particle sample volume observed to decrease.

5.1.4 Decreasing sample porosity

The behaviour of the total sample volume is an indicator of the sample porosity's behaviour as well. Figure 5.4 shows the sample porosity of the Ni particle sample. Therefore, a general decrease in sample porosity was observed, corresponding with the decrease in total sample volume. A decrease in porosity also implies the process of densification.
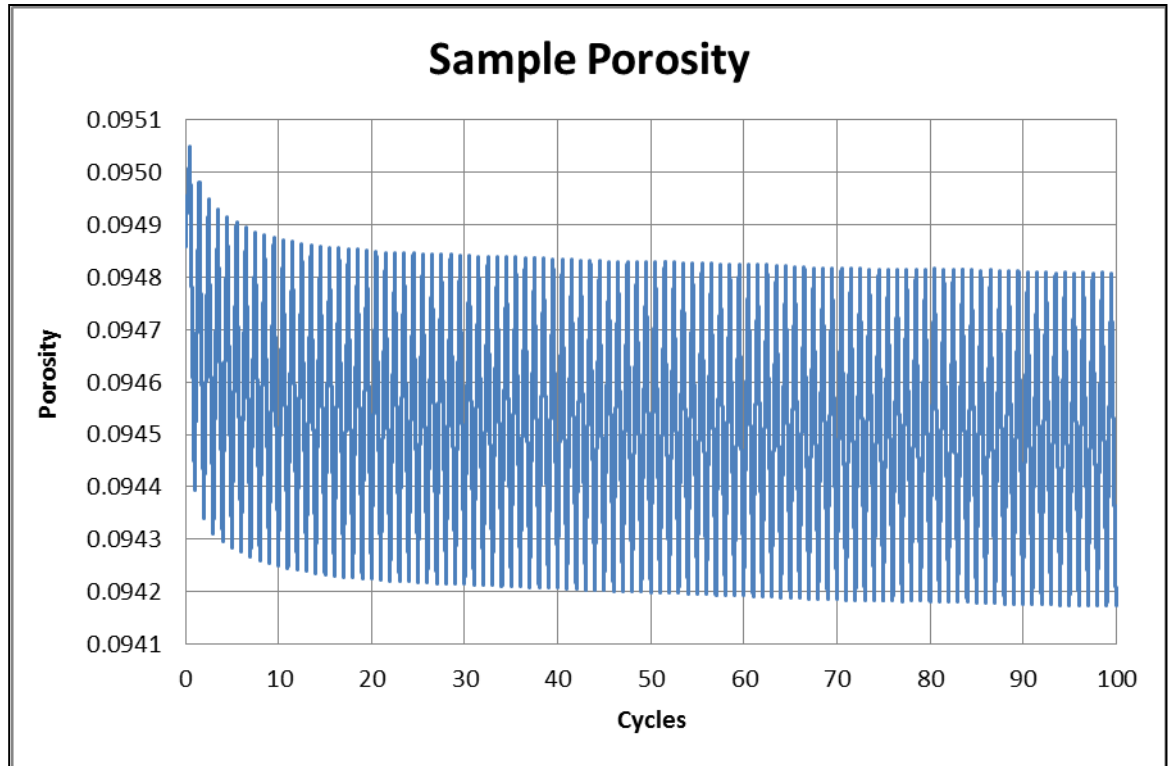
Figure 5.4: Sample porosity of the Ni particle sample

5.1.5 Changes in coordination number

The coordination number is a measure of the contacts per particle within the sample (including ball-wall contacts) as the sample undergoes cyclic straining. The coordination number of the Ni particle sample was observed to increase with cycles with no indication of approaching a steady value. Increase of coordination number was also observed in the Elliptic sample. Both Disc and Triangular sample's coordination number dropped at first cycle of the test but then quickly goes to a steady value as the cyclic straining progress. The number of inter-particle contacts does not seem to necessarily increase with densification. The coordination numbers' behaviour was observed to be somewhat related to the horizontal stress for each sample which will be further discussed in section 5.2.

5.1.6 Particle displacements

There are 8853 separate particles in each sample. It is impractical to describe the displacement of each and every particle. Hence, the overall particle displacements are summarized by the average and standard deviation of displacement.

Figure 5.5 shows the average and standard deviation of the resultant particle displacements for the Ni particle sample. Generally, most rapid particle displacement occurs in the early cycles of straining. The particle displacements per cycle were less after about 30 cycles. Results from all four samples indicate that the particles were settling into a particular position as changes in the average and standard deviation of displacements were small by the 100th strain cycle. The increase of the standard deviation of particle displacement implies that the spread of the particle displacements is also increasing in range with cycles. In short, the range of particle displacement values is larger as the cyclic straining progress. However, the values of both average and standard deviation are actually quite small for the Ni particles, in the order of 0.0001 m. It is noted however, that the particles are highly constrained in a 2-D space as oppose to a 3-D sample.
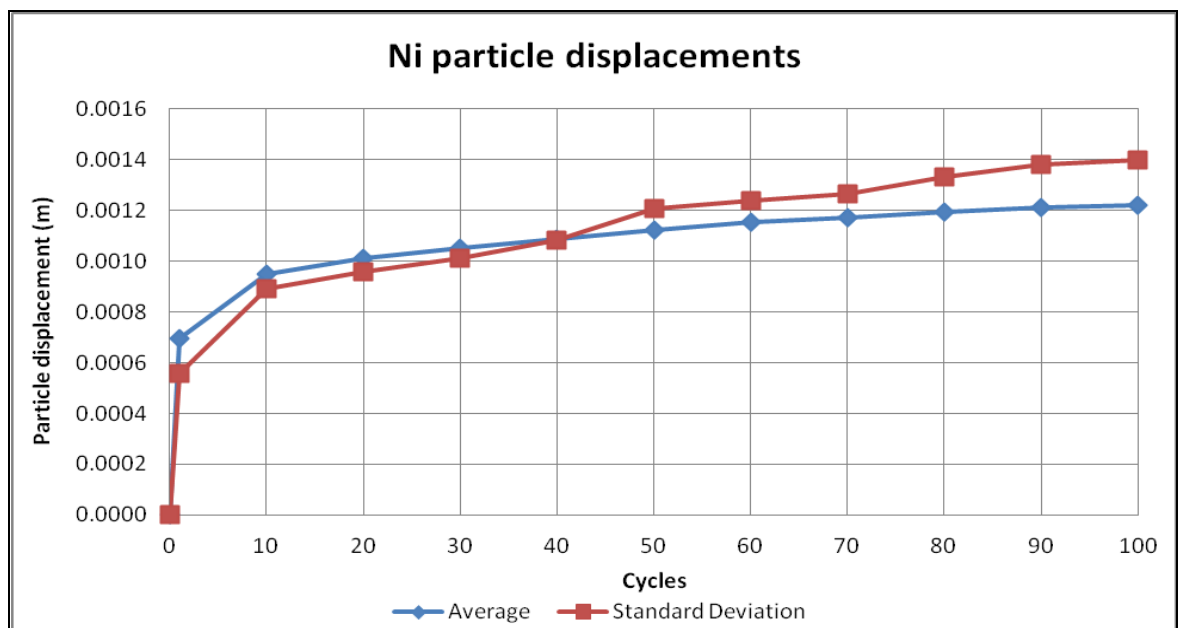
Figure 5.5: Average and standard deviation of particle displacements for Ni particle sample

5.1.7 Particles angles and angles turned

Figure 5.6 shows the rose plot for the particle angles of the Ni particles sample at the start and after 100 cyclic strains. The rose plots for particle angles at the start and 100th cycle for all four samples are shown in Appendix 5.

The orientation of particles for each sample is best described by a *rose plot*, a polar histogram. For this project the rose plot is divided into 12 sections, each representing a 30° angle range in which the particles' angles fall into. Initially, all four samples were quite evenly distributed in terms of particle angles. Not that much of a difference is seen when comparing the rose plot of particle angles at the start of the cyclic straining test and at the 100th cycle.

Ni particle angles at start	Ni particle angles at 100th cycle
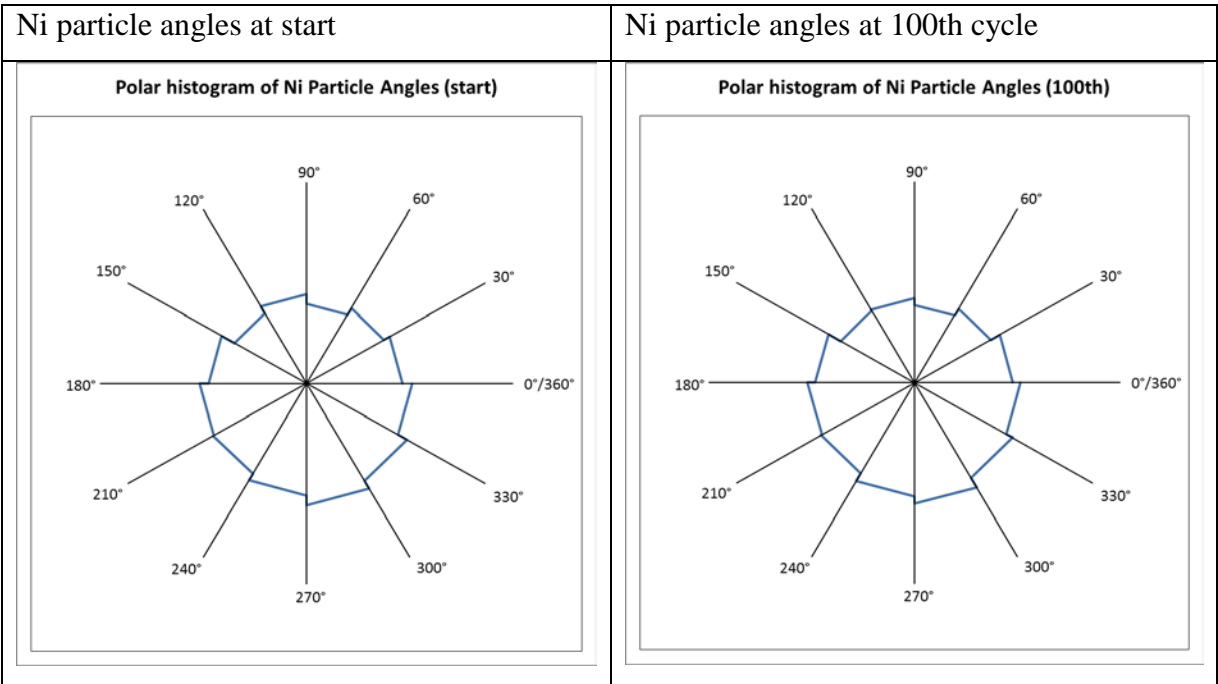
Figure 5.6: Rose plot of particle angles for the Ni particles sample at the start and after 100 cycles

Figure 5.7 shows the angles turned for the Ni particles sample. The angles turned of the non-circular particles were all less than 1.5 radians (a little less than 90°) by the 100th cycle. About 80% of the particles had angles turned in between –0.1 and +0.1 radians (about ±6°). Rotations of the Disc particles were far larger and completed several revolutions by the end of the 100th cycle. Histogram plots of the angles turned for each sample are shown in Appendix 6.
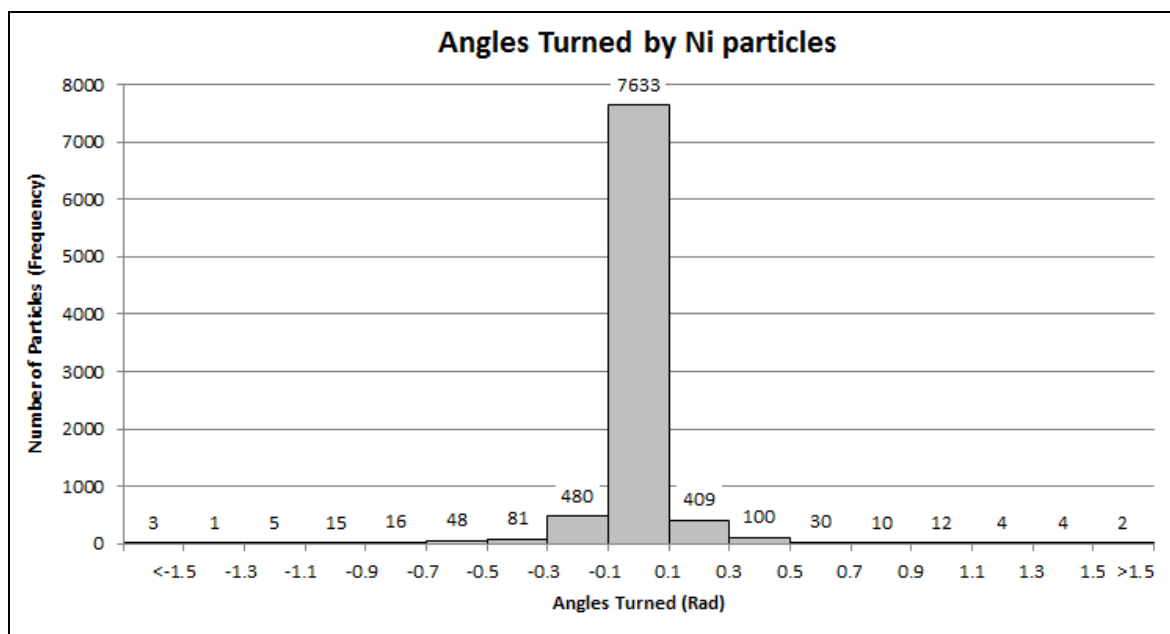
Figure 5.7: Histogram of angles turned for the Ni particle sample after 100 cycles

It was also noted that particle rotations are highly constrained in a 2-D space and therefore, the angles turned would be expected to be small. The small values of angles turned however cannot be construed as a lack of particle reorientation.

The absolute value of the angles turned disregards the direction of its rotation. It is a scalar measure of the rotation or rolling of the particles. The absolute angles turned by all the particles can also be summarized by the average and standard deviation as shown in Figure 5.8 for the Ni particle sample.

Results of the absolute angles turned generally have a similar trend to the particle displacements in that most rotation or rolling of the particles occurs at the early cycles. By the 100th cycle, the non-circular particles settled into a certain orientation and less rotation or rolling occurs. The standard deviation of the absolute angles turned is observed to increase with cycle implying a larger spread in the range of absolute angles turned.
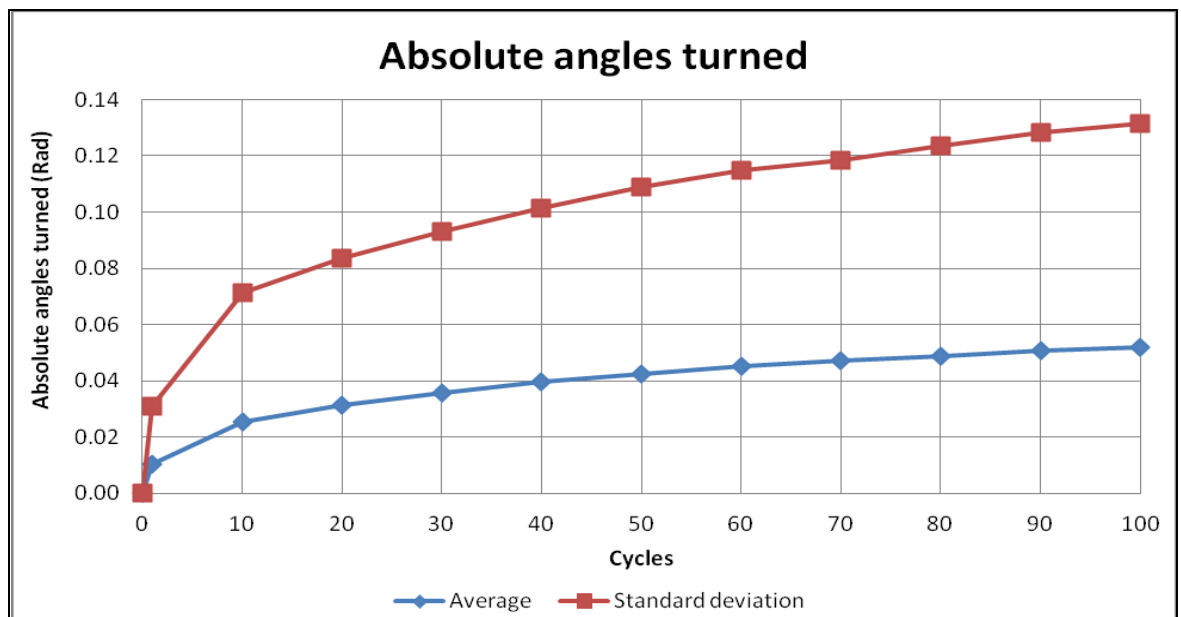
Figure 5.8: Average and standard deviation of absolute angles turned for Ni particle sample

Figure 5.9 shows the average and standard deviation of absolute angles turned for the Disc sample. The Disc particles have little resistance to rotation and rolling. The results indicate that some Disc particles may have completed several hundred revolutions. The plot of the average and standard deviation of the absolute angles turned indicate a linear relationship with number of cycles.

Figure 5.9: Average and standard deviation of absolute angles turned for Disc sample

5.2 Results of the four samples

The following table 5.1 shows the conditions of the samples at the end of 100 strain cycles. Average is shortened to "Avrg" and standard deviation is shortened to "StDev" for the particles' displacements and angles turned.

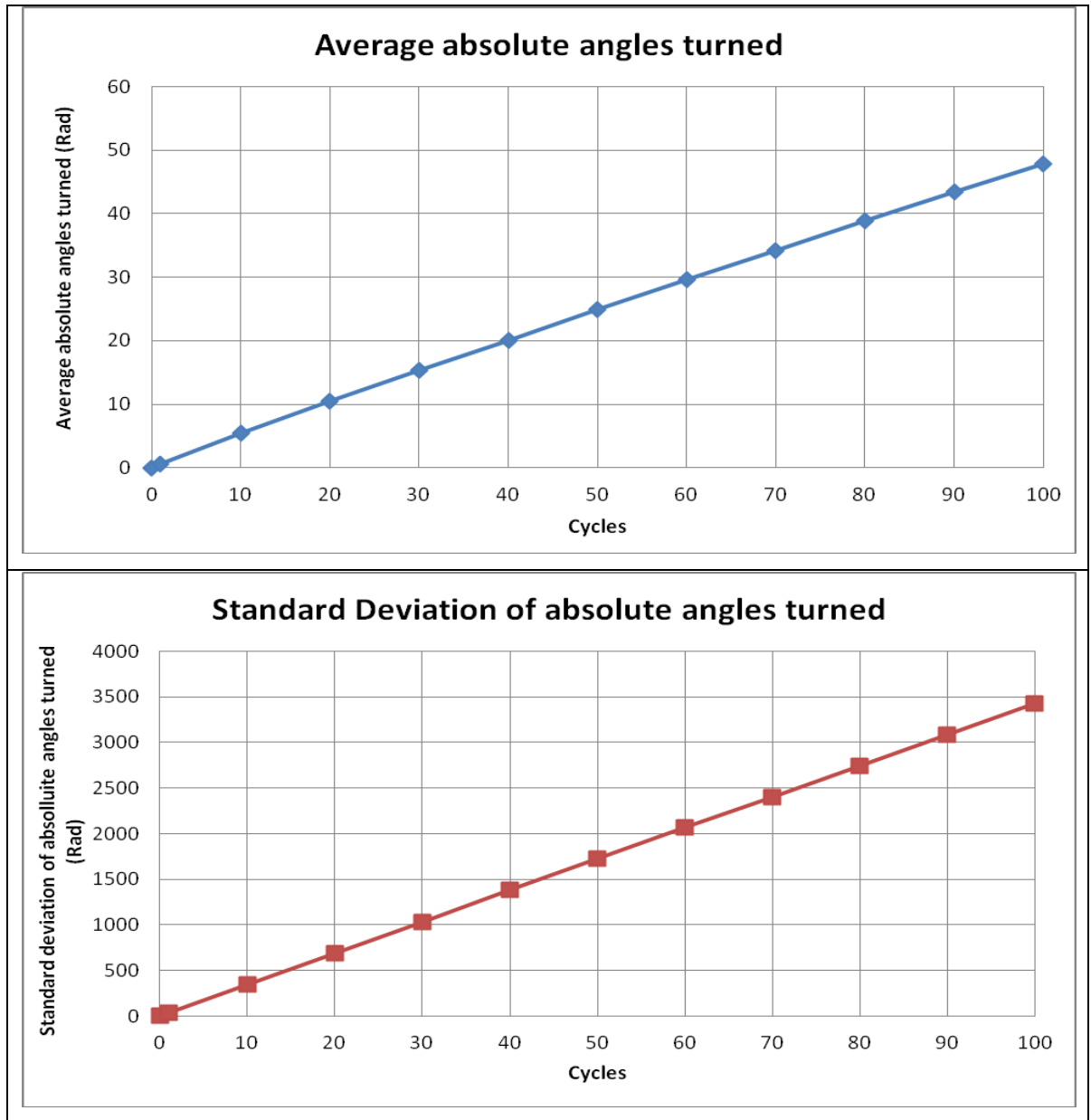The average and standard deviation of all particles displacement was small, in the order of 0.001m (the smallest Ni particle had a diameter of 0.01m). Other than the Disc particles, all the other shapes had average and standard deviation of angles turned that were no more than 0.4 radians (about 20°). This generally indicates that the micro-mechanical behaviour of the particles, whether displacing or rotating are small. Therefore, significant granular flow and/ or particle reorientation may not have occurred in the samples.

Table 5.1: Sample conditions at the end of 100th cycle

Samples		Ni particle	Disc	Elliptic	Triangular
Vertical Stress (Pa)		81257	80385	90009	80326
Horizontal Stress (Pa)		149610	128220	128050	142630
K		1.8412	1.5951	1.4226	1.7756
Sample Volume (m³)		7.9508	8.1313	8.0648	8.0857
Porosity, η_{sample}		0.09417	0.11436	0.10688	0.10953
Coordination Number		4.3461	3.4016	3.9162	5.0924
Particles Displacement (m)	**Avrg**	0.001222	0.002151	0.003814	0.000395
	StDev	0.001398	0.004750	0.004706	0.000640
Absolute Angles Turned (Radians)	**Avrg**	0.051990	47.894635	0.184962	0.010721
	StDev	0.131525	3423.74	0.330067	0.047629

The vertical stress at the end of the 100th cycle for all samples is no longer at 80 kPa. For the Ni particles, Discs and Triangular particles, it is only about 1 kPa more. The vertical stress for the Elliptic sample was at 90 kPa, about 10 kPa more than the designated value. Horizontal stress had increased to over 100 kPa for all samples. The overall stresses on a sample are best expressed by the earth pressure coefficient K, the ratio of the horizontal stress to the vertical stress.

Table 5.2 shows the earth pressure coefficient K for all samples before and after 100 cyclic strains. The earth pressure coefficient K of the Ni particles sample had tripled while that for the Elliptic sample had doubled. The Disc and Triangular sample's K was observed to have increased by about 0.4 and 0.7 respectively. Both the Disc and the Triangular samples had an earth pressure coefficient greater than 1.0 initially. This generally indicates that the horizontal earth pressure have increased significantly from their initial values for all samples.

Table 5.2: Earth pressure coefficient before and after 100 cycles

Samples	Ni particle	Disc	Elliptic	Triangular
K_0	0.6474	1.1855875	0.764525	1.03305
K (100th cycle)	1.8412	1.5951	1.4226	1.7756

Table 5.3 compares the sample volume and porosity for all samples before and after 100 cyclic strains. The sample volume and the porosity was observed to have decreased for all four samples, although the scale is at the order of 0.001 m^3 for the volume and similarly 0.001 (0.1%) for the porosity. This generally indicates that densification occurred albeit at a very small scale.

Table 5.3: Sample volume and porosity, before and after 100 cycles

Samples	Ni particle	Disc	Elliptic	Triangular
Initial sample volume (m^3)	7.9568	8.1351	8.0779	8.0871
Sample volume (m^3) at 100th cycle	7.9508	8.1313	8.0648	8.0857
Initial porosity, η_0	0.09486	0.11477	0.10832	0.10968
Sample porosity, η_{sample} at 100th cycle	0.09417	0.11436	0.10688	0.10953

Table 5.4 shows the coordination number for all samples before and after 100 cyclic strains. Coordination number for the Ni particle and Elliptic sample was observed to have increased. Coordination number for the Disc decreased slightly while the Triangular sample's decreased significantly. For the Disc sample, the decrease of 0.001 can be considered insignificant to the other samples which had changes greater than 0.1.

It was observed that the increase in coordination number corresponds to samples with initial earth pressure coefficient less than 1.0 (Ni particle and Elliptic). Conversely, the decrease in coordination number corresponds to samples with initial earth pressure coefficient greater than 1.0 (Disc and Triangular).

The increase in coordination number also corresponds with observable continuous increase of horizontal stress as is the case with the Ni particle and Elliptic samples. Decrease in coordination number seems to indicate that the sample reached a steady horizontal stress quickly, as is the case with the Disc and Triangular samples.

Table 5.4: The coordination numbers for all samples before and after 100 cycles

Samples	Ni particle	Disc	Elliptic	Triangular
Initial Coord. No.	4.1340	3.4030	3.7760	5.3560
Coord. No. at 100th cycle	4.3461	3.4016	3.9162	5.0924
Change in Coord. No.	+0.2121	-0.0014	+0.1402	-0.2636

5.2.1 Behaviour of Ni particles sample with cycles

The Ni particles sample's horizontal stress and coordination number increased every cycle with no indication that it had reached a steady value as shown in the following Figure 5.10. By the 100th cycle the horizontal stress had increased by about 98 kPa, reaching approximately 150 kPa and was still increasing albeit at a lower rate that started at about the 10th cycle. Similarly the coordination number was also still increasing by the 100th cycle but at a lower rate that started at about the 40th cycle. The sample volume and porosity was observed to decrease in the same way; with a lower rate after the 10th cycle or so as shown in Figure 5.3 and Figure 5.4.
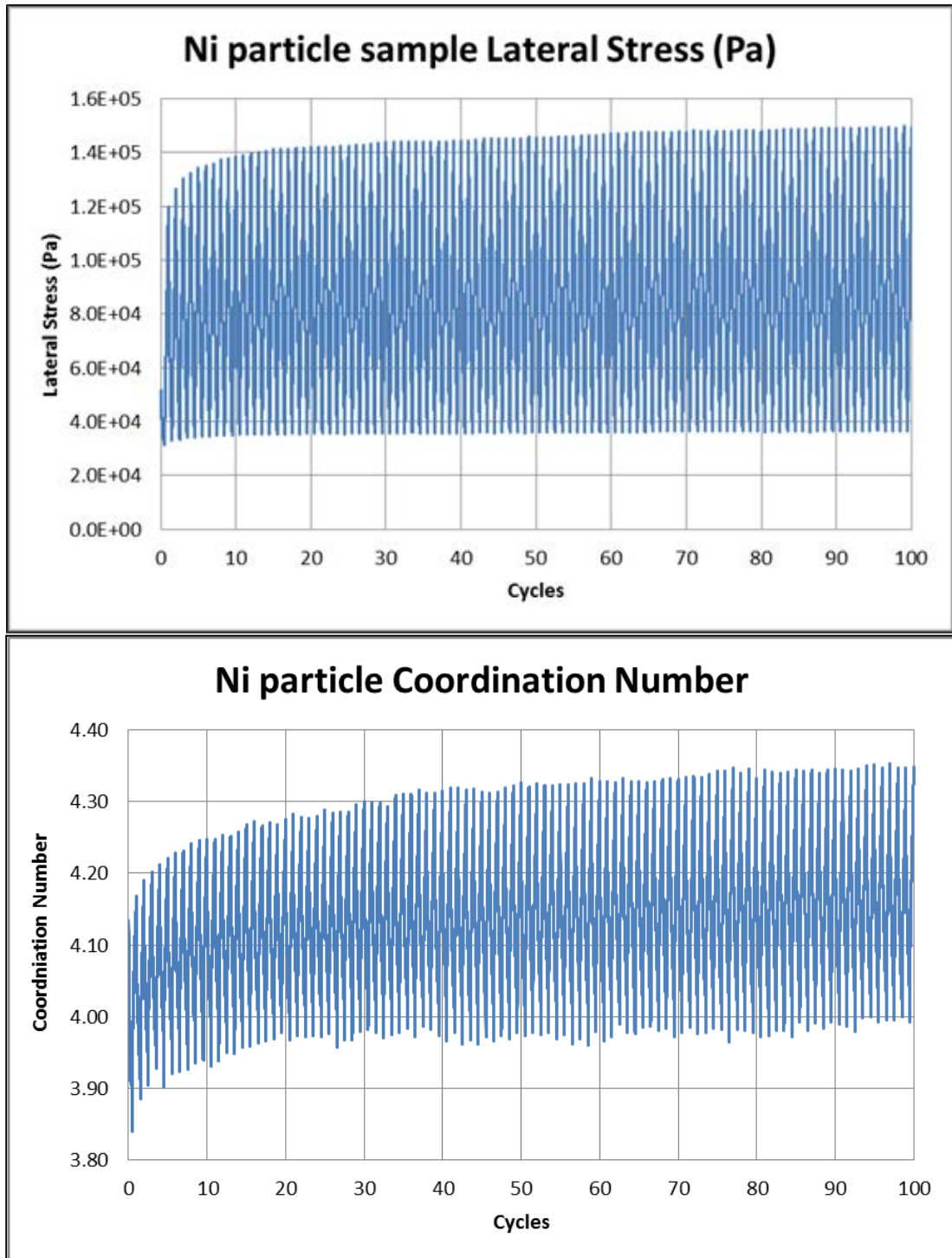
Figure 5.10: Lateral stress and coordination number of Ni particle sample

As for the particles' displacement and absolute angles turned, their average and standard deviation continued increasing at a very small rate as shown in Figure 5.5 and Figure 5.8. At the end of the 100th cycle, the particle displacement had an average of 0.0012 m and a standard deviation of 0.0014m. The absolute angles turned had an average of about 0.05 radians and a standard deviation of 0.13 radians at the 100th cycle. All results for Ni particles sample are shown in Appendix 7.

5.2.2 Behaviour of Disc particles sample with cycles

The Disc particles sample's horizontal stress increased by about 33 kPa to a steady value of approximately 128 kPa by the 20th strain cycle where no further increase. The coordination number appears to reach a steady value at about the 30th cycle, although careful inspection shows that it was still increasing but at a very minute rate. Figure 5.11 shows the lateral stress and coordination number of the Disc particle sample.
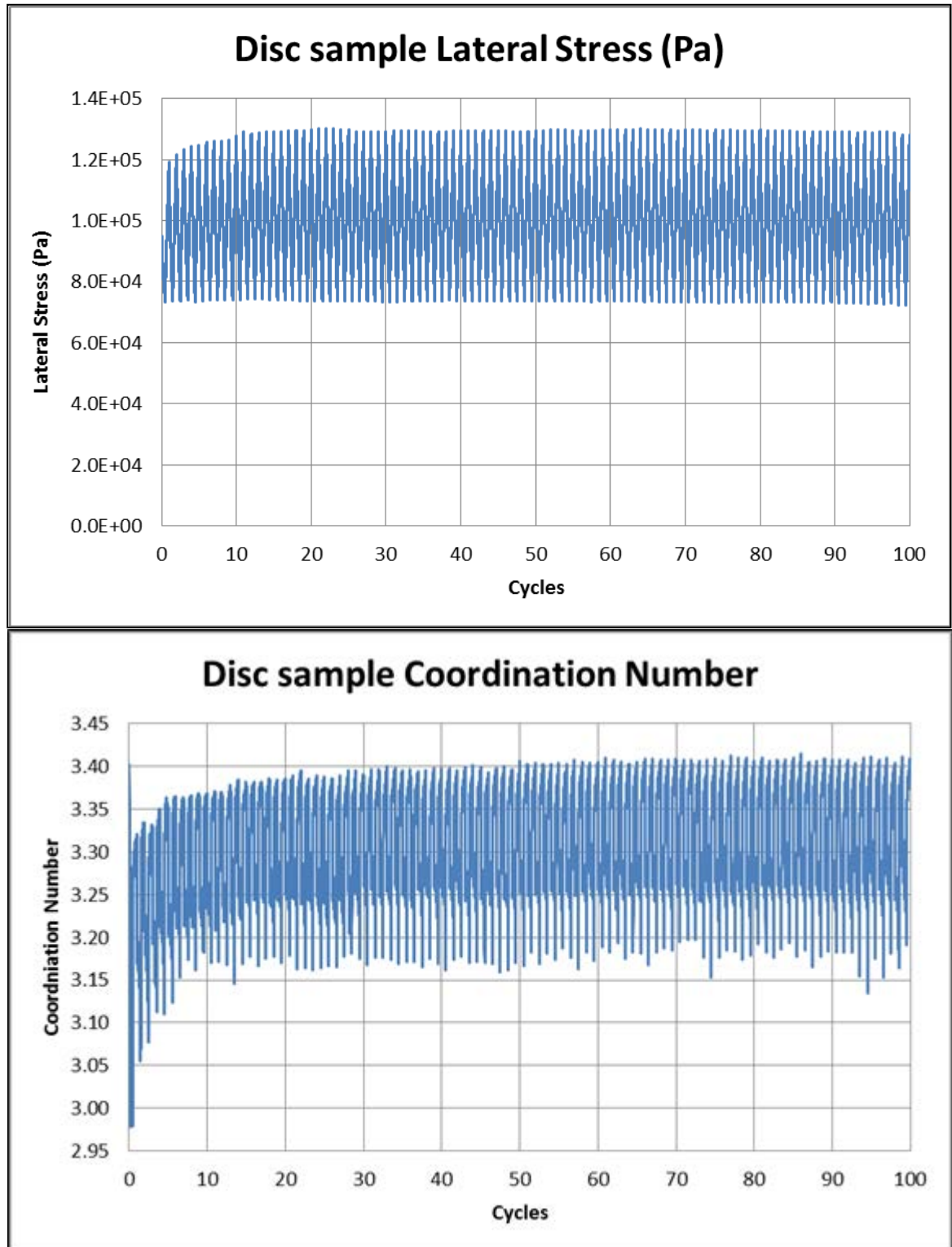
Figure 5.11: Lateral stress and coordination number of Disc sample

Sample volume and porosity were observed to continue decreasing although the rate of decrease was less after the 10th cycle. Further decrease in sample volume and porosity was indicated at the end of the 100th cycle.

Particle's average and standard deviation of displacement and absolute angles turned continued to increase with no indication of approaching a steady value. At the 100th cycle, the average displacement was about 0.0022 m and standard deviation was about 0.00475 m.

The absolute angles turned had a linear relationship with the strain cycles with an average value of about 47.9 radians and the standard deviation was about 3423 radians as shown in Figure 5.9. The absolute angles turned were very large when compared to the other three samples. However, there is no change in orientation for Disc particles despite the large angles turned as discussed in section 4.3. The Disc particles were able to rotate or roll for several revolutions with little resistance. All results for Disc particles sample are shown in Appendix 8.

5.2.3 Behaviour of Elliptic particles sample with cycles

The Elliptic particles sample's horizontal stress and coordination number increased by about 67 kPa to a steady value of around 128 kPa after the 10th cycle as shown in the following Figure 5.12. The horizontal stress however seems to oscillate erratically about the 120 kPa value. Further inspection indicate that the horizontal stress may still be increasing but at a very insignificant rate. This may also be true for the coordination number. Sample volume and porosity were decreasing at a lower rate by the 10th cycle or so. There was no indication of a steady value at the end of the 100th cycle and both sample volume and porosity were expected to continue decreasing.
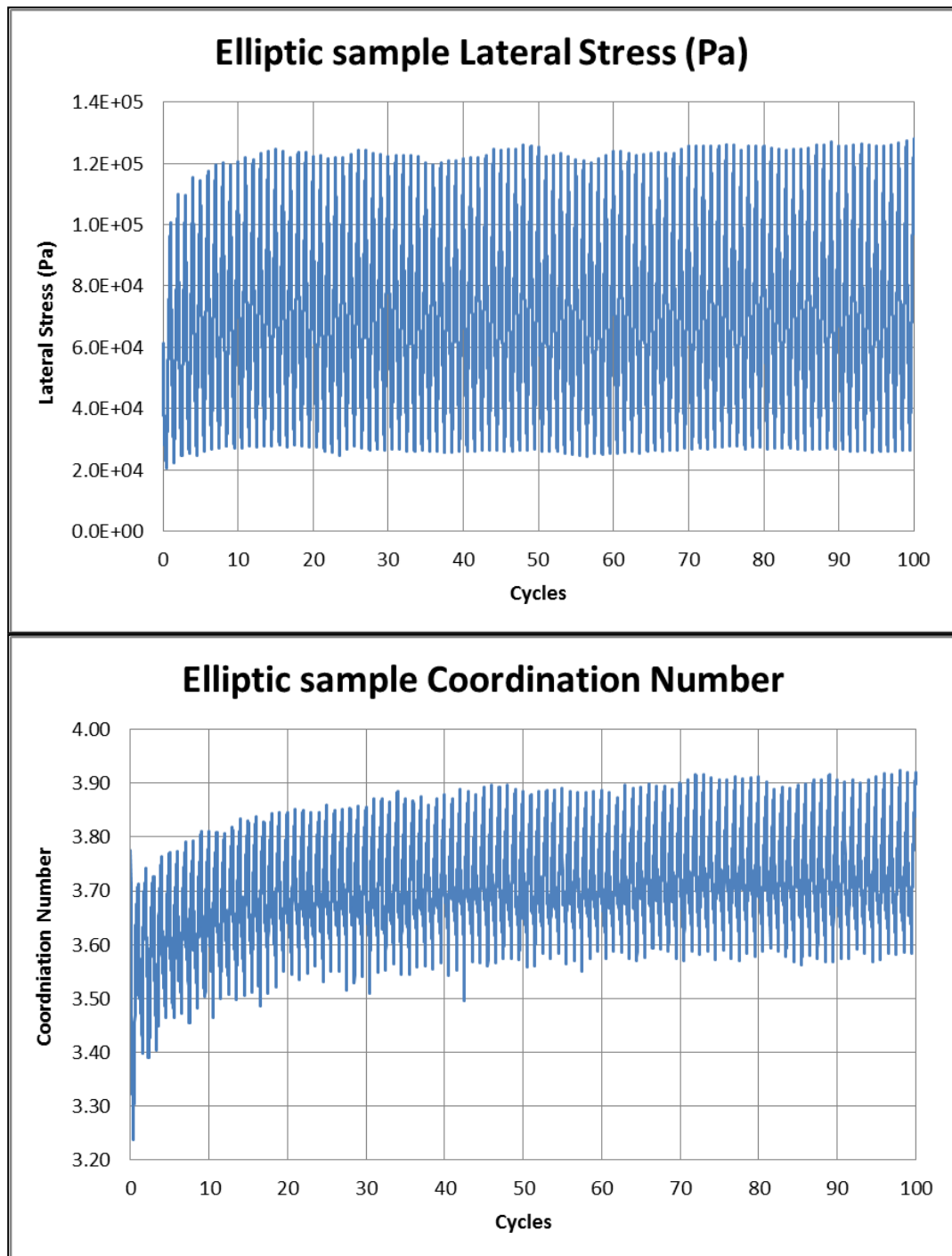
Figure 5.12: The lateral stress and coordination number of Elliptic sample

Particle's average and standard deviation of displacement and absolute angles turned continued to increase with no indication of approaching a steady value. At the 100th cycle, the average displacement was about 0.0038 m and standard deviation was about 0.0047m. The average absolute angles turned had a value of about 0.185 radians and the standard deviation was about 0.33 radians. Excluding the Disc sample, the Elliptic sample had the largest overall particle displacements and angles turned among the non-circular particles. This is suspected to be the cause of the larger vertical stress range observed in the Elliptic sample as noted in section 5.1.1. All results for Elliptic particles sample are shown in Appendix 9.

5.2.4 Behaviour of Triangular particles sample with cycles

The Triangular particles sample's horizontal stress and coordination number increased by about 60 kPa to a steady value of about 142 kPa by the 10th cycle as shown in the following Figure 5.13. Similarly, the sample volume and porosity also reaches a steady value by the 10th cycle. There was no indication of any further changes to these parameters at the 100th cycle.
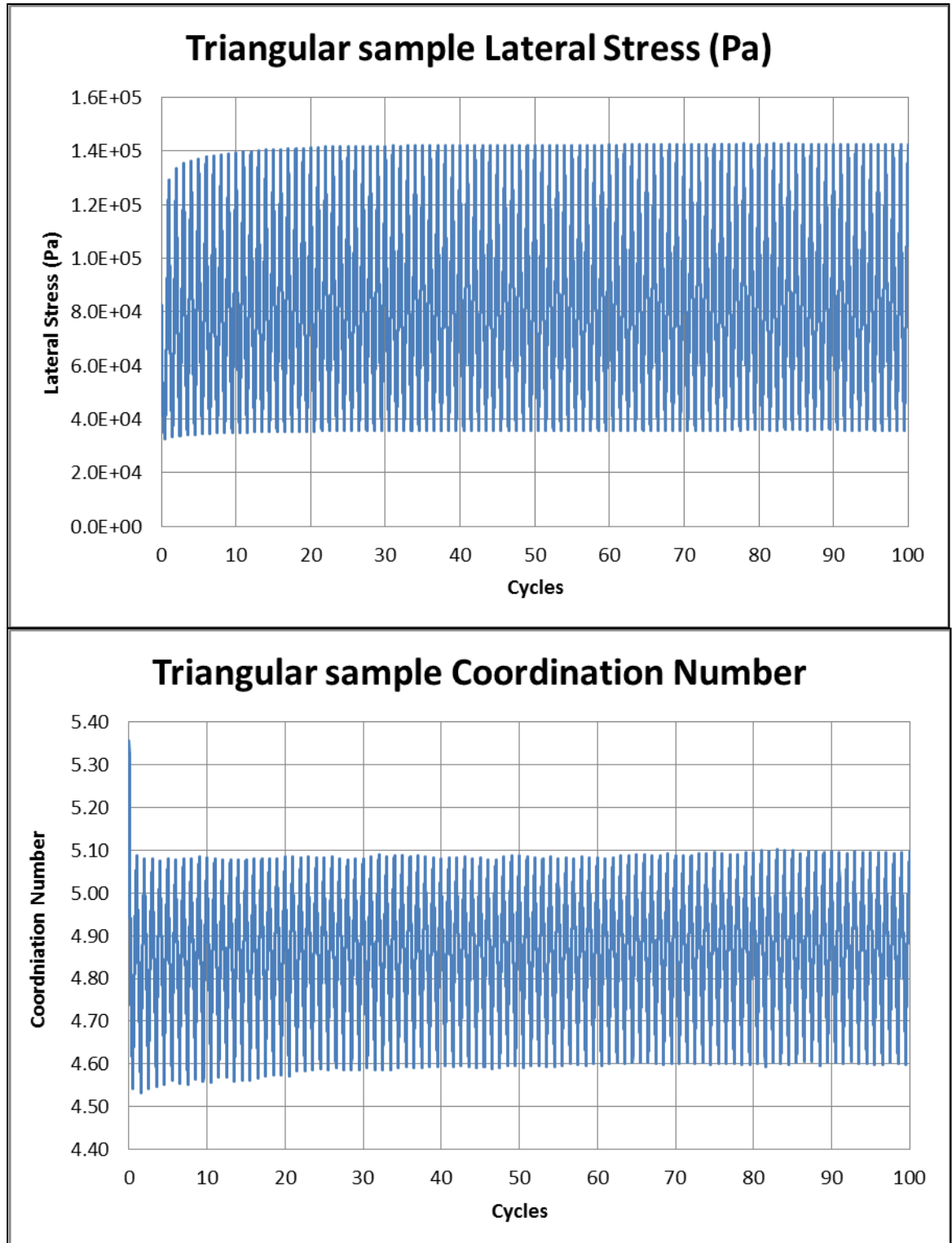
Figure 5.13: Lateral stress and coordination number of Triangular sample

Particles' displacement and absolute angles turned continued to increase with no indication of reaching a steady value. At the 100th cycle, the average displacement was about 0.0004 m and standard deviation was about 0.00064 m. The average absolute angles turned had a value of about 0.0107 radians and the standard deviation was about 0.047 radians. All results for Triangular particles sample are shown in Appendix 10.

5.3 The behaviour of particles of different sizes within samples

When the particles are separated in terms of the ten constituent sizes, it is apparent that it was the smallest particles in all four samples that had the largest particle displacement and angles turned. Figure 5.14 shows the average and standard deviation of particle displacement for the Ni particle sample in terms of the sizes after 100 cyclic strains.
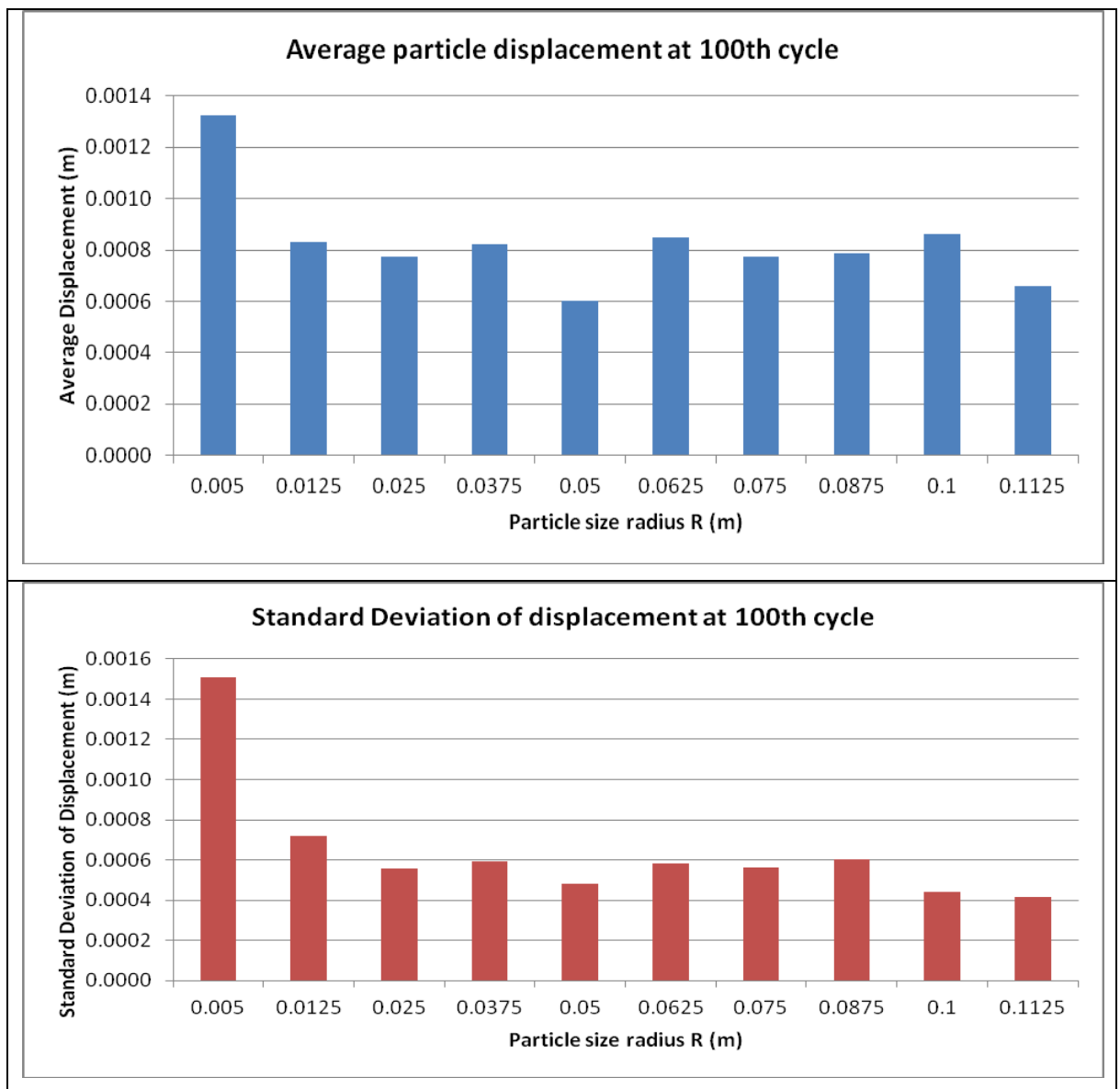
Figure 5.14: Average and standard deviation of particle displacement in terms of sizes for Ni particle

Figure 5.15 shows the average and standard deviation of absolute angles turned for Ni particle sample in terms of the sizes after 100 cyclic strains. In the results, the average and standard deviation of displacement and absolute angles turned of the smallest particles were significantly larger than the rest. The rest of the particle sizes appear to have average and standard deviation values that were packed closely with no correlation in terms of particle size.
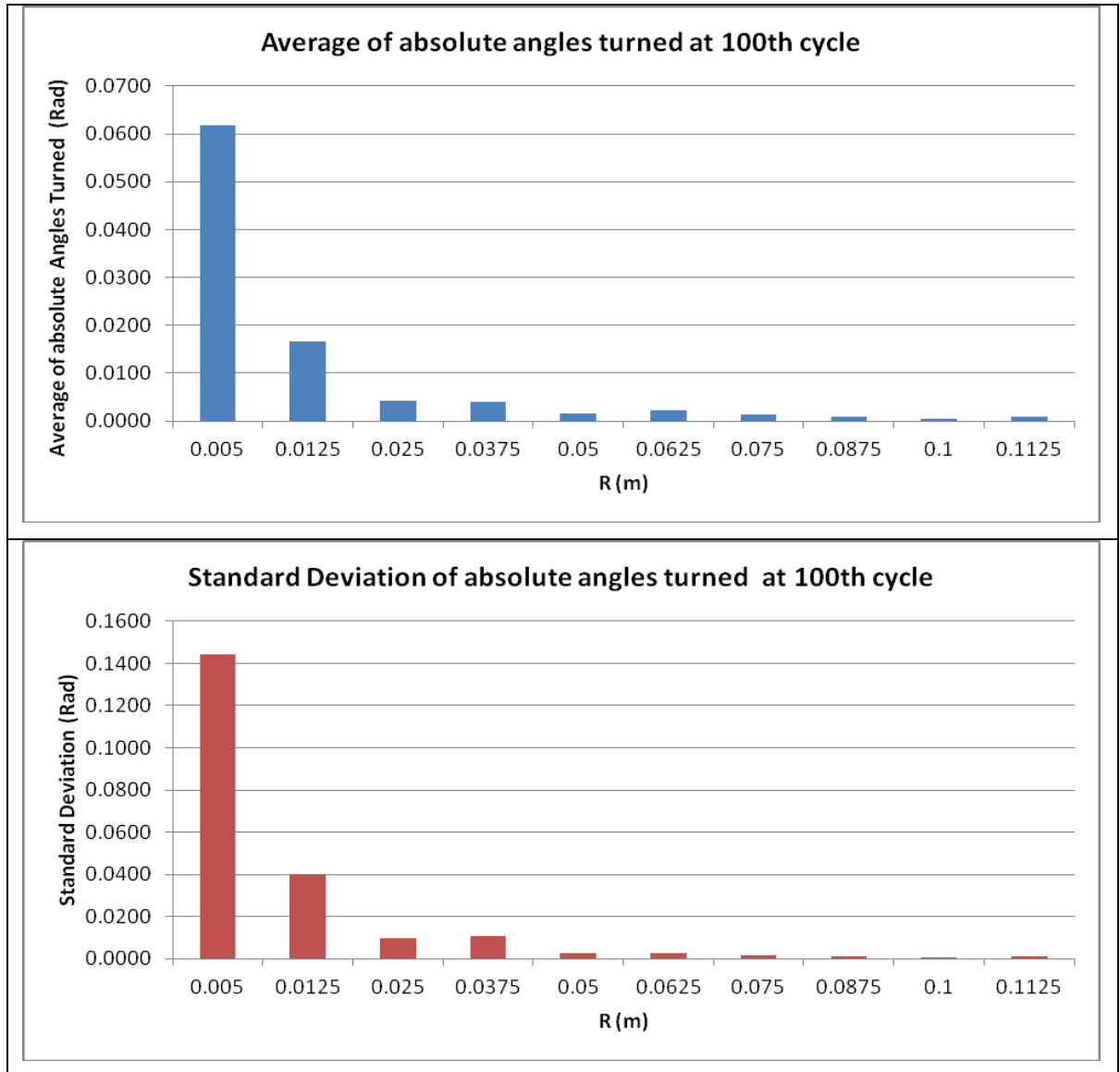
Figure 5.15: Average and standard deviation of absolute angles turned in terms of sizes for Ni particle

It is evident that the smallest particles have significantly larger activities (displacement and angles turned). Particle displacement and angles turned for each particle size over 100 cycles for all four samples are shown in Appendix 11. The average and standard deviations of the particle activities (displacement and angles turned) at the 100th cycle for all four particle shapes sample with respect to particle sizes are shown in Appendix 12.

Another point to note is that the particles in each sample were designed to be evenly distributed in terms of mass (see section 3.10) and not particle count. In terms of particle count, the smallest particles are in fact about 80% of the total number (8853) of particles as shown in the following Figure 5.16. The bigger particles would be surrounded by the smaller particles and held in place being prevented from displacing or rotating much. The smallest particles however, would be interacting with other particles of similar size to themselves as if they were in a uniformly graded environment. It is suspect as to whether or not this causes the smaller particles to both displace and rotate more than the bigger particles.
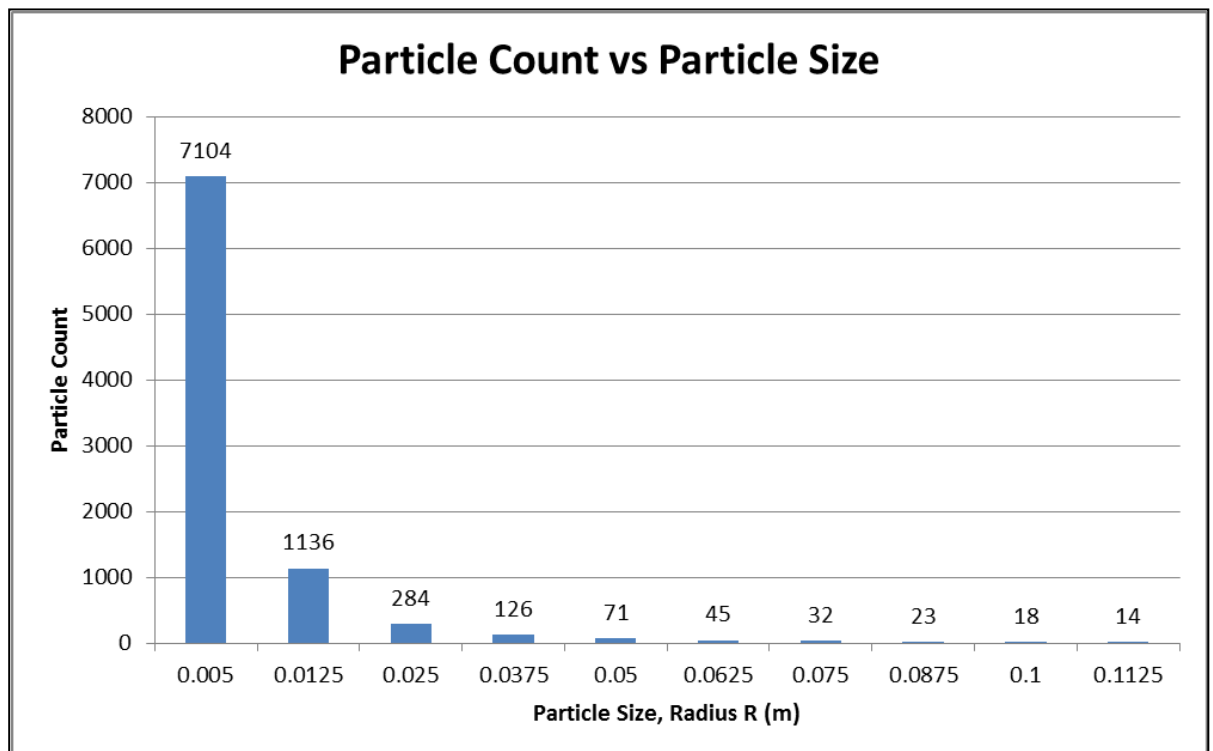

Figure 5.16: Particle count vs particle size

5.4 Implications of DEM simulation results

All four samples showed an increase in horizontal stress from their initial conditions when subjected to 100 cyclic strains. General decrease in sample volume and porosity was also observed, implying that densification occurred in all samples. It also implies that soil settlement can occur, but the change in volume were quite small (order of 0.001 m^3) further confirming that settlement is not an issue if the compaction follows the specification from the design manual (DMRB BA42/96, 2003).

5.4.1 Evidence of densification affecting horizontal stress

The Ni particles sample is the only sample with horizontal stress and coordination number that was observed to continue increasing with no indication of approaching a steady value. The sample volume and porosity of the Ni particles sample also continued decreasing with no indication of approaching a steady value, implying densification of the sample. The Triangular particles sample had horizontal stress, coordination number, sample volume and porosity that reached a steady value fairly quickly (by the 10th cycle). Lack of densification is implied when the sample volume and porosity doesn't continue to decrease in the Triangular particles sample. The steady value of horizontal stress and coordination number of the same Triangular particles sample is attributed to no further densification occurring.

This generally implies that densification of the sample can cause the horizontal stress build-up as suggested by most literatures (Ng C.W.W et al., 1998; England et al., 2000). Nonetheless, other results also show that even when densification does occur, the horizontal stress is not affected.

5.4.2 Evidence of densification NOT affecting horizontal stress

The Disc and Elliptic particles sample had sample volumes and porosities that were decreasing with no indication of approaching a steady value implying that densification occurred and will continue. However, both the Disc and Elliptic particles sample's horizontal stress and coordination number were observed to reach a steady value. Closer inspection indicate that the horizontal stress and coordination number was still increasing but at a very insignificant rate. This implies that densification of the sample does not directly correlate to an increase in horizontal stress and coordination number.

5.4.3 Evidence of particle shape affecting horizontal stress

The contrast of the results between the Disc and Elliptic particles sample (no stress build-up) versus the Ni particles sample (stress build-up) implies that densification is not necessarily the main factor that causes the build-up of horizontal stress when a granular material is subjected to cyclic loading. The main difference between these two groups of samples is their particle angularity. The Ni particles had an angularity of 0.5 while the Disc and Elliptic particles had an angularity of 1.0.

Xu (2005) also observed the lack of pressure build-up in a sample of glass ballotini (spherical shape) when subjected to triaxial cyclic loading tests. It was then postulated that perhaps the cause of pressure build-up in granular materials was due to the reorientation of non-spherical particles within the sample (Xu, 2005). This is further confirmed by the observable horizontal stress build-up in the non-circular Ni particles sample. However, the results also show that a majority of the particles in all four samples had angles turned that were less than ±6°, indicating that a lot of the particles may not have reoriented.

This suggests that having a non-rounded particle angularity would cause the horizontal stress build-up, with or without particle reorientation. However, the Triangular particles sample, which has the same form and angularity as the Ni particle, had a steady horizontal stress and coordination number. This highlights the limitations of defining particle shapes with form and angularity since the Ni particle and the Triangular particle are known intuitively to be very different particles. It is perhaps helpful to note that the Triangular particle shape is more *isotropic* whereas the Ni particle is *elongated* in its shape.

The Elliptic particle, which shares the same form as the Ni particle and the Triangular particle, actually had some build-up of horizontal stress, albeit at a very slow rate as to be deemed insignificant. This is in contrast with the Triangular particles which had a steady horizontal stress with no indication of any build-up at all since the 10th cycle. This would suggest that the build-up of lateral stress is due to the non-circular anisotropic shape of the particles.

The combination of isotropic grains and angularity was reported to slow down local and global phenomena of a granular material (Nouguier-Lehon et al., 2003). It was further pointed out from their biaxial tests that the behaviour of samples with isotropic grains is distinct from samples with anisotropic particles (i.e. elongated). From the DEM biaxial tests of this project, it can be inferred that the isotropy of the particles is an important factor. Anisotropic angular shaped particles might be responsible in causing the build-up of horizontal stress in a granular material being subjected to cyclic loading.

5.4.4 Coordination number affects horizontal stress

The coordination number is a better indicator of horizontal stress behaviour than densification of material. In all four samples, the coordination number better mimics the respective horizontal stress behaviour compared to the sample volume and porosity. It is believed that the increased in inter-particle contacts within the granular material resulted in the increase in horizontal stress.

It is not necessarily true that the sample with the largest coordination number will have the largest horizontal stress (Disc particles). It is the combination of the particle shape (anistropic, angular) and the increase in the number of contacts that results in the lateral earth pressure build-up as is the case with the Ni particles sample.

Rounded particles (particles with angularity = 1.0) had lower coordination number (3.4 for Disc and 3.8 to 3.9 for Elliptic) before and after the cyclic straining. Their final horizontal stresses were less than those of the *angular* particles (particles with angularity of 0.5) at the end of the 100th cycle. The angular particles had larger coordination number (4.1 to 4.3 for Ni particle and 5.3 to 5.1 for Triangular) and their horizontal stress was larger than the rounded particles.

The steady coordination number for the Disc sample was reflected by a steady horizontal stress throughout after an initial increase by about the 10th cycle. Similarly for the Elliptic sample, the small rate of increase in horizontal stress was replicated by the coordination number's behaviour.

The build-up of horizontal stress was most noticeable in the Ni particles sample and this was indicated in the increment of its coordination number. In comparison, the Triangular sample seemed to have reached a steady horizontal stress early on. The lack of horizontal stress build-up in the Triangular sample was indicated by the absence of an increase in the coordination number from its initial value. The Triangular samples' coordination number remains steady throughout the test just as the horizontal stress was at a steady value.

5.4.5 Particle displacement and angles turned

Data on particles displacement and angles turned generally showed that the particles' activity coincides with the sample's horizontal stress. Larger particle displacements and rotation (or rolling) occur at the start of the cyclic strain. The rate of change of the average displacements and angles turned were lower by the 30th to 50th strain cycle implying that the particles were more or less settled in their position and orientation.

There was no evidence of significant particle displacement as the largest average displacement at the 100th cycle was no more than 0.004m (4 mm) in a 2m by 4m sample space. The Elliptic particles sample had the largest average displacement. Standard deviations of particle displacement for all four samples were similar with the Disc and Elliptic particles having the largest value at slightly less than 0.005m. This suggests that significant granular flow may not have occurred.

All samples had a fairly isotropic orientation of particles (rounded rose plot) which was maintained at the end of 100 cyclic strains. Disc particles have no orientation though its large angles turned were probably due to its shape with nothing preventing its particles from rotating and/ or rolling almost freely.

As for the non-circular particles, the majority of the angles turned were about ±0.1 radians (about ± 6°) from their initial orientation. The histogram plots for all four samples show that the majority of the angles turned were heavily centred at 0.0 radians. The small angles turned does not dismiss that particle reorientation have occurred. The results may suggest that small reorientation of non-circular particle was enough to cause the increase in horizontal stress as suggested by Xu (2005).

Furthermore, most particle displacement and angles turned were associated with the smallest particles, significantly more than the other particle sizes. The implication of this is that should particle crushing and/ or breakage occur the whole dynamic of the granular body is changed with the presence of more small particles that can displace and rotate/roll more. It also implies an increase in the number of contacts per particle which is suspected as the main cause of the horizontal stress build up. In light of that, if the grading of the backfill material were to change, the material's overall behaviour would be expected to change as well.

The change in grading of a soil due to crushing is known to affect the overall behaviour of the material especially at the critical states (Wood and Maeda, 2008). In a DEM simulation, particle crushing and/ or breakage was observed to not develop uniformly throughout the granular material. The friction coefficient of the material, and by extension the strength of the material, was observed to be reduced as a consequence of granular crushing (Lobo-Guerrero and Vallejo, 2005).

5.4.6 The cause of horizontal stress build-up

In conclusion, the reorientation of non-circular particles is probably the cause of horizontal stress build-up although the angles of the particles' rotation were relatively small. Densification always occurs due to cyclic loading but is not the cause of horizontal stress build-up as evidenced by the results of the Disc and Triangular samples, in which the horizontal stress was at a steady value while the sample volume continued to decrease.

The results from DEM simulations show a reasonable correlation between increasing coordination number and increasing horizontal stress for the Ni particle. There is a similar although less obvious trend for the Elliptic sample. The Triangular sample had a steady horizontal stress and this was in correlation with its fairly steady coordination number. The Triangular particle is more isotropic in its shape than the Ni particle although they share the same form and angularity.

It can be concluded that the reorientation of anisotropic non-circular particles enables more contacts to be established within the material. This in turn increases the overall stiffness of the granular material and therefore an increase in horizontal stress is observed as the material is subjected to cyclic loading.

5.5 Summary of results

1. Four cyclic biaxial tests were done on samples with Ni particles, Discs, Elliptic and Triangular particles. Each sample was cyclically strained 100 times.

2. The vertical stress and the horizontal strain are two of the controlled parameters for the cyclic strain tests. Vertical stress was seen to oscillate about the designated 80 kPa but maintained an average at that value. The horizontal cyclic strain was designed to be 0.1%.

3. Sample volume was generally observed to decrease marginally from its initial value for all four samples. As the mass of the sample remains constant, this means that the sample undergoes small densification.

4. Sample porosity was observed to decrease with the decrease of sample volume.

5. Coordination number behaviour varies between the samples. It increased with cycles for the Ni particle and the Elliptic sample while the coordination number for the Disc and Triangular samples decreased.

6. Generally, large particle displacement occurs at the early stages of cyclic straining up to about the 30th cycle. Results from all four samples indicate that the particles were settling into a particular position.

7. The particle orientation for all four samples remains fairly isotropic (axisymmetric rose plot) throughout the cyclic test. The polar histograms of the particle angles before and after 100 cycles were similar.

8. The angles turned are the difference in angle for each particle within the respective samples. A majority of angles turned for all samples except the Disc particles sample, were between –0.1 and +0.1 radians (about ±6°).

9. Horizontal stress had increased by 98 kPa for the Ni particle, 33 kPa for the Disc, 67 kPa for the Elliptic and 60 kPa for the Triangular. All samples had an increase in horizontal stress due to 100 cyclic strains.

10. The Ni particles sample's behaviour in cyclic straining, build-up of horizontal stress, decrease in volume etc. are similar to what is expected of real backfill materials.

11. The Disc particles sample had horizontal stress and sample volume that reaches a steady value by the 20th cycle with no significant changes expected. Its sample volume and porosity were observed to continue decreasing without reaching a steady value. Particles were observed to continue to rotate indefinitely, completing several revolutions.

12. The Elliptic particles sample had a horizontal stress and coordination number that increased to a steady value by the 10th cycle with no significant changes observed

beyond that. The sample volume and porosity were observed to continue decreasing albeit at a smaller rate.

13. The Triangular particles sample had horizontal stress and coordination number that quickly reached a steady value with no indication of any further changes. The sample volume and porosity reached a steady value by the 10th strain cycle.

14. It was shown in that the smallest particles had the most activity in displacing and rotating compared to the other particles of larger sizes.

15. There was evidence in the results that showed densification both affecting and NOT affecting the horizontal stress build-up.

16. It was inferred from the results that sample containing anisotropic and angular shaped particles will have horizontal stress build-up when subjected to cyclic straining.

17. The coordination number was suggested to be a better of horizontal stress behaviour than densification of the material.

18. Particle displacements and angles turned were small for all samples. However, it was noted that particle displacement and rotation was constrained in 2-D. Small particle displacements may indicate that granular flow did not occur.

19. Small angles turned by the non-circular particles do not dismiss the significance of particle reorientation. Results suggest that small reorientation of non-circular particle was enough to cause the increase in horizontal stress.

20. It is concluded that the horizontal stress build-up in granular materials subjected to cyclic strains is mainly caused by the increase in the inter-particle contacts of anisotropic non-circular particles. New contacts were possibly formed within the sample, due to particle reorientation.

Chapter 6: Conclusions and recommendations

The build-up of lateral earth pressure behind an integral abutment is attributed to the cyclic loading of the backfill material due to the seasonal thermal changes experienced by the integral bridge. Most literature (Ng C.W.W et al., 1998; England et al., 2000) suggests that cyclic loading causes particle flow resulting in soil densification which explains the pressure build-up. Xu (2005) proposed that the pressure build-up in granular materials was due to the change in orientation of non-spherical particles instead and not necessarily densification. The aim of this research is to verify if densification and/ or particle reorientation causes pressure build-up by simulating granular materials being subjected to cyclic loading in a Discrete Element Method (DEM) model.

6.1 Success of research methodology

Laboratory experiments, field observations and scaled models have established that cyclic loading leads to lateral earth pressure build-up, for which densification and/ or particle reorientation was suggested as the cause. Numerical simulations of backfill materials under cyclic loading would help corroborate with the suggestions of what causes earth pressure build-up.

Common numerical simulations such as the finite element method consider the body of granular material as a continuum. This is useful for most cases when analysing a material's overall behaviour under stress or strain. However, soil densification and particle reorientation requires the observation of the individual particles' behaviour within the sample, for which the discrete element method is the most suitable analysis technique.

Discrete element models of a granular material were generated based on the design specification for backfill material (DMRB BA42/96, 2003). Particle shape and size cannot be accurately quantified, so an average shape for all the particles was utilized in the DEM model sample. A particle size distribution (PSD) consisting of ten sizes were designed to ensure that the sample was well-graded. For expediency, the particle sizes were enlarged three times and the sample size was set at 2 m by 4 m, reducing the total number of particles in the sample. The sample size must be large enough to contain about 10000 particles such that the sample behaves as a granular material.

Overall, the research methodology is considered successful as the granular material was sufficiently represented despite some limitations. Particle shape, surface friction and size distribution of the granular sample was incorporated as much as possible, as suggested

by O'Sullivan et al. (2002; 2004). The DEM model generated was good enough for the purpose of observing the micromechanical behaviour of the particles under cyclic loading.

6.2 Limitations of the study

1. The DEM models in this research project are 2-dimensional, and this limits the particles' displacement to the horizontal and vertical directions only. The particles' rotation is also limited to turning about an axis perpendicular to the 2-dimensional space. The reason for utilizing a 2-dimensional model is because a 3-dimensional DEM model would have very much longer simulation run times. A 3-dimensional model would also be more complex to prepare.

2. The particle shapes were crudely represented by clumping 2 to 4 discs together making a single form and angularity of all the particles for each sample. This is intended to be an average of the various shapes present within a granular backfill material. More discs could be used per clump to give the particles more variety in shapes culminating in a designated average particle form, angularity and surface roughness. However this would mean more discs to be generated and ultimately slower run times.

6.3 Main conclusions of thesis

1. The DEM biaxial test shows that lateral earth pressure build-up occurs in granular materials as a result of cyclic straining.

2. While densification of the material did occur due to cyclic straining, it is not the cause of lateral earth pressure increment.

3. The results from the DEM tests suggest that it is the increase in particle contacts that causes the increase in lateral earth pressure and not densification.

4. It is postulated that reorientation of anisotropic non-circular particles enables more inter-particle contacts to be established.

5. The majority of the non-circular particles' angles turned were no more than $\pm 6°$. Despite the small angles turned, the significance of particle reorientation cannot be dismissed.

6. Overall, therefore, the cause of lateral earth pressure build-up behind an integral abutment is seen as the increase in inter-particle contacts due to the reorientation of anisotropic non-circular particles.

7. The smallest particles in each sample had the most activity in both displacing and rotating (or rolling) in the course of the cyclic straining. The bigger particles tend to displace and/ or rotate far less. This implies that the particle reorientation that causes the build-up of lateral earth pressure occurs mainly among the small particles.

6.4 Recommendations for future work

It is clear that the limitation of this research project is mainly due to the lack of computing resource. To model the granular material with more details would extend the overall simulation run times. The current DEM samples used in this research project have a run time of about 2 weeks excluding sample preparation time which is much longer. Each sample took about a month to prepare due to the mixing process. Nonetheless, with the availability of better computers with larger memories and faster processors, it will be easier to include those details in future work. A more detailed model will enable better corroborative evidence for explaining the pressure build-up in granular materials when subjected to cyclic loading.

1. It was necessary to carry out the DEM tests in 2-dimensions as a precursor to modelling the integral abutment backfill in 3-dimensions. 3-dimensional modelling would give the particles more freedom; being able to displace in three directions and rotate about three axes. Generally, a 3-dimensional DEM model can represent a granular material more accurately than a 2-dimensional model even if it is a plane strain problem.

2. Real backfill material consists of a mixture of crushed rocks, gravel and sand with a variety of shapes. It is recommended to generate a model consisting of a *distribution* of particle form, angularity and surface roughness rather than a single constant value for all three parameters. This would better represent a backfill material.

3. Particle crushing and/ or breakage may occur in granular backfill material behind integral abutment. The main concern is that this changes the grading of the granular material to have more small particles which was observed to have more activity than larger particles in the DEM simulations for this project. It may be useful to consider the effects of particle breakage on the lateral earth pressure when the material is subjected to cyclic loading.

4. It was identified that the particle shape in combination with the coordination number is a better determinant of the horizontal stress behaviour. A specific area of interest would be isotropic and anisotropic angular particles. In short, the research question of what is the difference in how isotropic and anisotropic particle shapes affect the particle-particle contacts within a sample when subjected to cyclic loading.

The discrete element method is a powerful modelling tool, yet remains conceptually simple. It is useful in modelling soils and rocks, for which it was originally conceived. The DEM was especially useful in simulating integral bridge backfill materials in this project as the concern lies in the behaviour of the individual particles. The use of DEM will spread into other areas of engineering, where the modelling of discrete entities is required. While the availability of computing resource has always limited its use, the advent of more powerful computers will change the utilization of DEM in the near future.

References

1. Arockiasamy, M. and Sivakumar, M. (2005). *Effects of Restraint Moments in Integral Abutment Bridges*, Integral Abutments and Jointless Bridges (IAJB 2005), The 2005 FHWA Conference. Baltimore, Maryland.

2. Arsoy, S. (2000). *Experimental and Analytical Investigations of Piles and Abutments of Integral Bridges,* PhD Thesis, Department of Civil Engineering. Blacksburg, Virginia Polytechnic Institute and State University (Virginia Tech.)**:** 163 pages.

3. Arsoy, S., Duncan, J.M. and Barker, R.M. (2005). *Approach to Evaluating Damage from Thermal Bridge Displacements* Transportation Research Record (TRR): 1936(Soil Mechanics): 124-129.

4. Arsoy, S., Duncan, J.M. and Barker, R.M. (2004). *Behaviour of a Semiintegral Bridge Abutment under Static and Temperature-Induced Cyclic Loading*. Journal of Bridge Engineering 9(2): 193-199.

5. Banks, J. R. (2009). *Numerical Modelling of lateral stress on integral abutments due to cyclic loading*. EngD Thesis, University of Southampton.

6. Barker, K. J. and D. R. Carder (2000). *Performance of the two integral bridges forming the A62 Manchester Road Overbridge.* Highway Agency, Transport Research Laboratory, Crowthorne, Berks. TRL Report 436.

7. Barker, K. J. and D. R. Carder (2001). *Performance of an integral bridge over the M1-A1 Link Road at Bramham Crossroads*. Highway Agency, Transport Research Laboratory, Crowthorne, Berks. TRL Report TRL521.

8. Barker, K. J. and D. R. Carder (2006). *The long term monitoring of stresses behind three integral bridge abutments.* Concrete Bridge Development Group, Technical Paper 10.

9. Bonczar, C., Breña, S., Civjan, S., DeJong, J. Crellin, B. and Crovo, D. (2005). *Field Data and FEM Modelling of the Orange-Wendell Bridge.* Integral Abutments and Jointless Bridges (IAJB 2005), The 2005 FHWA Conference. Baltimore, Maryland.

10. Bonczar, C., Breña, S., Civjan, S., DeJong, J. and Crovo, D. (2005). *Integral Abutment Pile Behavior and Design – Field Data and FEM Studies.* Integral Abutments and Jointless Bridges (IAJB 2005), The 2005 FHWA Conference. Baltimore, Maryland.

11. Brena, S. F., Bonczar, C.H., Civjan, S.A., DeJong, J.T. and Crovo, D.S. (2007). *Evaluation of Seasonal and Yearly Behaviour of an Integral Abutment Bridge.* Journal of Bridge Engineering 12(3): 296-305.

12. Carder, D. R. and Hayes, J.P. (2000). *Performance under cyclic loading of the foundations of integral bridges.* Highway Agency, Transport Research Laboratory, Crowthorne, Berks. TRL Project Report 433.

13. Chen, T.J. and Fang, Y.S. (2008). *Earth pressure due to vibratory compaction.* Journal of Geotechnical and Geoenvironmental Engineering 134 (4): 437-444.

14. Cho, G.C., Dodds, J. and Santamarina, J.C. (2006). *Particle shape effects on packing density, stiffness and strength: natural and crushed sands.* Journal of Geotechnical and Geoenvironmental Engineering 132(5): 591-602.

15. Christou, P., Hoit, M. and McVay, M. (2005). *Soil Structure Analysis of Integral Abutment Bridges.* Integral Abutments and Jointless Bridges (IAJB 2005), The 2005 FHWA Conference. Baltimore, Maryland.

16. Civjan, S. A., Bonczar, C. H., Brena, S.F., DeJong, J.T. and Crovo, D.S. (2007). *Integral Abutment Bridge Behavior: Parametric Analysis of a Massachusetts Bridge.* Journal of Bridge Engineering 12(1): 64-71.

17. Clayton, C. R. I. and Reddy, A. C. O. (2006). *Influence of particle form on initial packing and dilation of particulate materials - a numerical study.* International Symposium on Geomechanics and Geotechnics of Particulate Media. Ube, Yamaguchi, Japan.

18. Clayton, C.R.I. and Symons, I.F. (1992). *The pressure of compacted fill on retaining walls.* Geotechnique 42(1): 127-130.

19. Clayton, C. R. I., Xu, M. and Bloodworth, A.G. (2006). *A laboratory study of the development of earth pressure behind integral bridge abutments.* Geotechnique 56(8): 561-571.

20. Cole, R. T. and K. M. Rollins (2006). *Passive Earth Pressure Mobilization during Cyclic Loading.* Journal of Geotechnical and Geoenvironmental Engineering 132(9): 1154-1164.

21. Conboy, D. and Stoothoff, E. (2005). *Integral Abutment Design and Construction: The New England Experience.* Integral Abutments and Jointless Bridges (IAJB 2005) The 2005 FHWA Conference. Baltimore, Maryland.

22. Cosgrove, E. F. and B. M. Lehane (2003). *Cyclic Loading of Loose Backfill placed adjacent to Integral Bridge Abutments.* International Journal of Physical Modelling in Geotechnics 3(3): 9-16.

23. Cundall, P. A. (2001). *A discontinuous future for numerical modelling in geomechanics?* Geotechnical Engineering 149(1): 41-47.

24. Dicleli, M. (2000). *Simplified Model for Computer Aided Analysis of Integral Bridges.* Journal of Bridge Engineering 5(3): 240-248.

25. Dicleli, M. (2005). *Integral Abutment-Backfill Behaviour on Sand Soil-Pushover Analysis Approach.* Journal of Bridge Engineering 10(3): 354-364.

26. Duncan, J. M. and Arsoy, S. (2003). *Effect of bridge-soil interactions on behavior of piles supporting integral bridges.* TRB Annual Meeting CD-ROM.

27. Dunker, K. F. and D. Liu (2007). *Foundations for Integral Abutments.* Practice Periodical on Structural Design and Construction 12(1): 22-30.

28. England, G.L., Tsang, N.C.M and Bush, D.I. (2000). *Integral Bridges: A fundamental approach to the time-temperature loading problem.* Thomas Telford, London.

29. Faraji, S., Ting, J. M., Crovo, D.S. and Ernst, H. (2001). *Nonlinear Analysis of Integral Bridges: Finite-Element Model.* Journal of Geotechnical and Geoenvironmental Engineering 127(5): 454-461.

30. Fennema, J. L., Laman, J. A., Linzell, D.G. (2005). *Predicted and Measured Response of an Integral Abutment Bridge.* Journal of Bridge Engineering 10(6): 666-677.

31. Frosch, R., Wenning, M. and Chovichien, V. (2005). *The In-service Behavior of Integral Abutment Bridges: Abutment-Pile Response* Integral Abutments and Jointless Bridges (IAJB 2005), The 2005 FHWA Conference. Baltimore, Maryland.

32. Georgiannou, V.N.; Tsomokos, A. and Stavrou, K. (2008) *Monotonic and cyclic behaviour of sand under torsional loading.* Geotechnique 58(2): 113-124.

33. Hanna, A. and Al-Rohmein, R. (2008) *At rest earth pressure of overconsolidated cohesionless soil.* Journal of Geotechnical and Geoenvironmental Engineering 134(3): 408-412

34. Hassiotis, S., Lopez, J. and Bermudez, R. (2005). *Full-Scale Testing of an Integral Abutment Bridge.* Integral Abutments and Jointless Bridges (IAJB 2005), The 2005 FHWA Conference. Baltimore, Maryland.

35. Hassiotis, S. and Roman, E. K. (2005). *A survey of current issues on the use of integral abutment bridges.* Bridge Structures (Taylor and Francis Group) 1(2): 81-101.

36. Highway Agency (1998). *The Design and Appearance of Bridges.* Design Manual for Roads and Bridges (DMRB)/BA41, HMSO, London. 1, Section 3, part 11.

37. Highway Agency (2001). *Design for Durability.* Design Manual for Roads and Bridges (DMRB)/ BD57, HMSO, London. 1, Section 3, part 7.

38. Highway Agency (2001). *Design for Durability (2).* Design Manual for Roads and Bridges (DMRB)/ BA57, HMSO, London. 1, Section 3, part 8.

39. Highway Agency (2001). *Loads for Highway Bridges.* Design Manual for Roads and Bridges (DMRB)/ BD37, HMSO, London. 1, Section 3, part 14.

40. Highway Agency (2003). *The Design of integral bridges.* Design Manual for Roads and Bridges (DMRB)/ BA42, HMSO, London. 1, Section 3, part 12.

41. Highway Agency (2005). *Specification for Highway Works: Earthworks.* Manual of Contract documents for Highway Works (MCHW), HMSO, London. 1, Series 600.

42. Hoppe, E. (2005). *Field Study of Integral Backwall with Elastic Inclusion.* Integral Abutments and Jointless Bridges (IAJB 2005). The 2005 FHWA Conference. Baltimore, Maryland.

43. Horvath, J. S. (2004). *Integral-Abutment Bridges: A Complex Soil-Structure Interaction Challenge.* Geotechnical Engineering for Transport Project (Geo-Trans 2004). American Society of Civil Engineers Geo-Institute.

44. Horvath, J. (2005). *Integral-Abutment Bridges: Geotechnical Problems and Solutions Using Geosynthetics and Ground Improvement.* Integral Abutments and Jointless Bridges (IAJB 2005). The 2005 FHWA Conference. Baltimore, Maryland.

45. Hsu, C.-C. and M. Vucetic (2004). *Volumetric Threshold Shear Strain for Cyclic Settlement.* Journal of Geotechnical and Geoenvironmental Engineering 130(1): 58-70.

46. Huang, J., French, C. E. and Shield, C.K. (2004). *Behaviour of Concrete Integral Abutment Bridges.* University of Minnesota and Local Road Research Board (LRRB), Minnesota Department of Transportation, Research Services Section.

47. Itasca Consulting Group Inc. (2002) *Particle Flow Code in 2 Dimensions User Guide* 2nd Edition.

48. Jensen, R. P., Bosscher, P. J., Plesha, M.E. and Edil T.B. (1999). *DEM Simulation of Granular Media - Structure Interface: Effects of Surface Roughness and Particle Shape.* International Journal for Numerical and Analytical Methods in Geomechanics 23(6): 531-547.

49. Jensen, R. P., Plesha, M. E., Edil, T.B., Bosscher, P.J. and Kahla, N.B. (2001). *Effect of Particle Shape on Interface Behavior of DEM-Simulated Granular Materials.* International Journal of Geomechanics 1(1): 1-19.

50. Khodair, Y. (2006) *Lateral Earth Pressure Behind an Integral Abutment.* Structure and Infrastructure Engineering pp1-14. Taylor and Francis.

51. Knickerbocker, D., Basu, P. and Wasserman, E. (2005). *Behavior of Two-Span Integral Bridges Unsymmetrical About the Pier Line.* Integral Abutments and Jointless Bridges (IAJB 2005). The 2005 FHWA Conference. Baltimore, Maryland.

52. Kumar, P. T. V., Paul, D. K., Kumar, R. and Agarwal, P. (2006). *Behavior of Integral Bridges under Temperature and Seismic Loading.* National Conference on Advances in Bridge Engineering. India.

53. Lawver, A., French, C.E. and Shield, C.K. (2000). *Field Performance of Integral Abutment Bridge.* Transportation Research Record (TRR) 1740(00-0654): 108-117.

54. Lehane, B. M., Keogh, D. L. and O'Brien, E.J. (1999). *Simplified elastic model for restraining effects of backfill soil on integral bridges.* Computers &Structures 73(1-5): 303-313.

55. Lobo-Guerrero, S. and Vallejo, L.E. (2005). *Discrete Element Method Evaluation of Granular Crushing Under Direct Shear Test Conditions.* Journal of Geotechnical and Geoenvironmental Engineering 131(10): 1295-1300.

56. Lock, R. J. (2002). *Integral Bridge Abutments.* M.Eng. Project Report, Department of Engineering, University of Cambridge, U.K. [CUED/D-SOILS/TR320]

57. Mosley, W.H. (1999) *Reinforced Concrete Design* (Fifth Edition), MacMillan, Basingstoke.

58. Marroquin, F. A. and Hermann, H. J. (2004). *Ratcheting of Granular Materials.* Physical Review Letters (American Physics Society) 92(5).

59. Maruri, R. and Petro, S. (2005). *Integral Abutments and Jointless Bridges (IAJB) 2004 Survey Summary.* Integral Abutments and Jointless Bridges (IAJB 2005). The 2005 FHWA Conference. Baltimore, Maryland.

60. Mayur Babu P.V. and Bhandari N.M. (2006) *A Comparative Study of Integral Bridge versus Simply Supported Bridge.* Advances in Bridge Engineering (March 24-25)

61. McGowan, K. (2005). *Measurement and Evaluation of the performance of an integral abutment bridge deck.* Thesis for MSc Mechanical Engineering, West Virginia University.

62. Mirghasemi, A. A., Rothenburg, L. and Matyas, E.L. (2002). *Influence of particle shape on engineering properties of assemblies of two dimensional polygon shaped particles.* Geotechnique 52(3): 209-217.

63. Mistry, V.C. (2005). *Integral Abutment and Jointless Bridges.* Integral Abutments and Jointless Bridges (IAJB 2005). The 2005 FHWA Conference. Baltimore, Maryland.

64. Mourad, S. and Tabsh, S.W. (1999). *Deck Slab Stresses in Integral Abutment Bridges.* Journal of Bridge Engineering 4(2): 125-130.

65. Ng, C.W.W., Springman, S.M. and Norrish, A.R.M. (1998). *Centrifuge Modelling of Spread-Base Integral Bridge Abutments.* Journal of Geotechnical and Geoenvironmental Engineering 124(5): 376-388.

66. Ni, Q (2003) *Effects of Particle Properties and Boundary Conditions on Soil Shear Behaviour: 3D Numerical Simulations.* PhD Thesis, University of Southampton.

67. Nouguier-Lehon, C., Cambou, B. and Vincens, E. (2003). *Influence of particle shape and angularity on the behaviour of granular materials: a numerical analysis.* International Journal for Numerical and Analytical Methods in Geomechanics 27: 1207-1226.

68. O'Sullivan, C., Bray, J. D. and Riemer, M.F. (2002). *Influence of Particle Shape and Surface Friction Variability on Response of Rod-Shaped Particulate Media.* Journal of Engineering Mechanics 128(11): 1182-1192.

69. O'Sullivan, C., Bray, J. D. and Riemer, M.F. (2004). *Examination of the Response of Regularly Packed Specimens of Spherical Particles Using Physical Tests and Discrete Element Simulations.* Journal of Engineering Mechanics 130(10): 1140-1150.

70. Oda, M. (1972). *Deformation mechanism of sand in triaxial compression tests.* Soils and Foundation 12(4): 45-63.

71. Oesterle, R. and Lofti, H. (2005). *Transverse Movement in Skewed Integral Abutment Bridges*. Integral Abutments and Jointless Bridges (IAJB 2005). The 2005 FHWA Conference. Baltimore, Maryland.

72. Oesterle, R. and Volz, J. (2005). *Effective Temperature and Longitudinal Movement in Integral Abutment Bridges*. Integral Abutments and Jointless Bridges (IAJB 2005). The 2005 FHWA Conference. Baltimore, Maryland.

73. Powrie, W., Ni, Q., Harkness, R.M. and Zhang, X. (2005). *Numerical modelling of plane strain tests on sands using a particulate approach.* Geotechnique 55(4): 297-306.

74. Powrie, W. (2004) *Soil Mechanics Concepts & Applications* (Second Edition). Spon Press, Taylor & Francis Group, London and New York.

75. Procter, D. C. and Barton, R. R. (1974). *Measurement of the angle of interparticle friction.* Geotechnique 24(4): 581-604.

76. Roeder, C. W. (2003). *Proposed Design Method for Thermal Bridge Movements.* Journal of Bridge Engineering 8(1): 12-19.

77. Rothenburg, L. and Bathurst, R. J. (1992). *Micromechanical features of granular assmemblies with planar elliptical particles.* Geotechnique 42(1): 79-95.

78. Rousé, P. C.; Fannin, R. J. and Shuttle, D.A. (2008). *Influence of roundness on the void ratio and strength of uniform sand.* Geotechnique 58(3): 227-231.

79. Rowe, P.W. (1962). *The stress-dilatancy relation for static equilibrium of an assembly of particles in contact.* Proceedings of the Royal Society. Vol. 269 of A, London. The Royal Society: 500-527.

80. Rowe, P.W. and Barden, L. (1964). *Importance of free end in triaxial testing.* Journal of the soil mechanics and foundations division. ASCE 90(SM1): 1-27.

81. Sallam, A.M. (2004) *Studies on Modelling Angular Soil Particles Using the Discrete Element Method* PhD Thesis, University of South Florida.

82. Santamarina, J.C. and Cho, G. C. (2004) *Soil behaviour: The role of particle shape.* Advances in Geotechnical Engineering: The Skempton Conference, Thomas Telford, London, 604-617.

83. Sazzad, M and Suzuki, K (2011) *Effect of Interparticle Friction on the Cyclic Behavior of Granular Materials using 2D DEM.* Journal of Geotechnical and Geoenvironmental Engineering 137(5): 545-549.

84. Shekar,V., Aluri, S. and GangaRao, H. (2005). *Integral Abutment Bridges with FRP Decks – Case Studies* Integral Abutments and Jointless Bridges (IAJB 2005). The 2005 FHWA Conference. Baltimore, Maryland.

85. Sitharam, T. G. (2003). *Discrete element modelling of cyclic behaviour of granular materials.* Geotechnical and Geological Engineering (Kluwer Academic Publishers) 21(4): 297-329.

86. Sitharam, T.G. and Nimbkar, M.S. (2000). *Micromechanical Modelling of Granular Materials: Effect of Particle Size and Gradation.* Geotechnical and Geological Engineering 18(2): 91-117

87. Springman, S.M., Norrish, A.R.M., and Ng, C.W.W. (1996). *Cyclic loading of sand behind integral bridge abutments.* TRL Report 146, Transport Research Laboratory, U.K.

88. Thomas, P.A. and Bray, J.D. (1999). *Capturing Nonspherical Shape of Granular Media with Disk Clusters.* Journal of Geotechnical and Geoenvironmental Engineering 125(3): 169-236.

89. Thornton, C. (2000). *Numerical simulations of deviatoric shear deformation of granular media.* Geotechnique 50(1): 43-53.

90. Ting, J.M., Khwaja, M., Meachun, L.R. and Rowell, J.D. (1993). *An ellipse-based discrete element model for granular materials.* International Journal for Numerical and Analytical Methods in Geomechanics 17: 603-623.

91. Tsang, N.C.M., England, G.L. and Dunstan, T. (2002). *Soil/ Structure Interaction of Integral Bridge with full height abutments.* 15th ASCE Engineering Mechanics Conference, Columbia University, New York.

92. Van Baars, S. (2005). *Differences between the Results of discrete element modelling and continuum modelling.* International Conference Powders and Grains. A.A. Balkerna, Rotterdam.

93. Vucetic, M. (1994). *Cyclic Threshold Shear Strains in Soils.* Journal of Geotechnical Engineering 120(12): 2208-2228.

94. William, G.W., Shoukry, S.N. and Riad, M.Y. (2005). *Thermal stresses in steel girder bridges with integral abutments.* Bridge Structures (Taylor and Francis Group) 1(2): 103-119.

95. Wood, D.M. (2004). *Geotechnical Modelling.* Spon Press, Taylor & Francis Group, London and New York.

96. Wood, D.M. and Maeda, K. (2008). *Changing Grading of soil: effect on critical states.* Acta Geotechnica 3:3-14

97. Wood, D.M. and Nash, D. (2000). *Earth pressure on an Integral Bridge Abutment: A Numerical Case Study.* Soils and Foundations 40(6): 23-38.

98. Xu, M. (2005) *The Behaviour of Soil behind Full-height Integral Abutments* PhD Thesis, University of Southampton.

99. Xu, M., Bloodworth, A.G. and Clayton, C.R.I. (2007). *Behaviour of a Stiff Clay behind Embedded Integral Abutments.* Journal of Geotechnical and Geoenvironmental Engineering 133(6): 721-730.

100. Xu, M., Bloodworth, A.G. and Lee, M.M.K (2003). *Numerical Analysis of the embedded abutments of integral bridges.* IABSE symposium Antwerp 2003: Structures for high-speed railway transportation 87: 110-111.

101. Yannotti, A., Alampalli, A. and White, H. (2005). *New York State Department of Transportation's Experience with Integral Abutment Bridges* Integral Abutments and Jointless Bridges (IAJB 2005). The 2005 FHWA Conference. Baltimore, Maryland.

102. Zhang, L. and C. Thornton (2007). *A numerical examination of the direct shear test.* Geotechnique 57(4): 343-354.

APPENDIX

APPENDIX 1:

Maximum dry density

calculation of sample mass

APPENDIX 1: Maximum dry density calculation of sample mass

The Ni particle shape was utilized for the estimation of the maximum dry density. A volume of solid is assumed to be at $1m^3$. For 10 particle sizes, each particle size would need to occupy $0.1m^3$. The volume occupied by a single particle for each size was obtained by trial and error in PFC2D. This enables the estimation of the number of particles for each size. The number of particles was then adjusted by trial and error to obtain an approximate equivalent mass between the different particle sizes.

Particle Size, R (m)	volume per particle (m³)	Est. Particle Count (to occupy 0.1m^3)	Adjusted No. Of Particles	Volume occupied (m^3)	Weight per particle (N)	Weight (N)	Mass (kg)
0.005	9.81748E-05	1018.5916	1020	0.100138266	3.005	3065.1	312.4465
0.0125	0.000628319	159.15494	160	0.100530965	18.78	3004.8	306.2997
0.025	0.002532909	39.480296	40	0.101316363	75.12	3004.8	306.2997
0.0375	0.005694137	17.561925	18	0.10249446	169	3042	310.0917
0.05	0.010131636	9.870074	10	0.101316363	300.5	3005	306.3201
0.0625	0.015845408	6.3109767	6	0.095072448	469.5	2817	287.156
0.075	0.022815817	4.3829244	4	0.091263267	676.1	2704.4	275.6779
0.0875	0.031042862	3.2213524	4	0.12417145	920.2	3680.8	375.209
0.1	0.04054618	2.4663236	2	0.08109236	1202	2404	245.0561
0.1125	0.051306135	1.9490846	2	0.10261227	1521	3042	310.0917
			1266	≈1.0			≈3034.65

Distribution of Mass according to particle size
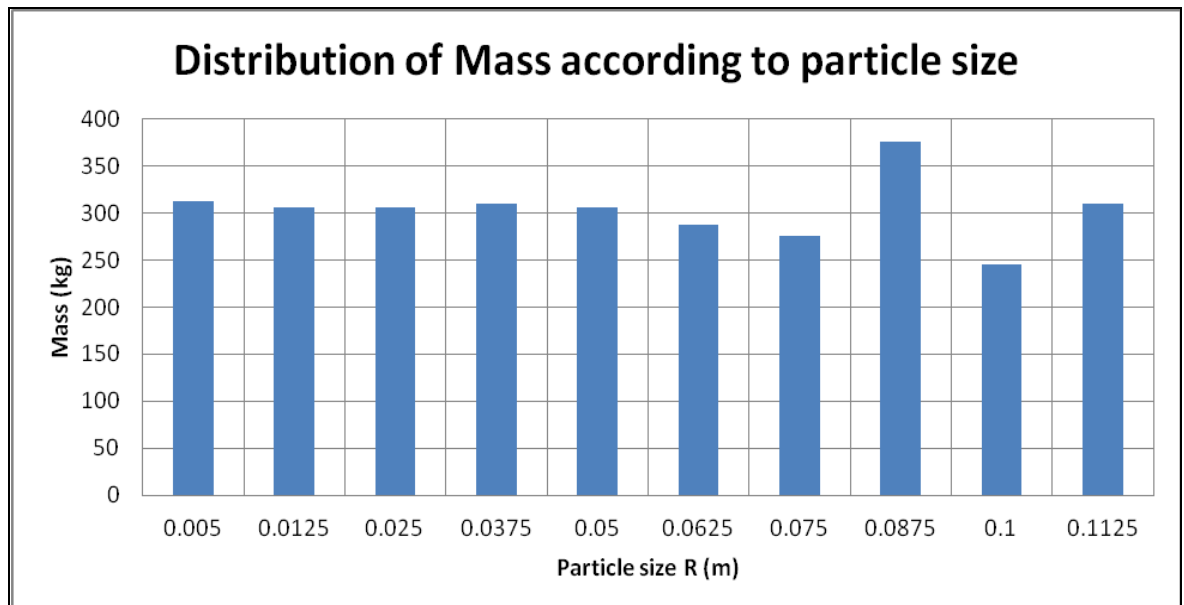
The PFC2D was programmed to generate the adjusted particle count for each respective size. The particles were then compacted into a 1m wide box. The estimated height of 1.0597 m of the compacted particles enables an approximation volume of the sample. With a total mass of 3034.65 kg and the sample volume of 1.0597 m^3, the maximum dry density of the sample can be estimated.

APPENDIX 1: Maximum dry density calculation of sample mass

```
;Ni's particle w/ shape factor 1.5
def backfill1
 ang=angularity
 xc3=x0
 yc3=y0
 br=radius
 sr=ang*br
 idc3=id_start
 yinc=1.2 ;2.1*radius
 loop row (1,n_row)
  loop col (1,n_col)
  idc2=idc3-1
  idc1=idc2-1
  xc2=xc3+br
  xc1=xc2+sr
    command
     ball id=idc1 x=xc1 y=yc3 rad=sr
     ball id=idc2 x=xc2 y=yc3 rad=sr
     ball id=idc3 x=xc3 y=yc3 rad=br
     clump id=idc1 perm range id=idc1,idc3
    endcommand
    idc3=idc3+3
    xc3=xc3+3.1*br
  endloop
  yc3=yc3+yinc
  xc3=x0
 endloop
end
;generate particles for calculating maximum density
def gg10
command
set id_start=3 x0=0.1 y0=2.1 radius=0.00375 n_col=131 n_row=54
backfill1
set id_start=@idc3 y0=2.12 radius=0.0075 n_col=109 n_row=16
backfill1
set id_start=@idc3 y0=2.14 radius=0.01125 n_col=71 n_row=11
backfill1
set id_start=@idc3 y0=2.17 radius=0.015 n_col=22 n_row=20
backfill1
set id_start=@idc3 y0=2.21 radius=0.01875 n_col=20 n_row=14
backfill1
set id_start=@idc3 y0=2.26 radius=0.0225 n_col=15 n_row=13
backfill1
set id_start=@idc3 y0=2.31 radius=0.02625 n_col=13 n_row=11
backfill1
set id_start=@idc3 y0=2.37 radius=0.03 n_col=11 n_row=10
backfill1
set id_start=@idc3 y0=2.44 radius=0.03375 n_col=29 n_row=3
backfill1
set id_start=@idc3 y0=2.53 radius=0.0375 n_col=10 n_row=7
backfill1
endcommand
end
```

APPENDIX 1: Maximum dry density calculation of sample mass
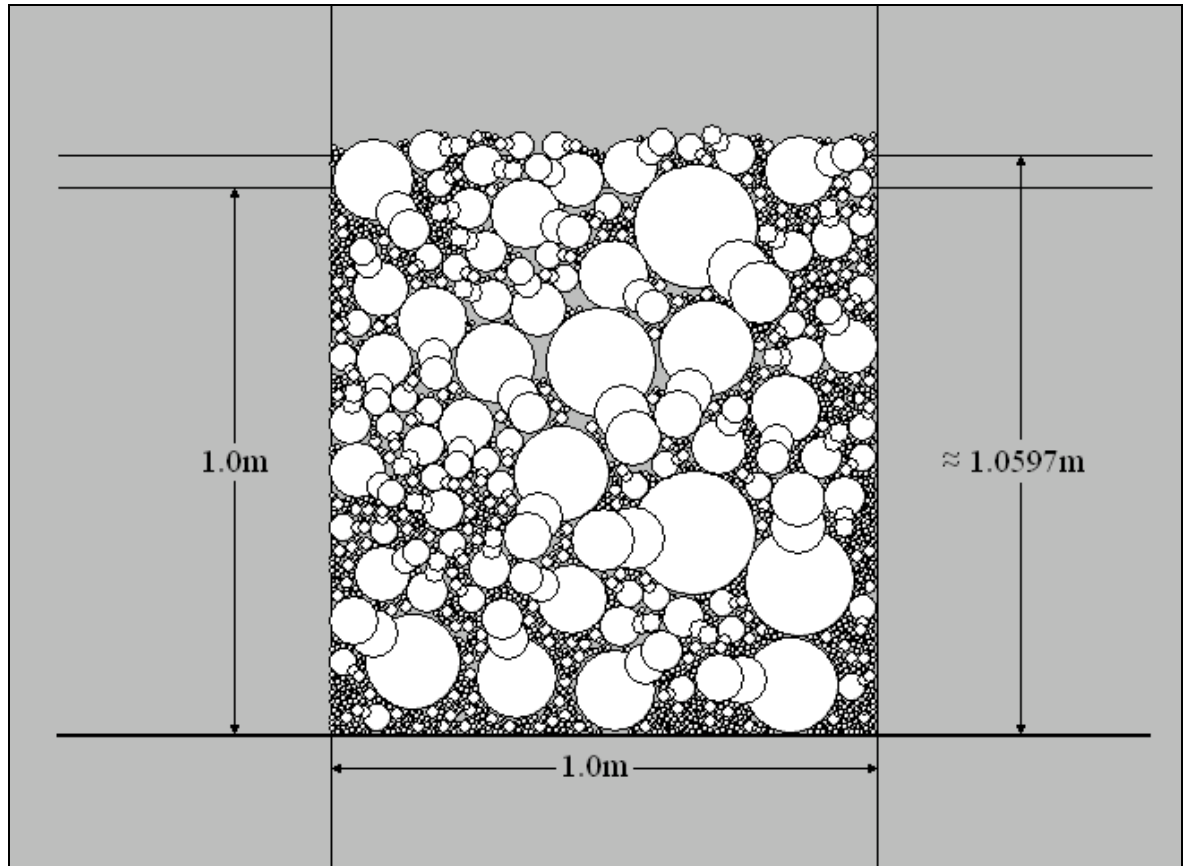
The maximum dry density for the 'Ni' particles sample is therefore;

Total Mass = 3034.65 kg

Total Volume = 1.0597 m^3

$$\rho_{dry\ max} = \frac{Total\ mass}{Total\ volume} = \frac{3034.65kg}{1.0597m^3}$$

$$\rho_{dry\ max} = 2863.6862kg/m^3 \approx 2863.69kg/m^3$$

$$\therefore \rho_{95\%} = \rho_{design} = 0.95 \times 2863.69 = \underline{\underline{2720.3055kg/m^3}} \approx 2720.5kg/m^3$$

For the designated 2m by 4m sample space (i.e. 8 m^3);
Total mass $= 2720.5 \times 8 = \underline{\underline{21764kg}}$

As the well-graded sample will have 10 particle sizes, each particle size will have to have a mass of 2176.4 kg.

APPENDIX 2:

Number of particles for the 2 m by 4 m sample

APPENDIX 2: Number of particles for the 2 m by 4 m sample

There are 10 particle sizes and each size will have a mass of 2176.4 kg each in order to be 95% of maximum dry density. With the knowledge of a single Ni particle's mass for the respective sizes, the number of particles for each size can be estimated.

Particle Size, R(m)	mass per particle (Kg)	volume per particle (m³)	Particle count (2176.4/ mass per particle)	Refined particle count	Mass (kg)
0.005	0.30632	9.81748E-05	7104.986356	7104	2176.097859
0.0125	1.914373	0.000628319	1136.873482	1136	2174.727829
0.025	7.657492	0.002532909	284.2183706	284	2174.727829
0.0375	17.22732	0.005694137	126.3342249	126	2170.642202
0.05	30.63201	0.010131636	71.04986356	71	2174.872579
0.0625	47.85933	0.015845408	45.4749393	45	2153.669725
0.075	68.91947	0.022815817	31.57888478	32	2205.423038
0.0875	93.80224	0.031042862	23.20200391	23	2157.45158
0.1	122.528	0.04054618	17.76246589	18	2205.504587
0.1125	155.0459	0.051306135	14.03713609	14	2170.642202
			Total	**8853**	**21763.75943**
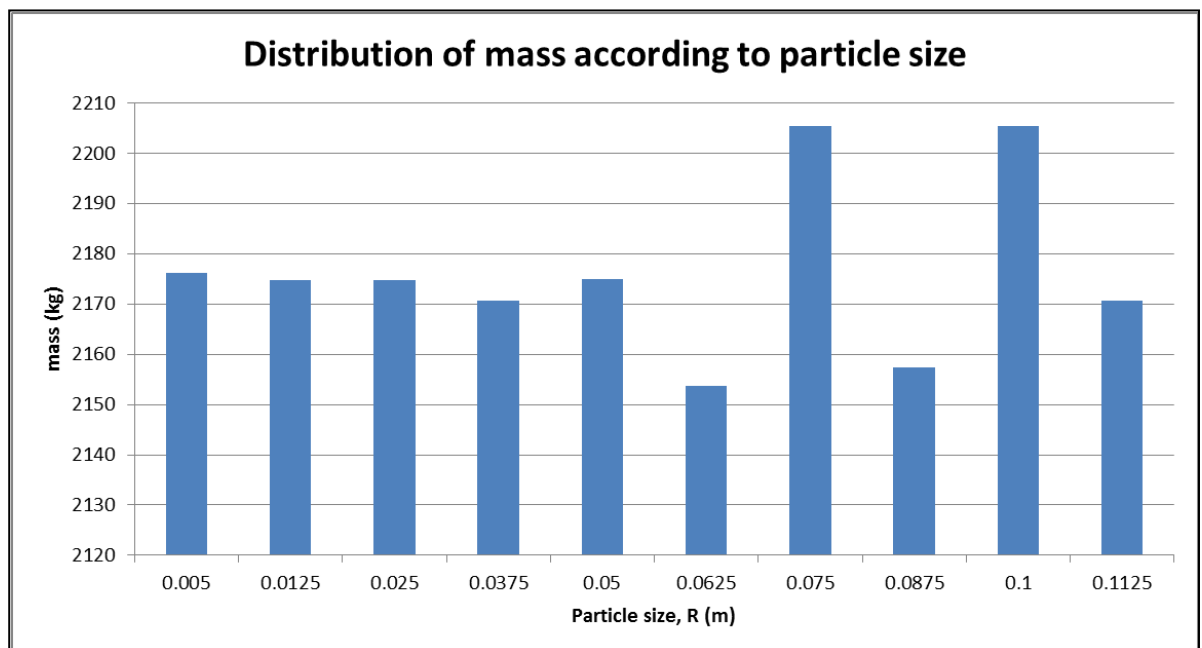
The number of particles was adjusted such that the mass per particle size group was evenly distributed. The mass was more difficult to fine tune for larger particles. Bearing in mind that the target mass for each size class was 2176.4 kg. The total mass was approximately 21763.76 kg. For a sample volume that is approximately 8 m^3, this implies a sample density of about 21763.76/ 8 $\approx$ 2720.5 kg/m^3, which was the design density.

APPENDIX 3:

Generating particles for the four shaped samples

APPENDIX 3: Generating particles for the four shaped samples

```
;Ni particle w/ shape factor 1.5 and form 2/3
def backfill1
 ang=angularity
 xc3=x0
 yc3=y0
 br=radius
 sr=ang*br
 idc3=id_start
 yinc=1.2 ;2.1*radius
 loop row (1,n_row)
  loop col (1,n_col)
  idc2=idc3-1
  idc1=idc2-1
  xc2=xc3+br
  xc1=xc2+sr
    command
     ball id=idc1 x=xc1 y=yc3 rad=sr
     ball id=idc2 x=xc2 y=yc3 rad=sr
     ball id=idc3 x=xc3 y=yc3 rad=br
     clump id=idc1 perm range id=idc1,idc3
    endcommand
    idc3=idc3+3
    xc3=xc3+3.1*br
  endloop
  yc3=yc3+yinc
  xc3=x0
 endloop
end
;generating 8853 Ni particles
def gg10
command
set id_start=3 x0=0.1 y0=2.1 radius=0.005 n_col=96 n_row=74
backfill1
set id_start=@idc3 y0=2.12 radius=0.0125 n_col=71 n_row=16
backfill1
set id_start=@idc3 y0=2.14 radius=0.025 n_col=71 n_row=4
backfill1
set id_start=@idc3 y0=2.17 radius=0.0375 n_col=14 n_row=9
backfill1
set id_start=@idc3 y0=2.21 radius=0.05 n_col=71 n_row=1
backfill1
set id_start=@idc3 y0=2.26 radius=0.0625 n_col=9 n_row=5
backfill1
set id_start=@idc3 y0=2.31 radius=0.075 n_col=16 n_row=2
backfill1
set id_start=@idc3 y0=2.37 radius=0.0875 n_col=23 n_row=1
backfill1
set id_start=@idc3 y0=2.44 radius=0.1 n_col=9 n_row=2
backfill1
set id_start=@idc3 y0=2.53 radius=0.1125 n_col=7 n_row=2
backfill1
endcommand
end
prop dens=2600 kn=5e8 ks=5e8 fric=0.5
```

APPENDIX 3: Generating particles for the four shaped samples

```
;generating 8853 Disc particles w/ form 1.0 and angularity 1.0
def gg10
 command
 gen id 1,7104 radius=0.00568 x=0,4 y=1,10
 gen id 7105,8240 radius=0.0142 x=0,4 y=1,10
 gen id 8241,8524 radius=0.0284 x=0,4 y=1,10
 gen id 8525,8650 radius=0.0426 x=0,4 y=1,10
 gen id 8651,8721 radius=0.0568 x=0,4 y=1,10
 gen id 8722,8766 radius=0.071 x=0,4 y=1,10
 gen id 8767,8798 radius=0.08521 x=0,4 y=1,10
 gen id 8799,8821 radius=0.0994 x=0,4 y=1,10
 gen id 8822,8839 radius=0.1136 x=0,4 y=1,10
 gen id 8840,8853 radius=0.1278 x=0,4 y=1,10
 end command
end
prop dens=3021 kn=5e8 ks=5e8 fric=0.5
```

APPENDIX 3: Generating particles for the four shaped samples

```
;Elliptic particle w/ shape factor 1.5, form 2/3 and angularity 1.0
def backfill3
 xc2=x0
 yc2=y0
 br=radius
 idc2=id_start
 yinc=1.2 ;2.1*radius
 loop row (1,n_row)
  loop col (1,n_col)
  idc1=idc2-1
  xc1=xc2+br
   command
    ball id=idc2 x=xc2 y=yc2 rad=br
    ball id=idc1 x=xc1 y=yc2 rad=br
    clump id=idc2 perm range id=idc1,idc2
   endcommand
   idc2=idc2+2
   xc2=xc2+3.1*br
  endloop
  yc2=yc2+yinc
  xc2=x0
 endloop
end
;generating 8853 Elliptic particles
def gg10
 command
 set id_start=2 x0=0.1 y0=2.1 radius=0.00448 n_col=96 n_row=74
 backfill3
 set id_start=@idc2 y0=2.12 radius=0.0112 n_col=71 n_row=16
 backfill3
 set id_start=@idc2 y0=2.14 radius=0.02239 n_col=71 n_row=4
 backfill3
 set id_start=@idc2 y0=2.17 radius=0.03358 n_col=14 n_row=9
 backfill3
 set id_start=@idc2 y0=2.21 radius=0.04478 n_col=71 n_row=1
 backfill3
 set id_start=@idc2 y0=2.26 radius=0.05598 n_col=9 n_row=5
 backfill3
 set id_start=@idc2 y0=2.31 radius=0.06717 n_col=16 n_row=2
 backfill3
 set id_start=@idc2 y0=2.37 radius=0.07836 n_col=23 n_row=1
 backfill3
 set id_start=@idc2 y0=2.44 radius=0.08956 n_col=9 n_row=2
 backfill3
 set id_start=@idc2 y0=2.53 radius=0.10075 n_col=7 n_row=2
 backfill3
 endcommand
end
prop dens=2431 kn=5e8 ks=5e8 fric=0.5
```

APPENDIX 3: Generating particles for the four shaped samples

```
;Triangular particle w/ form 0.8 and angularity 0.5
def backfill4
 ang=angularity
 xc4=x0
 yc4=y0
 br=radius
 sr=ang*br
 idc4=id_start
 yinc=3.1*radius
 loop row (1,n_row)
  loop col (1,n_col)
  idc3=idc4-1
  idc2=idc3-1
  idc1=idc2-1
  xc3=xc4+0.866*br
  yc3=yc4-(br-sr)
  xc2=xc4
  yc2=yc4+br
  xc1=xc4-0.866*br
  yc1=yc3
   command
    ball id=idc1 x=xc1 y=yc1 rad=sr
    ball id=idc2 x=xc2 y=yc2 rad=sr
    ball id=idc3 x=xc3 y=yc3 rad=sr
    ball id=idc4 x=xc4 y=yc4 rad=br
    clump id=idc1 perm range id=idc1,idc4
   endcommand
   idc4=idc4+4
   xc4=xc4+2.1*br
  endloop
  yc4=yc4+yinc
  xc4=x0
 endloop
end
;generating 8853 triangular particles
def gg10
command
set id_start=4 x0=0.1 y0=2.1 radius=0.00477 n_col=96 n_row=74
backfill4
set id_start=@idc4 y0=2.12 radius=0.01194 n_col=71 n_row=16
backfill4
set id_start=@idc4 y0=2.14 radius=0.02387 n_col=71 n_row=4
backfill4
set id_start=@idc4 y0=2.17 radius=0.03581 n_col=14 n_row=9
backfill4
set id_start=@idc4 y0=2.21 radius=0.04775 n_col=71 n_row=1
backfill4
set id_start=@idc4 y0=2.26 radius=0.05969 n_col=9 n_row=5
backfill4
set id_start=@idc4 y0=2.31 radius=0.07163 n_col=16 n_row=2
backfill4
set id_start=@idc4 y0=2.37 radius=0.08356 n_col=23 n_row=1
backfill4
set id_start=@idc4 y0=2.44 radius=0.0955 n_col=9 n_row=2
backfill4
set id_start=@idc4 y0=2.53 radius=0.10743 n_col=7 n_row=2
backfill4
endcommand
end
prop dens=2444 kn=5e8 ks=5e8 fric=0.5
```

APPENDIX 4:

PFC2D codes

APPENDIX 4: PFC2D codes

Creating the four walls to make up the sample space:

```
SET disk on ; treat balls as disks of unit thickness
; ----------------------------------------------------
;Step 1
def make_walls  ; create walls with overhang of extend
  extend = 1.0
  _x0 = -extend*width
  _y0 = 0.0
  _x1 = width*(1.0 + extend)
  _y1 = 0.0
  command
    wall id=1 kn=w_stiff nodes (_x0,_y0) (_x1,_y1)
  end_command
  _x0 = width
  _y0 = -extend*height
  _x1 = width
  _y1 = height*(1.0 + extend)
  command
    wall id=2 kn=w_stiff nodes (_x0,_y0) (_x1,_y1)
  end_command
  _x0 = width*(1.0 + extend)
  _y0 = height
  _x1 = -extend*width
  _y1 = height
  command
    wall id=3 kn=w_stiff nodes (_x0,_y0) (_x1,_y1)
  end_command
  _x0 = 0.0
  _y0 = height*(1.0 + extend)
  _x1 = 0.0
  _y1 = -extend*height
  command
    wall id=4 kn=w_stiff nodes (_x0,_y0) (_x1,_y1)
  end_command
end
; ----------------------------------------------------
def assemble  ; assemble sample
  s_stiff = 0.0 ; initial stiffnesses
  n_stiff = 5e8
  w_stiff = 5e8
  tot_vol = height * width * 1.0
  make_walls
end
; ----------------------------------------------------
def cws  ; change lateral wall stiffnesses
  command
    wall id 2 kn=w_stiff
    wall id 4 kn=w_stiff
  end_command
end
; ----------------------------------------------------
macro zero 'ini xvel 0 yvel 0 spin 0'

plot create assembly
plot add ball white wall black
plot show
set height=2.0 width=4.0
```

APPENDIX 4: PFC2D codes

Programming the upper wall to maintain an 80 kPa stress:

```
;step 2
def get_gain  ; determine servo gain parameters for x and y
  alpha = 0.5 ; relaxation factor
  count = 0
  avg_stiff = 0
  cp    = contact_head  ; find avg. number of contacts on x-walls
  if x_servo=1 then
  loop while cp # null
    if c_ball1(cp) = wadd2
      count = count + 1
      avg_stiff = avg_stiff + c_kn(cp)
    end_if
    if c_ball1(cp) = wadd4
      count = count + 1
      avg_stiff = avg_stiff + c_kn(cp)
    end_if
    if c_ball2(cp) = wadd2
      count = count + 1
      avg_stiff = avg_stiff + c_kn(cp)
    end_if
    if c_ball2(cp) = wadd4
      count = count + 1
      avg_stiff = avg_stiff + c_kn(cp)
    end_if
    cp = c_next(cp)
  end_loop
  nxcount = count / 2.0
  avg_stiff = avg_stiff / count
  gx = alpha * (height * 1.0) / (avg_stiff * nxcount * tdel)
  count = 0
  avg_stiff = 0
  endif
  cp = contact_head       ; find avg. number of contacts on y-walls
  if y_servo=1 then
  loop while cp # null
    if c_ball1(cp) = wadd1
      count = count + 1
      avg_stiff = avg_stiff + c_kn(cp)
    end_if
    if c_ball1(cp) = wadd3
      count = count + 1
      avg_stiff = avg_stiff + c_kn(cp)
    end_if
    if c_ball2(cp) = wadd1
      count = count + 1
      avg_stiff = avg_stiff + c_kn(cp)
    end_if
    if c_ball2(cp) = wadd3
      count = count + 1
      avg_stiff = avg_stiff + c_kn(cp)
    end_if
    cp = c_next(cp)
  end_loop
  nycount = count / 2.0
  avg_stiff = avg_stiff / count
  gy = alpha * (width * 1.0)/ (avg_stiff * nycount * tdel)
  endif
end
```

APPENDIX 4: PFC2D codes

Programming the upper wall to maintain an 80 kPa stress:

```
def get_ss ; determine average stress and strain at walls
  xdif  = w_x(wadd2) - w_x(wadd4)
  ydif  = w_y(wadd3) - w_y(wadd1)
  new_xwidth = width  + xdif
  new_height = height + ydif
  wsxx  = 0.5 * (w_xfob(wadd4) - w_xfob(wadd2)) / (new_height * 1.0)
  wsyy  = 0.5 * (w_yfob(wadd1) - w_yfob(wadd3)) / (new_xwidth * 1.0)
  wexx  = 2.0 * xdif / (width  + new_xwidth)
  weyy  = 2.0 * ydif / (height + new_height)
  wevol = wexx + weyy
end
; ----------------------------------------------------
def servo
  while_stepping
  get_ss                   ; compute stresses & strains
  if x_servo = 1
   udx = gx * (wsxx - sxxreq)
   w_xvel(wadd4) = 0
   w_xvel(wadd2) = -udx
  end_if
  if y_servo = 1           ; switch stress servo on or off
    udy = gy * (wsyy - syyreq)
    w_yvel(wadd1) = 0
    w_yvel(wadd3) = -udy
  end_if
end
; ----------------------------------------------------
def iterate
  loop while 1 # 0
    get_gain
    if abs((wsxx - sxxreq)/sxxreq) < sig_tol then
      if abs((wsyy - syyreq)/syyreq) < sig_tol then
        exit
      end_if
    end_if
    command
      cycle 100
    end_command
  end_loop
end
; ----------------------------------------------------
def wall_addr
  wadd1 = find_wall(1)
  wadd2 = find_wall(2)
  wadd3 = find_wall(3)
  wadd4 = find_wall(4)
end
wall_addr
zero
set sxxreq=-8e4 syyreq=-8e4 sig_tol=0.001 x_servo=0 y_servo=1
```

APPENDIX 4: PFC2D codes

Programming the parameters to be monitored and running 100 cyclic strains:

```
;6 parameters monitored
measure id=1 x=2 y=1 radius=3
hist wexx ;(1)horizontal strain, should be 0.001 back and forth
hist wsxx ;(2)horizontal stress
hist weyy ;(3)vertical strain
hist wsyy ;(4)vertical stress, should maintain at 80kPa
hist measure porosity id=1 ;(5)multiply by total volume to get void
volume
hist measure coord id=1 ;(6)coordination number within measure circle
;--------------------------------------------------------------------
def cyclicload
TS=total_step
N=TS/100
;push and adjust in steps of 100 for N times
 loop load(1,N)
   command
    get_gain
    cyc 100
   endcommand
 endloop
end
;--------------------------------------------------------------------
;cycling, 'summer' 100x
def cycload80k
command
hist nstep=200
set dt=1e-5
save starting.sav
;expand---------------------
wall id 2 xvel=0.005
wall id 4 xvel=0
set total_step=80000
cyclicload
save cyc001_0.1%.sav
;compress
wall id 2 xvel=-0.005
wall id 4 xvel=0
cyclicload
save cyc001_compl.sav
;expand-----------------------
wall id 2 xvel=0.005
wall id 4 xvel=0
cyclicload
save cyc002_0.1%.sav
;complress
wall id 2 xvel=-0.005
wall id 4 xvel=0
cyclicload
save cyc002_compl.sav
;---------------------<and so on and so forth, until…>--------------
wall id 2 xvel=0.005
wall id 4 xvel=0
cyclicload
save cyc100_0.1%.sav
;complress
wall id 2 xvel=-0.005
wall id 4 xvel=0
cyclicload
save cyc100_compl.sav
endcommand
end
```

APPENDIX 5:

Rose plots for

particle angles

APPENDIX 5: Rose plots for particle angles

The Ni particles sample.

Angles (degrees)	Number of Ni Particles	
	start	100th cycle
0°-30°	700	717
30°-60°	651	643
60°-90°	595	586
90°-120°	668	635
120°-150°	607	624
150°-180°	714	725
180°-210°	778	780
210°-240°	782	787
240°-270°	837	851
270°-300°	910	905
300-330°	843	825
330°-360°	768	775

Polar histogram of Ni Particle Angles (start)

Polar histogram of Ni Particle Angles (100th)
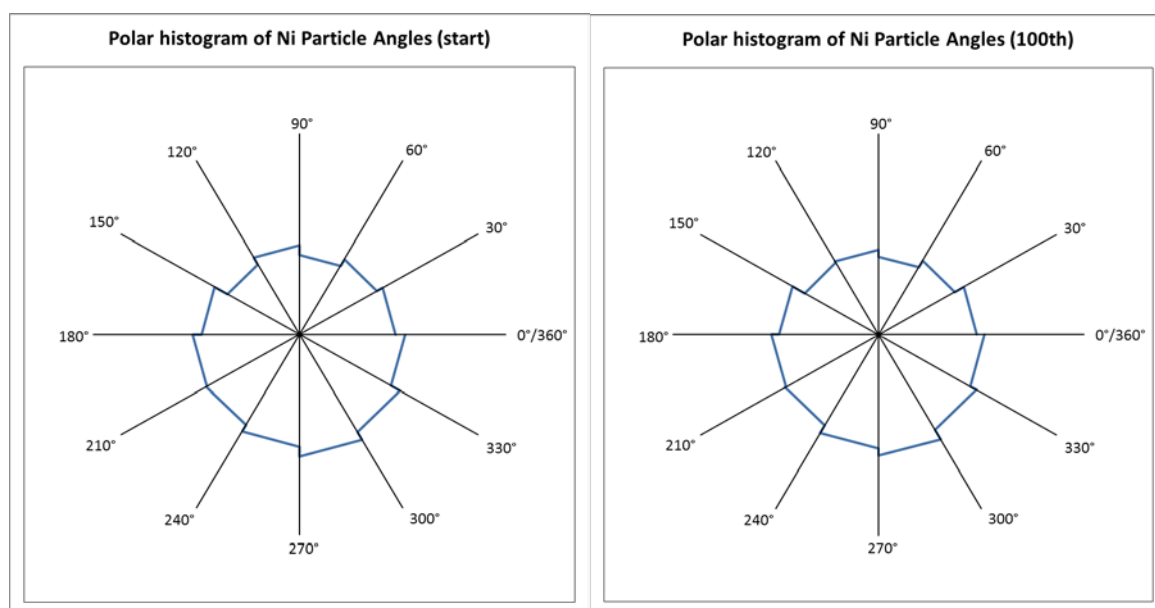
APPENDIX 5: Rose plots for particle angles

The Disc particles sample. Note that circular discs have no orientation.

Orientation (degrees)	Number of Disc Particles	
	start	100th cycle
0°-30°	1203	1193
30°-60°	883	833
60°-90°	693	730
90°-120°	664	632
120°-150°	545	568
150°-180°	522	521
180°-210°	500	523
210°-240°	497	531
240°-270°	597	581
270°-300°	731	705
300-330°	867	913
330°-360°	1151	1123
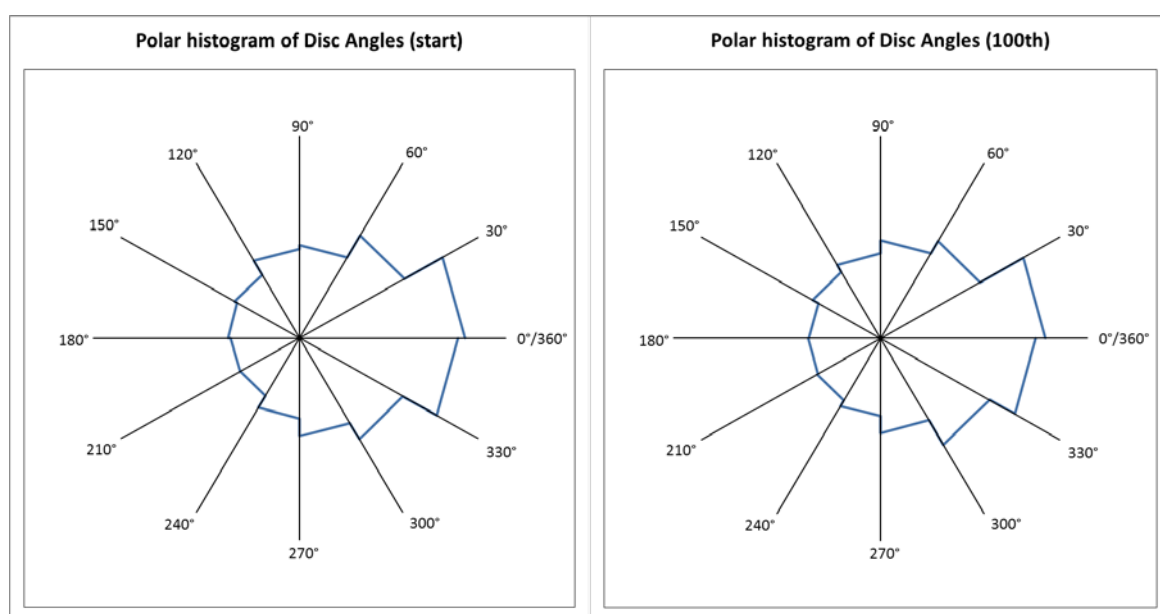
APPENDIX 5: Rose plots for particle angles

The Elliptic particles sample.

Orientation (degrees)	Number of Elliptic Particles	
	start	100th cycle
0°-30°	772	782
30°-60°	827	829
60°-90°	719	685
90°-120°	746	702
120°-150°	650	698
150°-180°	735	700
180°-210°	724	762
210°-240°	748	824
240°-270°	818	721
270°-300°	730	698
300-330°	648	728
330°-360°	736	724
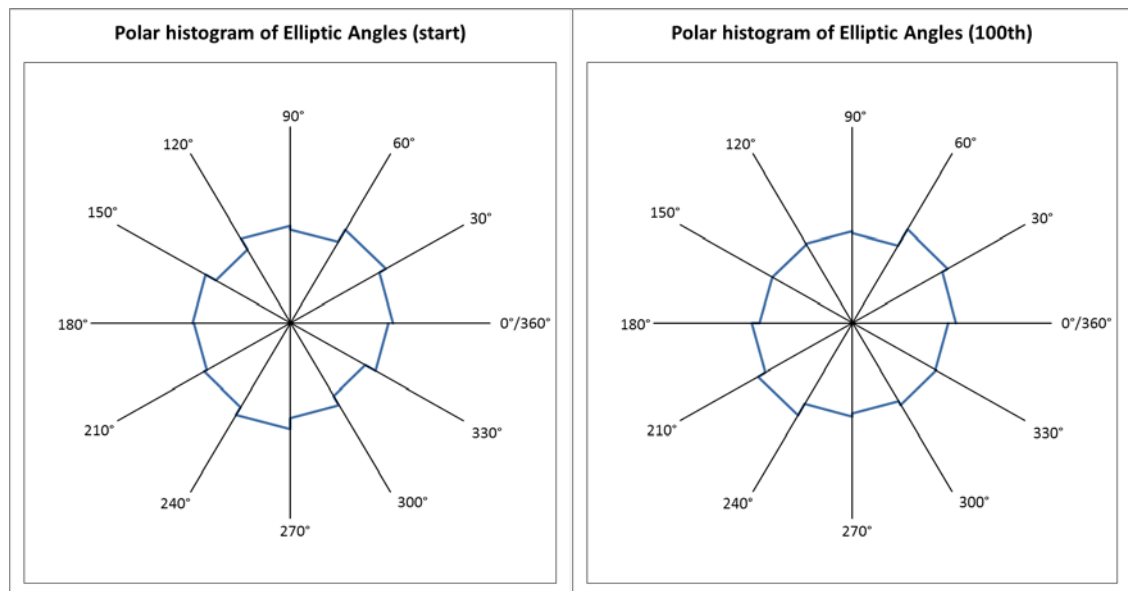
APPENDIX 5: Rose plots for particle angles

The Triangular particles sample.

Orientation (degrees)	Number of Triangular Particles	
	start	100th cycle
0°-30°	737	738
30°-60°	696	697
60°-90°	760	758
90°-120°	739	740
120°-150°	759	752
150°-180°	721	722
180°-210°	730	738
210°-240°	693	692
240°-270°	789	783
270°-300°	712	718
300-330°	780	781
330°-360°	737	734
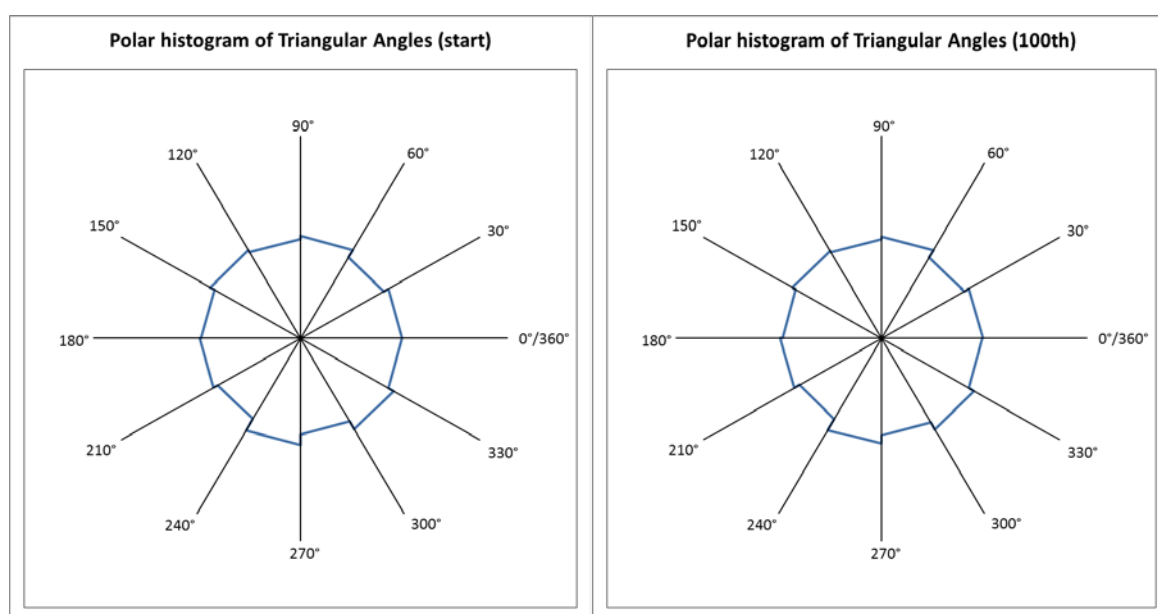
APPENDIX 6:

Histogram of angles turned at the 100th cycle

APPENDIX 6: Histogram of angles turned at the 100th cycle
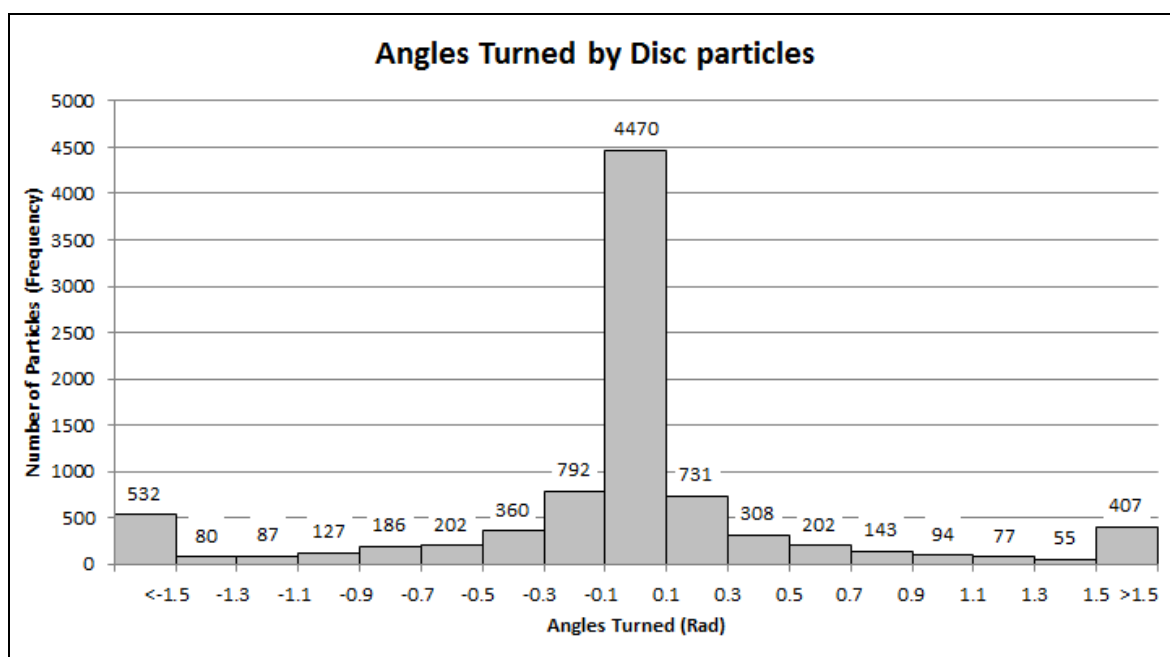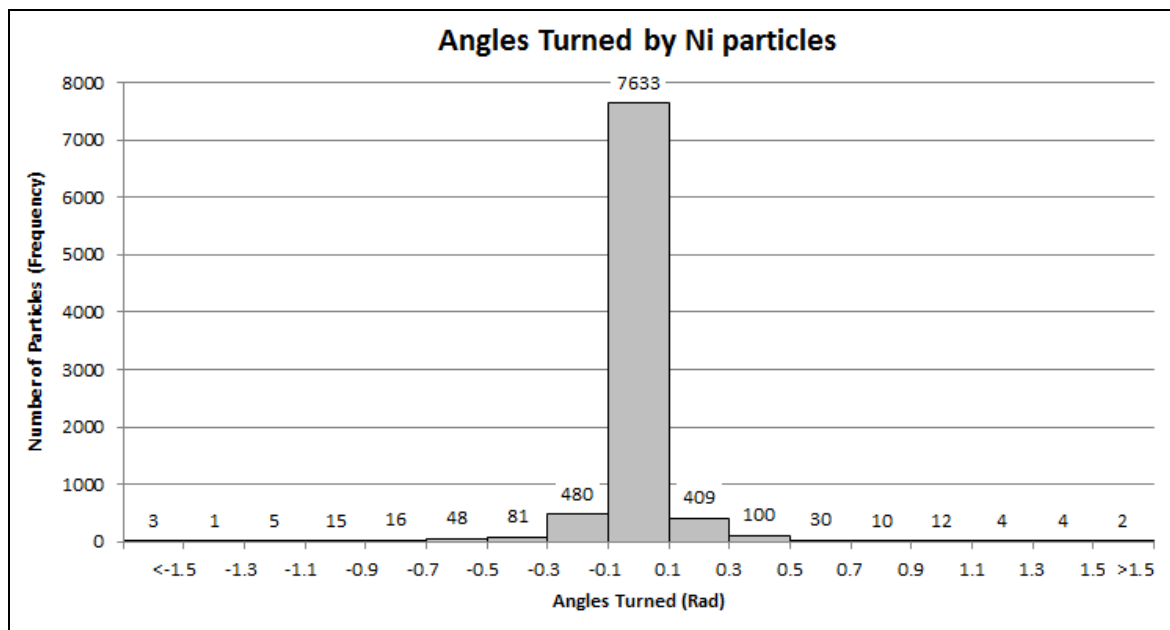
Angles Turned by Ni particles

Number of Particles (Frequency) vs Angles Turned (Rad)

Values: 3, 1, 5, 15, 16, 48, 81, 480, 7633, 409, 100, 30, 10, 12, 4, 4, 2

Angles Turned by Disc particles

Number of Particles (Frequency) vs Angles Turned (Rad)

Values: 532, 80, 87, 127, 186, 202, 360, 792, 4470, 731, 308, 202, 143, 94, 77, 55, 407

APPENDIX 6: Histogram of Angles Turned at the 100th cycle

Angles Turned by Elliptic particles

Angles Turned by Triangular particles
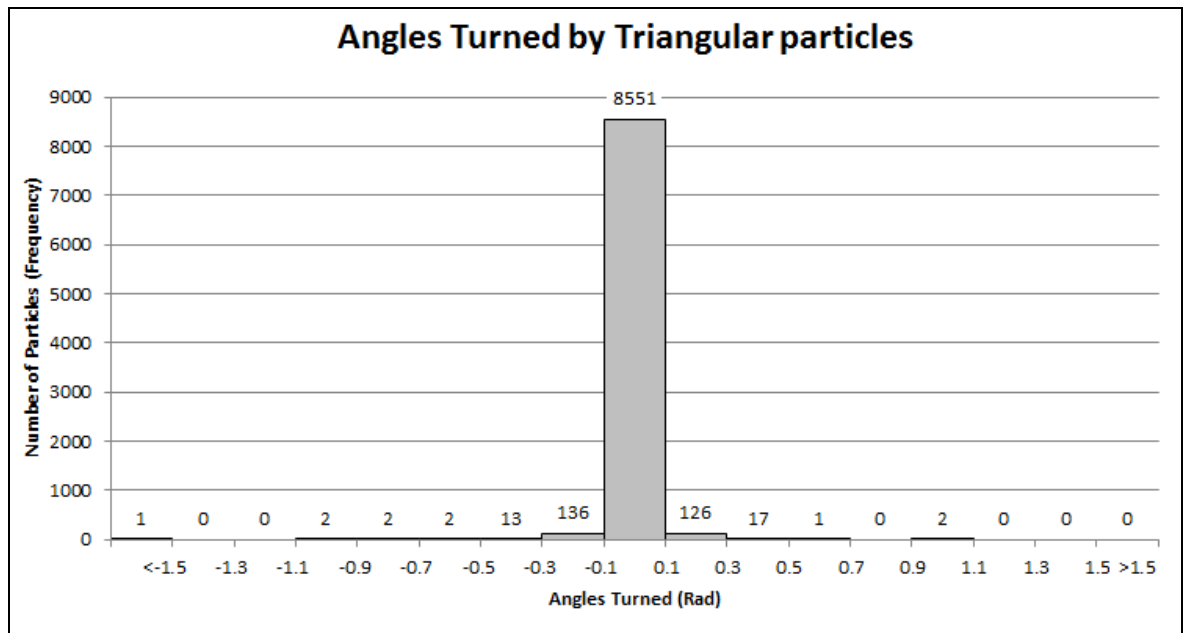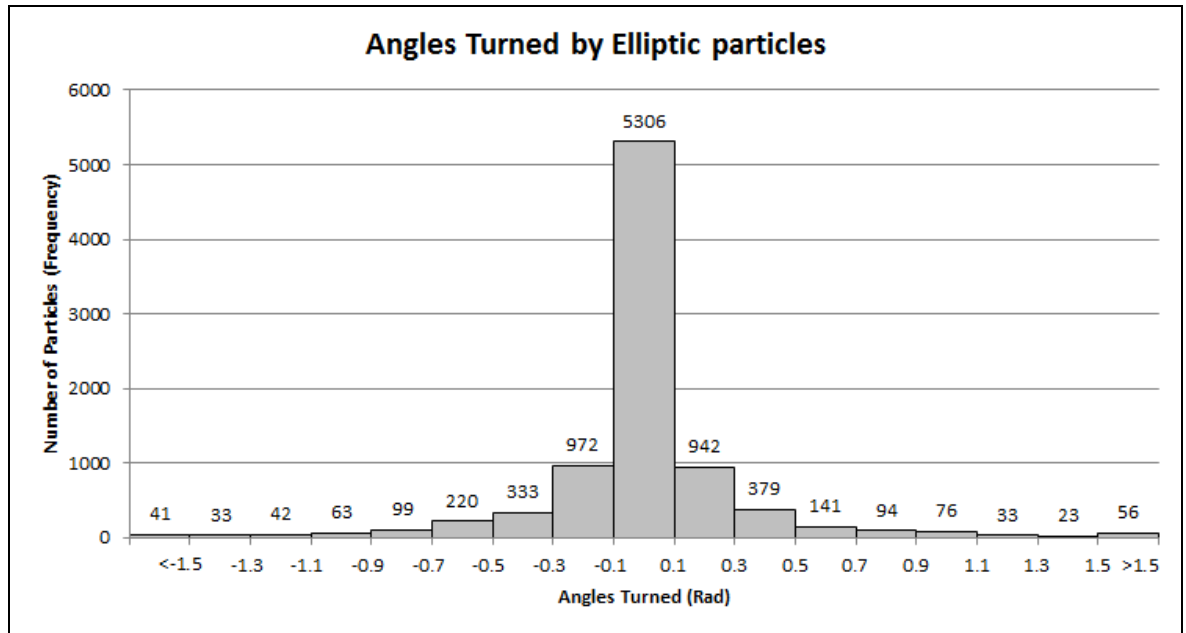
The majority of the angles turned over 100 cyclic strains remain largely within ±0.1 radians (or about ±6°). The total number of particles for all four samples is 8853. As such, the percentage of particles' with angles turned within the ±0.1 radians are 86.2% for the '=Ni particles; 50.5% for the 'Disc' particles; 59.9% for the Elliptic particles and 96.6% for the Triangular particles.
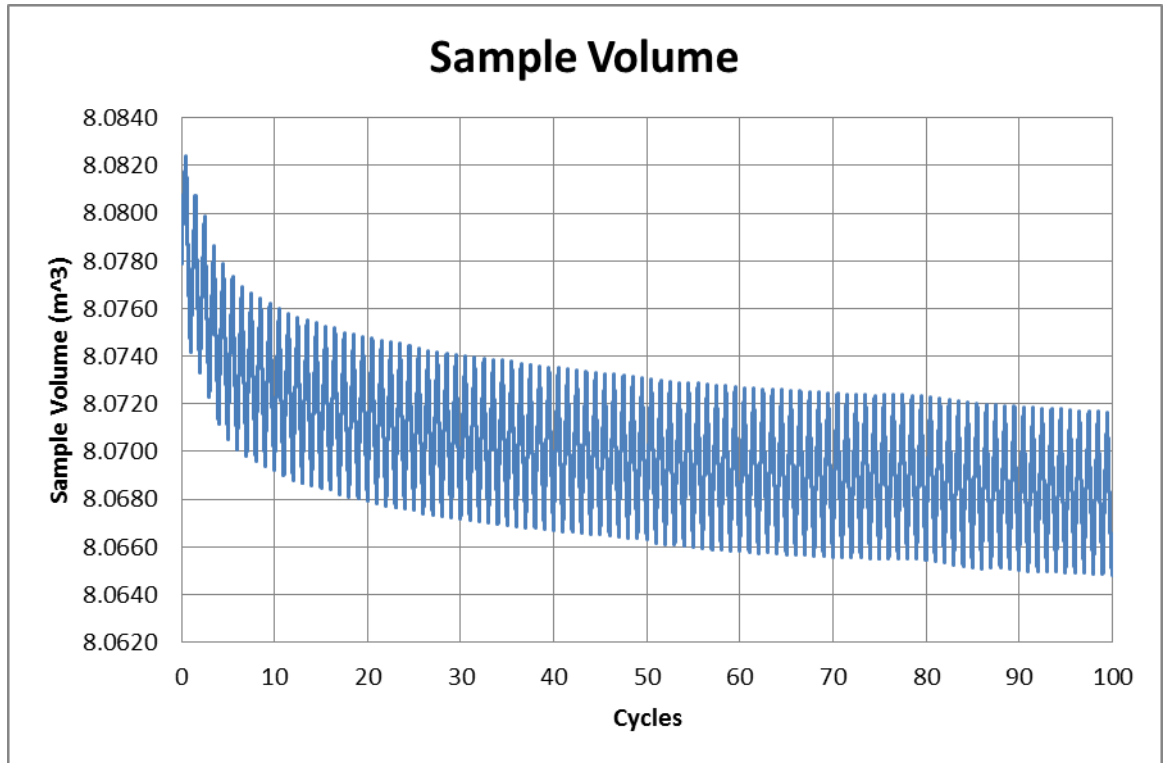
APPENDIX 7:

Results for Ni particles sample
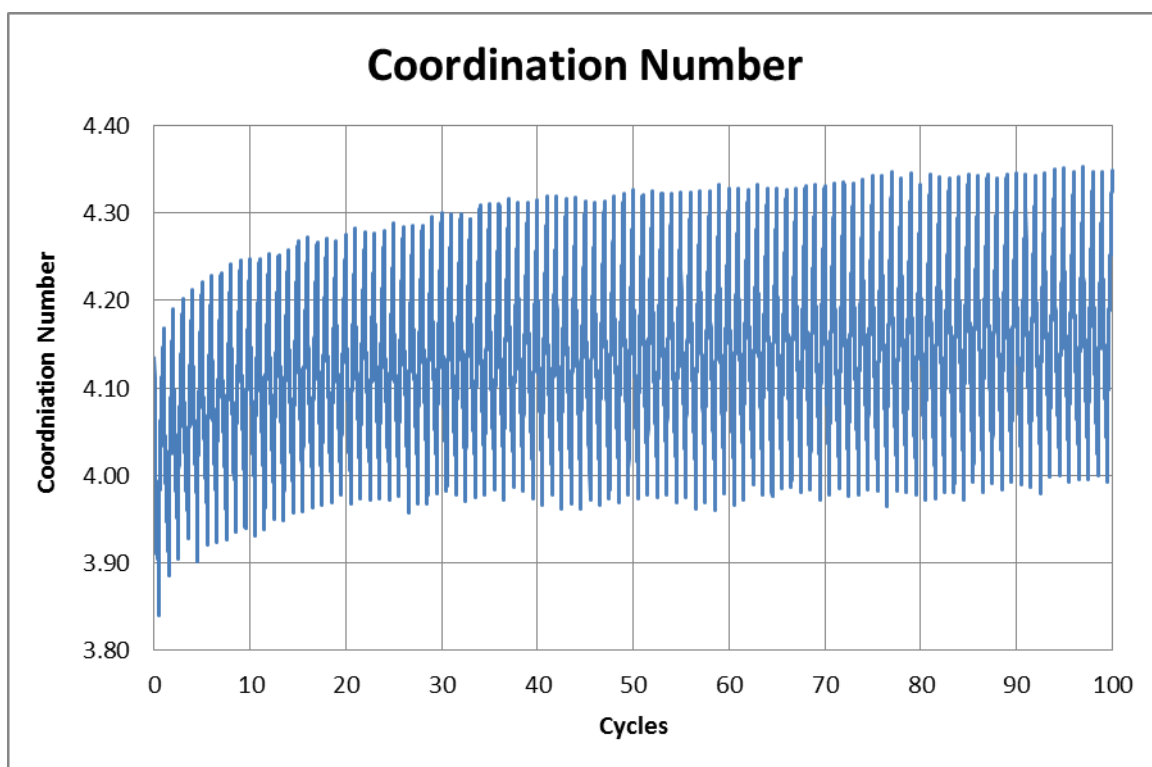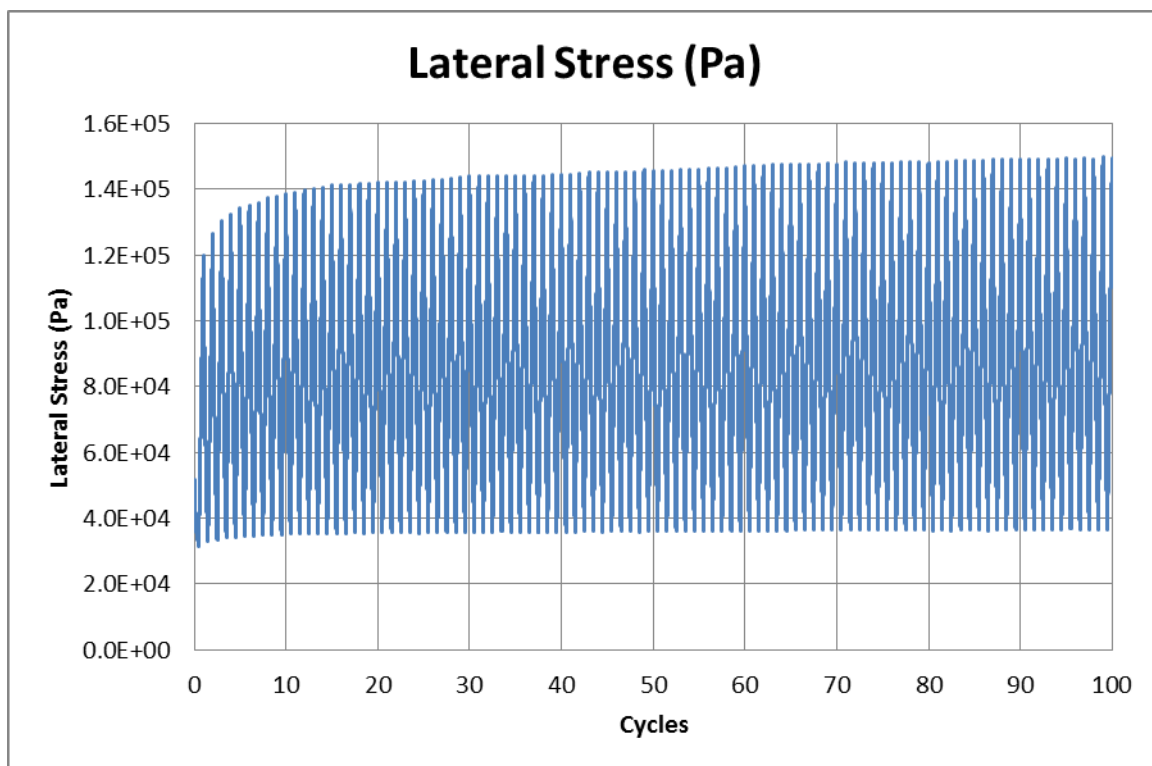
APPENDIX 7: Results for Ni particles sample

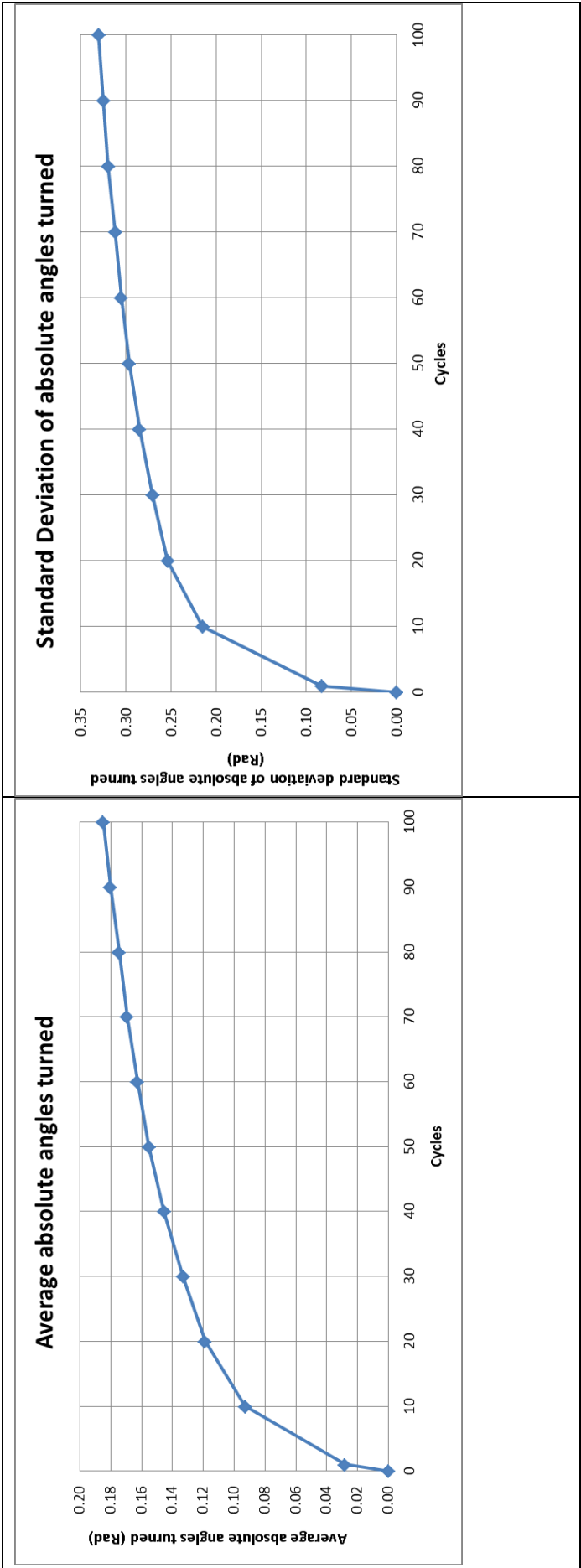# APPENDIX 7: Results for Ni particles sample

Sample Volume

Sample Porosity
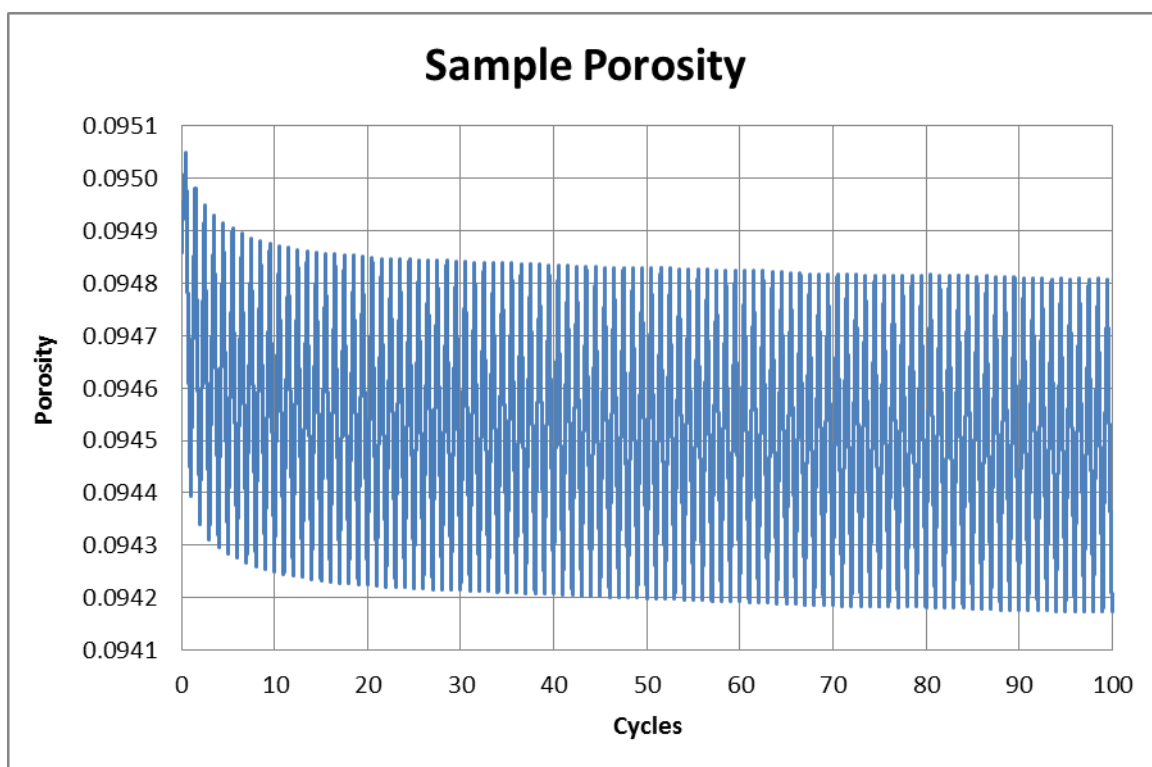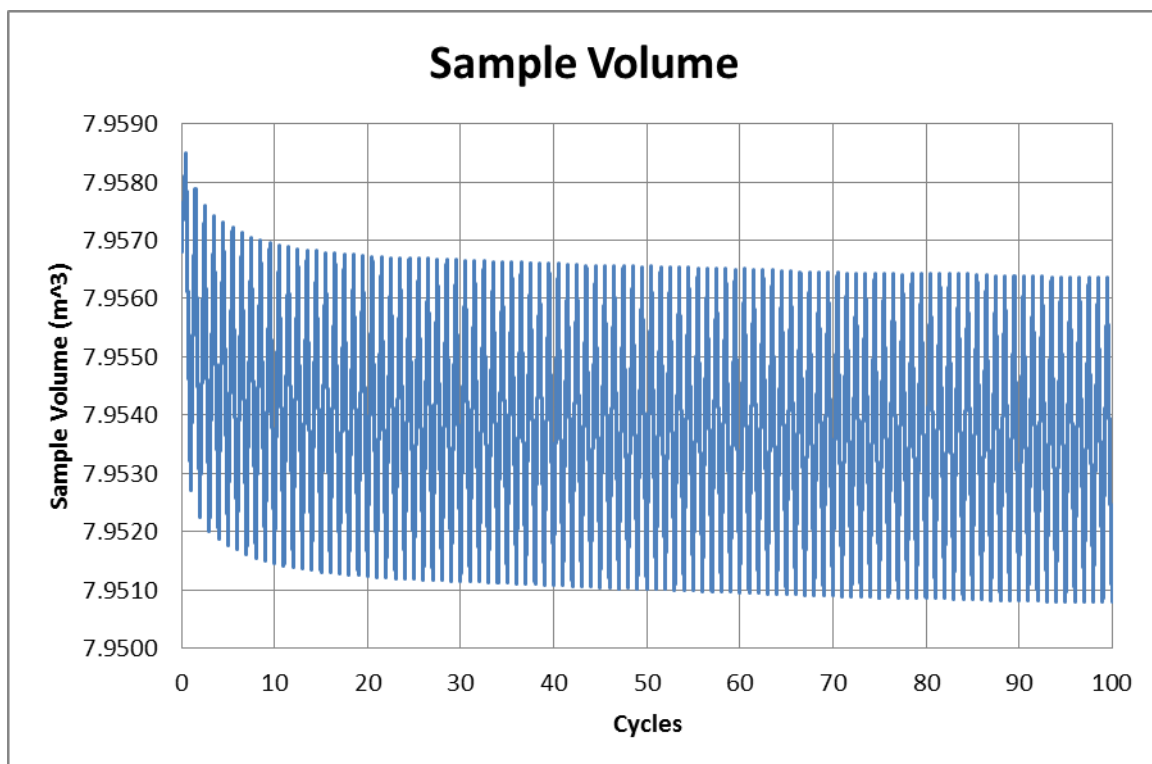
APPENDIX 7: Results for Ni particles sample (Displacement)

cycles	0	1	10	20	30	40	50	60	70	80	90	100
average (m)	0	0.000693	0.000951	0.001013	0.001049	0.001087	0.001124	0.001152	0.001172	0.001196	0.001211	0.001222
standard deviation (m)	0	0.000557	0.00089	0.000956	0.001012	0.001083	0.001208	0.001237	0.001263	0.001332	0.00138	0.001398
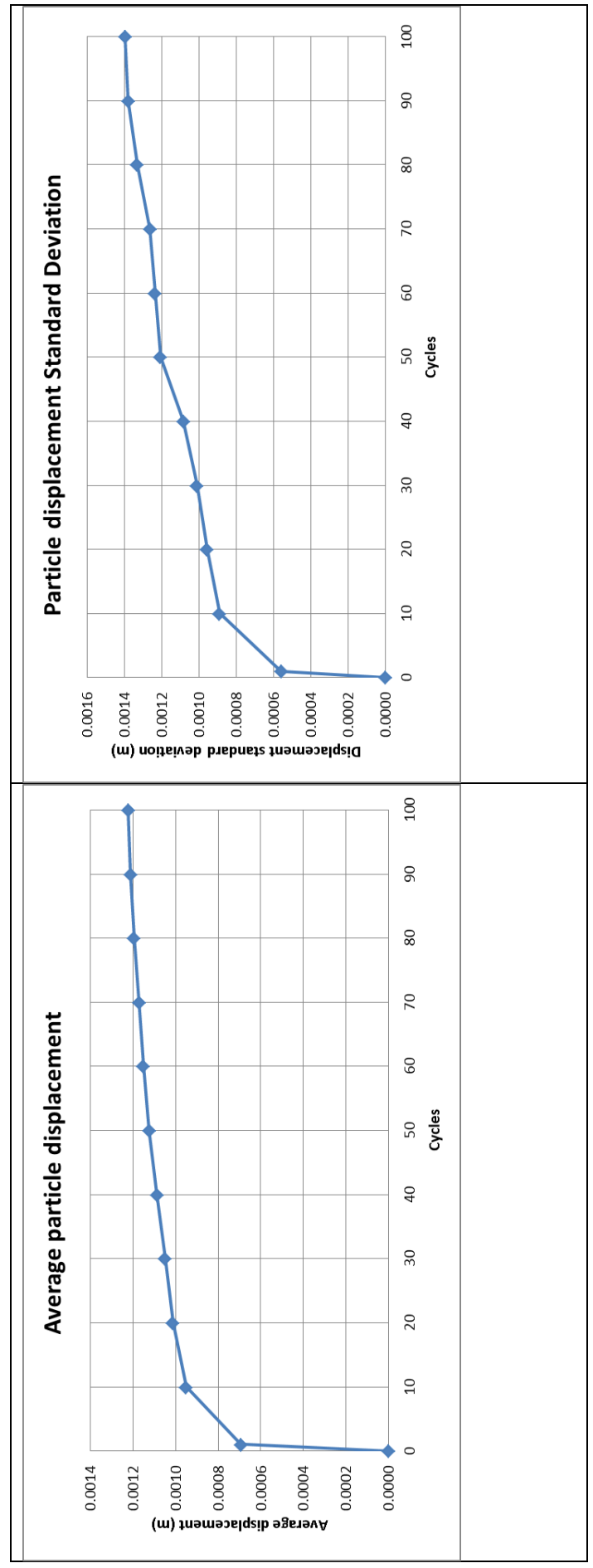
Particle displacement Standard Deviation

Average particle displacement

APPENDIX 7: Results for Ni particles sample (Absolute angles turned)

cycles	0	1	10	20	30	40	50	60	70	80	90	100
average (Rad)	0	0.010386	0.025362	0.031564	0.035883	0.039606	0.042594	0.045029	0.047085	0.048864	0.050656	0.05199
standard deviation (Rad)	0	0.030876	0.071204	0.083468	0.093246	0.101239	0.108741	0.11486	0.118459	0.123698	0.128466	0.131525
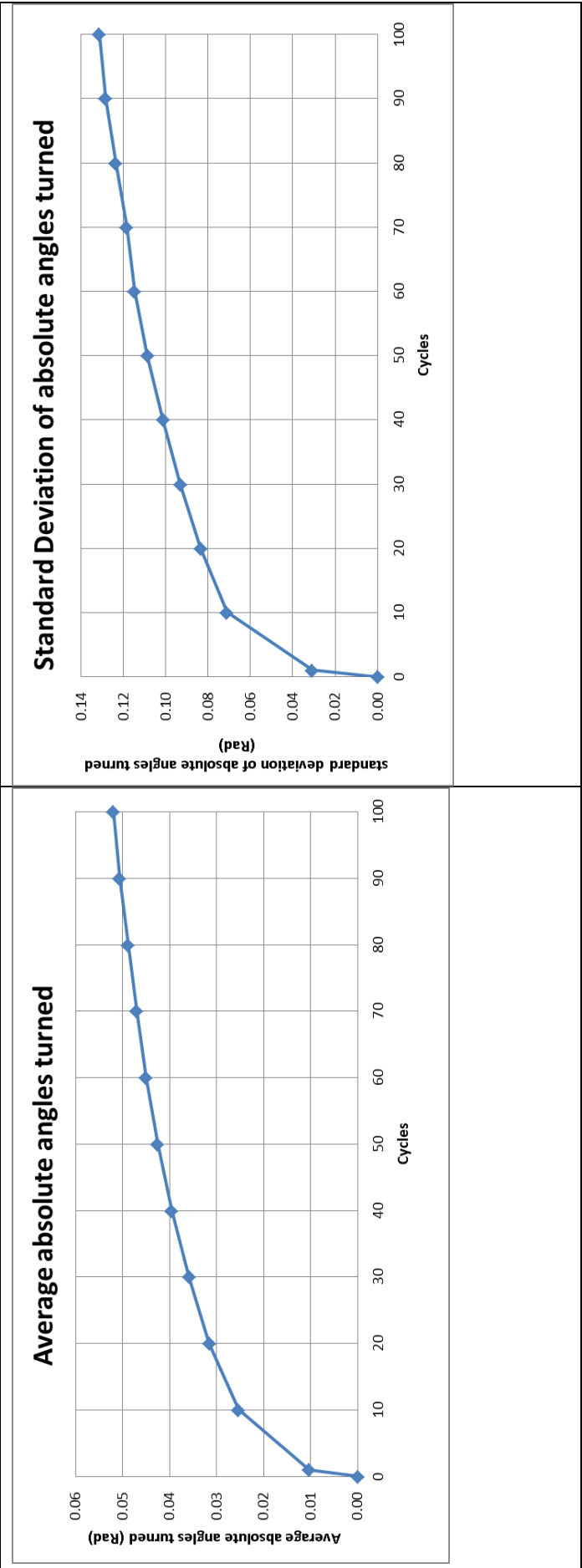
Standard Deviation of absolute angles turned

Average absolute angles turned

APPENDIX 8:

Results for Disc particles sample

APPENDIX 8: Results for Disc particles sample

APPENDIX 8: Results for Disc particles sample

Sample Volume

Sample Porosity
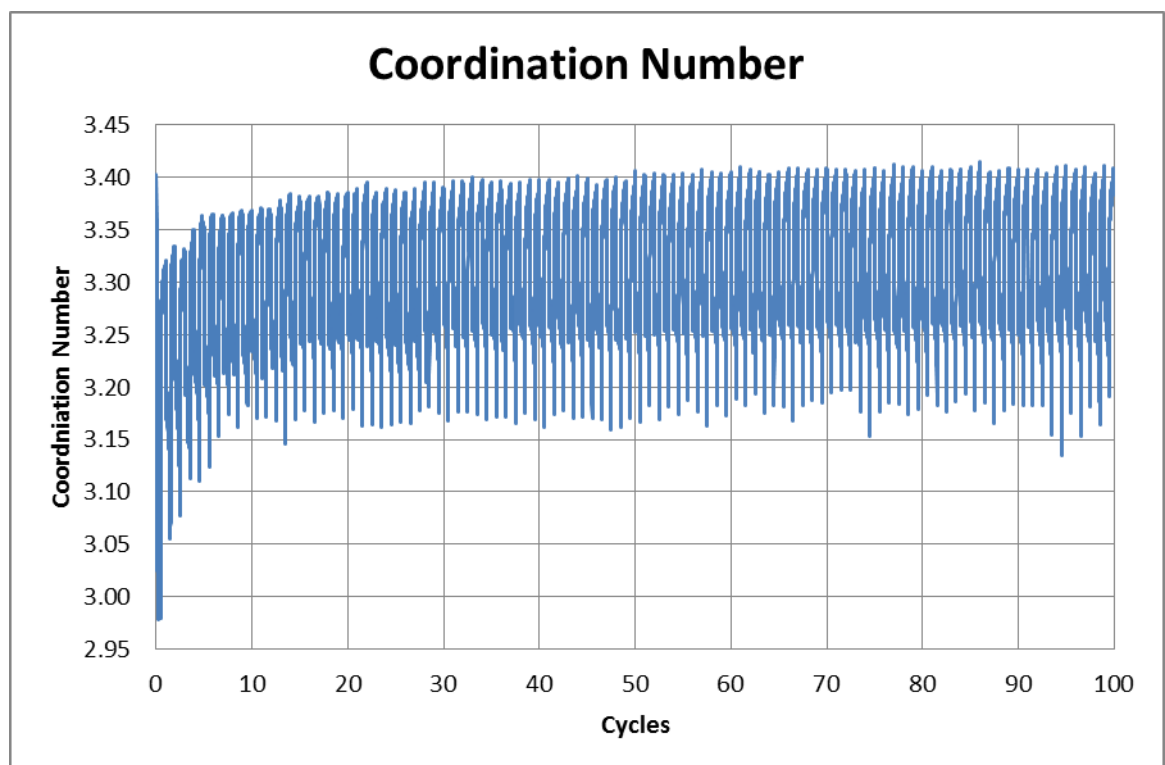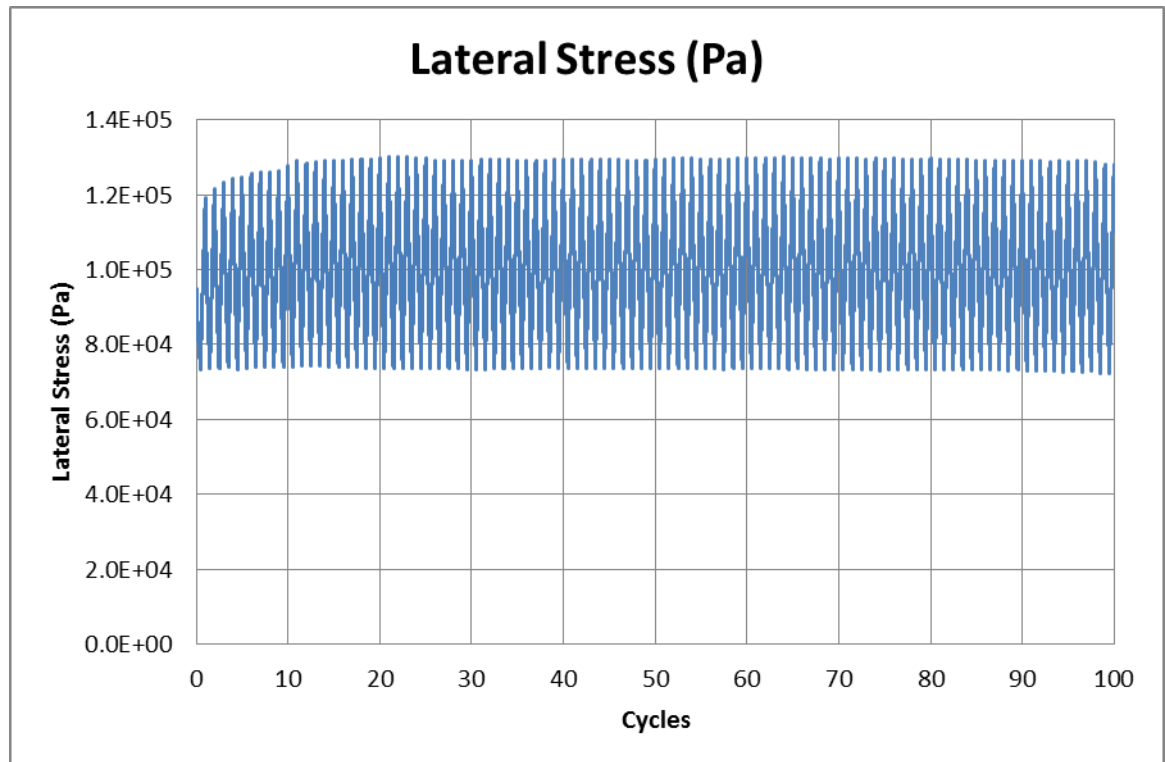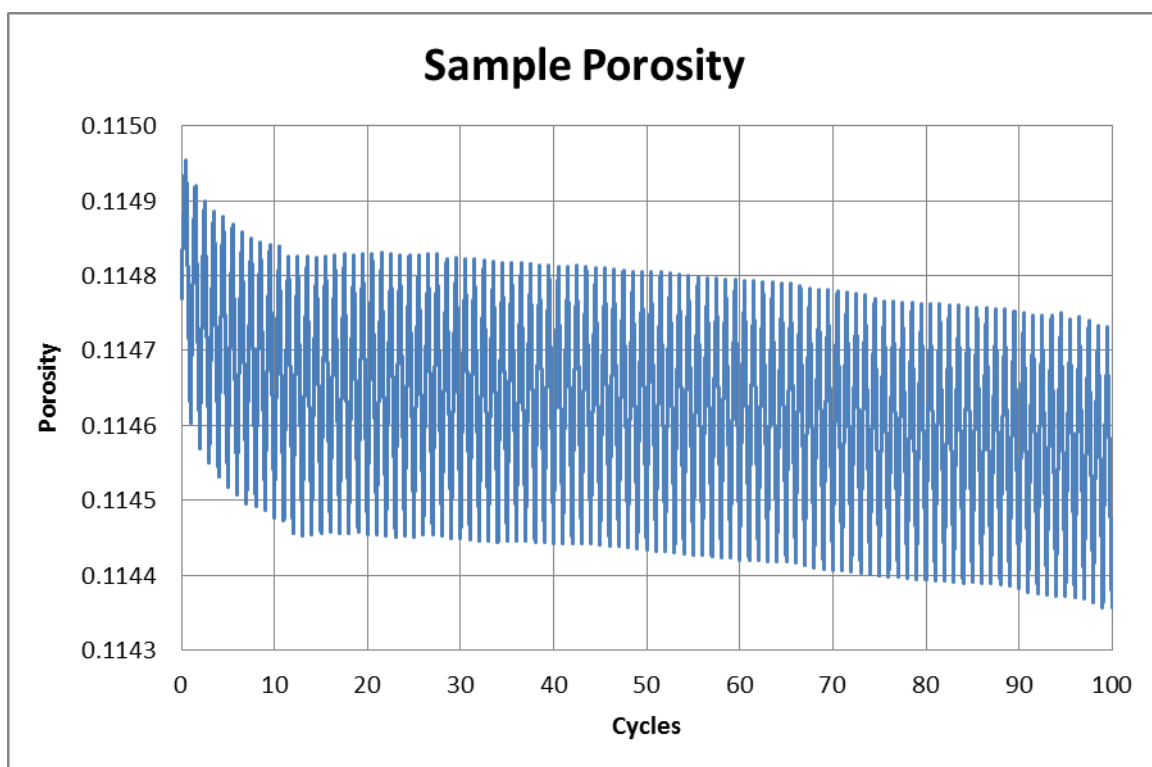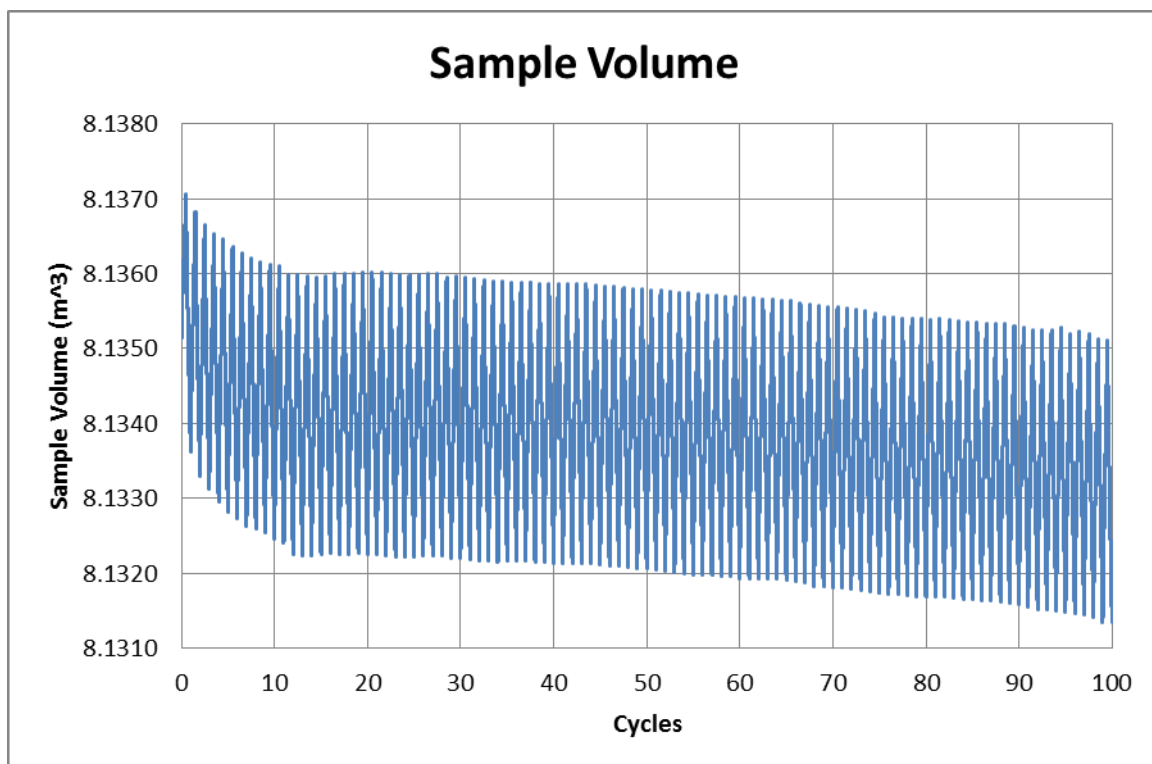
APPENDIX 8: Results for Disc particles sample (Displacement)

cycles	0	1	10	20	30	40	50	60	70	80	90	100
average (m)	0	0.000489	0.001236	0.001522	0.001653	0.001735	0.001827	0.001886	0.001944	0.002001	0.00206	0.002151
standard deviation (m)	0	0.001177	0.003344	0.003938	0.004125	0.004273	0.004363	0.004412	0.004491	0.004599	0.004664	0.00475
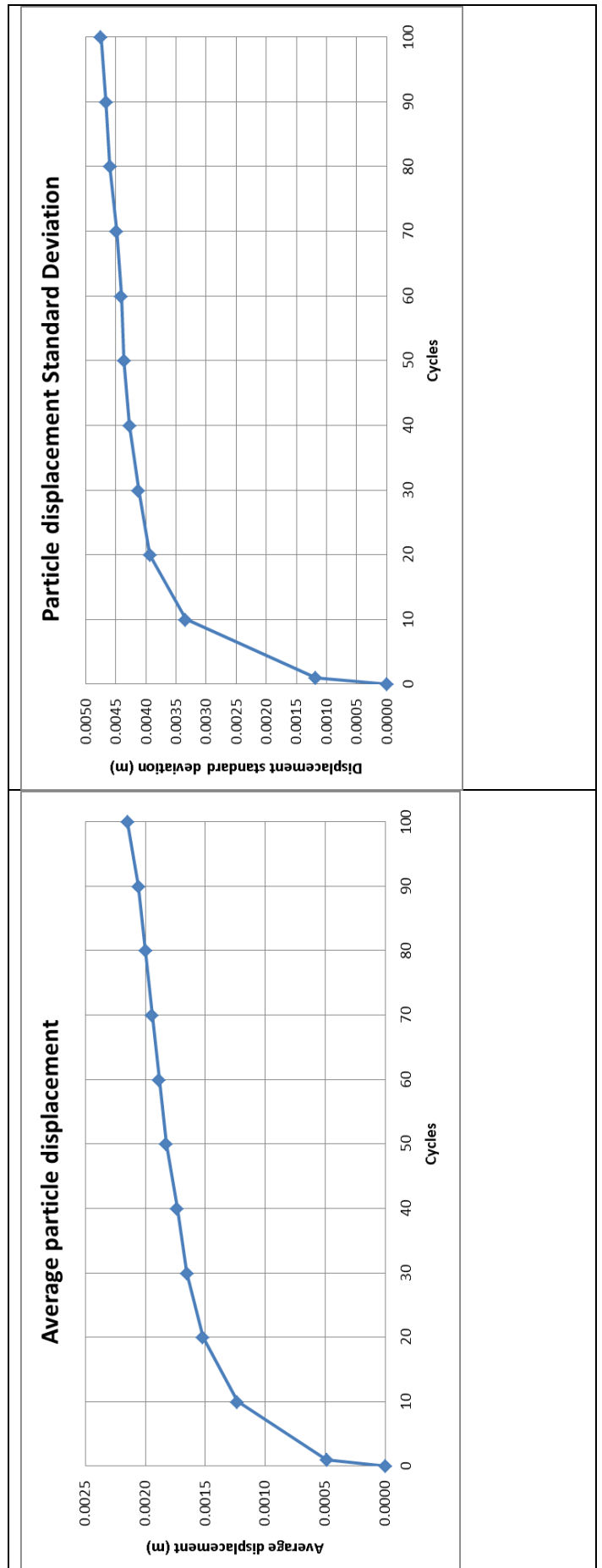
Particle displacement Standard Deviation

Average particle displacement

APPENDIX 8: Results for Disc particles sample (Absolute angles turned)

cycles	0	1	10	20	30	40	50	60	70	80	90	100
average (Rad)	0	0.578986	5.427399	10.49377	15.35101	20.11652	24.84984	29.54018	34.18752	38.7973	43.3631	47.89463
standard deviation (Rad)	0	34.56523	347.7663	693.5924	1037.08	1380.503	1723.304	2065.256	2406.182	2746.435	3085.014	3423.74
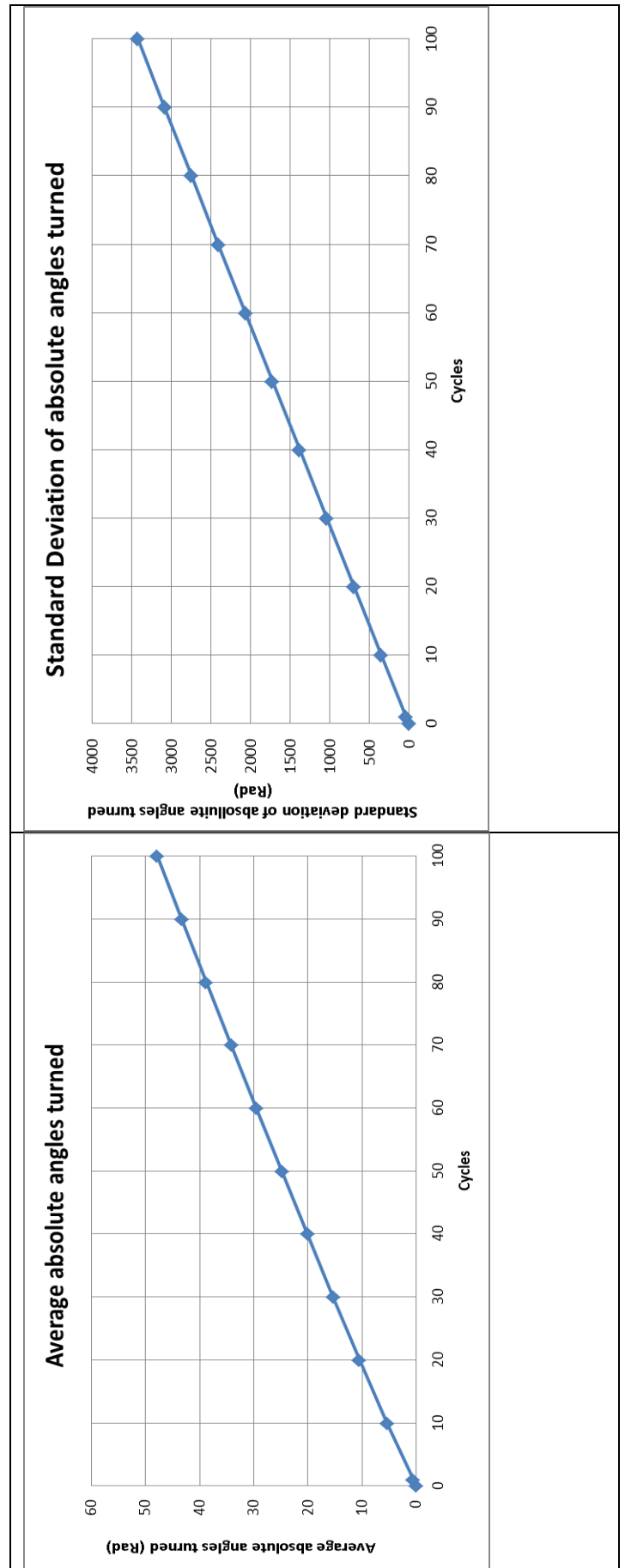
Standard Deviation of absolute angles turned

Average absolute angles turned

APPENDIX 9:

Results for Elliptic particles sample

APPENDIX 9: Results for Elliptic particles sample
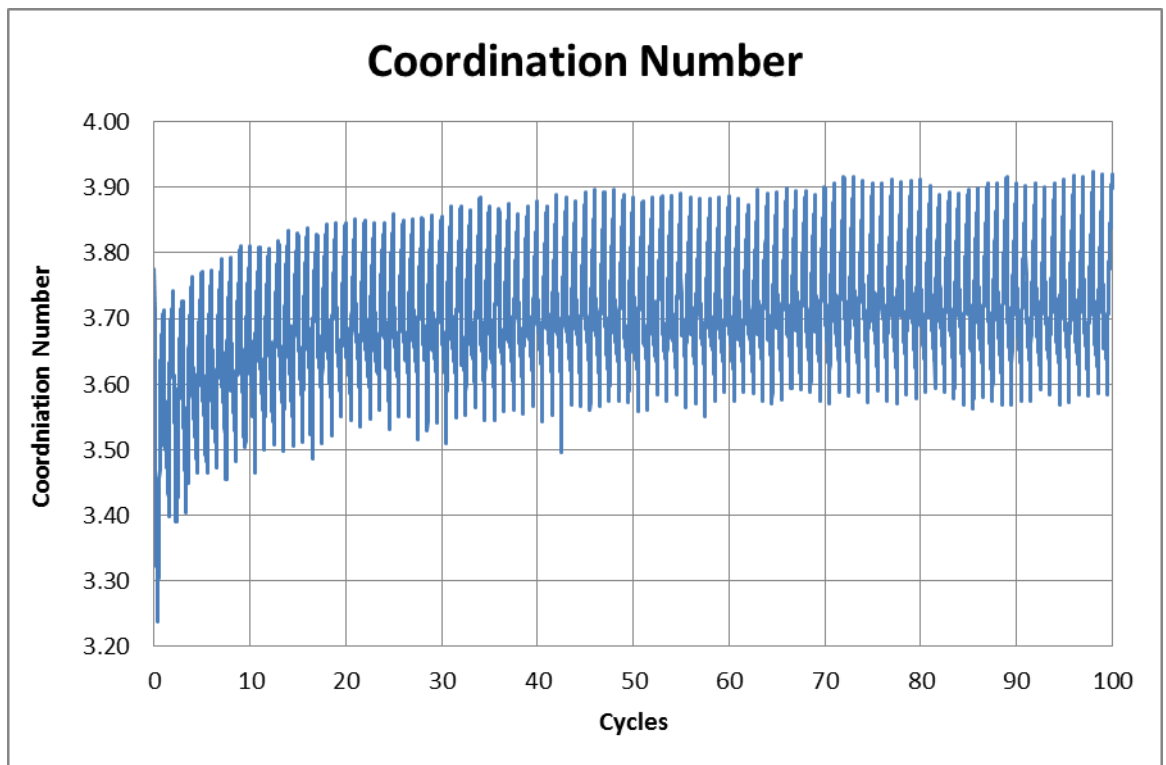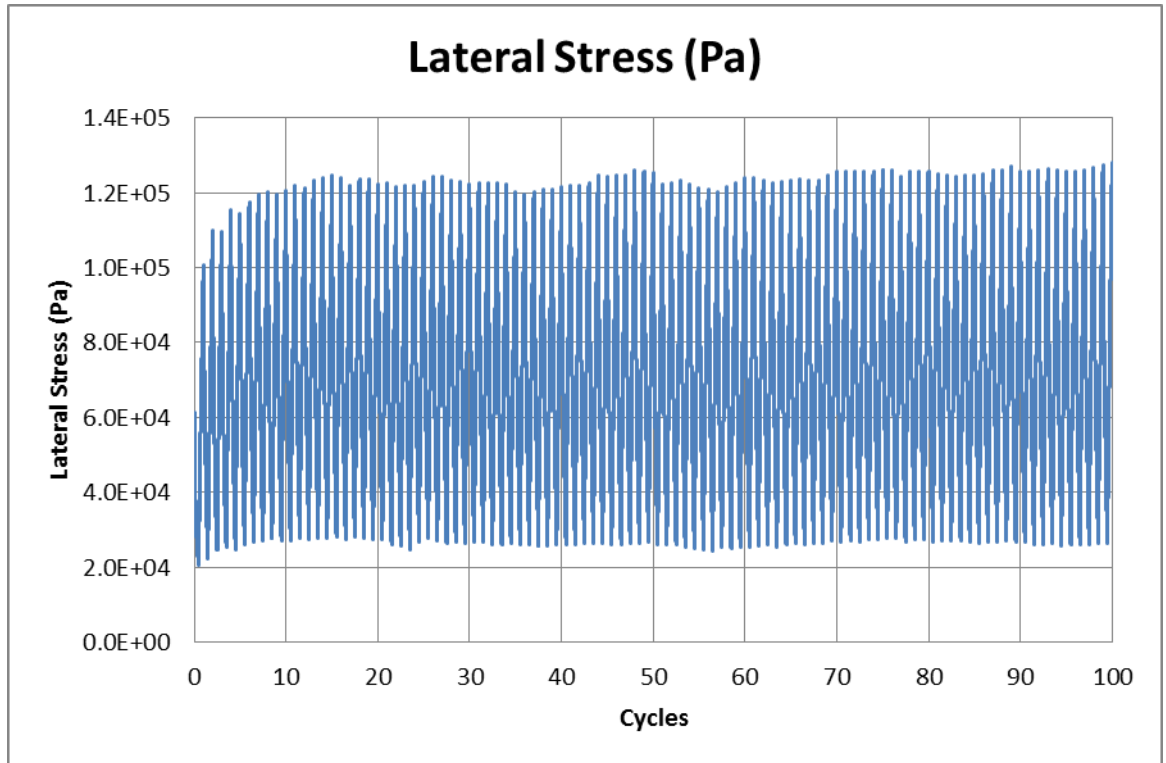
APPENDIX 9: Results for Elliptic particles sample
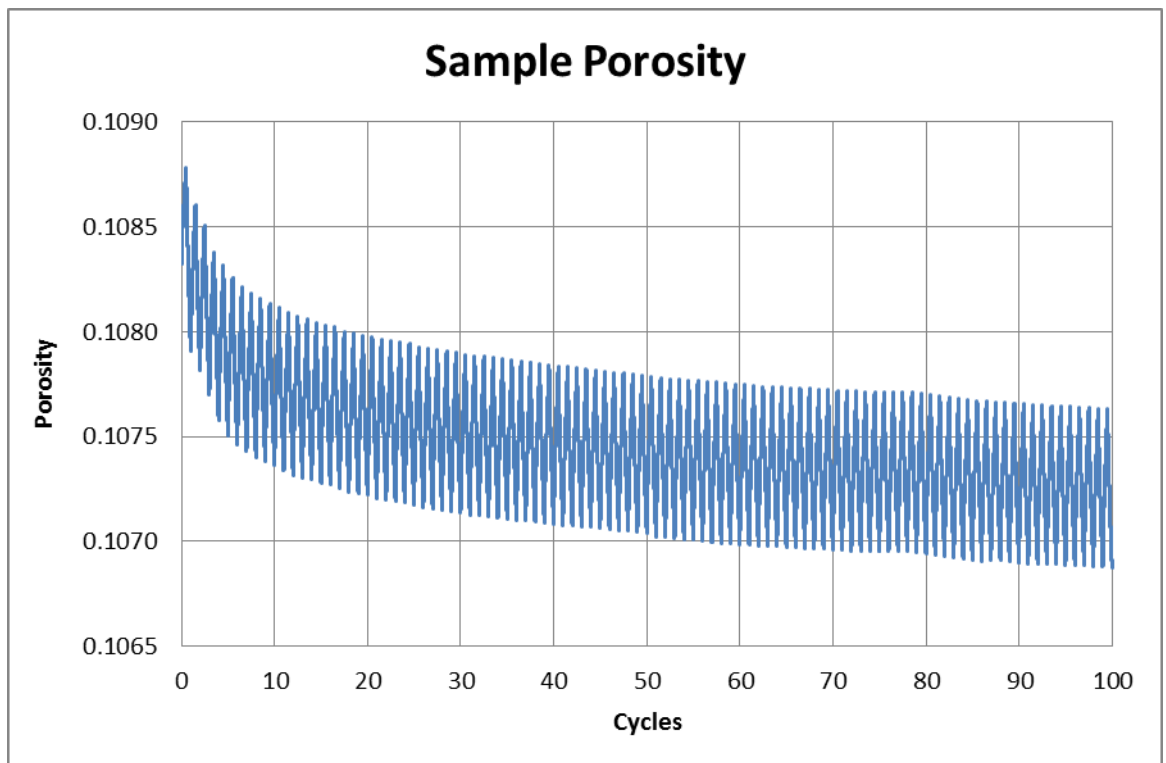
APPENDIX 9: Results for Elliptic particles sample (Displacement)

cycles	0	1	10	20	30	40	50	60	70	80	90	100
average (m)	0	0.000779	0.002243	0.002664	0.002934	0.003134	0.003288	0.003453	0.00356	0.003647	0.003745	0.003814
standard deviation (m)	0	0.000962	0.003284	0.003739	0.003915	0.004112	0.004242	0.004384	0.004497	0.004635	0.004672	0.004706

Particle displacement Standard Deviation

Average particle displacement

154
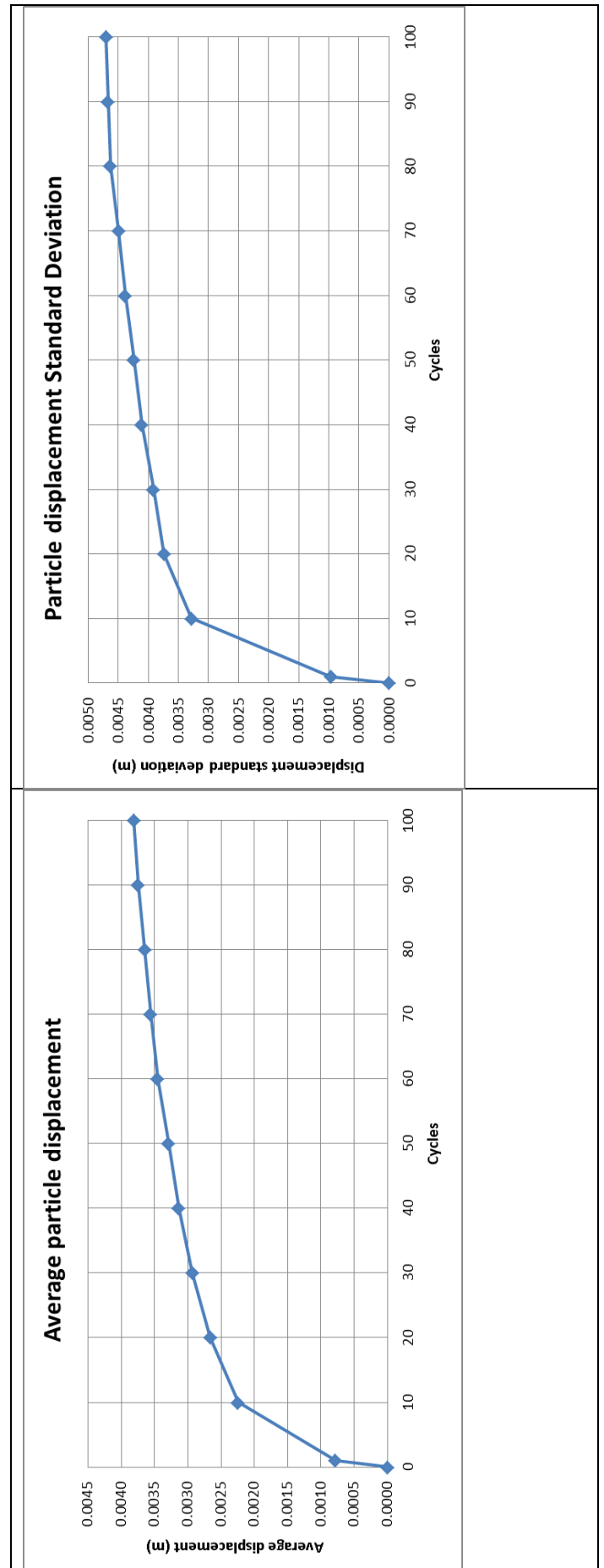
APPENDIX 9: Results for Elliptic sample (Absolute angles turned)

cycles	0	1	10	20	30	40	50	60	70	80	90	100
average (Rad)	0	0.028231	0.092826	0.11902	0.132996	0.145563	0.155323	0.162802	0.169468	0.174591	0.180232	0.184962
standard deviation (Rad)	0	0.083033	0.214762	0.253433	0.270202	0.284882	0.296154	0.305088	0.311797	0.31941	0.324964	0.330067

Standard Deviation of absolute angles turned

Average absolute angles turned

APPENDIX 10:

Results for Triangular

particles sample

APPENDIX 10: Results for Triangular particles sample

APPENDIX 10: Results for Triangular particles sample

Sample Volume

Sample Porosity
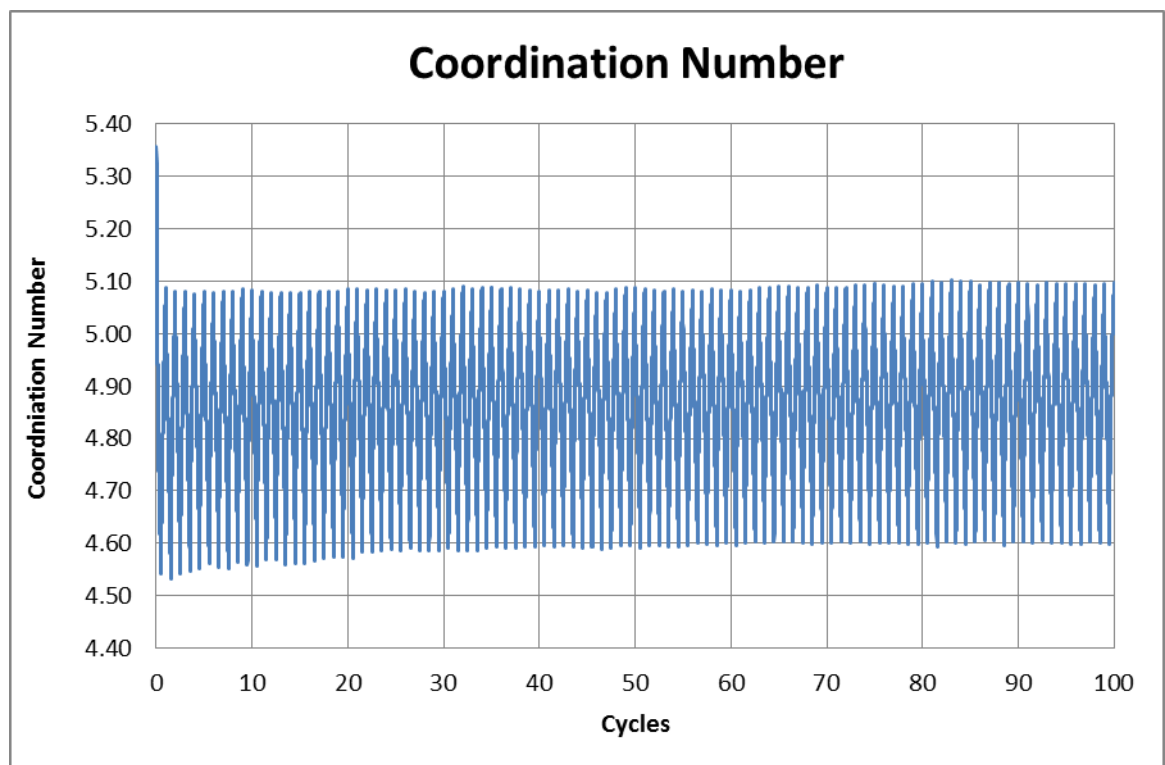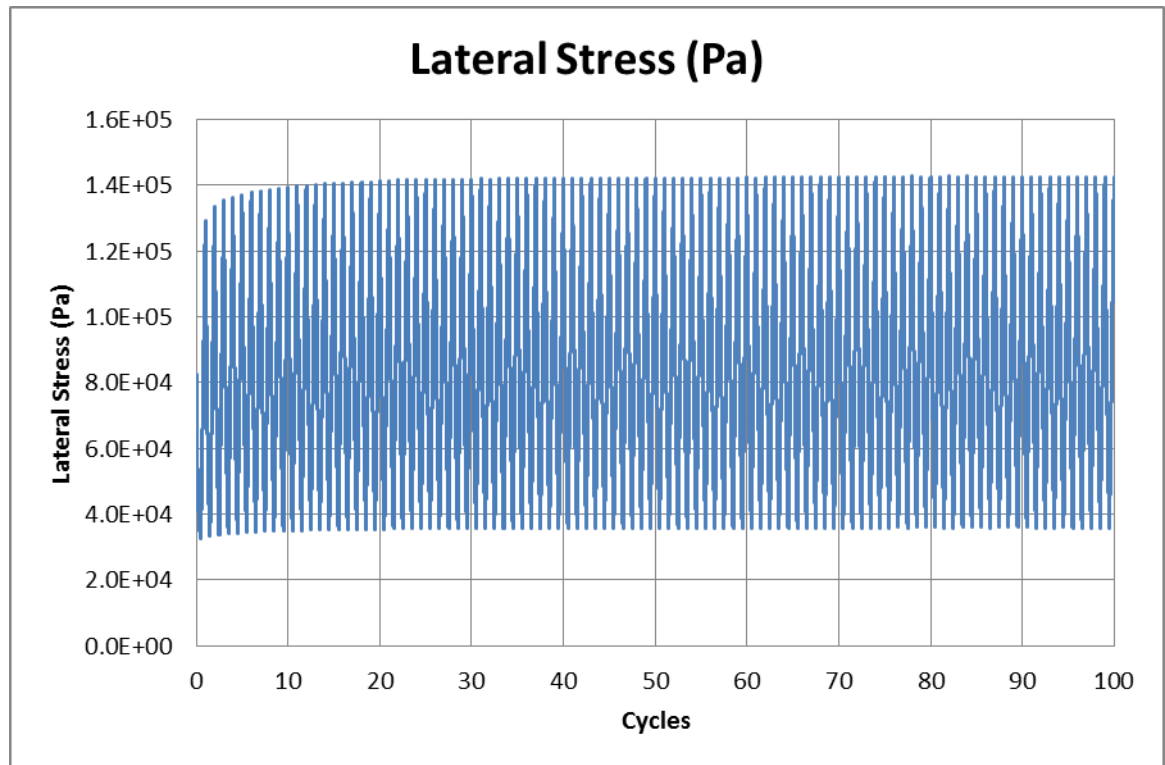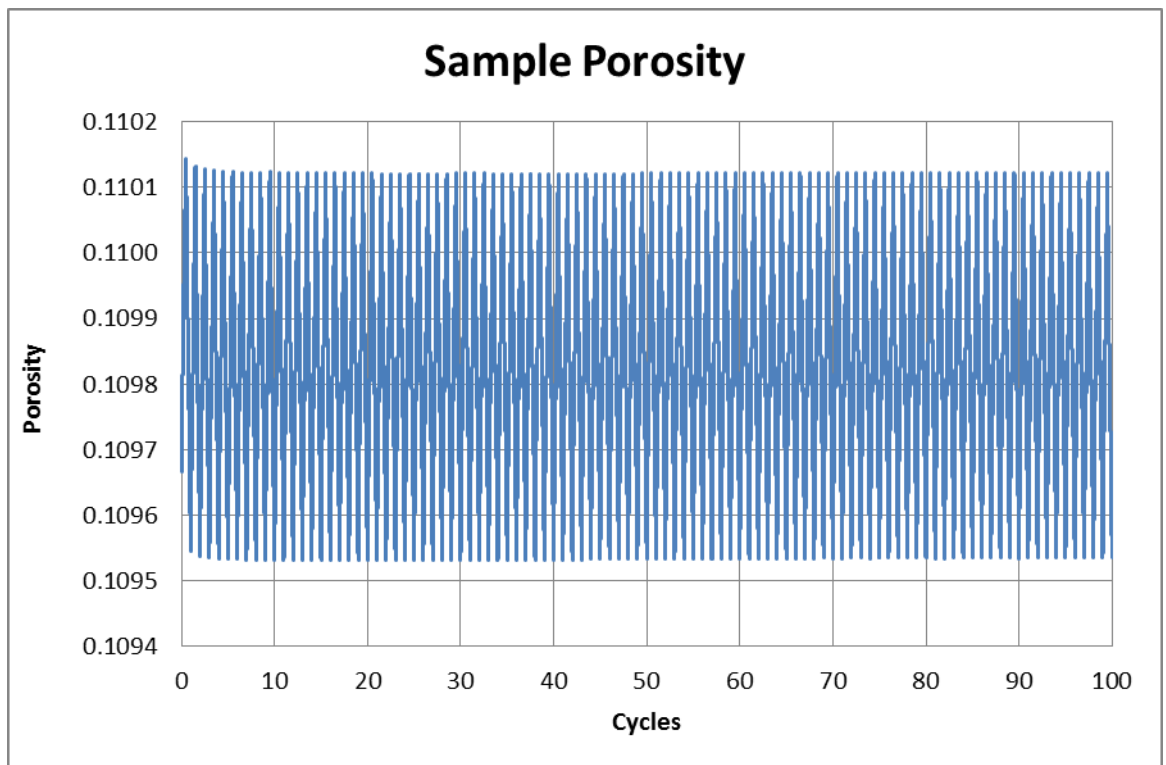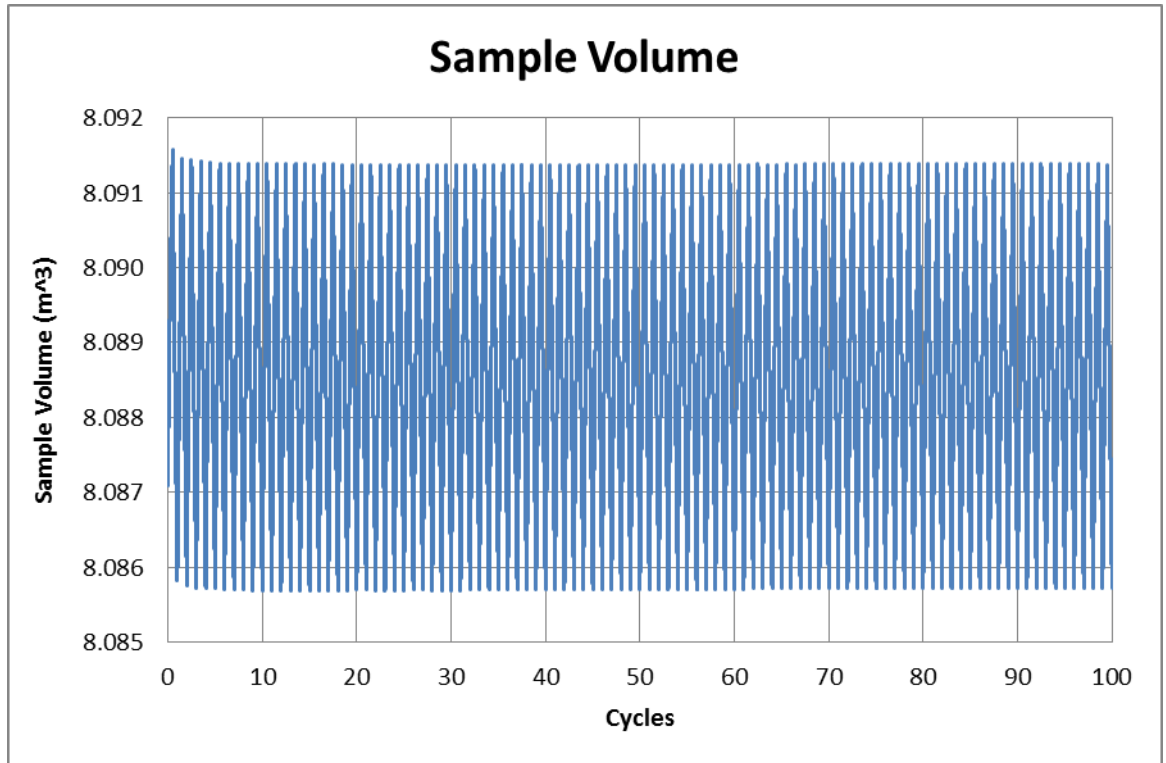
APPENDIX 10: Results for Triangular sample (Displacement)

cycles	0	1	10	20	30	40	50	60	70	80	90	100
average (m)	0	0.000273	0.000347	0.000356	0.000364	0.000372	0.000376	0.000378	0.000381	0.000381	0.000393	0.000395
standard deviation (m)	0	0.000434	0.000495	0.000531	0.000547	0.000578	0.000638	0.000585	0.000656	0.000597	0.000678	0.00064

Particle displacement Standard Deviation

Average particle displacement
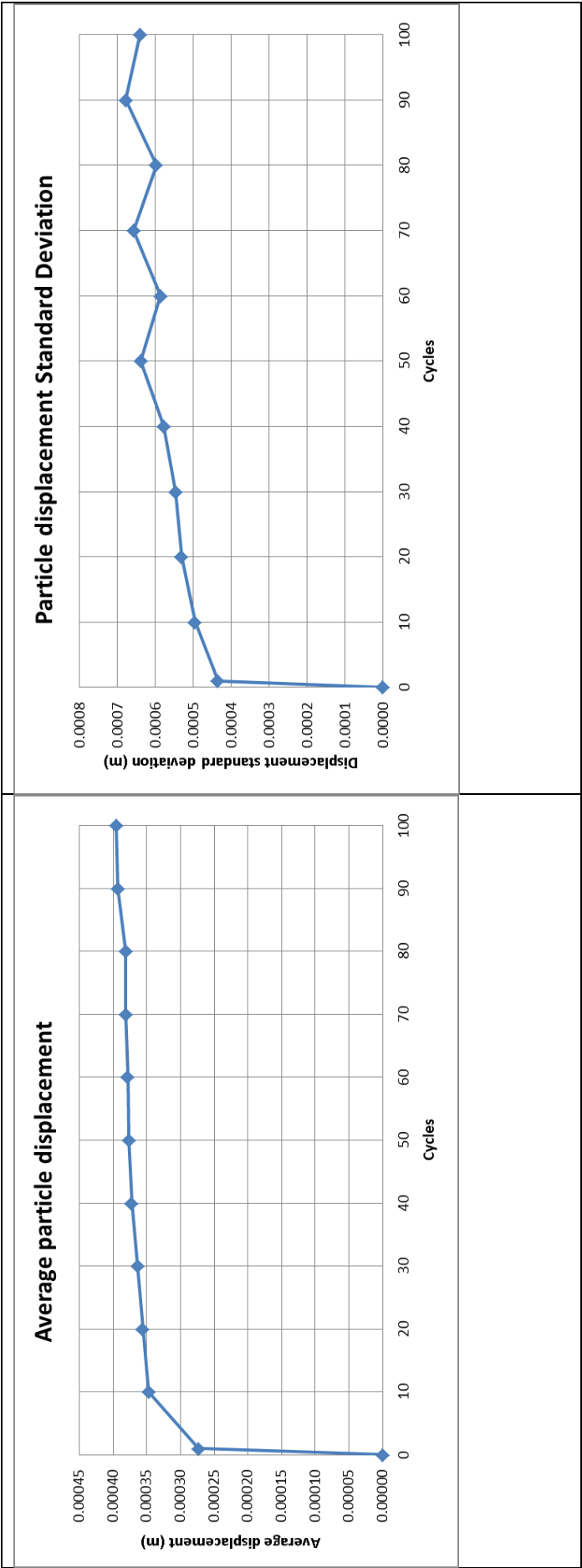
APPENDIX 10: Results for Triangular sample (Absolute angles turned)

cycles	0	1	10	20	30	40	50	60	70	80	90	100
average (Rad)	0	0.003174	0.006831	0.008012	0.008479	0.009165	0.009479	0.009645	0.009826	0.010201	0.010447	0.010721
standard deviation (Rad)	0	0.020762	0.031429	0.034733	0.036351	0.041824	0.042773	0.043187	0.04392	0.046184	0.047015	0.047629

Standard Deviation of absolute angles turned

Average absolute angles turned
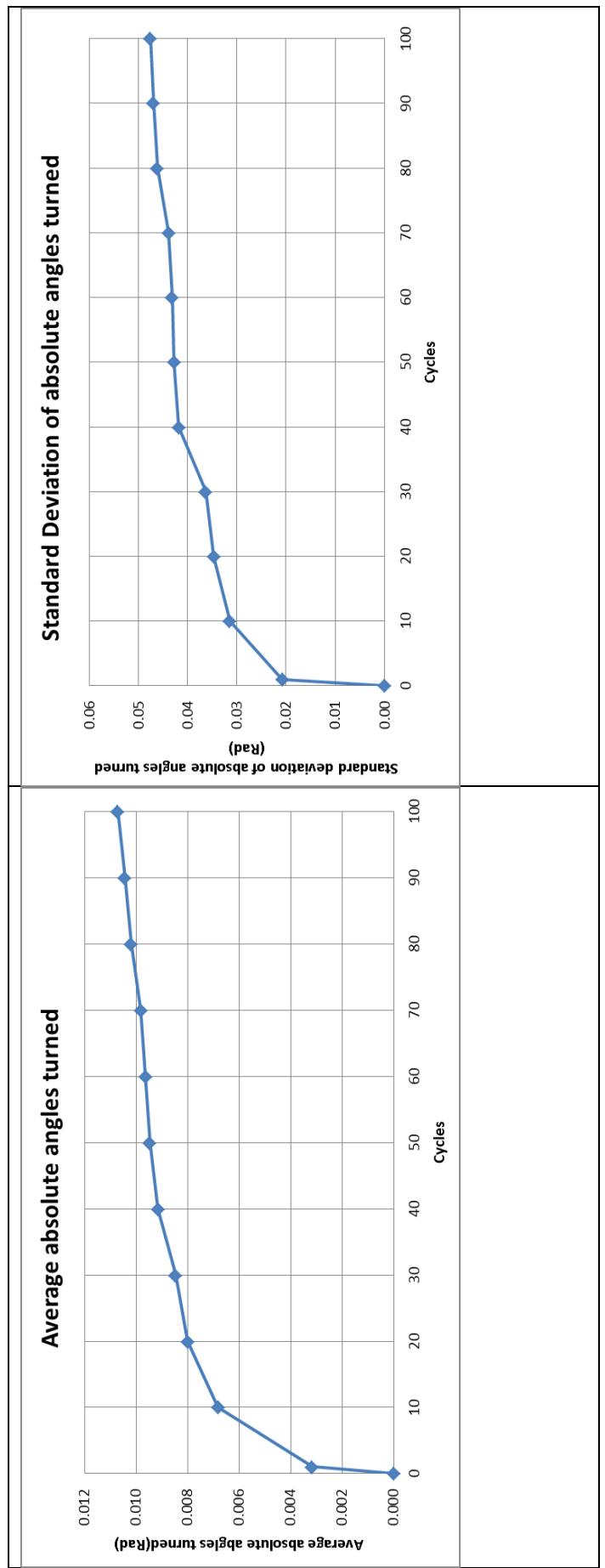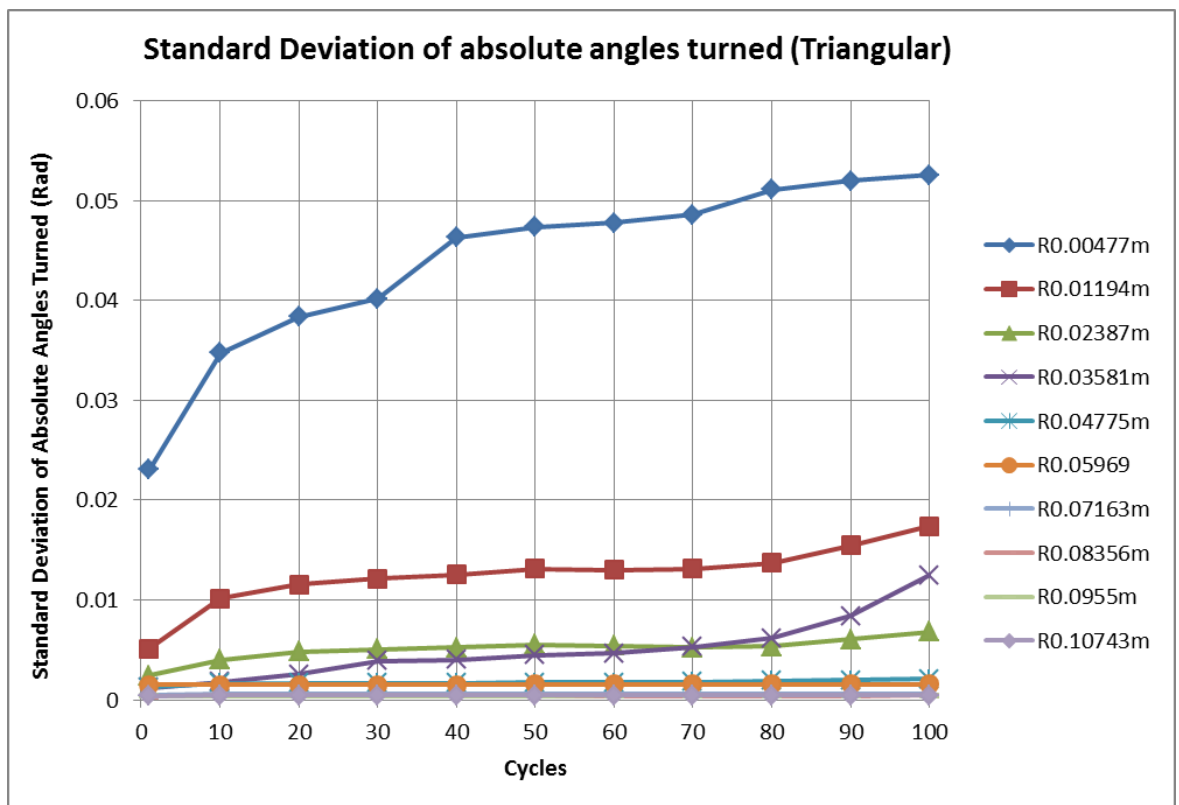
APPENDIX 11:

Particle activity in terms of sizes

APPENDIX 11: Particle activity in terms of sizes (Ni particles)

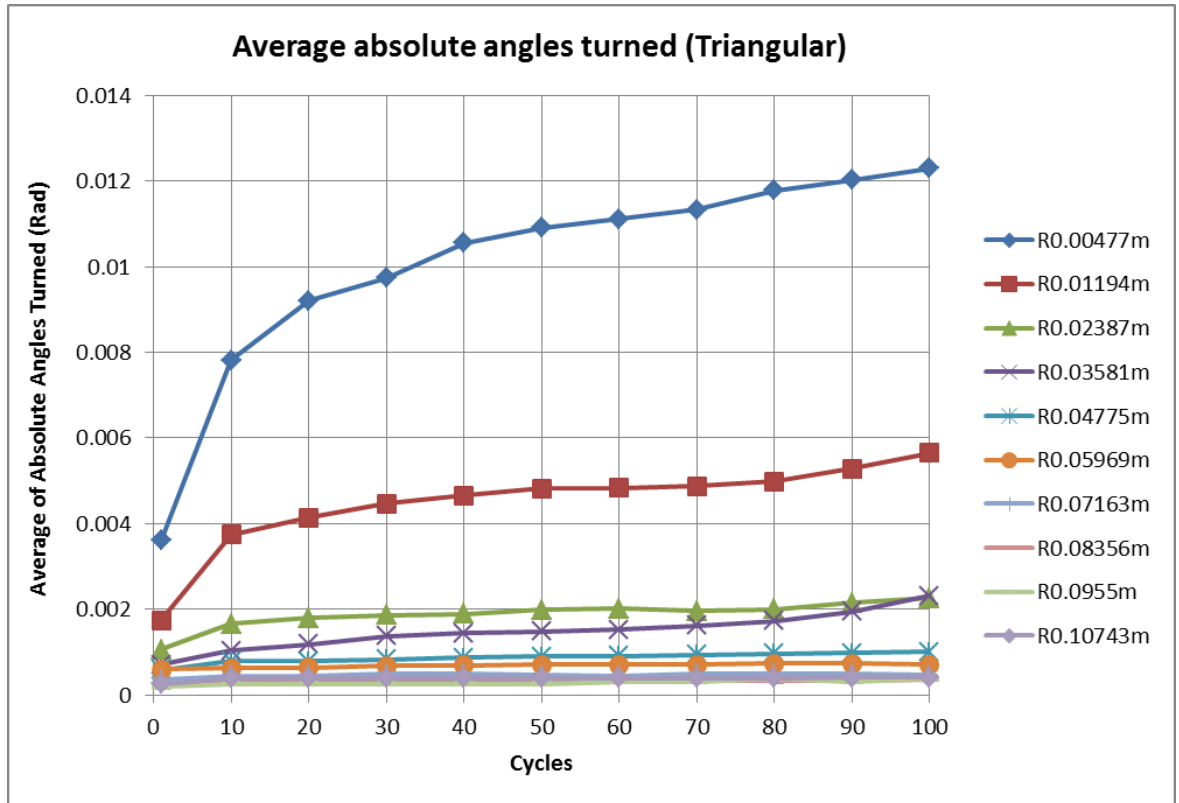# APPENDIX 11: Particle activity in terms of sizes (Ni particles)
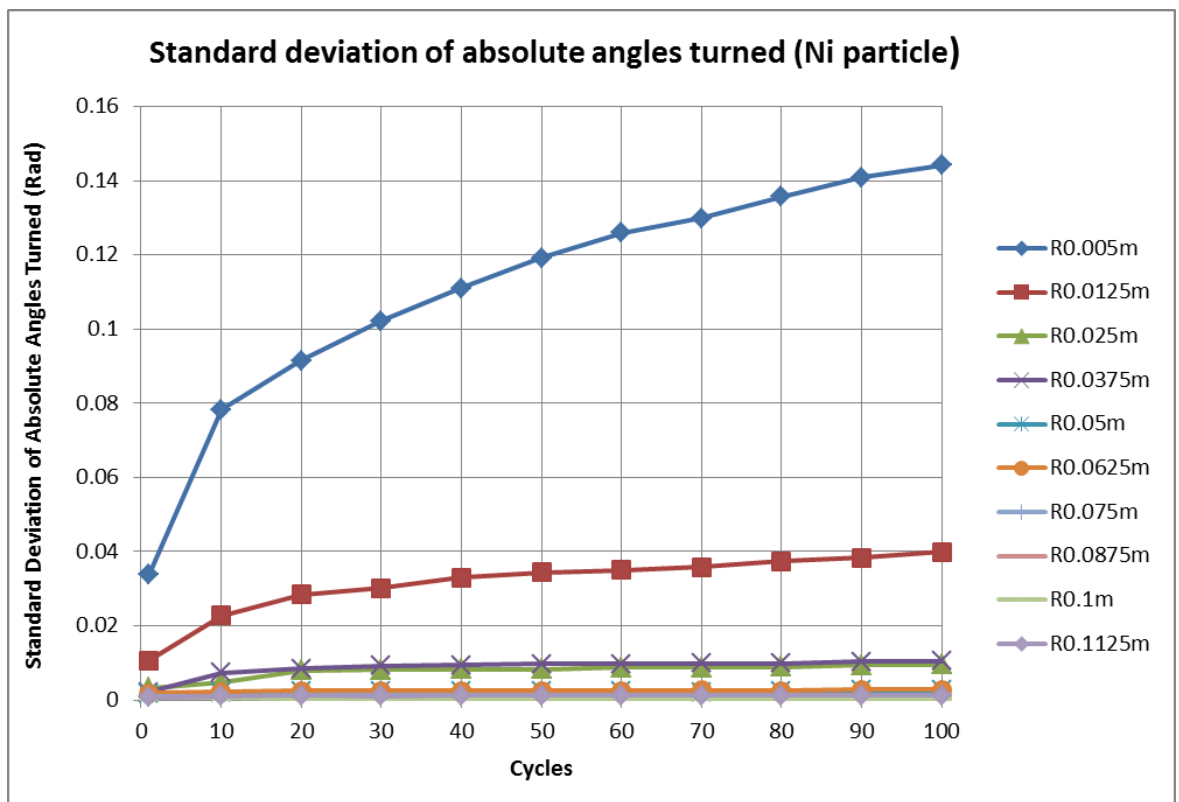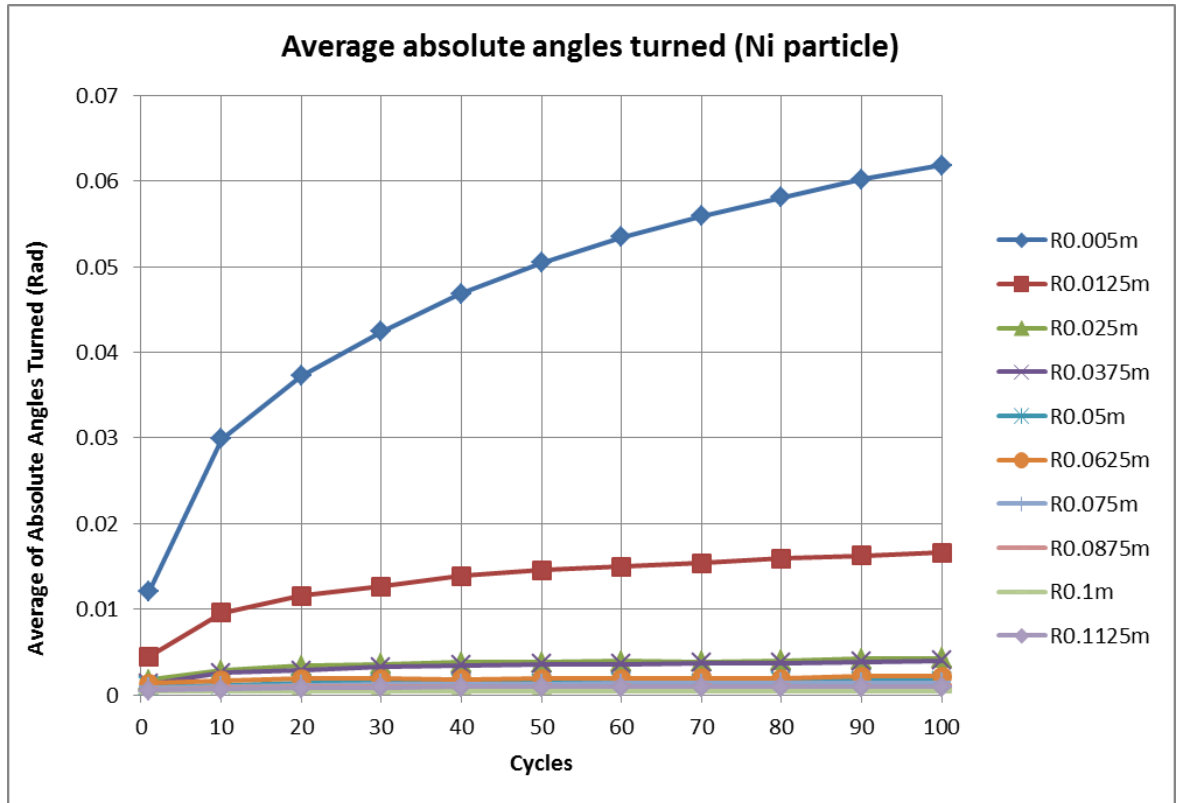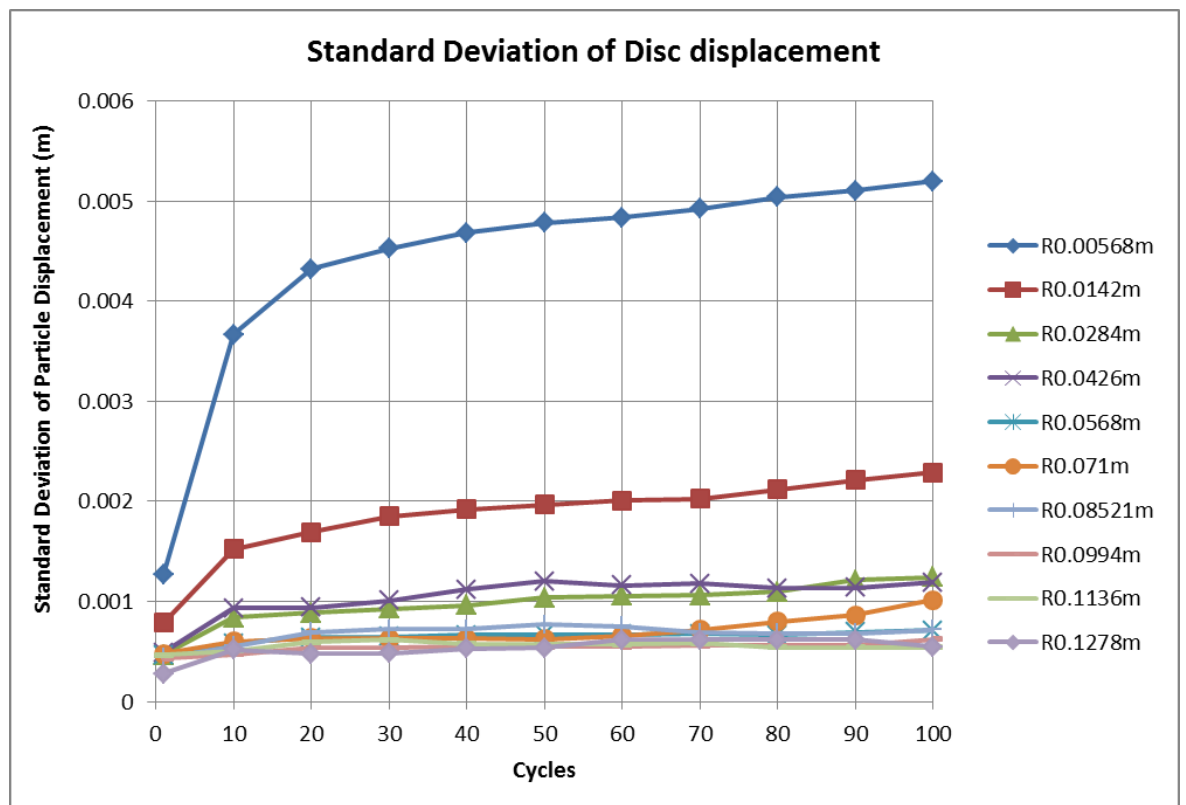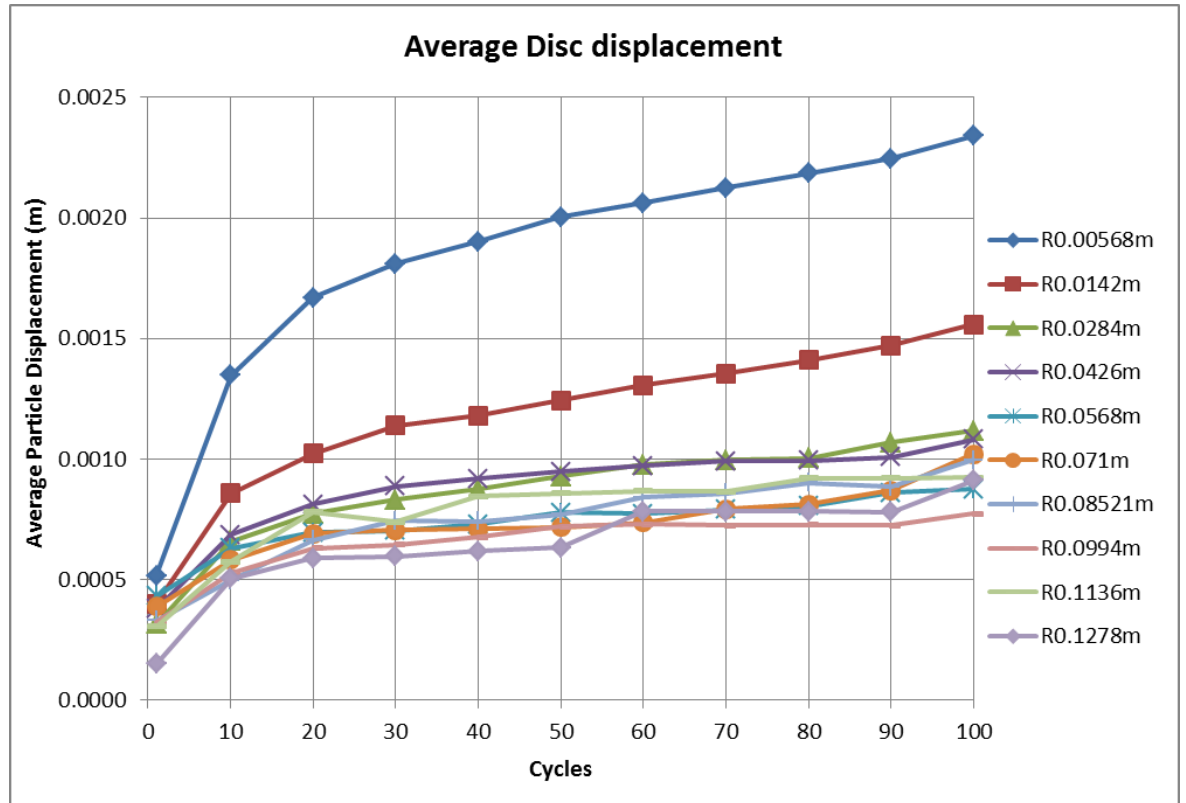
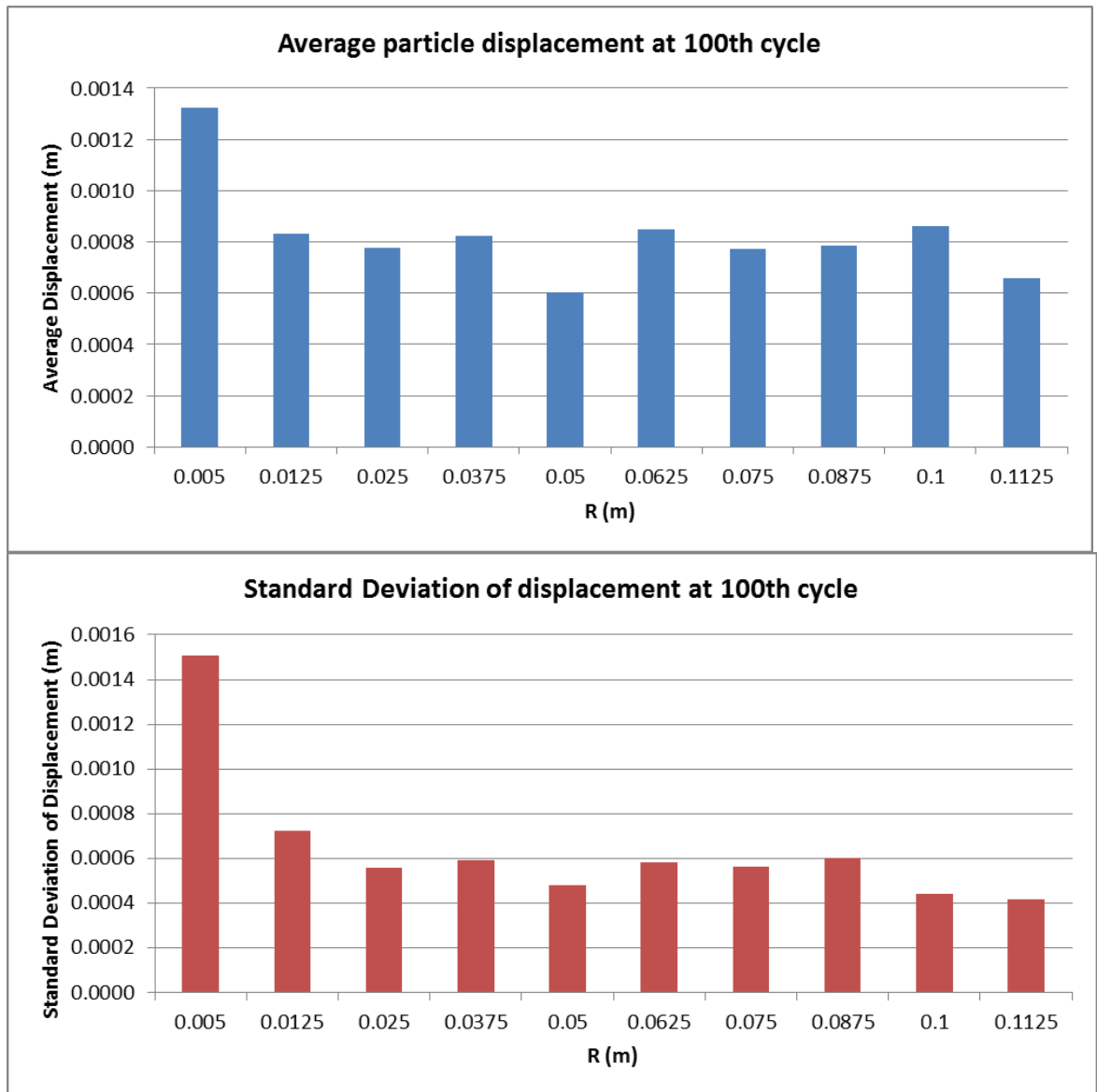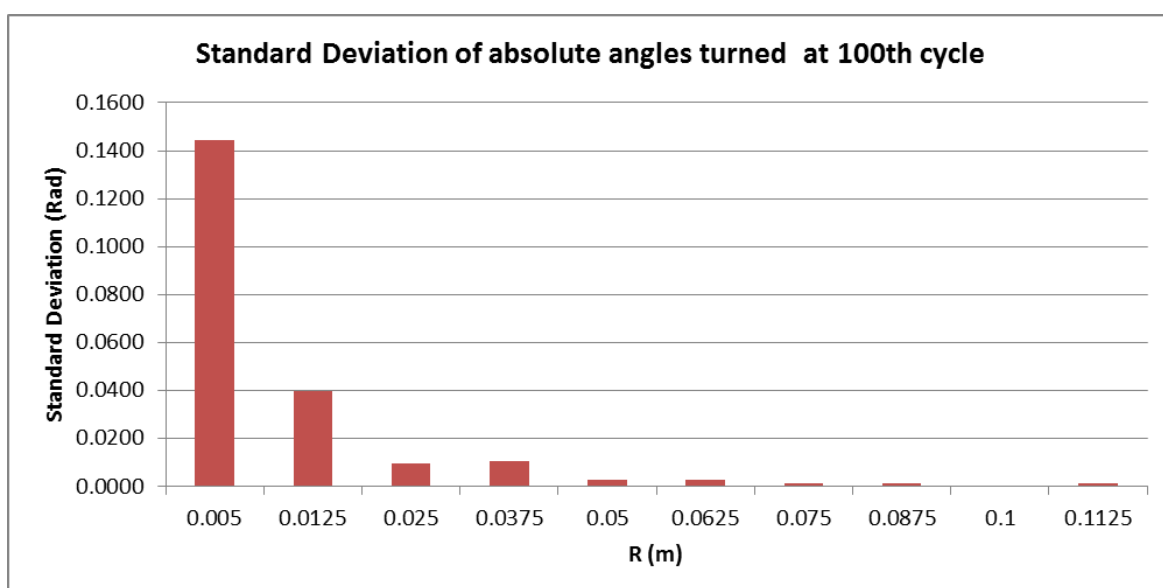Average absolute angles turned (Ni particle)

Standard deviation of absolute angles turned (Ni particle)

163

APPENDIX 11: Particle activity in terms of sizes (Disc particles)

Average Disc displacement

Standard Deviation of Disc displacement

APPENDIX 11: Particle activity in terms of sizes (Disc particles)

Average of absolute angles turned (Disc)

Standard Deviation of absolute angles turned (Disc)

APPENDIX 11: Particle activity in terms of sizes (Elliptic particles)

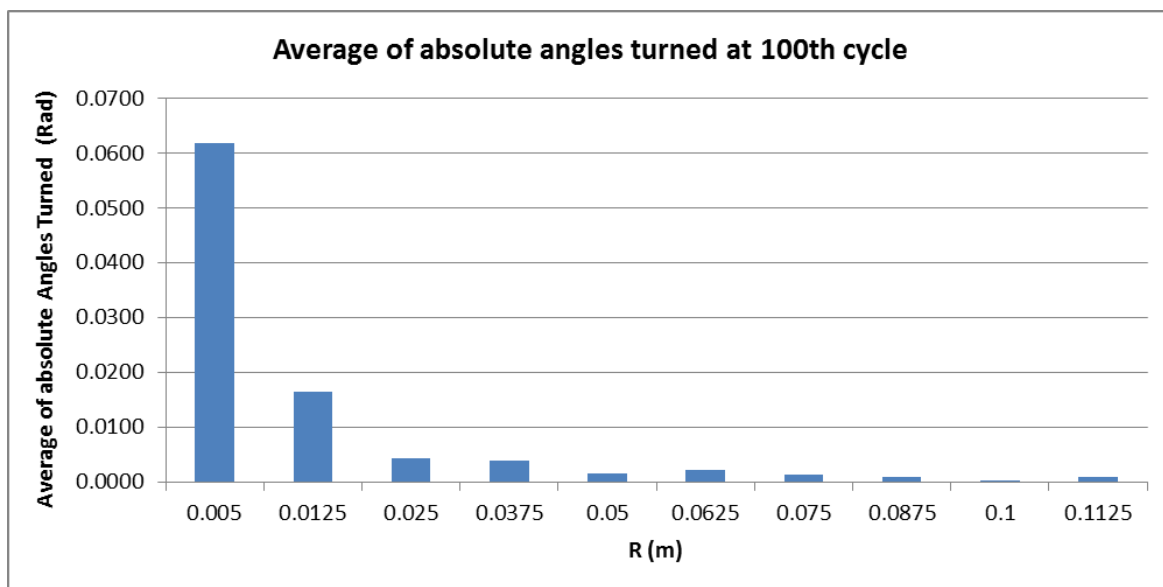# APPENDIX 11: Particle activity in terms of sizes (Elliptic particles)

Average of absolute angles turned (Elliptic)

Standard Deviation of absolute angles turned (Elliptic)

APPENDIX 11: Particle activity in terms of sizes (Triangular particles)

Average Triangular displacement

Standard Deviation of Triangular displacement

APPENDIX 11: Particle activity in terms of sizes (Triangular particles)

Average absolute angles turned (Triangular)

Standard Deviation of absolute angles turned (Triangular)
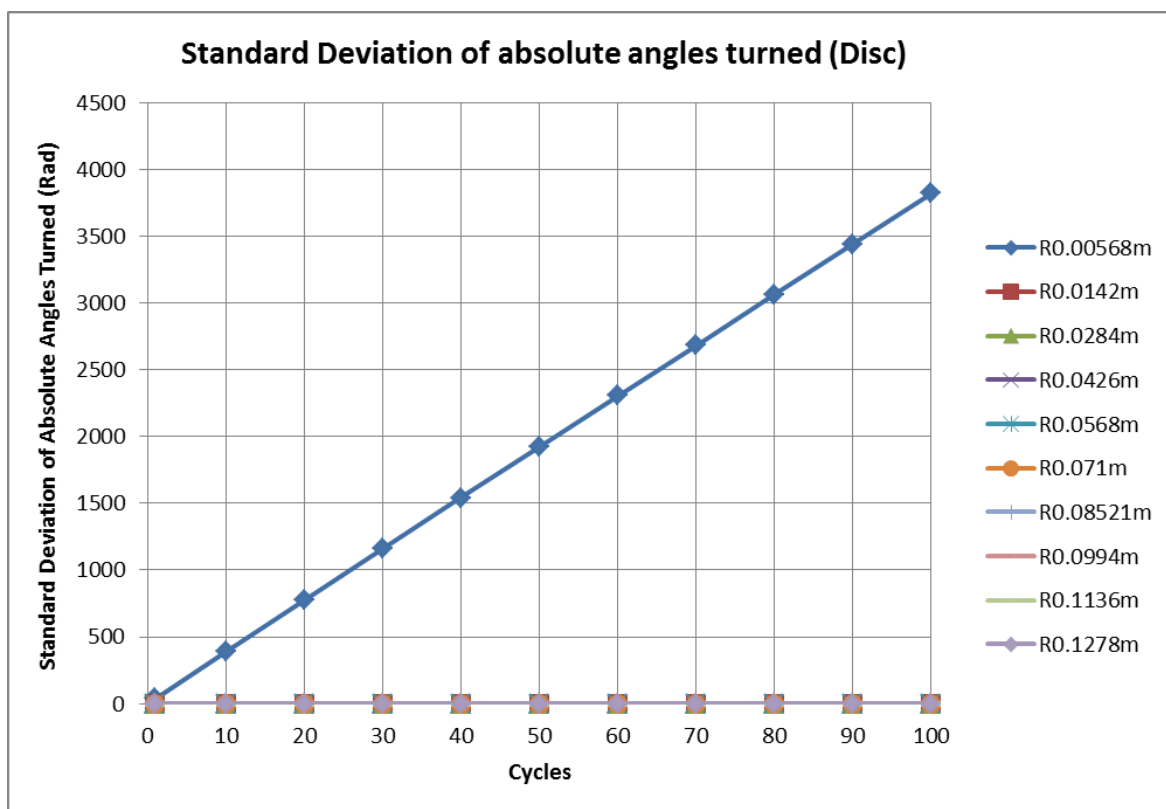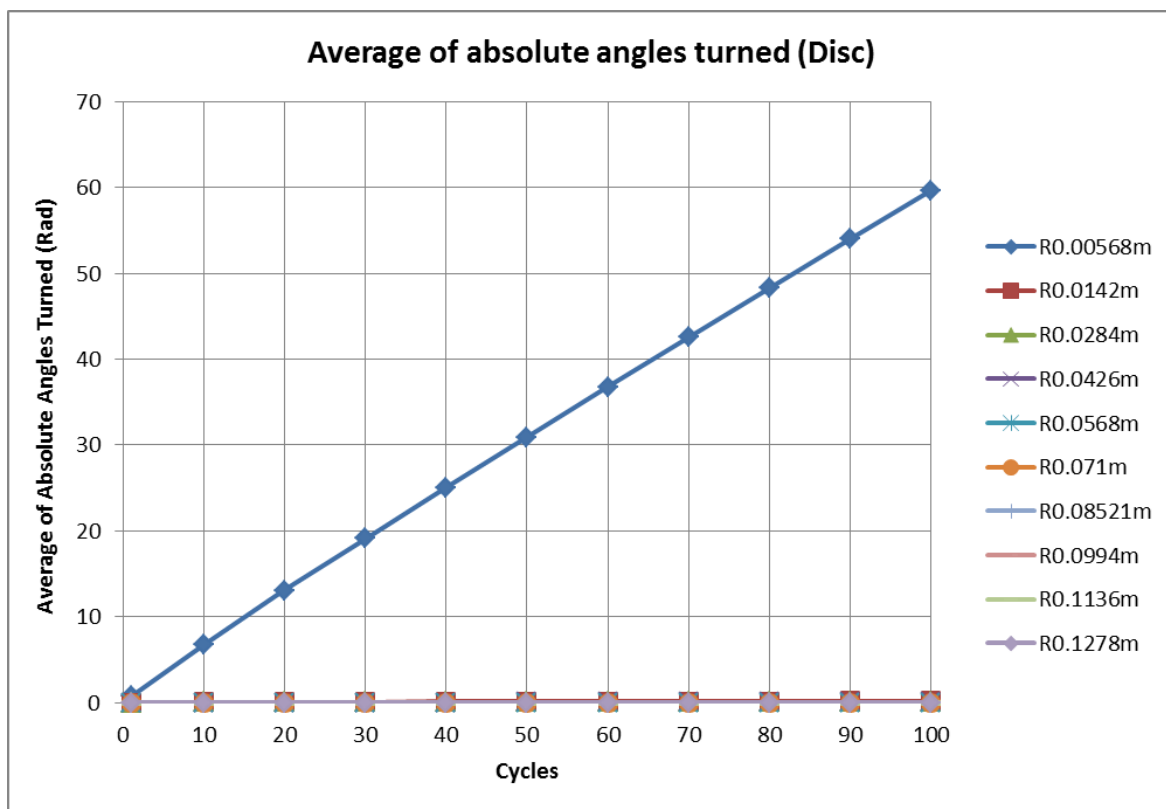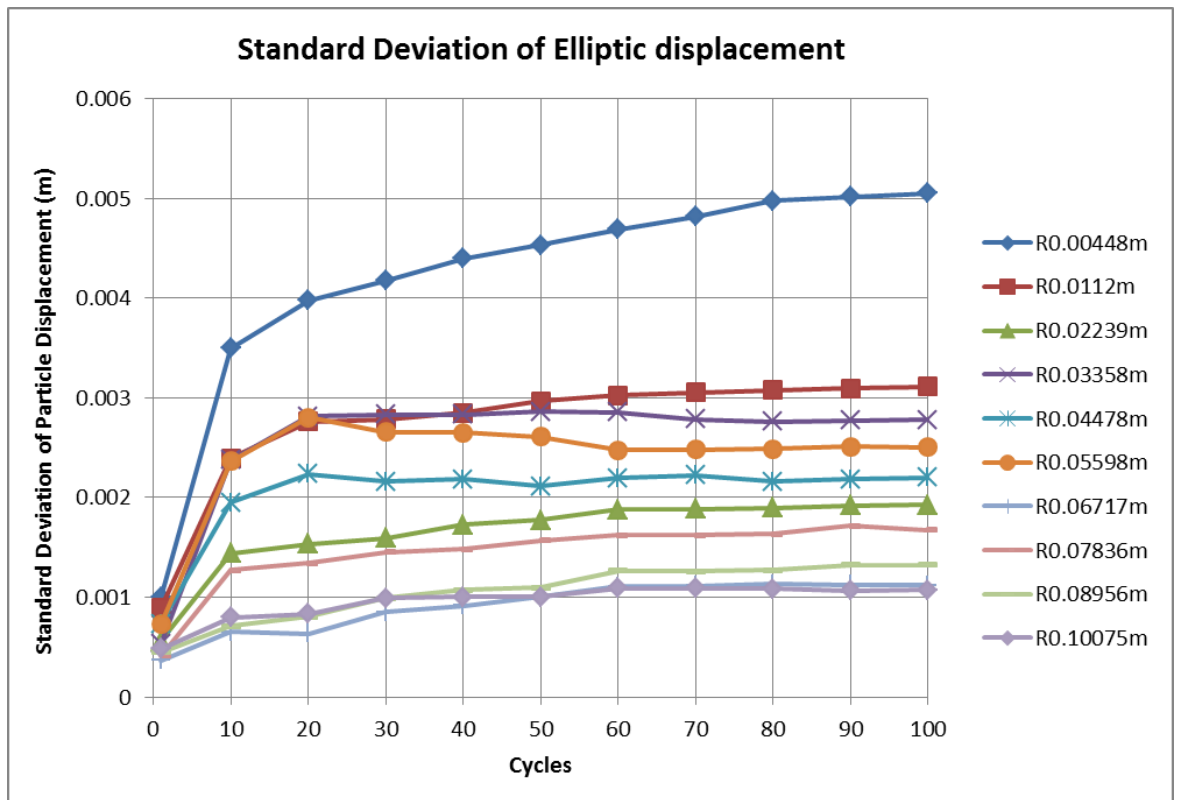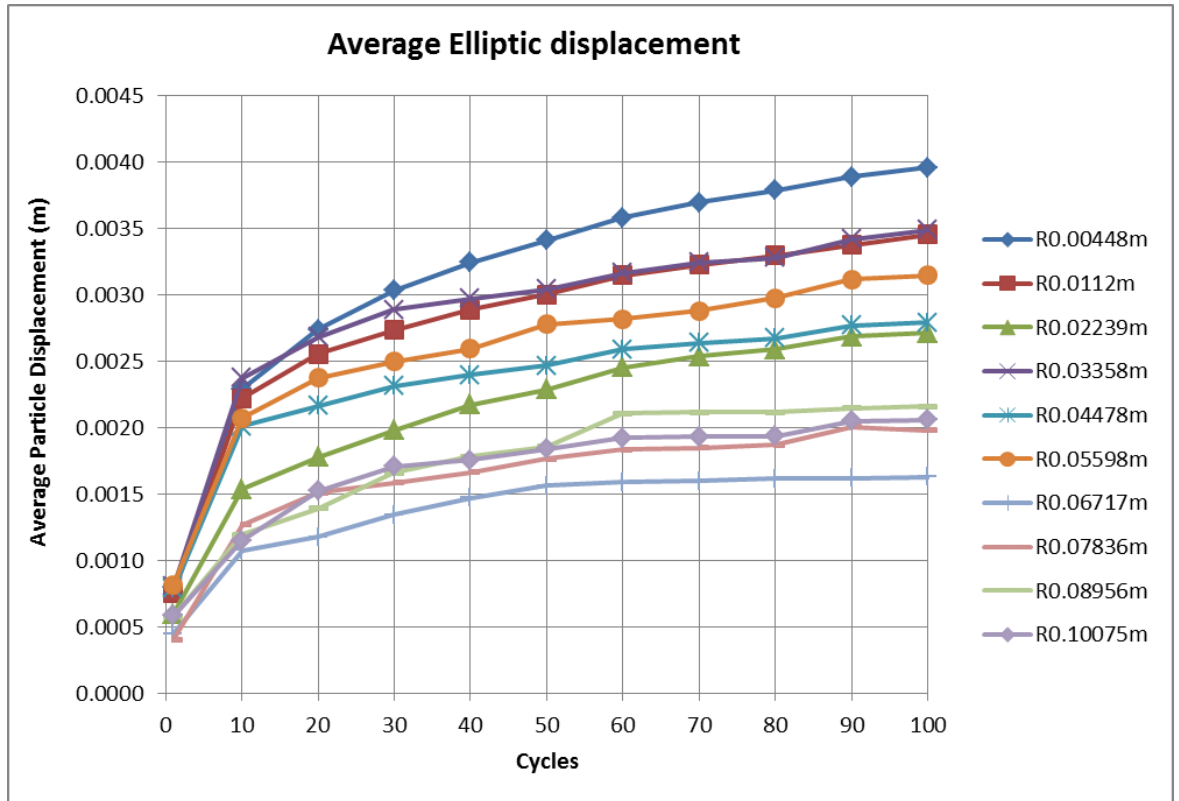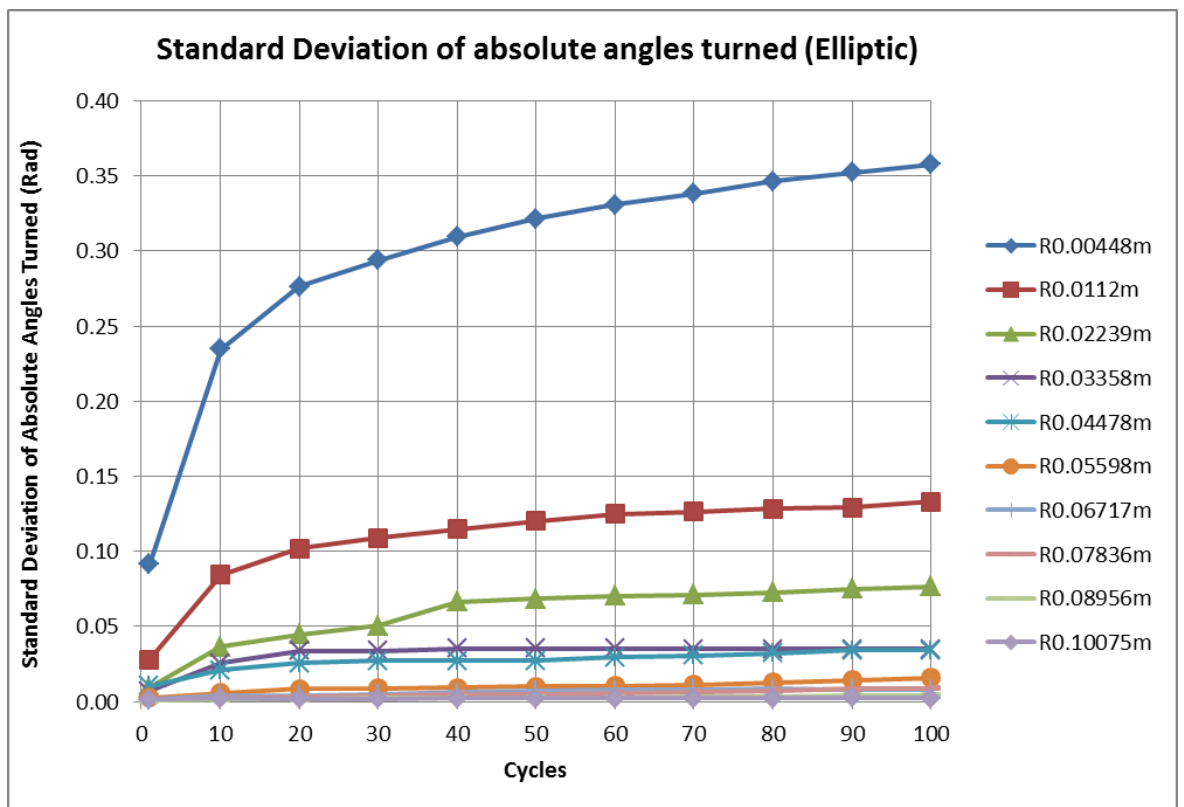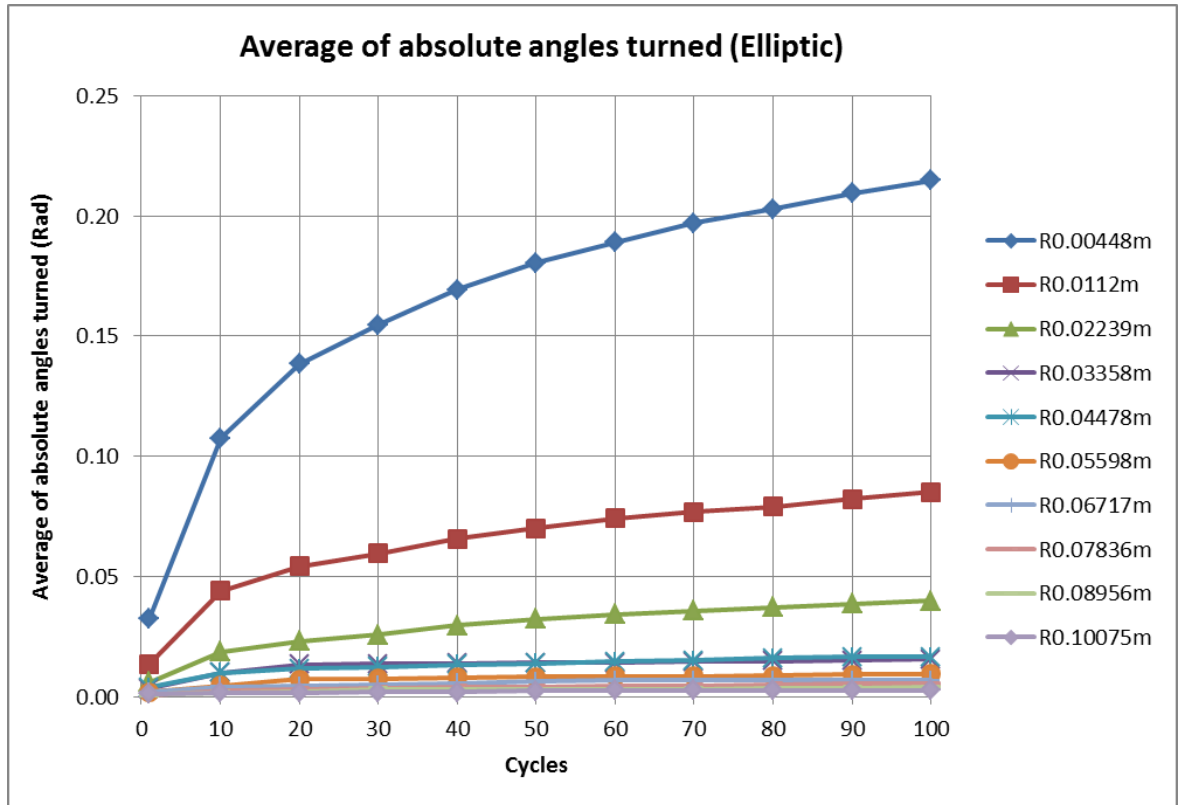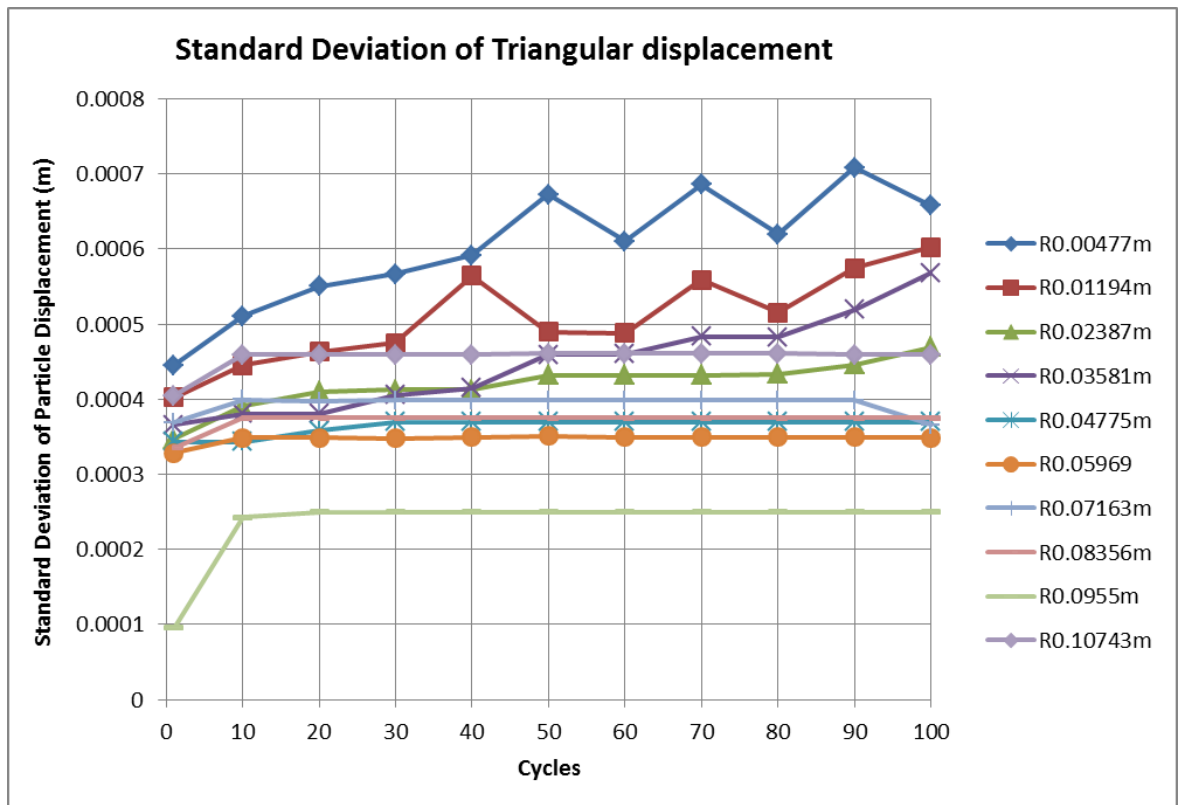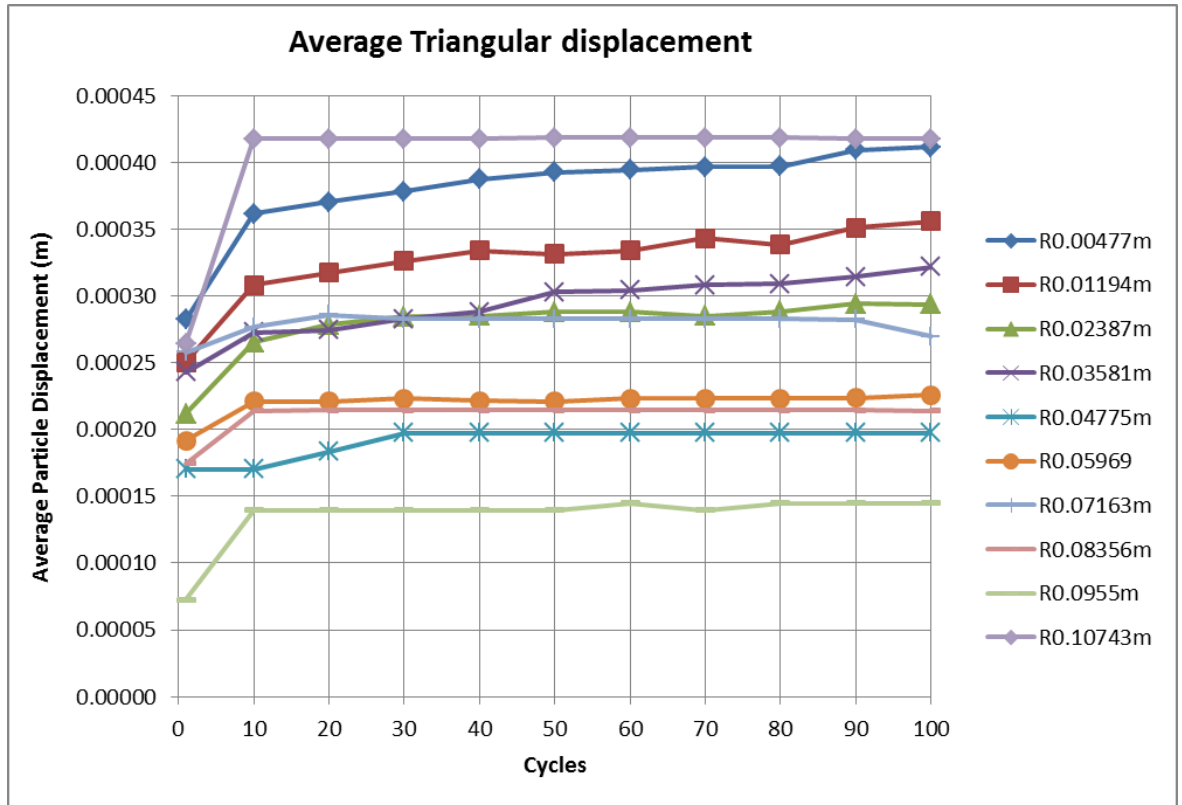
APPENDIX 12:

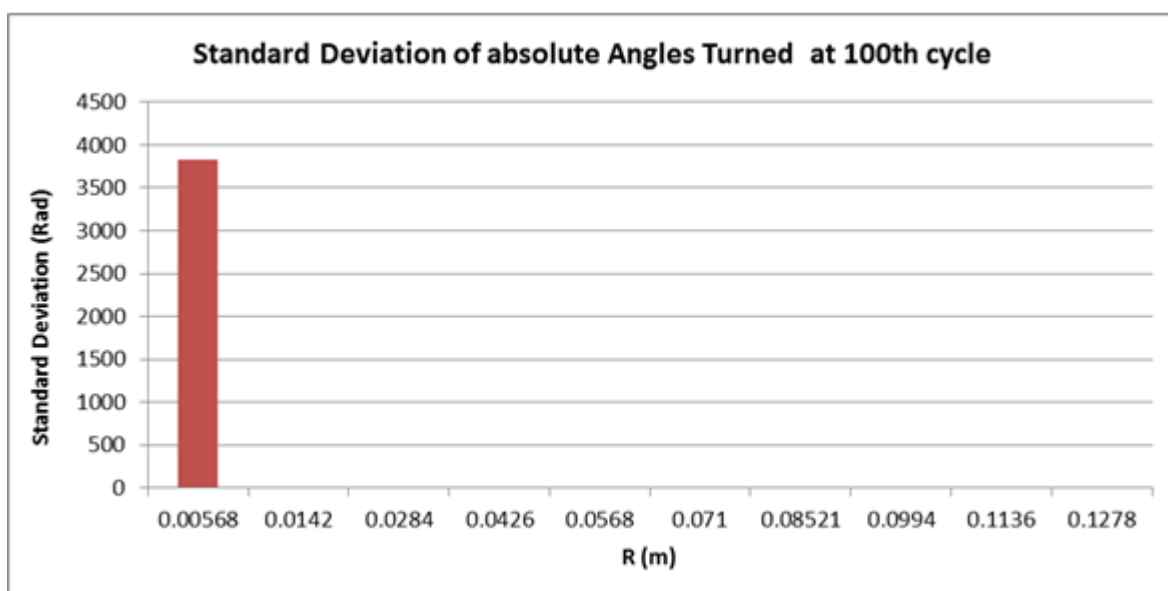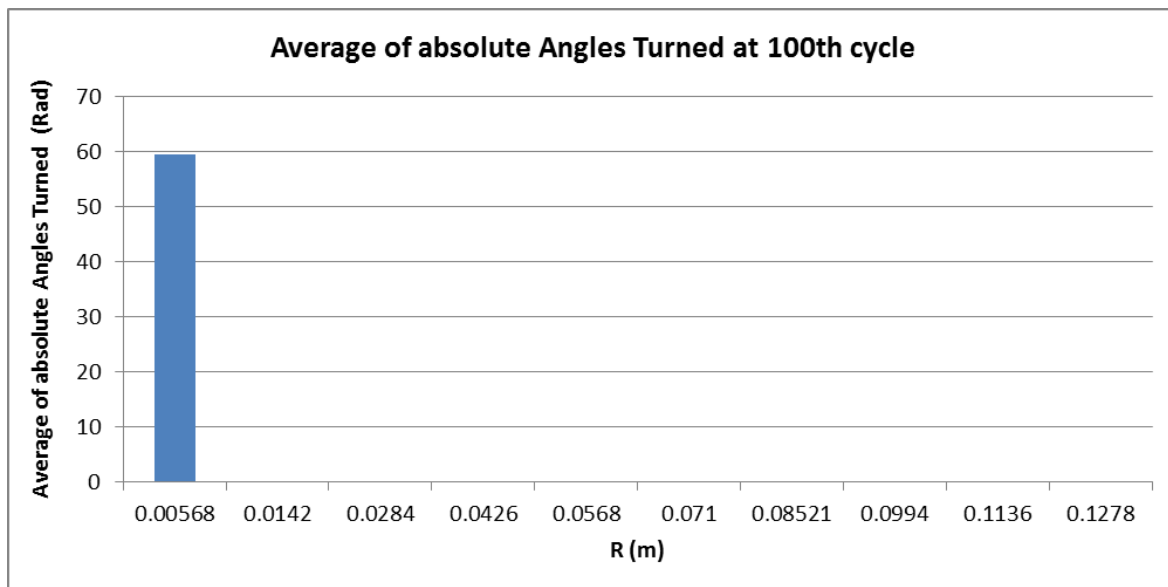# Particle activity at the end of 100th cycle

APPENDIX 12: Particle activity at the end of 100<u>th</u> cycle (Ni particle)

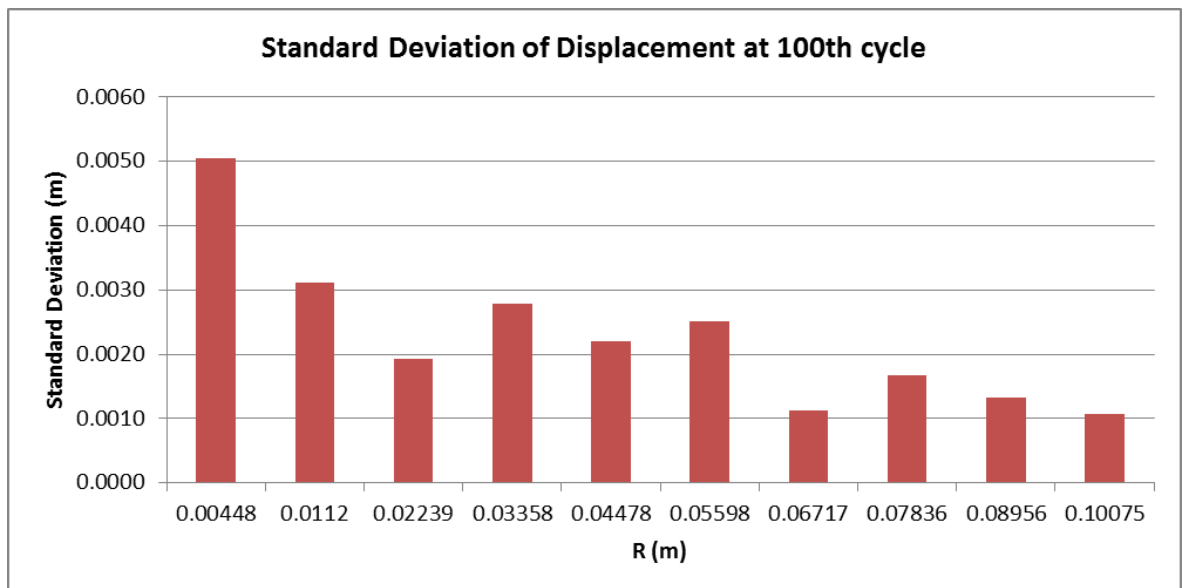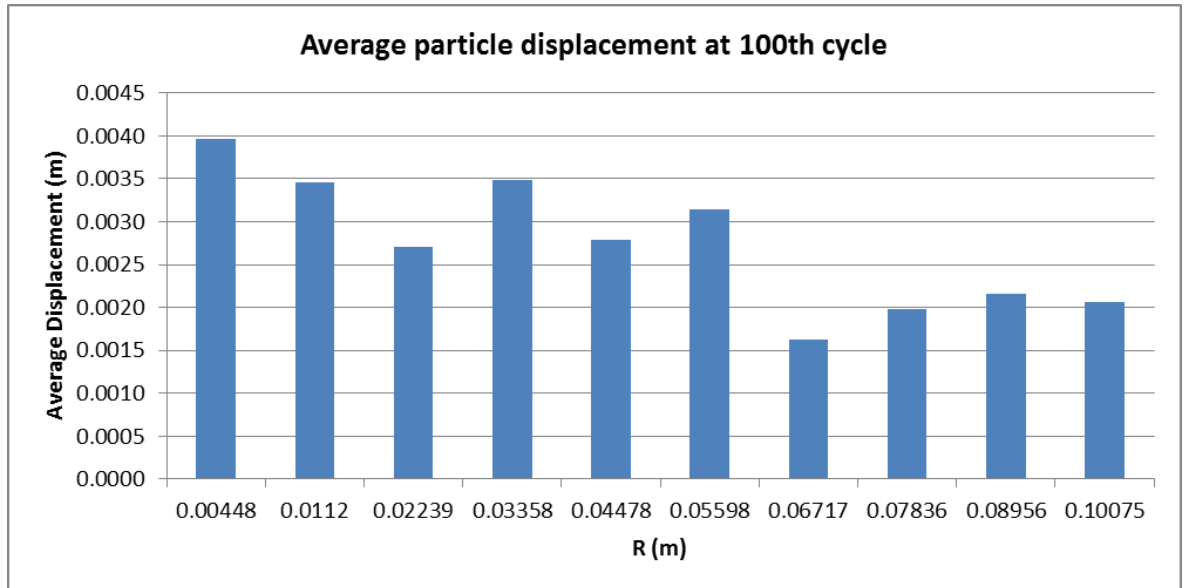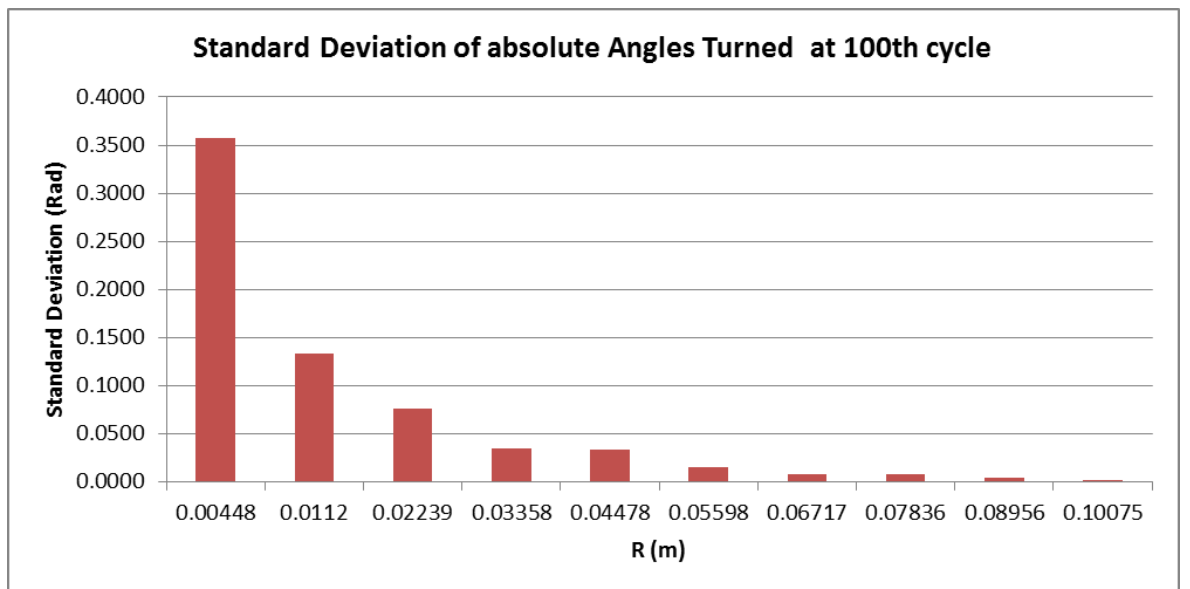# APPENDIX 12: Particle activity at the end of 100<u>th</u> cycle (Ni particle)
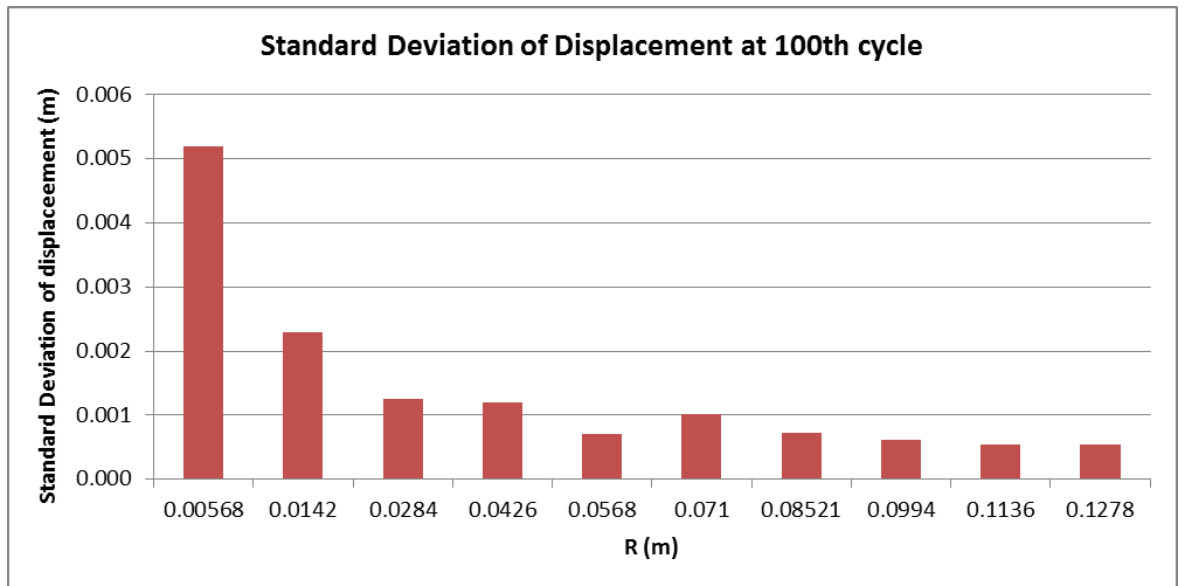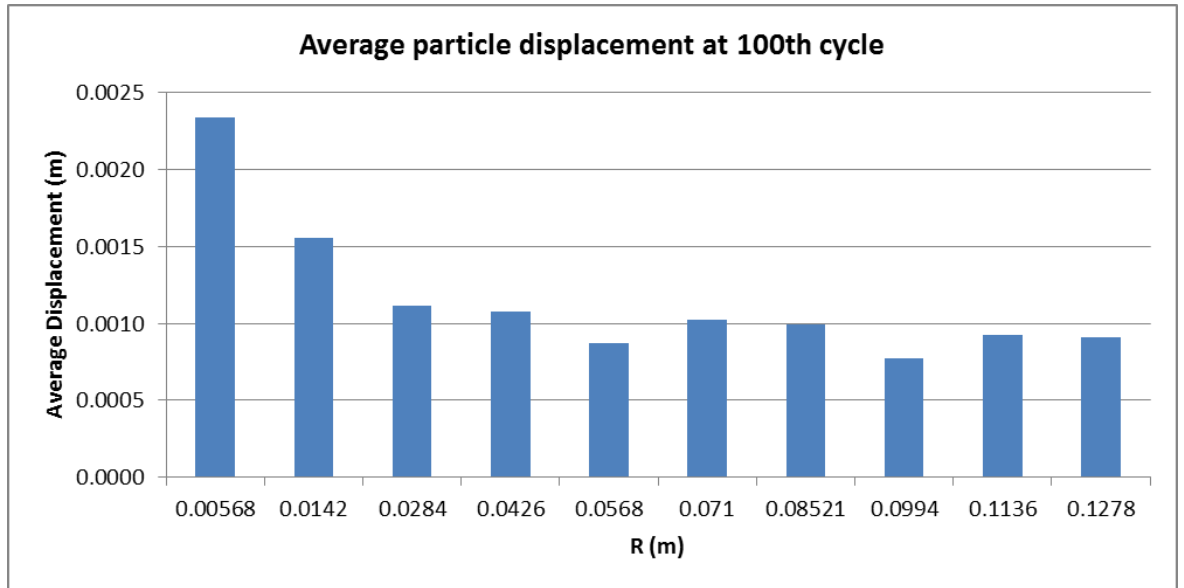
Average of absolute angles turned at 100th cycle

Standard Deviation of absolute angles turned at 100th cycle

APPENDIX 12: Particle activity at the end of 100th cycle (Disc)

Average particle displacement at 100th cycle

Standard Deviation of Displacement at 100th cycle

APPENDIX 12: Particle activity at the end of 100th cycle (Disc)

Average of absolute Angles Turned at 100th cycle

Standard Deviation of absolute Angles Turned at 100th cycle

APPENDIX 12: Particle activity at the end of 100<u>th</u> cycle (Elliptic)

Average particle displacement at 100th cycle

Standard Deviation of Displacement at 100th cycle

Average of absolute Angles Turned at 100th cycle

Standard Deviation of absolute Angles Turned at 100th cycle

APPENDIX 12: Particle activity at the end of 100th cycle (Triangular)
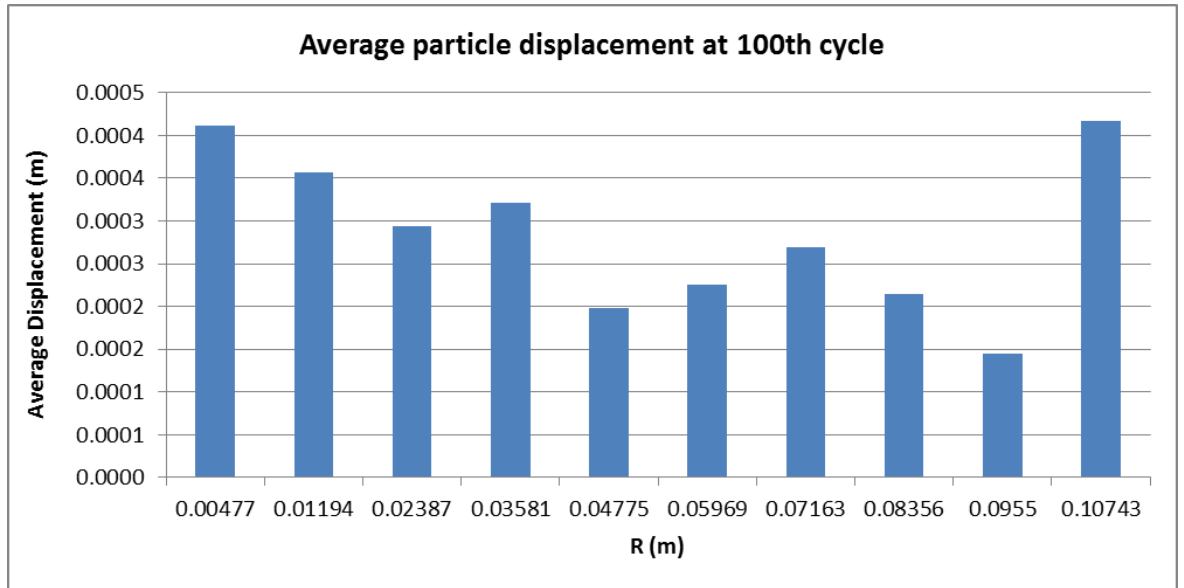

Average particle displacement at 100th cycle

Standard Deviation of Displacement at 100th cycle

APPENDIX 12: Particle activity at the end of 100th cycle (Triangular)

Average of absolute Angles Turned at 100th cycle

Standard Deviation of absolute Angles Turned at 100th cycle